X-ray scattering of halide perovskites and their derivatives: Crystallographic insights for photovoltaics and piezoelectrics.

A thesis submitted in fulfilment of the requirements

for the degree of Doctor of Philosophy

by

Esther Yi-Hang Hung

Department of Physics

University of Oxford

July 2026

"Seeing a person or piece of creation trampled should always disrupt something in us. It should always do something to the soul. And when you trace that trampling back across generations and systems and powers, a quiet sorrow is born in you."

- Cole Arthur Riley

"There is no such thing as a single-issue struggle, because we do not lead single-issue lives.

Our struggles are particular, but we are not alone.

What we must do is commit ourselves to some future that can include each other and to work toward that future with the particular strengths of our individual identities."

- Audre Lorde

Abstract

This thesis presents studies of hybrid organic-inorganic metal halides using X-ray diffraction techniques, focusing on their applications in piezoelectricity and photovoltaics. The development of sustainable energy materials is crucial in addressing global climate change, with applications spanning from small-scale energy harvesting for wearable electronics to large-scale grid-connected photovoltaics. A fundamental understanding of structure-property relationships is essential for designing materials with enhanced performance.

The symmetry of atomic arrangements governs material properties, yet determining these symmetries can be challenging. X-ray scattering provides a powerful means to probe material structure, as its wavelength matches atomic spacings, enabling direct measurement of electron density distributions. Understanding materials from an atomistic perspective enables their tailoring of specific properties. The first part of this thesis focuses on the structural design and characterisation of several novel, lead-free organic-inorganic metal halides and their phase transitions. The second part of this thesis focuses on the modulation of solution-based crystalline growth of lead-free organic-inorganic metal halides, to improve their photovoltaic performance. Throughout, the structural characterisation measurements are accompanied by a range of complementary techniques, such as thermal analysis, nuclear magnetic resonance spectroscopy, piezoelectric measurements and computational modelling, in order to provide a comprehensive understanding of the materials and their properties.

We begin in Chapter 1 with a rationale for the study of sustainable energy materials, in particular hybrid organic-inorganic metal halides, for piezoelectricity and photovoltaics, and the importance of understanding their structure-property relationships.

We then present in Chapter 2 the background theory to understanding crystal structure and the connection to their electronic and electrical properties. This is followed by a review of the current state of the art of hybrid organic-inorganic metal halide piezoelectric materials and their design principles, including the limitations of the current state of the art. An introduction to metal halide perovskites, including an overview of the challenges associated with the synthesis and characterisation of hybrid organic-inorganic metal halide perovskites is also given.

Chapter 3 presents a detailed overview of the experimental procedures followed throughout this thesis, including the synthesis, characterisation and analysis of the materials studied. A detailed description of the various X-ray diffraction techniques used is given, including the data collection, reduction and analysis procedures.

A novel, lead-free halobismuthate piezoelectric system $(TMIM)_3Bi_2I_9$ is introduced in Chapter 4. By constructing an organic-inorganic system with a low-dimensional inorganic core paired with a polar organic cation with strong organic-inorganic interactions, we are able to demonstrate high piezoelectric performance - with an up-to four-fold increased compared with other halobismuthate piezoelectric materials.

For furthering the understanding of the structural design principles for hybrid organic-inorganic metal halide systems, Chapter 5 follows with our exploration of structural modifications to the $(TMIM)_3Bi_2I_9$ system leading to three distinct novel systems. We reveal how systematic changes can maintain polar and non-centrosymmetric structures, providing valuable insights into the design principles of hybrid organic-inorganic metal halide systems.

Chapter 6 describes a series of related halobismuthate and haloantimonate systems and their crystal structures which were synthesised and characterised as part of our investigations in Chapter 4 and Chapter 5.

Finally, we study not just the final crystal structure, but the process of crystalline growth from solution, in the context of metal halide perovskites, in Chapter 7. In particular, we investigate intermediate phase pathways in Pb and Sn-based perovskites, in order to rationalise their differences despite their structural similarity in the final 3D perovskite phase. We find that certain novel intermediates can be introduced into the growth process, providing future opportunities to improve the photovoltaic performance of Sn-containing systems via control of their crystallisation pathways.

Acknowledgements

First and foremost, I would like to thank my supervisors, Prof. Henry J. Snaith and Dr. Harry C. Sansom, for their guidance and support throughout these last few years. Being the first 'Snaithling' to embark on a project on novel piezoelectrics has emboldened my growth in independence and initiative. Thank you Henry, for trusting and challenging me with this project.

Harry, thank you for your excitement for the weird and wonderful world of non-perovskites, crystals and X-rays. Thank you for putting up with my uncertainties and frustrations, and your continued guidance, optimism and encouragement even from beyond Oxford. Your support and kindness has been beyond what I could have hoped for in a supervisor.

And Clare Moloney, who the Snaith group would be utterly lost without - thank you.

My growth in ability to lead, carry out and complete projects with questions and curiosity is in large part thanks to being immersed amongst the excellent and varied scientific minds of my office-mates, colleagues, beamtime teams and collaborators - thank you all. Not only for your time in listening to my questions and your generosity in time and knowledge, but also for the funny science chats, pub nights and frequent procrastination.

In particular, I thank my closest collaborators and dear friends Benny and Joel. Benny, for being up for delving in to the world of piezoelectricity with me, for many long and late nights spent with big magnets and X-rays, and for your guidance, enthusiasm and encouragement in moments when mine was lacking. Joel, thank you for your guidance even beyond academia, for championing open, curious and collaborative science, and for handing me the GIWAXS baton - I really ran with it.

I thank figure skating, which has offered me daily, expressive release from the pains of failed experiments and confusing data. Thank you to the figure skaters and coaches for facilitating me, as a beginner, to fall in love more and more with a sport so breathtakingly gorgeous, athletic and exhilarating.

To all the beautiful people close to me, who I'm lucky to say are far too many to list here - the London pals, the figure skaters, the scientists and the wonderfully miscellaneous groups - thank you for backing me. You have been, and continue to be, invaluable to me and a maintainer of my sanity in more ways than you know.

The journey prior to this was frequently turbulent and painful, but the period coinciding with my PhD has marked the first in my adult life of living, rather than surviving. I am grateful for my mind and body, which has, for the first time, experienced full health and stability in the last few years. Much of how I have gotten

to where I am today, submitting this thesis, is due to the support of professionals, hospitals and loved ones. Thank you for believing for me when I stopped. I literally would not be here today without you. Thank you to those who have loved and joined me whilst I have become myself, healed, and found - and continue to find - joy during recovery and beyond. It gets better.

My faith and spirituality has evolved and changed significantly over the last few years, and remains a complex journey which I continue to gently venture along. However, I am thankful for how it has been foundational to shaping the life I desire to live; to care for people and the earth with fairness and justice. This is the reason for the work I do.

媽媽, 我非常感謝你的禱告, 你的信仰和你的温柔但堅定的靈魂。Your astounding resilience and unwavering, sacrificial dedication to loving us is my inspiration and my strength. Moses, thank you for your pragmatism and for putting up with my crazies over the years. Thank you Sam, who has, more than anyone else in the world, shaped the person I'm proud to be today. *I dedicate this to you.*

Contents

Abstract vii

Acknowledgements ix

List of Figures xiv

List of Tables xxi

List of Publications xxiii

1 Introduction 1
- 1.1 Background . . . 1
  - 1.1.1 Symmetry . . . 1
- 1.2 The global energy crisis . . . 2
- 1.3 Organisation of the Thesis . . . 4

2 Theory 8
- 2.1 Introduction . . . 8
- 2.2 Symmetry in crystalline materials . . . 8
  - 2.2.1 Periodic structures: Lattices and unit cells . . . 8
  - 2.2.2 Point symmetry operations . . . 10
  - 2.2.3 Symmetry groups and crystal systems . . . 11
  - 2.2.4 Space groups and additional symmetry operations . . . 11
- 2.3 Probing crystal structure . . . 12
  - 2.3.1 Reciprocal space . . . 13
  - 2.3.2 Diffraction . . . 14
  - 2.3.3 Structure factor . . . 16
    - 2.3.3.1 The Bragg condition . . . 17
- 2.4 Structure-property relationships . . . 19

2.4.1 Neumann's Principle . . . 19
2.4.2 Symmetry requirements for piezoelectrics and ferroelectrics . . 20
2.4.3 Semiconductors . . . 23
2.4.3.1 A brief introduction to semiconductors . . . 23
2.4.4 The photovoltaic effect . . . 24
2.5 Phase transitions . . . 26
2.5.1 Landau's theory for phase transitions . . . 27
2.6 Piezoelectricity and Ferroelectricity . . . 29
2.6.1 Traditional piezoelectrics . . . 30
2.6.2 The case for hybrid organic-inorganic piezoelectrics . . . 31
2.6.3 Design principles of organic-inorganic metal halide piezoelectrics 31
2.7 Photovoltaics . . . 34
2.7.1 Perovskite structures and their polymorphs . . . 35
2.7.2 Solution processing of perovskites: Crystallization processes . 39
2.7.3 Solvent-based intermediate phases of metal halide perovskites . . . 41
2.8 Chapter Summary . . . 43

3 Materials and Methods 57
3.1 Fabrication . . . 57
3.1.1 Materials . . . 57
3.1.2 Synthesis of (TMCM)Cl and (TMBM)Br . . . 58
3.1.3 Single crystal growth . . . 59
3.1.3.1 Antisolvent vapour diffusion . . . 59
3.1.3.2 Slow-cooling . . . 60
3.1.3.3 Layered diffusion . . . 61
3.1.3.4 Single crystal growth of $CsSnI_3$·3DMSO . . . 61
3.1.4 Thin film processing . . . 62
3.1.4.1 Thin films of $(TMIM)_3Bi_2I_9$ . . . 62
3.1.5 Powders . . . 63
3.2 Blade-coated thin films for *in situ* GIWAXS . . . 64
3.2.1 Solution preparations . . . 64
3.3 Characterisation . . . 65
3.3.1 Single crystal X-ray diffraction (SCXRD) . . . 65
3.3.1.1 Data processing . . . 65
3.3.2 Powder or thin-film X-ray Diffraction . . . 67
3.3.2.1 Data processing . . . 67
3.3.3 Grazing incidence wide-angle scattering . . . 67
3.3.3.1 Synchrotron grazing incidence wide angle scattering measurements . . . 69
3.3.3.2 Data processing: an overview . . . 69
(i) Calibration . . . 69

(ii) Detector and polarization corrections 70
(iii) Masking 70
(iv) Grazing incidence geometry corrections 70
Data reduction 70
3.3.3.3 GIWAXS data processing protocols used 71
3.3.4 Solid state nuclear magnetic resonance (NMR) spectroscopy . 71
3.3.4.1 Solid state NMR spectroscopy measurements 72
3.3.5 Piezoresponse force microscopy 73
3.3.5.1 Piezoelectric measurements 74
3.3.6 Second harmonic generation (SHG) 74
3.3.7 Density functional theory (DFT) calculations 75
3.3.7.1 Electrostatic potential calculations 75
3.3.7.2 DFT and polarization calculations of $(TMIM)_3Bi_2I_9$ and $[(CH_3)_4N]_3Bi_2I_9$ 76
3.3.7.3 DFT relaxations 77
3.3.8 Molecular dynamics simulations using machine learning potentials 77
3.3.9 Polarization analysis 78

4 Tailoring a novel, lead-free organic-inorganic halobismuthate for large piezoelectricity 83
4.1 Abstract 83
4.2 Introduction 84
4.3 Results and Discussion 85
4.3.1 Designing halobismuthates for high piezoresponse 85
4.3.2 Phase transition behaviour: Differential scanning calorimetry . 90
4.3.3 Phase transition behaviour: Variable temperature SCXRD . . 91
4.3.4 Phase transition behaviour: Variable temperature solid-state NMR spectroscopy 95
4.3.5 Piezoelectric response 98
4.4 Summary 106

5 Tuning polar order in $(TMXM)_3M_2X_9$ materials via structural modifications 114
5.1 Introduction 114
5.2 Results and Discussion 116
5.2.1 Thermal analysis 116
5.2.2 Single crystal structural analysis 118
5.2.3 Second harmonic generation 122
5.2.4 Probing molecular dynamics with NMR 122
5.2.5 An aside: Unusual phase transition behaviour - reversible cyclic twinning 125

5.3 Conclusion . . . 137

6 Unfinished business: Yet more crystal structures 141
6.1 Background and introduction . . . 141
6.2 Results and discussion . . . 142
6.2.1 Extending the $(TMXM)_3Bi_2X_9$ family . . . 142
6.2.2 $(TMXM)_3Bi_2X_9{\cdot}X_2$ family . . . 142
6.2.3 $(FMTMA)_3Bi_2X_9$ family . . . 146
6.3 Conclusion . . . 149

7 Understanding and engineering the intermediate phase behaviour in PbSn perovskites 150
7.1 Abstract . . . 150
7.2 Introduction . . . 151
7.3 Results and Discussion . . . 154
7.3.1 Intermediate phases in pure-Pb perovskites . . . 154
7.3.2 Mixed Pb:Sn perovskites . . . 156
7.3.3 Solvent-based Cs-induced Intermediate Phase . . . 159
7.3.4 Hexagonal polymorphs in Pb-Sn perovskites: Theoretical investigations . . . 163
7.3.5 Hexagonal polymorphs in Pb-Sn perovskites: DMA-induced phase control . . . 166
7.4 Conclusion . . . 172

8 Conclusions and future outlook 180
8.1 Concluding Remarks . . . 183
8.2 Future outlook . . . 183

A Crystallographic Data and structural analysis 185
A.1 Simple point charge model calculations . . . 185
A.1.1 Point charge calculations for $(TMIM)_3Bi_2I_9$ . . . 185
A.1.2 Point charge calculations for $[(CH_3)_4N]_3Bi_2I_9$ . . . 186
A.2 Berry phase polarisation calculations . . . 187
A.3 Crystallographic data for $(TMIM)_3Bi_2I_9$ . . . 188
A.4 Thermal ellipsoids for $(TMIM)_3Bi_2I_9$ . . . 193

B Chapter 5: Crystallographic Data 200
B.1 Crystallographic Data for $(TMBM)_3Bi_2Br_9$ . . . 200
B.2 Crystallographic Data for $(TMIM)_3Sb_2I_9$ . . . 201

C Chapter 6:Crystallographic Data 203

C.1 Crystallographic data for $CsSnI_3 \cdot 3(C_2H_6OS)$ 203

List of Figures

1.1 Global fossil fuel consumption. Reproduced from Our World in Data, Statistical Review of World Energy 2024[3] . . . 3

2.1 Crystal structure of Graphene, reproduced from ICSD collection code 193439 . . . 9
2.2 Simple primitive cubic crystal structure of Po, which is the only element in the periodic table that crystallizes in a simple cubic structure[3]. 17
2.3 Geometric construction of Bragg's law. The path difference between waves scattered from adjacent planes is $2d_{hkl}\sin\theta$, leading to constructive interference when this equals $n\lambda$. . . . 18
2.4 The Ewald sphere construction in reciprocal space. Diffraction occurs when the sphere intersects a reciprocal lattice point, satisfying both the Bragg condition and the Laue condition $\mathbf{Q} = \mathbf{G}$. . . . 19
2.5 Schematic of the non-centrosymmetric and polar subgroups of the crystallographic point groups. . . . 22
2.6 **a** AM 1.5 Solar spectrum and **b** Detailed balance limit [5] . . . 25
2.7 High-temperature paraelectric **a**, **c** and low-temperature ferroelectric **b**, **d** of barium titanate ($BaTiO_3$) and sodium nitrite ($NaNO_2$), respectively. . . . 27
2.8 Energy landscape of a second-order **a** and first-order **b** phase transition. 29
2.9 Application of quasi-spherical theory to the parent structure $[(CH_3)_4]CdCl_3$ to form the ferroelectric $[(CH_3)_3NCH_2Cl]CdCl_3$. Reprinted with permission from Zhang et al. [34]. Copyright 2019 American Chemical Society. . . . 32
2.10 Visualisation of common structural distortions of perovskites: **a** cubic (α), b tetragonal (β) and c orthorhombic (γ) . . . 37
2.11 Transitions to non-perovskite phases from **a** 3D corner-sharing perovskite to **b** δ-$CsMX_3$ (M=Pb,Sn) or **c** 2H, **d** 4H and **e** 6H hexagonal polytypes. Pink spheres represent the A cation . . . 38
2.12 Crystal structures of known solvent intermediate phases. Crystal structures of $MA_2Pb_3I_8{\cdot}2DMF$ **c** and $MA_3PbI_5{\cdot}DMF$ **c** were reproduced with permission from reference [115], copyright 2017 American Chemical Society. . . . 42

3.1 Microscope image of the single crystal growth of $CsSnI_3$·3DMSO. The purple squares identified to be CsI crystals. 62
3.2 Microscope image of the single crystal growth of $CsSnI_3$·3DMSO. The mixture on the slide after 1 day. 63
3.3 Comparison of **a** Bragg-Brentano and **b** grazing incidence X-ray diffraction geometries. In grazing incidence, the incident beam angle α_i remains fixed while the detector scans through 2θ. 68
3.4 Schematic diagram of the GIWAXS experimental setup showing the key components: X-ray source, sample stage, and 2D detector. The incident beam strikes the sample at a shallow angle α_i, and scattered X-rays are collected on the 2D detector. This image was produced and provided by Dr. J.A. Smith. 68

4.1 Inducing non-centrosymmetry for high piezoresponse. **a** Room temperature crystal structure of $[(CH_3)_3CH_2NI]_3Bi_2I_9$, or $(TMIM)_3Bi_2I_9$. **b** Crystal structure of $[(CH_3)_4N]_3Bi_2I_9$, reproduced from ICSD code 170840. Hydrogen atoms are omitted for clarity. **c** Electrostatic potential (ESP) surface of $(TMIM)_3Bi_2I_9$, where the colour scheme represents electrostatic potential from red (more negative) to blue (more positive), where the sigma hole on the iodine (blue region) is shown oriented as being oriented towards the inorganic framework. **d** Calculated net polarization for $[(CH_3)_4N]_3Bi_2I_9$ and $[(CH_3)_3CH_2NI]_3Bi_2I_9$. The electrostatic potential calculations were performed by Dr. D.J.Kubicki, and the polarization calculations were performed by Dr. S. Saha . . . 86
4.2 Electrostatic potential (ESP) map of $TMIM^+$. The colour map represents the distribution of charge across the cation; red and blue correspond to regions of lesser and greater positive charge, respectively. The ESP map was calculated by Dr. D.J. Kubicki. 88
4.3 Differential scanning calorimetry (DSC) trace of $(TMIM)_3Bi_2I_9$. DSC measurements were done by Dr. N. Hawkins, and analysed by E.Y.H. Hung 91
4.4 Crystal structures and (hk0) reciprocal space reconstructions of $(TMIM)_3Bi_2I_9$ at 0 and 130 °C, respectively. The reciprocal space reconstructions have been plotted on a logarithmic intensity scale to enhance the visibility of diffuse scattering features. 92
4.5 Tilting of $(Bi_2I_9)^{3-}$ dimer with temperature. α, β and γ refer to the angle with respect to the a, b and c-axis, respectively. 93
4.6 Thermogravimetric analysis (TGA) of $(TMIM)_3Bi_2I_9$. 94
4.7 Temperature dependence of ^1H and ^{13}C NMR spin-lattice relaxation times, T_1 observed for $(TMIM)_3Bi_2I_9$. Dotted lines joining the points represent the quadratic fit used to fit the region at temperatures below the phase transition. The NMR measurements were conducted in collaboration with Dr. B.M. Gallant, and the analysis was performed by Dr. B.M. Gallant. 95

4.8 Variable-temperature **a** ^{14}N **b** ^{13}C and **c** ^{209}Bi solid state nuclear magnetic resonance (NMR) spectra. The NMR measurements were conducted in collaboration with Dr. B.M. Gallant, and the analysis was performed by Dr. B.M. Gallant and Dr. D.J. Kubicki. 96
4.9 Intrinsic piezoresponse via *in situ* electric field measurements. **a** Left: Visualisation of crystal mounted on Kapton, connected to copper electrodes. Right: microscope image of crystal connected to electrodes. **b** Crystal growth morphology of $(TMIM)_3Bi_2I_9$, simulated using the Bravais Friedel Donnay Harker (BFDH) method in Mercury. **c** Percentage change of lattice parameters and unit cell volume with applied electric field, where field is swept from positive to negative. The error bands on each measurement are indicated by the shaded region about each point. 99
4.10 Thin films of $(TMIM)_3Bi_2I_9$. **a** Images of thin films on FTO-coated glass. **b** XRD patterns and simulated peak positions based on the single crystal data. XRD is fitted using a Pawley fit, with the fitted parameters shown in Table 4.2. 101
4.11 Highest piezoelectric response for a halobismuthate. Piezoresponse force microscopy: **a** Topography, **b** piezoelectric amplitude and **c** phase images. Switching spectroscopy PFM measurements: **d** Phase-voltage (top) and **e** Amplitude-voltage (bottom) loops, where the dashed line indicates the linear fit used to calculate the piezoelectric coefficient. Box plots showing $d_{33,\text{eff}}$ values calculated from **f** amplitude-voltage loops from PFM, and **g** single crystals respectively where the whiskers show the entire range of data. Champion values for each measurement are circled. For the piezoelectric coefficients calculated from PFM, the absolute values obtained from the negative and positive gradient are indicated. **h** Comparison of piezoelectric coefficients d_{ij} with previously reported piezoelectric halobismuthates, where the median value from PFM measurements is indicated for $(TMIM)_3Bi_2I_9$[4, 41–50]. **i** Comparison of phase transition temperature and piezoelectric coefficients with previously reported piezoelectric materials, where the decomposition temperature is used when no piezo-to-non-piezoelectric transition temperature is reported. Full data shown in Table 2.2. The PFM measurements were conducted in collaboration with Dr. R. Harniman and Dr. K. Kaja and analysed by E.Y.H. Hung. 104
4.12 The corresponding points used for phase-voltage and amplitude-voltage loop measurements: **a** Topography, **b** PFM amplitude and **c** PFM Phase 105

5.1 Microscope images of single crystals of $(TMBM)_3Bi_2Br_9$, $(TMCM)_3Bi_2Cl_9$ and $(TMIM)_3Sb_2I_9$ obtained as structural modifications to $(TMIM)_3Bi_2I_9$. 116

5.2 Thermal analysis of microcrystalline, mechanosynthesised powders of $(TMBM)_3Bi_2Br_9$, $(TMCM)_3Bi_2Cl_9$, and $(TMIM)_3Sb_2I_9$: **a** Differential scanning calorimetry (DSC), where the peak areas used to calculate the molar enthalpy (ΔH) and entropy (ΔS) change are marked. **b** Thermogravimetric analysis (TGA) measurements, where the data for $(TMIM)_3Bi_2I_9$ is plotted for comparison. TGA data was not taken for $(TMIM)_3Sb_2I_9$. DSC measurements were conducted by N. Hawkins and analysed by E.Y.H. Hung. TGA measurements were conducted by B.M. Gallant. 117
5.3 Single raw diffraction image with resolution rings overlaid **a**, **b** and (hk0) Miller plane reconstructions **c**, **d** of $(TMBM)_3Bi_2Br_9$ and $(TMCM)_3Bi_2Cl_9$ respectively. 119
5.4 Crystal structure of $(TMCM)_3Bi_2Cl_9$ at 250 K **a**, **b** and 315 K **c**, **d**. . 120
5.5 Room temperature crystal structures of **a** $(TMBM)_3Bi_2Br_9$, **b** $(TMCM)_3Bi_2Cl_9$, **c** $(TMIM)_3Bi_2I_9$ and **d** $(TMIM)_3Sb_2I_9$. The structures are solved by first assigning the atoms of the inorganic framework (larger electron density in the Fourier map) before seeking to identify the locations of the organic cations. For the more disordered structures, only the nitrogen atoms can be clearly resolved. 128
5.6 Room temperature (20 °C) **a** and high temperature (130 °C) **b** crystal structure of $(TMIM)_3Sb_2I_9$. Crystallographic data for $(TMIM)_3Sb_2I_9$ is given in Appendix B, Table B.2. 129
5.7 Temperature-dependent second harmonic generation (SHG) measurements of **a,b** $(TMBM)_3Bi_2Br_9$ and **c,d** $(TMCM)_3Bi_2Cl_9$. The SHG peak intensity values with varying temperature are plotted in **b,d**, to show more clearly the trend with temperature. The change in shape and width of the peaks is affected by the size of the crystal and small changes in the orientation of illumination. These measurements were conducted by F.M. Adamczyk and M. Stein. 130
5.8 Temperature-dependent second harmonic generation (SHG) measurements of **a,b** $(TMIM)_3Bi_2I_9$ and **c,d** $(TMIM)_3Sb_2I_9$. The SHG peak intensity values with varying temperature are plotted in **b,d**, to show more clearly the trend with temperature. The change in shape and width of the peaks is affected by the size of the crystal and small changes in the orientation of illumination. These measurements were conducted by F.M. Adamczyk and M. Stein. 131
5.9 XRD measurements of $(TMBM)_3Bi_2Br_9$, $(TMCM)_3Bi_2Cl_9$ and $(TMIM)_3Sb_2I_9$. We note that the XRD pattern for $(TMCM)_3Bi_2Cl_9$ contains peaks which have not been indexed to the space group $P6_3mc$, and has not been otherwise identified as belonging to any other phase. 132
5.10 ^1H and ^{13}C spin-lattice relaxation (T_1) measurements for **a** $(TMBM)_3Bi_2Br_9$, **b** $(TMCM)_3Bi_2Cl_9$ and **c** $(TMIM)_3Sb_2I_9$. These measurements were conducted in collaboration with Dr. B.M. Gallant, and the analysis was performed by Dr. B.M. Gallant. 133

5.11 Variable temperature NMR spectra: Variable temperature solid state NMR spectra of ^{14}N in **a** $(TMBM)_3Bi_2Br_9$, **b** $(TMCM)_3Bi_2Cl_9$ and **c** $(TMIM)_3Sb_2I_9$. The NMR measurements were conducted in collaboration with Dr. B.M. Gallant, and the analysis was performed by Dr. B.M. Gallant. 134
5.12 Variable temperature NMR spectra: Variable temperature solid state NMR spectra of ^{13}C in **a** $(TMBM)_3Bi_2Br_9$, **b** $(TMCM)_3Bi_2Cl_9$ and **c** $(TMIM)_3Sb_2I_9$. For $(TMIM)_3Sb_2I_9$, the signals (at lower chemical shifts) corresponding to the CH_3 methyl groups are very weak, and thus are not shown here. The NMR measurements were conducted in collaboration with Dr. B.M. Gallant, and the analysis was performed by Dr. B.M. Gallant. 134
5.13 Lattice parameter changes of $(TMBM)_3Bi_2Br_9$ while cooling. 135
5.14 Fitting of the indexed peaks of the low-temperature phase of $(TMBM)_3Bi_2Br_9$ after flash cooling. 135
5.15 Unusual phase behaviour: $(TMBM)_3Bi_2Br_9$ reciprocal space reconstructions of the (hk1), (hk0), (h0l) and (0kl) Miller planes at 300 K (**a-d**), 265 K (**e-h**) and upon heating back up to 300 K (**i-l**). 136

6.1 $(TMXM)_3Bi_2X_9$ family of compounds. **a** $(TMIM)_3BiBr_6$, **b** $(TMIM)_3Bi_2Cl_9$, **c** $(TMCM)_3Bi_2I_9$, **d** $(TMCM)_3Bi_2Br_9$. For **b-d**, significant diffuse scattering is present in the raw-diffraction pattern, paired with a lack of Bragg peaks beyond 1.0 Å resolution. We attribute this to significant disorder of the organic cations which means we are unable to resolve their positions in the crystal structures. Mostly only the nitrogen atoms are discernible. These measurements were taken on a lab-based diffractometer. 143
6.2 $(TMXM)_3Sb_2X_9{\cdot}X_2$ family of compounds. 145
6.3 Crystal structures of **a** $(FMTMA)_3Bi_2I_9$, **b** $(FMTMA)_3Bi_2Br_5I_4$ and **c** $(FMTMA)_3Bi_2I_7Cl_2$. 147

7.1 Crystal structures of the hexagonal polytypes. **a** (bottom) Parallel and (top) perpendicular views of the crystal structures of μ-$EASnI_3$ and θ-$GASnI_3$ (only the latter is shown) crystallizing in the 6H type. **b** (bottom) Parallel and (top) perpendicular views of the crystal structure of θ-$ACASnI_3$ crystallizing in the 4H type. **c** (bottom) Parallel and (top) perpendicular views of the crystal structures of κ-$EASnI_3$ and $IMSnI_3$ (only the latter is shown) crystallizing in the 9R type. Reprinted with permission from Stoumpos et al.[28]. Copyright 2017 American Chemical Society. 153

7.2 *In situ* GIWAXS. 1D azimuthal integration **a-c**, and phase evolution behaviour **d-f** of $FA_{0.6}MA_{0.4}PbI_3$, $FA_{0.6}MA_{0.3}Cs_{0.1}PbI_3$ and $FA_{0.83}Cs_{0.17}PbI_3$ (FA^+ = formamidinium$^+$, MA^+ = methylammonium$^+$) respectively. Diffuse scattering at 0.25 - 0.75 $Å^{-1}$, and 1.60-2.25 $Å^{-1}$ indicative of non-crystalline solute phases. Crystal structures of **g** 2(DMSO)-$MA_3Pb_2I_8$ and **h** 2H (δ)-$FAPbI_3$. The *in situ* GIWAXS measurements were performed in collaboration with Dr. J. Smith, and analysed by E. Hung. 155

7.3 Pb:Sn: *In situ* GIWAXS. 1D azimuthal integration **a-c** of $FA_{0.6}MA_{0.4}Pb_{0.5}Sn_{0.5}I_3$, $FA_{0.6}MA_{0.3}Cs_{0.1}Pb_{0.5}Sn_{0.5}I_3$ and $FA_{0.83}Cs_{0.17}Pb_{0.5}Sn_{0.5}I_3$ respectively, and **d** corresponding (100) perovskite peak intensity with time. Vertical line indicates beginning of temperature ramp. In all samples, gas quenching is applied from 30 seconds. The *in situ* GIWAXS measurements were performed in collaboration with J.A. Smith, and analysed by E. Hung. 157

7.4 Pure Sn perovskite compositions. 1D azimuthal integration of *in situ* GIWAXS patterns of **a**, **b**$MASnI_3$ and **c**, **d** $FASnI_3$ compositions from pure DMSO and DMF precursor solutions, respectively. The *in situ* GIWAXS measurements were performed in collaboration with J.A. Smith, and analysed by E. Hung. 159

7.5 Visualisation of MX_2 adducts: **a** PbI_2·DMSO **b** PbI_2·2DMSO **c** PbI_2·DMF **d** SnI_2·DMSO **e** SnI_2·2DMSO **f** SnI_2·DMF. Hydrogen atoms omitted for clarity. The crystallographic data from **a-c** are reproduced with permission from Cao et al. Copyright 2016 American Chemical Society[39]. The crystallographic data for **d-f** are reproduced from the Cambridge Crystallographic Data Centre (CCDC) with reference numbers 1558257, 1558258, and 1558255 respectively. 160

7.6 Caesium-induced Sn-containing intermediate phase: 1D azimuthally integrated GIWAXS patterns for **a** $FA_{0.7}Cs_{0.3}Pb_{0.5}Sn_{0.5}I_3$, **b** $CsPb_{0.5}Sn_{0.5}I_3$, and **c** $CsSnI_3$. In **c**, the data is shown from the onset of crystallization to clearly highlight the intermediate phase peaks. For all three compositions, the temperature ramp was initiated immediately upon detection of the perovskite phase formation. 161

7.7 A novel, Cs and Sn-containing perovskite-solvate phase: $CsSnI_3$·3DMSO. **a** Microscope image and **b**, **c** solved crystal structure. Hydrogen atoms are omitted for clarity. 163

7.8 Visualisations of coordination connectivity with Sn in **a** cubic-$CsSnI_3$, **b** SnI_2·DMSO, **c** SnI_2·2DMSO and **d** SnI_2·3DMSO. Hydrogen atoms are omitted for clarity. **a** is reproduced from the Inorganic Crystal Structure Database (ICSD) with collection code 262924. The crystallographic data for **b-c** are reproduced from the Cambridge Crystallographic Data Centre (CCDC) with reference numbers 1558257 and 1558258, respectively. **d** is reproduced with permission from Hao et al. Copyright 2015 American Chemical Society[42] 164

7.9 DFT-calculated relative energies of $FAPbI_3$ and $FASnI_3$ polymorphs with respect to their 2H polymorph. Energies are shown in kJ/mol per formula unit. The x-axis indicates the structure type, with increasing corner-sharing octahedra from left to right. Error bars represent the standard deviation of the energy, typically of size ± 0.0003 kJ/mol/f.u.. These calculations were performed by P. Ahlawat. 165
7.10 Relative energies of $FAPbI_3$ and $FASnI_3$ polymorphs from molecular dynamics simulations using machine learning potentials. Energies are shown in kJ/mol per formula unit. The x-axis indicates the structure type, with increasing corner-sharing octahedra from left to right. Error bars represent the standard deviation of the energy. These calculations were performed by P. Ahlawat. 167
7.11 Scanning electron microscopy (SEM) images of thin films deposited via spin-coating, from different precursor solution compositions. The white particulates in the images are likely to be SnF_2 particles. Both the sample preparation and the SEM measurements were taken by M. Farrar. 169
7.12 *In situ* GIWAXS measurements of the formation of hexagonal phases with DMACl addition. **a** DMF:DMSO 3:1 (reproduced from Figure 7.3c for comparison), **b** DMF, **c** DMF and 40 mol% DMACl. 2H-perovskite peaks are indicated by the yellow asterisks. Unknown phases are indicated by the blue and purple circles. In the deposition of all 3 compositions, nitrogen gas quenching was applied at 30s. For the neat-DMF-based and DMF:DMACl compositions, gas quenching was applied for 120s and 270s, respectively. These measurements were taken by J.A. Smith and analysed by E.Y.H. Hung 171

A.1 Oak Ridge Thermal Ellipsoid Plot (ORTEP) diagram of $(TMIM)_3Bi_2I_9$at 273K, ellipsoids at 50%. 193
A.2 ORTEP diagram of $(TMIM)_3Bi_2I_9$at 293K, ellipsoids at 50%. 194
A.3 ORTEP diagram of $(TMIM)_3Bi_2I_9$at 313K, ellipsoids at 50%. 194
A.4 ORTEP diagram of $(TMIM)_3Bi_2I_9$at 323K, ellipsoids at 50%. 195
A.5 ORTEP diagram of $(TMIM)_3Bi_2I_9$at 333K, ellipsoids at 50%. 195
A.6 ORTEP diagram of $(TMIM)_3Bi_2I_9$at 343K, ellipsoids at 50%. 196
A.7 ORTEP diagram of $(TMIM)_3Bi_2I_9$at 353K, ellipsoids at 50%. 196
A.8 ORTEP diagram of $(TMIM)_3Bi_2I_9$at 363K, ellipsoids at 50%. 197
A.9 ORTEP diagram of $(TMIM)_3Bi_2I_9$at 373K, ellipsoids at 50%. 197
A.10 ORTEP diagram of $(TMIM)_3Bi_2I_9$at 383K, ellipsoids at 50%. 198
A.11 ORTEP diagram of $(TMIM)_3Bi_2I_9$at 393K, ellipsoids at 50%. 198
A.12 ORTEP diagram of $(TMIM)_3Bi_2I_9$at 403K, ellipsoids at 50%. 199
A.13 ORTEP diagram of $(TMIM)_3Bi_2I_9$at 413K, ellipsoids at 50%. 199

List of Tables

2.1 The seven crystal systems and their characteristics. 12
2.2 Comparison of piezoelectric coefficients (d_{ij}) and transition temperatures (T_c) for various piezoelectric materials. 34

4.1 N$\cdots$Bi distances (error) in $(TMIM)_3Bi_2I_9$ at room temperature and 140 °C, from SCXRD data analysis. 93
4.2 Pawley fit parameters for the XRD patterns of the mechanosynthesised powder, thin film on plain glass and thin film on FTO. 100

5.1 Thermodynamic parameters. The phase transition temperatures given are the average between the heating and cooling loop for each pair of endo- and exo-therms. R is the molar gas constant. 116
5.2 Fitted lattice parameters from Pawley fits of powder XRD data. . . . 123
5.3 Unit cell parameters for the three domain components. 127

6.1 Crystal structure parameters for $(TMXM)_3Bi_2X_9$ compounds. 144
6.2 Crystal structure parameters for $(TMXM)_3Sb_2X_9{\cdot}X_2$ compounds. . . 146
6.3 Crystallographic data for the three compounds $(FMTMA)_3Bi_2I_9$, $(FMTMA)_3Bi_2Br_5I_4$ and $(FMTMA)_3Bi_2I_7Cl_2$ at 100 K 148

7.1 Comparison of tolerance factors for $FASnI_3$ and $FAPbI_3$, indicating similar perovskite formability. Calculated using references [1, 2, 36–38] and Equations 2.35, 2.34, 2.37. Ionic radii of Sn^{2+} and Pb^{2+} used for this calculation are 1.15 and 1.18 Å respectively. For the Bartel tolerance factor, the ideal range is $\tau < 4.18$. 158

A.1 Point charge model calculations for the dimers in $(TMIM)_3Bi_2I_9$ . . . 186
A.2 Point charge model calculations for the cations in $(TMIM)_3Bi_2I_9$ . . . 186
A.3 Total point charge polarisation for $(TMIM)_3Bi_2I_9$ 186
A.4 Point charge model calculations for the dimers in $[(CH_3)_4N]_3Bi_2I_9$ . . 187
A.5 Point charge model calculations for the cations in $[(CH_3)_4N]_3Bi_2I_9$ . . 187
A.6 Total point charge polarisation for $[(CH_3)_4N]_3Bi_2I_9$ 187

A.7 Calculated polarisation vectors using Berry phase theory. All calculations in group (i) were conducted based on or by modifying the crystal structure of $(TMIM)_3Bi_2I_9$ in space group $Pna2_1$ at a temperature of 293 K (Fig. 1a in main text). The calculation for $Cs_3Bi_2I_9$ ($[(CH_3)_4N]_3Bi_2I_9$) in group (ii) was conducted by replacing the $[(CH_3)_4N]^+$ cation with Cs^+ in the crystal structure of $[(CH_3)_4N]_3Bi_2I_9$ in the space group $P3_1c$ as reported by Feldmann et al. (2001), discusseed in Chapter 4. 188
A.8 Crystallographic data for $(TMIM)_3Bi_2I_9$at temperatures 273-323 K . 189
A.9 Crystallographic data for $(TMIM)_3Bi_2I_9$at temperatures 333-363 K . 190
A.10 Crystallographic data for $(TMIM)_3Bi_2I_9$at temperatures 373-403 K . 191
A.11 Crystallographic data for $(TMIM)_3Bi_2I_9$at 413 K 192

B.1 Crystallographic data for $(TMBM)_3Bi_2Br_9$ at 315 K 201
B.2 Crystallographic data for $(TMIM)_3Sb_2I_9$ at temperatures 280 and 413 K 202

C.1 Crystallographic data for $CsSnI_3{\cdot}3(C_2H_6OS)$ at 293 K 204

List of Publications, Patents and Conference Presentations

*These authors contributed equally to the work.

- **Chapter 4** *Tailoring a novel, lead-free organic-inorganic halobismuthate for large piezoelectricity.* **Esther Y-H Hung**, Benjamin M. Gallant, Robert Harniman, Jakob Mö bs, Santanu Saha, Charles Godfrey, Shrestha Banerjee, Nikolaos Farmakidis, Harish Bhaskaran, Marina Filip, Paolo Radaelli, Nakita K Noel, Dominik J. Kubicki, Harry C. Sansom, Henry J. Snaith. *(Manuscript in preparation.)*

- **Chapter 5** *Tuning the polar order of $(TMXM)_3M_2X_9$ materials via structural modifications.* **Esther Y-H Hung**, Benjamin M. Gallant, Florian M. Adamczyk, Markus Stein, Alexander Kapp, Daniel Anders, Sangam Chatterjee, Dominik J. Kubicki, Harry C. Sansom, Henry J. Snaith. *(Manuscript in preparation.)*

- **Chapter 7** *Unravelling the Kinetics of Intermediate Phase Behaviour in PbSn perovskites.* **Esther Y-H Hung**, Joel A. Smith, Paramvir Ahlawat, Michael Farrar, Saqlain Choudhary, Benjamin M. Gallant, Fengning Yang, Lennart Reb, Karl-Augustin Zaininger, Daniel T.W. Toolan, Rachel C. Kilbride, Eva Unger, Dominik J. Kubicki, Henry J. Snaith *(Manuscript in preparation.)*

- *Understanding the degradation of methylenediammonium and its role in phase-stabilizing formamidinium lead triiodide.* Elisabeth A. Duijnstee, Benjamin M. Gallant, Philippe Holzhey, Dominik J. Kubicki, Silvia Collavini, Bernd K. Sturdza, Harry C. Sansom, Joel Smith, Matthias J. Gutmann, Santanu Saha, Murali Gedda, Mohamad I. Nugraha, Manuel Kober-Czerny, Chelsea Xia, Adam D. Wright, Yen-Hung Lin, Alexandra J. Ramadan, Andrew Matzen, **Esther Y.H. Hung**, Seongrok Seo, Suer Zhou, Jongchul Lim, Thomas D. Anthopoulos, Marina R. Filip, Michael B. Johnston, Robin J. Nicholas, Juan Luis Delgado, Henry J. Snaith. J. Am. Chem. Soc. 2023, 145 (18), 10275-10284. *10.1021/jacs.3c01531*.

- *A green solvent enables precursor phase engineering of stable formamidinium lead triiodide perovskite solar cells.* Benjamin M. Gallant, Philippe Holzhey, Joel A. Smith, Saqlain Choudhary, Karim A. Elmestekawy, Pietro Caprioglio, Igal Levine, Alexandra A. Sheader, **Esther Y.H. Hung**, Fengning Yang, Daniel T.W. Toolan, Rachel C. Kilbride, Karl-Augustin Zaininger, James M. Ball, M. Greyson Christoforo, Nakita K. Noel, Laura M. Herz, Dominik J. Kubicki, Henry J. Snaith. Nat. Comms, 2024, 15 (1), 10110 *10.1038/s41467-024-54113-4*.

- *Effects of Bi and Sb ion incorporation on the optoelectronic properties of mixed lead-tin perovskites.* Florine M. Rombach, Luca Gregori, Anika Sidler, Jayne Whitworth, Stefan Zeiske, Heon Jin, **Esther Y.H. Hung**, Silvia Motti, Pietro Caprioglio, Ardalan Armin, M Lenz, Daniele Meggiolaro, Fillipo D. Angelis, Henry J. Snaith. J. Mater. Chem. C, 2025,13, 5161-5171 *10.1039/D4TC02162B*.

- *Exposing bonding-favourable facets of perovskites for tandem solar cells.* Junke Wang*, Shuaifeng Hu*, Zehua Chen*, Zhongcheng Yuan, Pei Zhao, Akash Dasgupta, Fengning Yang, Jin Yao, Minh Anh Truong, Gunnar Kusch, **Esther Y.H. Hung**, Nick R. M. Schipper, Laura Bellini, Guus J. W. Aalbers, Rachel A. Oliver, Atsushi Wakamiya, René. A.J. Janssen, and Henry J. Snaith. *(Submitted to Journal of Advanced Materials)*

- *Truly non-toxic solvent system for large-area perovskite thin film fabrication: a step towards industrialization of perovskite solar modules.* Ehsan Rezaee, **Esther Y.H. Hung**, Benjamin M. Gallant, Dominik J. Kubicki, Henry J. Snaith and Dimitar Kutsarov. *(Manuscript in preparation)*

- *2D-3D interface engineering for stable phase, wide bandgap perovskite solar cells.* Nurssultan Mussakhanuly, Robert Lee Chin, **Esther Y.H. Hung**, Yihao Wang, Henry J. Snaith and Nakita K. Noel. *(Manuscript in preparation)*

Patents

- *Novel, lead-free hybrid organic-inorganic piezoelectrics.* **Esther Y.H. Hung**, Harry C. Sansom, Henry J. Snaith. *GB2406892.6 and registration date: May 2024.*

Conference presentations

- "A novel, lead-free 0D $A_3M_2X_9$ perovskite ferroelectric" 6^{th} International Conference on Perovskite Solar Cells and optoelectronics (PSCO 2023) poster presentation. Oxford, UK.

- "A novel, lead-free halide perovskite derivative for ferro- and piezo-electric applications" Hybrid and Organic Photovoltaics 2024 (HOPV24) oral presentation. Valencia, Spain.

- "A novel, lead-free halobismuthate perovskite derivative with excellent piezoelectricity" 7^{th} International Conference on Perovskite Solar Cells and optoelectronics (PSCO 2024) Oral presentation. Perugia, Italy.

- "A novel, lead-free halobismuthate perovskite derivative with excellent piezoelectricity" poster presentation. Young Crystallographer's Conference, Germany 2024. **Poster Prize winner**

- "Introducting halobismuthates as high-performing piezoelectric materials". Materials Research Society Spring Meeting 2025 (MRS 2025). Oral presentation. Seattle, USA.

- "Unravelling the Kinetics of Intermediate Phase Behaviour in PbSn perovskites" 8^{th} Hybrid and Organic Photovoltaics 2025 (HOPV25) poster presentation. Rome, Italy.

Chapter 1

Introduction

1.1 Background

1.1.1 Symmetry

Patterns and rhythms, or *symmetries*, are woven into the laws of the physical universe: from the colour SU(3) and flavour SU(2) gauge symmetries of quarks under the Standard Model of particle physics, the Schwarzschild metric in general relativity, to the symmetries of crystals and the structure of materials.

Day-to-day, we observe symmetries in the shape of snowflakes, the human body, and the geometry of natural structures. In 1918, Emmy Noether proved a simple yet profound theorem: Behind every conserved quantity, there is a symmetry[1, 2]. In its most fundamental form, symmetry governs the fundamental particles and forces of the universe. Within the study of materials, symmetry governs the micro and macroscopic properties of materials, with a profound impact: the resulting electronic properties of semiconductors, for example, have revolutionised the modern world.

The inspiring patterns built into the fabric of our natural world and the physical universe, might allow us to further appreciate the beauty of nature. Even more so, it might allow us to understand nature as an entity to nurture, protect and preserve. On this front, we are failing:

1.2 The global energy crisis

Human exploitation of the Earth's natural resources has led to one of the greatest challenges ever faced by humans; global warming. Since the 1850s, the Industrial Revolution and the pursuit of economic growth and higher living standards have driven widespread reliance on fossil fuels—coal, natural gas, and oil—for electricity and heat. Global fossil fuel consumption has more than doubled in the last 50 years (Figure 1.1), faster than the rate of population growth[3]. This dependence has made fossil fuel combustion the largest source of global greenhouse gas emissions, which trap heat in the atmosphere and contribute significantly to rising global temperatures. The ten warmest years in the 175-year record since pre-industrial times have all occurred during the last decade (2015-2024). The year 2024 was the warmest year since global records began in 1850 at 1.29 °C above the 20^{th} century average of 13.9 °C, 0.10°C more than the previous record set in 2023[4]. McKay et al. (2022) report that exceeding 1.5 °C warming, the limit under the Paris Agreement, may trigger multiple climate tipping points such as the breakdown of major ocean systems and thawing of boreal permafrost, which could have abrupt, irreversible and dangerous impacts on humanity[5].

Already, colossal impacts of human-induced climate change have been observed. There has been a loss of 26 metric tons of ice per square meter from 1970 to 2020 in the loss of sea ice and glaciers - even if warming is limited to 1.5 °C, it is forecast that half of global glacier mass will be lost by 2100[6]. Furthermore, the extraction of fossil fuels and extreme weather patterns induced by climate change are causing devastation to the livelihoods of hundreds of thousands of vulnerable communities, leading to forced displacement[7, 8]. There was a record 32.6 million internal displacements in 2022 due to disasters, most of which were weather-related[9]. Current estimates suggest that climate-related displacement will increase to 216 million by 2050 - approximately 1 in 45 people on Earth[10].

Under current nationally determined contributions to mitigate greenhouse gas emissions, global warming is projected to reach 2.7 °C warming, significantly surpassing the 1.5 °C limit of the Paris Agreement[6]. It is the responsibility of the global

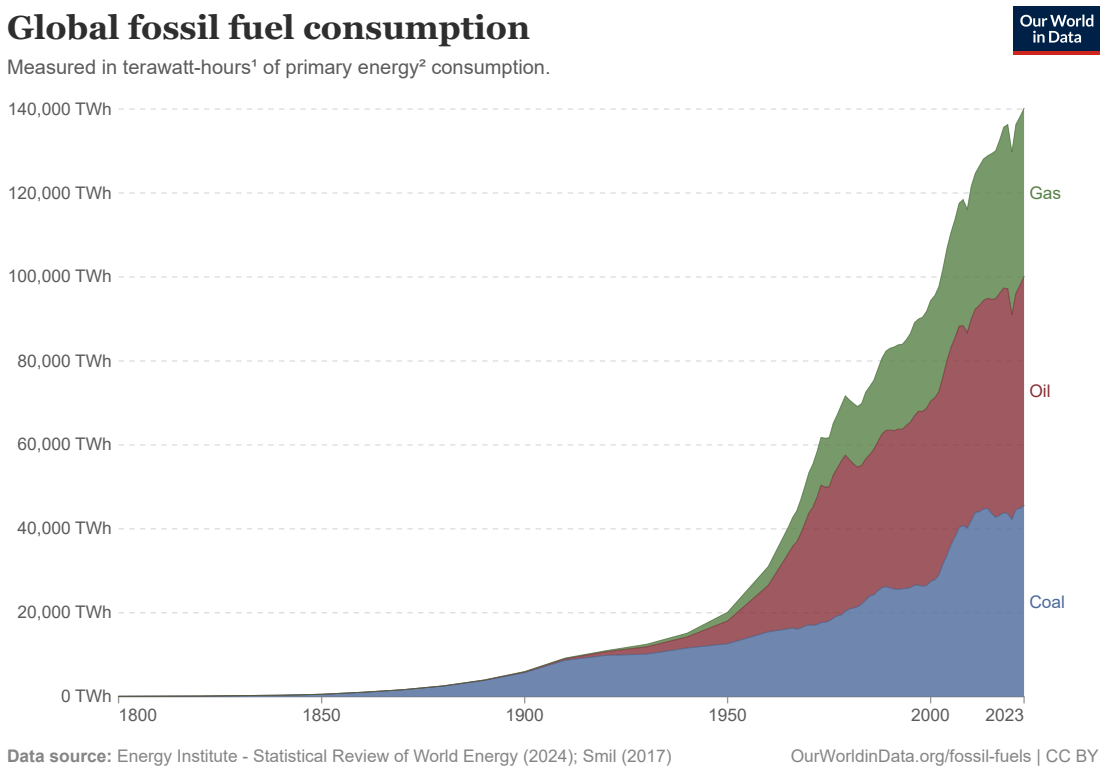


FIGURE 1.1: Global fossil fuel consumption. Reproduced from Our World in Data, Statistical Review of World Energy 2024[3]

community, most importantly the wealthier nations that have driven much of climate change[11], to take action to mitigate the effects of climate change and prevent further warming.

Developing better and alternative energy technologies is an essential part of this. Harvesting sunlight, the most abundant source of energy on Earth, is one of the most promising technologies for this, with the sun providing 342 W/m^2 of energy on the Earth's surface, equivalent to 44 million electric power plants[12]. Researchers are also actively exploring alternative energy technologies. Among these, mechanical energy harvesting via piezoelectric transduction has emerged as particularly promising for ambient energy harvesting, offering significant advantages over electrostatic,

electromagnetic, and triboelectric transduction methods[13–15].

Materials discovery and understanding is a key part of this - and even more fundamentally, their atomic structure. The arrangement of atoms in a material, governed by the principles of symmetry, determines its fundamental properties and potential applications. Just as symmetry underpins the conservation laws of physics, it also governs the electronic, optical, and mechanical properties of materials that are crucial for energy technologies. Understanding and manipulating these symmetries allows us to design materials with tailored properties for specific energy applications, whether it's optimising the piezoelectric response of materials for mechanical energy harvesting or engineering the band structure of semiconductors for efficient solar energy conversion. This thesis explores how we can harness the power of symmetry to design and understand materials that could help address our energy challenges.

1.3 Organisation of the Thesis

First, Chapter 2 gives a brief overview of the fundamental concepts of symmetry within the context of crystallography and structure-property relationships in the design of piezoelectric and photovoltaic materials. An explanation of how crystal structure is probed using X-ray diffraction is given, followed by considering structure-property relationships using Neumann's principle. An introduction to the design of hybrid organic-inorganic metal halides piezo- and ferroelectrics is given, with a review of prior work on their design and focus on engineering their phase transition properties. Hybrid metal halide perovskites are finally introduced, with detailed focus on their structures and distortions, and their synthesis and phase evolution as thin films.

Chapter 3 details the experimental methods used in this thesis; the synthesis of materials and the key structural characterisation technique used in this thesis, X-ray diffraction. A background to X-ray scattering techniques and their data analysis is given, particularly single-crystal X-ray diffraction (SCXRD) and grazing incidence wide angle X-ray scattering (GIWAXS). The experimental methods for variable temperature solid-state nuclear magnetic resonance (NMR), differential scanning

calorimetry (DSC) and second harmonic generation (SHG) are also given. The piezoelectric characterisation techniques used in this thesis are also given.

Chapter 4 focusses on the detailed study of the design of the novel, lead-free organic-inorganic $(TMIM)_3Bi_2I_9$ and its phase transitions. Comprehensive structural characterisation using SCXRD, solid-state NMR spectroscopy and thermal analysis reveals that, by carefully selecting the composition and inorganic framework of the material crystal structure, a large polarization can be achieved which leads to high piezoelectric behaviour.

This work is followed in Chapter 5 by a study of structural modifications to the parent compound $(TMIM)_3Bi_2I_9$ with the halide- and halogen-substituted, and metal ion-substituted, variants of the material using SCXRD, solid-state NMR spectroscopy, thermal analysis and SHG.

Chapter 6 details the synthesis and structural characterisation of a range of novel, lead-free halobismuthate and haloantimonate compounds that were studied as part of this thesis. These include mixed-halide variants of $(TMIM)_3Bi_2I_9$, and variants with a much larger organic cation.

Chapter 7 presents *in situ* studies of lead and lead-tin halide perovskite thin film crystallization using synchrotron GIWAXS, complemented by DFT and molecular dynamics simulations with machine learning potentials. Our findings reveal that tin incorporation thermodynamically stabilises 3D corner-sharing perovskite structures, consistent with experimental observations. While pure-Pb systems exhibit both solvent-based and perovskite polytype intermediate phases, Sn-containing systems only show crystalline intermediates in Cs-rich compositions. Notably, Sn-containing systems thermodynamically disfavour polytype phases compared to pure-Pb systems in standard photovoltaic compositions. To address this, we introduce dimethylammonium as a novel organic cation, enabling the growth of the final perovskite phase through a temporary polytype phase in Sn-containing systems.

Finally, Chapter 8 gives a conclusion and outlook on the future work covered in this thesis.

Bibliography

[1] E. Noether, "Invariante variationsprobleme," *Nachrichten von der Gesellschaft der Wissenschaften zu Göttingen, Mathematisch-Physikalische Klasse*, pp. 235–257, 1918.

[2] D. E. Rowe, "Emmy Noether and her theorems," *Annalen der Physik*, vol. 536, p. 2300479, 2024.

[3] H. Ritchie and P. Rosado, "Fossil fuels," *Our World in Data*, 2017. https://ourworldindata.org/fossil-fuels.

[4] N. N. C. for Environmental Information, "Monthly global climate report for annual 2024," 2025.

[5] D. I. McKay, A. Staal, J. F. Abrams, R. Winkelmann, B. Sakschewski, S. Loriani, I. Fetzer, S. E. Cornell, J. Rockström, and T. M. Lenton, "Exceeding 1.5°c global warming could trigger multiple climate tipping points," *Science*, vol. 377, 2022.

[6] J. C. Stroeve, D. Notz, J. Dawson, E. A. G. Schuur, D. Dahl-Jensen, and C. Giesse, "Disappearing landscapes: The Arctic at +2.7°c global warming," *Science*, vol. 387, pp. 616–621, 2025.

[7] N. Healy, J. C. Stephens, and S. A. Malin, "Embodied energy injustices: Unveiling and politicizing the transboundary harms of fossil fuel extractivism and fossil fuel supply chains," *Energy Research & Social Science*, vol. 48, pp. 219–234, 2019.

[8] B. Terminski, "Oil-induced displacement and resettlement: Social problem and human rights issue," *Journal of Refugee Studies*, 2011.

[9] T. I. D. M. Centre, "Global report on internal displacement 2023," 2023.

[10] V. Clement, K. K. Rigaud, A. de Sherbinin, B. Jones, S. Adamo, J. Schewe, N. Sadiq, and E. Shabahat, "Groundswell part 2: Acting on internal climate migration," 2021.

[11] N. Taconet, A. Mejean, and C. Guivarch, "Influence of climate change impacts and mitigation costs on inequality between countries," *Climatic Change*, pp. 15–34, 2019.

[12] N. Aeronautics and S. Administration, "The balance of power in the earth-sun system," 2005.

[13] N. Sezer and M. Koç, "A comprehensive review on the state-of-the-art of piezoelectric energy harvesting," *Nano Energy*, vol. 80, p. 105567, 2021.

[14] S. Roundy and P. K. Wright, "A piezoelectric vibration based generator for wireless electronics," *Smart Materials and Structures*, vol. 13, p. 1131, 2004.

[15] S. Roundy, E. S. Leland, J. Baker, E. Carleton, E. Reilly, E. Lai, B. Otis, J. M. Rabaey, P. K. Wright, and V. Sundararajan, "Improving power output for vibration-based energy scavengers," *IEEE Pervasive Computing*, vol. 4, pp. 28–36, 2005.

Chapter 2

Theory

2.1 Introduction

This chapter provides a brief overview of the key concepts and principles of crystallography and symmetry, in relation to the investigation of novel piezoelectric materials and the study of crystalline photovoltaic systems. Much of this material draws from the more detailed treatments in Ashcroft and Mermin's Solid State Physics[1] and Dove's Structure and Dynamics[2].

2.2 Symmetry in crystalline materials

2.2.1 Periodic structures: Lattices and unit cells

Solid crystalline materials are arranged in ordered, periodic structures called crystal lattices or crystal structures. These periodic arrangements can be described mathematically using lattice vectors and unit cells.

Definition A *lattice* is a grid of points defined by a set of linearly independent *lattice vectors* $\mathbf{a}_i$ ($i = 1, 2, 3$ in 3D).

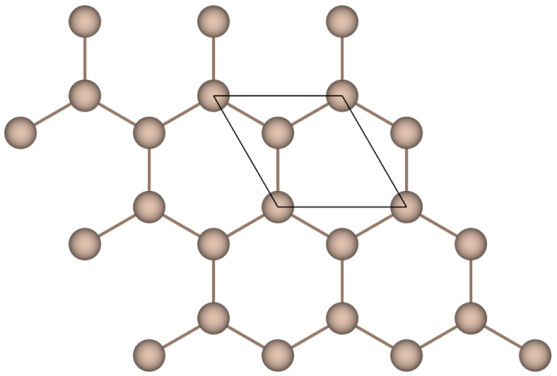


FIGURE 2.1: Crystal structure of Graphene, reproduced from ICSD collection code 193439

Thus, a given lattice point can be described by:

$$\mathbf{R} = \sum_{i=1}^{3} n_i \mathbf{a}_i \qquad\qquad n_i \in \mathbb{Z} \tag{2.1}$$

And the lattice itself can be described by:

$$\mathbf{L}(\mathbf{r}) = \sum_{\mathbf{R}} \delta(\mathbf{r} - \mathbf{R}) \tag{2.2}$$

where $\mathbf{a}_i$ are the primitive lattice vectors and n_i are integers.

Definition A *unit cell* of a lattice is a region of space or a motif that you can repeat again to construct the entire lattice. In other words, a unit cell contains entirely the symmetry of the whole lattice. This is often referred to as a *Bravais* lattice; an infinite array of discrete points generated by Equation 2.1. While the choice of a unit cell is not unique, a primitive unit cell is a minimum-volume cell that generates the entire lattice through translation; the primitive cell itself is also not unique.

A simple 2D example of this is graphene (Figure 2.1), which exhibits a repeating hexagonal lattice structure representing a honeycomb.

2.2.2 Point symmetry operations

Having established the fundamental building blocks of crystalline materials - lattices and unit cells - we now turn to the concept of symmetry, which governs the arrangement and properties of these structures.

A *symmetry operation* is a transformation that leaves an object unchanged and preserves all attributes of the object. If the new object generated by symmetry is indistinguishable from the old object, it is said to be *invariant*. A *point symmetry operation* leaves at least one point stationary. The main point symmetry elements are:

- Rotation (about an axis): A rotation through an angle $\theta = 360°/n$ about an axis, where n is an integer
- Inversion (through a point): A reflection through a center point, transforming $r \to -r$ with the origin as the inversion point

From this, we also generate two important point symmetry operations:

- Roto-inversion: A combination of rotation followed by inversion through a point
- Reflection in a mirror plane: Equivalent to a 180° rotation followed by an inversion through a mirror plane

Rotation symmetry is denoted by n for a n-fold or $360°/n$ rotation about an axis. A combination of rotation and inversion, called a *roto-inversion*, is denoted by $\bar{n}$, indicating a n-fold rotation followed by inversion through a point. A mirror plane is denoted by m.

The symmetry operations can be represented mathematically as follows:

- Rotation: $R_z(\theta) = \begin{pmatrix} \cos\theta & -\sin\theta & 0 \\ \sin\theta & \cos\theta & 0 \\ 0 & 0 & 1 \end{pmatrix}$, where $\theta = 360°/n$

- Inversion: $I = \begin{pmatrix} -1 & 0 & 0 \\ 0 & -1 & 0 \\ 0 & 0 & -1 \end{pmatrix}$
- Roto-inversion: $\bar{n} = I \cdot R(\theta)$
- Reflection: $m = I \cdot R(180°)$

2.2.3 Symmetry groups and crystal systems

Symmetry operations can be combined to form a *group*: an algebraic structure consisting of a set of elements that satisfy four fundamental axioms: *closure*, *associativity*, the existence of an *identity* element and the existence of an *inverse* element. A *point group* is a group of point symmetry elements that leave at least one point invariant. Although there are infinitely many possible point groups, only 32 are compatible with the translational periodicity of three-dimensional crystal lattices - these are known as the *crystallographic point groups*.

To fully describe periodic crystal structures, we must additionally consider *translational symmetry* in conjunction with point symmetries. Together, they define the 7 crystal systems: *triclinic*, *monoclinic*, *orthorhombic*, *tetragonal*, *trigonal*, *hexagonal* and *cubic* (Table 2.1). Each system is characterised by specific relationships between its lattice parameters and symmetry elements.

Each Bravais lattice has a *lattice type* depending on its translational symmetry: P (primitive), C (base-centred), I (body-centred), F (face-centred).

2.2.4 Space groups and additional symmetry operations

In 3D crystals, additional symmetry operations may arise when a translational component is combined with a point symmetry operation. When the translational part is aligned with a rotation axis, the result is a roto-translation. These include:

- Screw axes: denoted as e.g., 2_1 for a twofold rotation followed by a translation of half of the lattice vector.

- Glide planes: denoted as, e.g., a for a mirror plane followed by a translation of half the lattice vector parallel to the a-axis, or diagonal n and diamond d for glides along face diagonals by 1/2 and 1/4, respectively.

The Bravais lattice types are combined with the point groups they form 61 space groups. By additionally considering the additional symmetry elements of screw axes and glide planes, there are a total of 230 possible space groups. These space groups provide a complete description of the symmetry of any 3D crystalline material.

TABLE 2.1: The seven crystal systems and their characteristics.

Crystal System	Point Group	Lattice Parameters	Symmetry Elements
Triclinic	$1, \bar{1}$		None
Monoclinic	$2, m, 2/m$	$\alpha = \gamma = 90°$	One 2-fold axis or mirror plane
Orthorhombic	$222, mm2, mmm$	$\alpha = \beta = \gamma = 90°$	Three perpendicular 2-fold axes or mirrors
Tetragonal	$4, \bar{4}, 4/m$	$\alpha = \beta = \gamma = 90°$	One 4-fold axis
	$422, 4mm, \bar{4}2m, 4/mmm$		
Trigonal	$3, \bar{3}$	$a = b = c$	One 3-fold axis
	32, 3m, $\bar{3}m$	$\alpha = \beta = \gamma \neq 90°$	
Hexagonal	$6, \bar{6}, 6/m$	$a = b$	One 6-fold axis
	$622, 6mm, \bar{6}m2, 6/mmm$	$\alpha = \beta = 90°$, $\gamma = 120°$	
Cubic	$23, m\bar{3}$	$a = b = c$	Four 3-fold axes
	$432, \bar{4}3m, m\bar{3}m$	$\alpha = \beta = \gamma = 90°$	

2.3 Probing crystal structure

Understanding the atomic arrangement in crystalline materials is fundamental to materials science. While we can describe crystal structures in real space using lattice vectors and unit cells, determining these structures experimentally requires a different mathematical framework - that of reciprocal space. This section introduces

the concept of reciprocal space and shows how it naturally connects to diffraction experiments, our primary tool for determining crystal structures.

2.3.1 Reciprocal space

The concept of reciprocal space provides a powerful mathematical framework for understanding crystal structures and their experimental characterisation. While real (or direct) space describes the physical positions of atoms in a crystal, reciprocal space represents the Fourier transform of the crystal lattice, providing a natural description of crystal planes and diffraction phenomena in the frequency domain. This is crucial for linking the geometric properties of crystal structures to measurable physical phenomena, including crystal morphology, vibrational behaviour, and diffraction patterns.

The reciprocal lattice is defined as the Fourier transform of the direct lattice. For a crystal lattice described by lattice vectors $\mathbf{R} = \sum_{i=1}^{3} n_i \mathbf{a}_i$, the reciprocal lattice is given by its Fourier transform:

$$L(\mathbf{Q}) = \int \sum_{\mathbf{R}} \delta(\mathbf{r} - \mathbf{R}) e^{i\mathbf{Q}\cdot\mathbf{r}} d^3r \tag{2.3}$$

$$= \sum_{\mathbf{R}} e^{i\mathbf{Q}\cdot\mathbf{R}} \tag{2.4}$$

where $\mathbf{Q}$ is the Fourier conjugate variable, or the wave vector in reciprocal space. The sum over all lattice points $\mathbf{R}$ results in constructive interference only when $\mathbf{Q} \cdot \mathbf{R} = 2\pi m$ for integer m, which defines the reciprocal lattice vectors $\mathbf{G}$:

$$\mathbf{G} = \sum_{i=1}^{3} m_i \mathbf{b}_i \tag{2.5}$$

Where integers m_i are hereon referred to as h, k, l for $i = 1, 2, 3$ respectively, also known as the *Miller indices*, and $\mathbf{b}_i$ are the reciprocal lattice (or *dual*) basis vectors. These basis vectors are defined by the orthogonality condition:

$$\mathbf{a}_i \cdot \mathbf{b}_j = 2\pi\delta_{ij} \tag{2.6}$$

which leads to the explicit form:

$$\mathbf{b}_i = 2\pi \frac{\mathbf{a}_i \times \mathbf{a}_j}{\mathbf{a}_i \cdot \mathbf{a}_j \times \mathbf{a}_k} \epsilon_{ijk}, \tag{2.7}$$

Where ϵ_{ijk} is the Levi-Civita tensor and δ_{ij} is the Kronecker-delta tensor.

Further, $e^{i\mathbf{G}\cdot\mathbf{R}} = 1$ implies that $\mathbf{G} \cdot \mathbf{R} = 2\pi m \; \forall \; \mathbf{R}$, where m is an integer.

2.3.2 Diffraction

When a crystal is exposed to radiation (X-rays, neutrons, or electrons), the scattered intensity pattern contains information about the atomic arrangement. To understand this process mathematically, we begin by considering a general periodic function $V(\mathbf{r})$ that describes some property of the crystal (e.g., electron density for X-rays or nuclear density for neutrons). By definition, this function must be periodic over the lattice; $V(\mathbf{r}) = V(\mathbf{r} + \mathbf{R}) \; \forall \; \mathbf{R} \in \mathbb{Z}^3$.

Assuming $V(\mathbf{r})$ is weak, we apply time-dependent perturbation theory under the first Born approximation to determine the scattering amplitude for X-rays and neutrons. Using Fermi's Golden Rule, we then calculate the transition rate from an initial to a final state, which is proportional to:

$$|\langle \mathbf{k}_i | V(\mathbf{r}) | \mathbf{k}_f \rangle|^2 \tag{2.8}$$

The incident and scattered radiation can be approximated to plane waves with wave vectors $\mathbf{k}_i$ and $\mathbf{k}_f$ respectively. Considering only elastic scattering, we have that $|\mathbf{k}_i| = |\mathbf{k}_f|$; thus for plane wave states the matrix element $\langle \mathbf{k}_i | V(\mathbf{r}) | \mathbf{k}_f \rangle$, or the

diffracted amplitude, is the Fourier transform of $V(\mathbf{r})$;

$$\langle \mathbf{k}_i | V(\mathbf{r}) | \mathbf{k}_f \rangle = \int V(\mathbf{r}) e^{i(\mathbf{k}_i - \mathbf{k}_f)\cdot \mathbf{r}} \tag{2.9}$$

Where $\mathbf{Q} = \mathbf{k}_i - \mathbf{k}_f$ is the scattering vector.

By exploiting the periodicity of the crystal, we can decompose the integral over the unit cells:

$$\langle \mathbf{k}_i | V(\mathbf{r}) | \mathbf{k}_f \rangle = \sum_R \int_{unit\ cell} d^3x e^{i\mathbf{k}(\mathbf{x}+\mathbf{R})} f(\mathbf{x}+\mathbf{R}) \tag{2.10}$$

$$= \sum_R e^{i\mathbf{k}\cdot\mathbf{R}} \int_{unit\ cell} d^3x e^{i\mathbf{k}\cdot\mathbf{x}} f(\mathbf{x}) \tag{2.11}$$

The first factor is the Fourier transform of the lattice, and only produces a non-zero value if $\mathbf{k}$ is on the reciprocal lattice (or, $\mathbf{k} = \mathbf{G}$, also known as the *Laue condition*). The second factor is the *structure factor*, and thus Equation 2.11 can be rewritten as:

$$\langle \mathbf{k}_i | V(\mathbf{r}) | \mathbf{k}_f \rangle = (2\pi)^3 \sum_{\mathbf{G}} \delta^3(\mathbf{k} - \mathbf{G}) \left(\int_{unit\ cell} d^3x e^{i\mathbf{k}\cdot\mathbf{x}} f(\mathbf{x}) \right) \tag{2.12}$$

$$= (2\pi)^3 \sum_{\mathbf{G}} \delta^3(\mathbf{k} - \mathbf{G}) \cdot S(\mathbf{G}) \tag{2.13}$$

Where $S(\mathbf{G})$ is the structure factor, given by:

$$S(\mathbf{G}) = \int_{unit\ cell} d^3x e^{i\mathbf{G}\cdot\mathbf{x}} f(\mathbf{x}) \tag{2.14}$$

2.3.3 Structure factor

The structure factor $S(\mathbf{G})$ describes how the arrangement of atoms within the unit cell affects the diffraction pattern. It can be further decomposed into a sum of atomic form factors $f_j(\mathbf{G})$:

$$S(\mathbf{G}) = \sum_j f_j(\mathbf{G}) e^{i\mathbf{G}\cdot\mathbf{r}_j} \tag{2.15}$$

where $f_j(\mathbf{G})$ is the atomic form factor representing the scattering power of atom j at position $\mathbf{r}_j$ in the unit cell. The atomic form factor depends on the type of radiation used:

- For X-ray diffraction: $f_j(\mathbf{G}) \approx Z_j$, where Z_j is the atomic number, as X-rays scatter from electron density
- For neutron diffraction: $f_j(\mathbf{G}) \approx b_j$, where b_j is the nuclear scattering length, as neutrons scatter from atomic nuclei

This fundamental result shows that diffraction occurs only when the scattering vector $\mathbf{Q}$ equals a reciprocal lattice vector $\mathbf{G}$, and the intensity of the diffracted beam is proportional to $|S(\mathbf{G})|^2$. This is the basis for determining crystal structures through diffraction experiments.

The structure factor has two important symmetry properties that are crucial for determining crystal symmetry from diffraction patterns:

1. The intensity $|S(\mathbf{G})|^2$ contains the full point group symmetry of the crystal.
2. Friedel's Law: $|S(\mathbf{G})|^2 = |S(-\mathbf{G})|^2$ whether or not the crystal has inversion symmetry. Therefore the symmetry of the diffraction pattern, or the Laue class, is equal to the crystal point group augmented by an inversion centre.

For simple crystal structures, the structure factor can be calculated explicitly. For example:

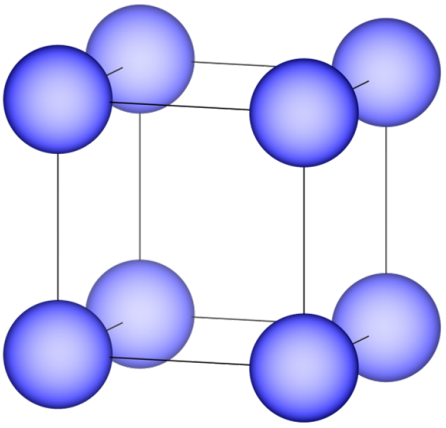


FIGURE 2.2: Simple primitive cubic crystal structure of Po, which is the only element in the periodic table that crystallizes in a simple cubic structure[3].

- Primitive cubic: With atoms only at the corners of the unit cell ($[0,0,0]$), the structure factor is simply:

$$S_{(hkl)}^{cubic} = \sum_j f_j \tag{2.16}$$

- Face-centred cubic: With additional atoms at face centers ($[\frac{1}{2},\frac{1}{2},0]$, $[\frac{1}{2},0,\frac{1}{2}]$, $[0,\frac{1}{2},\frac{1}{2}]$), the structure factor becomes:

$$S_{(hkl)}^{fcc} = f_j\left(1+(-1)^{h+k}+(-1)^{h+l}+(-1)^{k+l}\right) \tag{2.17}$$

This leads to systematic absences when h,k,l are mixed even and odd numbers

2.3.3.1 The Bragg condition

The Bragg condition provides an intuitive real-space description of diffraction that is mathematically equivalent to the reciprocal space formulation. Consider a beam of radiation (X-rays or neutrons) incident on a crystal at angle θ to a set of crystal planes with spacing d_{hkl} (Figure 2.3). Constructive interference occurs when the path difference between waves scattered from adjacent planes is an integer multiple of the wavelength λ:

$$2d_{hkl}\sin\theta = n\lambda \tag{2.18}$$

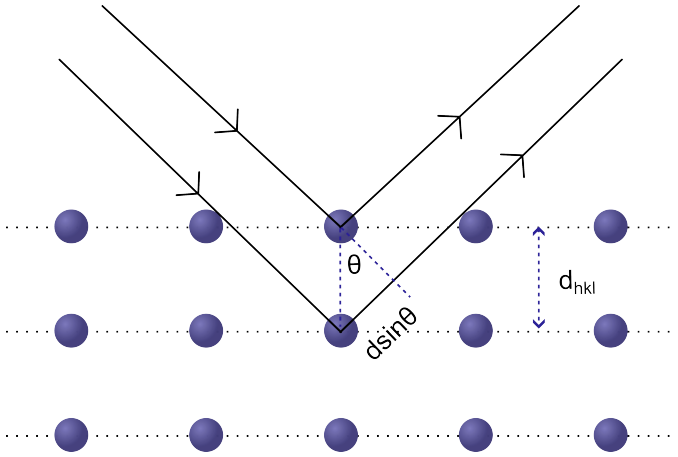


FIGURE 2.3: Geometric construction of Bragg's law. The path difference between waves scattered from adjacent planes is $2d_{hkl}\sin\theta$, leading to constructive interference when this equals $n\lambda$.

where n is an integer representing the order of diffraction. This condition can be derived from the reciprocal space formulation by considering that the scattering vector $\mathbf{Q} = \mathbf{k}_f - \mathbf{k}_i$ must equal a reciprocal lattice vector $\mathbf{G}$ for constructive interference to occur.

The Ewald sphere construction (Figure 2.4) provides a geometric interpretation of the diffraction condition in reciprocal space. The sphere, with radius $2\pi/\lambda$, represents all possible elastic scattering events. Diffraction occurs when the Ewald sphere intersects a reciprocal lattice point, satisfying both the Bragg condition and the Laue condition $\mathbf{Q} = \mathbf{G}$.

The measured diffraction intensity depends on several experimental factors:

- **Polarization factor**: $\mathbf{P} = |\epsilon_i \cdot \epsilon_f|^2$, where ϵ_i and ϵ_f are the polarization vectors of the incident and scattered radiation
- **Absorption**: Attenuation of the diffracted beam due to interactions with the sample, dependent on sample geometry and X-ray wavelength
- **Lorentz factor**: Accounts for the time a reciprocal lattice point spends in the diffraction condition as the crystal rotates
- **Structure factor**: $|S(\mathbf{G})|^2$ as discussed in the previous section

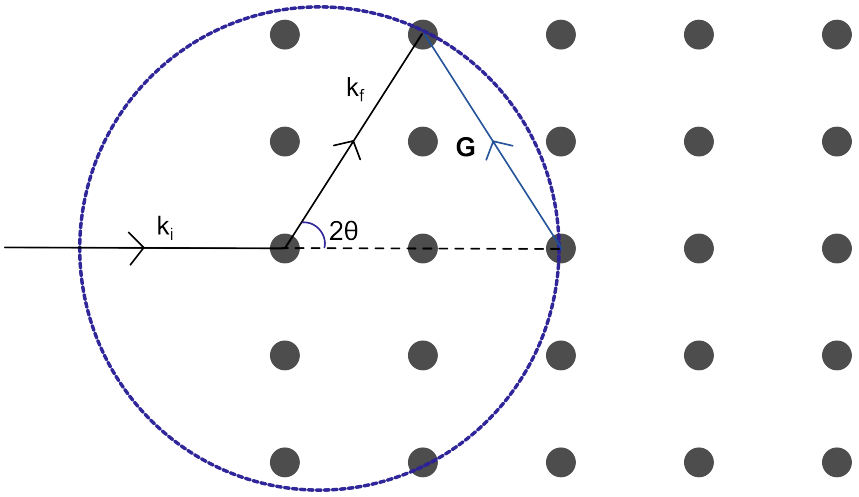


FIGURE 2.4: The Ewald sphere construction in reciprocal space. Diffraction occurs when the sphere intersects a reciprocal lattice point, satisfying both the Bragg condition and the Laue condition $\mathbf{Q} = \mathbf{G}$.

To conclude: diffraction experiments give us two key pieces of information about crystal structures. The positions of diffraction peaks (through the Bragg condition) reveal the symmetry and dimensions of the unit cell. The intensities of these peaks (through the structure factor $|S(\mathbf{G})|^2$) tell us how atoms are arranged within that cell. Together, these allow us to determine the complete crystal structure.

2.4 Structure-property relationships

2.4.1 Neumann's Principle

One key result that arises from the symmetry of crystalline solids is *Neumann's Principle*:

Definition Any bulk physical property exhibits at least the symmetry of the crystal structure.

Examples of bulk properties, to name only a few, include the resistivity, relative permittivity, refractive index and heat capacity.

As an example, we can consider the conductivity σ of a crystal given by $\mathbf{j} = \sigma\mathbf{E}$, where σ is a second-rank tensor. If we know that the crystal contains two-fold rotational symmetry, σ must be invariant under this operation:

$$\sigma = \begin{pmatrix} \sigma_{11} & \sigma_{12} & \sigma_{13} \\ \sigma_{21} & \sigma_{22} & \sigma_{23} \\ \sigma_{31} & \sigma_{32} & \sigma_{33} \end{pmatrix} \tag{2.19}$$

$$\sigma' = 2_z\sigma = \begin{pmatrix} \sigma_{11} & \sigma_{12} & -\sigma_{13} \\ \sigma_{21} & \sigma_{22} & -\sigma_{23} \\ -\sigma_{31} & -\sigma_{32} & \sigma_{33} \end{pmatrix} \tag{2.20}$$

Therefore, we have that $\sigma_{ij} = 0 \qquad \forall \quad i \neq j$

2.4.2 Symmetry requirements for piezoelectrics and ferroelectrics

Another example, importantly for this thesis, is piezoelectricity, which describes the coupling between a first-rank tensor - either the electrical displacement $\mathbf{D}$ or the electric field $\mathbf{E}$ - and a second-rank tensor; the strain $\mathbf{S}$ or stress σ:

$$S_{ij} = d_{kij}E_k \tag{2.21}$$

$$D_k = d_{kij}\sigma_{ij} \tag{2.22}$$

where d_{kij} is the third-rank piezoelectric tensor, which can have $3^3 = 27$ individual tensor components. These are the direct and converse piezoelectric effects respectively.

If we further know that this crystal has inversion symmetry given by the operator I, by Neumann's principle the piezoelectric tensor must also follow this inversion symmetry:

$$\begin{aligned} T \cdot d_{ijk} &= I_{ip} I_{jq} I_{kr} d_{pqr} && (2.23)\\ &= (-1)^3 \delta_{ip} \delta_{jq} \delta_{kr} d_{pqr} && (2.24)\\ &= -d_{pqr} && (2.25)\\ & && (2.26) \end{aligned}$$

Therefore all elements of a piezoelectric tensor are zero for a crystal with inversion symmetry. It is clear therefore, that a critical condition for a piezoelectric material is a lack of inversion symmetry.

Physically, this makes sense: if a crystal has inversion symmetry, the local polarization $\mathbf{P_z}$ induced by application of an external stress would be countered by an equal and opposite polarization $-\mathbf{P_z}$, cancelling out the net polarization across the crystal.

Furthermore, due to the stress and strain tensors being symmetric ($\sigma_{ij} = \sigma_{ji}$ and $S_{ij} = S_{ji}$), the number of individual tensor components of d_{kij} reduces to 18. Voigt notation therefore allows us to simplify how the piezoelectric tensor is represented - $d_{ijk} \implies d_{ij}$:

$$d = \begin{pmatrix} d_{111} & d_{112} & d_{113} & d_{121} & d_{122} & d_{123} & d_{131} & d_{132} & d_{133} \\ d_{211} & d_{212} & d_{213} & d_{221} & d_{222} & d_{223} & d_{231} & d_{232} & d_{233} \\ d_{311} & d_{312} & d_{313} & d_{321} & d_{322} & d_{323} & d_{331} & d_{332} & d_{333} \end{pmatrix} \tag{2.27}$$

$$d = \begin{pmatrix} d_{11} & d_{12} & d_{13} & d_{14} & d_{15} & d_{16} \\ d_{21} & d_{22} & d_{23} & d_{24} & d_{25} & d_{26} \\ d_{31} & d_{32} & d_{33} & d_{34} & d_{35} & d_{36} \end{pmatrix} \tag{2.28}$$

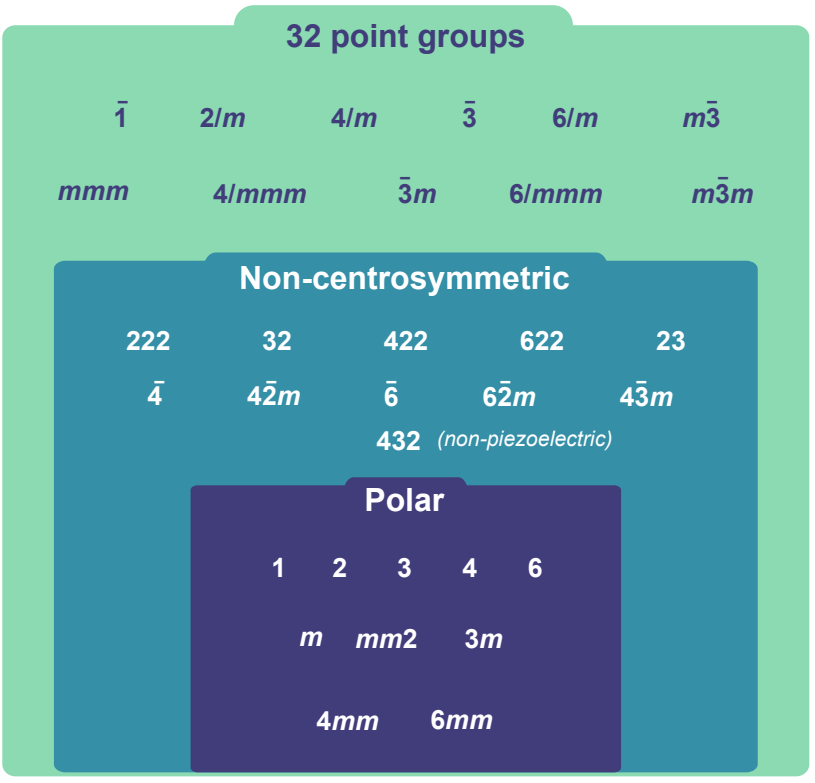


FIGURE 2.5: Schematic of the non-centrosymmetric and polar subgroups of the crystallographic point groups.

Under Voigt notation, i denotes the component of electric displacement or field in terms of the Cartesian reference frame, and $k = 1-3$ and $k = 4-6$ is used to define mechanical stress and shear stress respectively[4].

Further application of Neumann's Principle also means that for different point group symmetries, the number of independent piezoelectric tensor components reduce further.

For example, if a piezoelectric crystal contains a single symmetry axis C_n ($n = 1, 2, 3, 4, 6$) with the possible addition of symmetry σ_v, then it can also be pyroelectric and ferroelectric and have the ability to exhibit spontaneous polarization in the absence of an external electric field.

Out of the 32 point groups, 21 are non-centrosymmetric, where 20 of them are capable of exhibiting piezoelectricity. Out of the 20 piezoelectric point groups, 10 are polar and thus capable of exhibiting pyroelectricity; temperature-dependent spontaneous polarization: 1, 2, m, $mm2$, 4, $4mm$, 3, $3m$, 6, and $6mm$ (Figure 2.5). If

this polarization arises as a result of a phase transition whereby the crystal does not have a spontaneous polarization above a certain temperature (the Curie temperature, T_C), and the polarization can be reversed by an applied electric field, then the crystal is *ferroelectric*.

2.4.3 Semiconductors

2.4.3.1 A brief introduction to semiconductors

Crystal symmetry plays a crucial role in determining the electronic structure of materials. As the work of this thesis does not focus on optoelectronics, only a very brief introduction to the topic will be given here.

The transport of electrons in a crystal is determined by the periodic potential of the crystal lattice, which can be described by the Bloch theorem:

$$\psi_{n\mathbf{k}}(\mathbf{r}) = e^{i\mathbf{k}\cdot\mathbf{r}} u_{n\mathbf{k}}(\mathbf{r}) \tag{2.29}$$

where $\psi_{n\mathbf{k}}(\mathbf{r})$ is the wavefunction of the electron, $u_{n\mathbf{k}}(\mathbf{r})$ is a periodic function with the same periodicity as the crystal lattice, and $\mathbf{k}$ is the wavevector. Solutions to this equation are known as Bloch states, and the energy bands represent the allowed energy levels for electrons in the crystal. Crystal symmetry and periodicity constrain the Bloch states to exist within the first Brillouin zone, which is the primitive unit cell of the reciprocal lattice. For example, for a cubic lattice with lattice constant a; Bloch states must exist between $0 < |k| < \pi/\mathrm{a}$.

In a semiconductor, the electronic structure can be described by the band theory, which describes the behaviour of electrons in a crystal in terms of energy bands. The valence band E_v is the highest energy band occupied by electrons, and the conduction band E_c is the lowest energy band unoccupied by electrons. The band gap E_g is the energy difference between the valence and conduction bands.

2.4.4 The photovoltaic effect

Photons with energy greater than E_g can excite electrons from the valence band to the conduction band, creating electron-hole pairs. The electron and holes generated upon absorption of a photon can be collected and transported to the surface of the semiconductor, where they can be used to generate electricity. The energy of the photon is given by

$$E = h\nu = \frac{hc}{\lambda} \tag{2.30}$$

where ν is the frequency of the photon, λ is the wavelength of the photon, h is Planck's constant, and c is the speed of light. Any excess energy above E_g is lost through thermalisation processes, while photons with energy below E_g are not absorbed and thus cannot contribute to the photovoltaic effect. Consequently, a semiconductor's bandgap determines the spectral range of sunlight that can be effectively harvested. The solar spectrum, which originates from the Sun's photosphere, can be approximated as a black body spectrum at 5778 K (Figure 2.6). However, atmospheric absorption and scattering significantly modify this spectrum before it reaches the Earth's surface. To account for these effects, the standardised Air-Mass 1.5 (AM1.5) spectrum is commonly used as a reference for terrestrial solar energy applications (Figure 2.6a), representing the yearly average solar irradiance at mid-latitudes.

The theoretical efficiency limit for a single-junction solar cell, known as the *detailed balance limit*, was first established by Shockley and Queisser in 1961[6], modelled on an idealised solar cell considering only radiative recombination as a loss mechanism. Later, Tiedje et al. (1984)[7] expanded this framework by incorporating the effect of free carrier absorption and Auger recombination. Their enhanced model, based on the AM1.5 solar spectrum, produced the efficiency curve shown in Figure 2.6b and predicts a maximum efficiency of 29.8% for crystalline silicon solar cells (E_g = 1.1 eV).

Higher efficiencies can be achieved by exploring alternative materials systems (Section 2.7), particularly those with tunable bandgaps such as halide perovskites. These

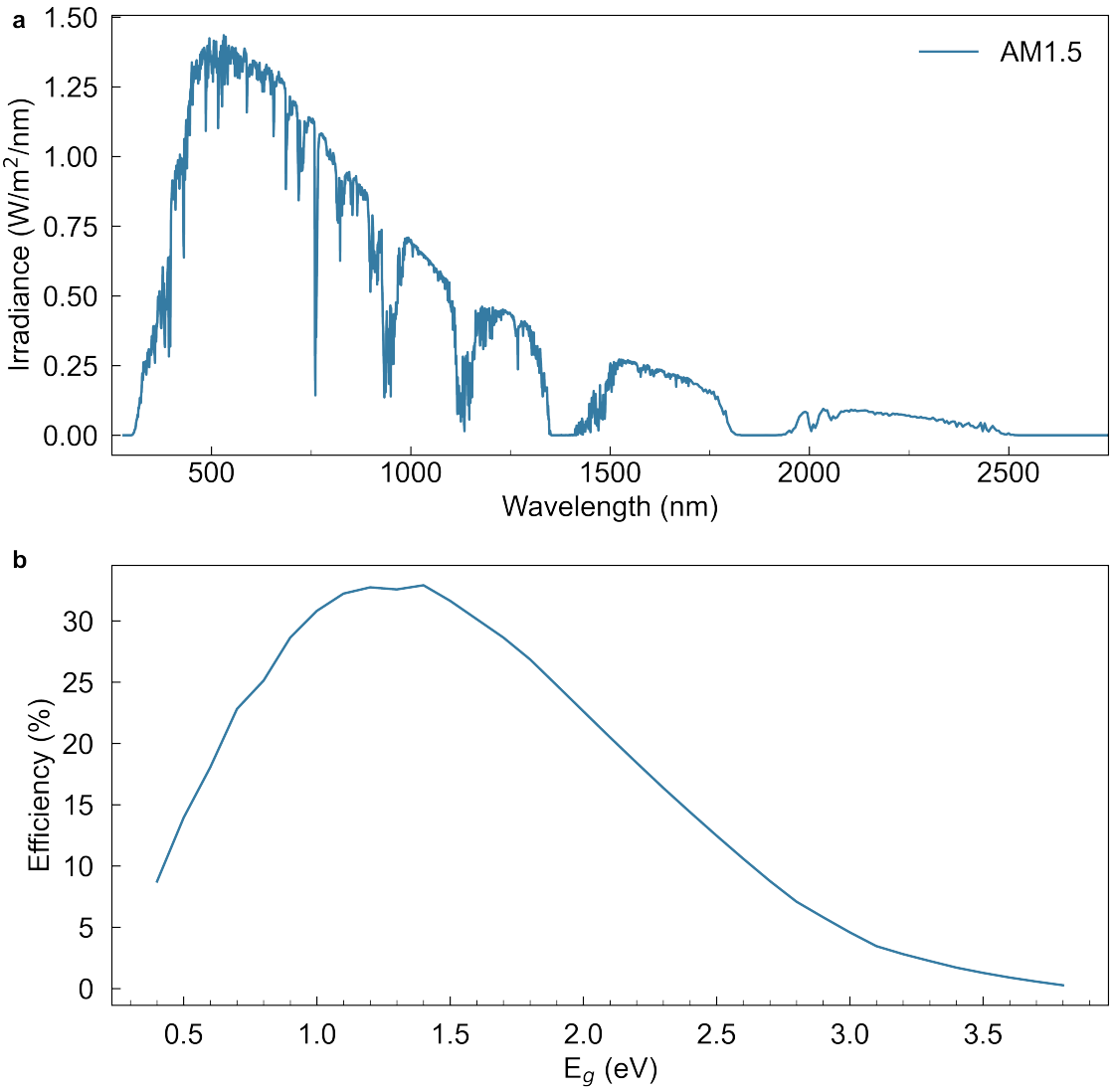


FIGURE 2.6: **a** AM 1.5 Solar spectrum and **b** Detailed balance limit [5]

materials enable the construction of multi-junction solar cells, where multiple layers of different semiconductors with distinct bandgaps are stacked together. This architecture allows for more efficient harvesting of the solar spectrum, as each layer can be optimised to absorb specific wavelength ranges, ultimately surpassing the single-junction efficiency limit.

2.5 Phase transitions

The physical properties of crystalline materials are fundamentally governed by their crystal structure and symmetry. Structural phase transitions, which involve changes in the atomic arrangement and symmetry of a crystal, can dramatically enhance or modify these properties. This is particularly evident in functional materials such as dielectrics, piezoelectrics, and pyroelectrics, where the coupling between structural changes and physical properties is crucial for their performance. Understanding these phase transitions is therefore essential for both fundamental materials science and technological applications.

These transformations between a lower symmetry phase at low temperature and a higher-symmetry phase at high temperature are typically categorised as either displacive or order-disorder transitions. Displacive transitions, such as those observed in ferroelectric materials, are characterised by a cooperative shift in atomic positions, leading to a change in the crystal structure[8]. In contrast, order-disorder transitions involve a change in the configuration or local coordination of groups of atoms, where the high-temperature phase exhibits dynamic disorder that becomes ordered upon cooling. A simple example of an order-disorder transition is the solid-liquid phase transition, where the ordered crystalline structure loses its long-range order and transforms into a disordered liquid state.

In the specific case of ferroelectric transitions, the transformation typically occurs from a ferroelectric to a paraelectric phase at a characteristic temperature known as the critical or Curie temperature T_c. This temperature is analogous to the Curie temperature in ferromagnetic systems, marking the loss of spontaneous polarization in the high-temperature phase.

A well-known example of a displacive transition occurs in ferroelectric barium titanate ($BaTiO_3$), which adopts a paraelectric cubic perovskite structure (point group $m\bar{3}m$) above its T_c at 120 °C. Below this temperature, the central Ti atom shifts off-centre within the TiO_6 octahedron, breaking cubic symmetry and resulting in a tetragonal phase (point group $4mm$) with a net dipole moment caused by this displacement (Figure 2.7a,b). In contrast, sodium nitrite ($NaNO_2$) exhibits an order-disorder transition[9]. Above its T_c of 165 °C, $NaNO_2$ adopts a paraelectric

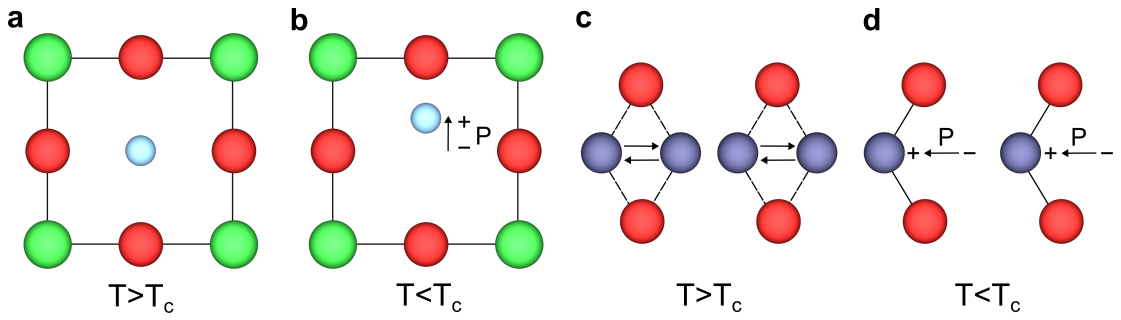


FIGURE 2.7: High-temperature paraelectric **a**, **c** and low-temperature ferroelectric **b**, **d** of barium titanate ($BaTiO_3$) and sodium nitrite ($NaNO_2$), respectively.

cubic structure in which the nitrite (NO_2^-) ions exhibit dynamic orientational disorder, averaging to a zero net dipole moment. Below T_c, these ions become ordered, breaking symmetry and inducing a net dipole moment (Figure 2.7c,d).

2.5.1 Landau's theory for phase transitions

The nature of these transitions can be quantitatively described using Landau's phenomenological theory of phase transitions, which provides a powerful framework connecting crystallography to thermodynamics. This theory has been successfully applied to describe a wide range of phenomena including ferromagnetism, superconductivity, superfluidity, and structural phase transitions in crystalline materials[10].

A temperature-driven phase transition is characterised by an *order parameter*, a physical quantity that distinguishes between the high- and low-temperature phases. The order parameter is zero in the high-symmetry phase (above the critical temperature T_c) and becomes non-zero in the low-symmetry phase (below T_c). In different systems, the order parameter can represent various physical quantities: atomic displacements in structural transitions, magnetisation in ferromagnets, or polarization in ferroelectrics. The nature of the transition is classified based on how the order parameter evolves at T_c: a discontinuous jump indicates a *first-order* transition, while a continuous growth from zero signifies a *second-order* transition.

In order to derive information about the equilibrium properties of a system, one must begin at the free energy F of the system. Landau's theory expresses the Helmholtz free energy F as a Taylor expansion in terms of the order parameter η:

$$\Delta F(\eta, T) = a_1(T)\eta + a_2(T)\eta^2 + a_3(T)\eta^3 + a_4(T)\eta^4 + \dots \tag{2.31}$$

With coefficients $a_1(T)$, $a_2(T)$, $a_3(T)$, $a_4(T)$, etc. being temperature-dependent parameters that determine the nature of the phase transition, the free energy must be invariant under the symmetry operations of the crystal, including of the high-temperature phase. Therefore, in the case of a centrosymmetric crystal above T_c, symmetry considerations require that only even powers of η can appear, reducing the free energy to:

$$\Delta F(\eta, T) = \alpha(T)\eta^2 + \beta(T)\eta^4 + \dots \tag{2.32}$$

By minimising the free energy with respect to the order parameter η, the equilibrium value of η can be found, depending on the coefficients $\alpha(T)$ and $\beta(T)$. For a second-order transition, $\alpha(T)$ changes sign at T_c, while $\beta(T)$ remains positive. This leads to a continuous change in the equilibrium value of η as temperature varies. In contrast, for a first-order transition, both $\alpha(T)$ and $\beta(T)$ can change sign, resulting in a discontinuous jump in the order parameter (2.8).

The heat capacity C_p of the system can be derived from the free energy as:

$$C_p = -T\frac{\partial^2 F}{\partial T^2} \tag{2.33}$$

And it can be shown that for a second-order transition, a finite step jump in the heat capacity is observed at T_c, while for a first-order transition, the heat capacity spikes at T_c. Therefore, measurements of the heat capacity via for example differential scanning calorimetry can be used to determine the nature of the phase transition.

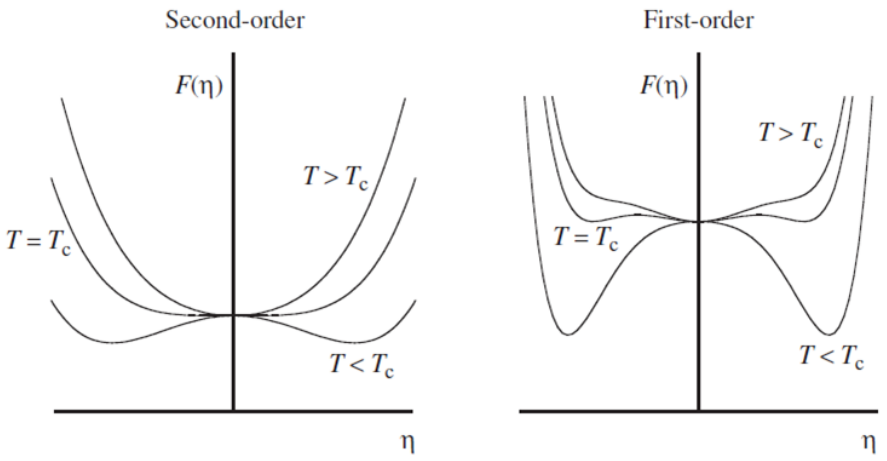


FIGURE 2.8: Energy landscape of a second-order **a** and first-order **b** phase transition.

2.6 Piezoelectricity and Ferroelectricity

Piezoelectricity is the ability of non-centrosymmetric crystalline materials to generate electrical polarization under an applied mechanical force, or conversely, mechanical strain under an applied electrical field. This phenomenon was first demonstrated in 1880 by Jacques and Pierre Curie in quartz and Rochelle salt. The fundamental principle of piezoelectricity was soon recognised for its far-reaching implications; notably, a piezoelectric quartz crystal played a crucial role in the discovery of the radioactive elements polonium and radium by Marie and Pierre Curie in 1898.

Since then, piezoelectric materials have been employed in a wide range of applications, including ultrasound transducers for medical imaging, stethoscopes, inkjet printer nozzles, and mechanical energy harvesters[11]. Mechanical energy is continuously present in the form of vibrations, as well as acoustic, hydraulic, and fluid energy, making ambient mechanical energy harvesting a highly promising field. This has sparked intense research interest, as such technologies could enable self-powered electronics and Internet of Things (IoT), including portable devices, sensors, and biomedical applications such as electrostimulation therapy and wireless, low-power, body-implantable medical devices[12, 13].

Most high-performance piezoelectric materials are also ferroelectric, meaning they

exhibit spontaneous electric polarization that can be reversed by an applied external electric field[14]. Ferroelectricity was first discovered by Joseph Valasek in 1921 in Rochelle salt[15]. The observation of this phenomena led to the discovery of a series of ferroelectric oxides such as $BaTiO_3$, $PbTiO_3$, $Pb(Mg_{1/3}Nb_{2/3})O_3$(PMN), $(K_{0.5}Na_{0.5})NbO_3$ and $PbZrO_3$-$PbTiO_3$ (lead zirconium titanate, known as PZT), all exhibiting exceptional piezoelectric performance compared with non-ferroelectrics [16]. Among these, the solid-solution PZT stands out due to its exceptional piezoelectric performance (high d_{ij}).

The link between piezoelectricity and ferroelectricity can be seen in $BaTiO_3$. When subjected to compression along specific crystallographic directions, the relative displacement of charged ions increases, enhancing crystal tetragonality (i.e., increasing the c/a ratio) and thereby strengthening the dipole moment, leading to a greater piezoelectric response.

2.6.1 Traditional piezoelectrics

Despite the successes of piezoelectric and ferroelectric ceramics and their extensive use in devices like sensors, actuators, and energy harvesting systems, there remains significant disadvantages with their use and processing. First, their synthesis require high-temperature sintering processes with tight compositional control[17]. Secondly, ceramics are highly brittle and heavy-weight[18], limiting applications requiring lightweight mechanical flexibility. This renders ceramic oxides unsuitable for IoT and flexible applications despite their high d_{ij}s. Importantly, most high-performance ferroelectrics are lead-containing; more than 60% by weight in the case of PZT[19]. This raises significant environmental and regulatory concerns as global restrictions on toxic substances continue to tighten under measures such as the European Union Restriction of Hazardous Substances (RoHS)[20]. Although significant work has gone into exploring high-performance lead-free ceramics, their T_cs are too low for industrial application compared with lead-containing ceramics (Table 2.2).

These limitations have driven research toward non-toxic, flexible organic piezoelectric and ferroelectric materials. The polymer poly(vinylidene fluoride) (PVDF), discovered to be ferroelectric in 1969[21, 22], and its copolymer poly(vinylidene

fluoride-co-trifluoroethylene) (P(VDF-TrFE)) have been extensively studied and applied across various technologies. However, their piezoelectric coefficients (d_{33} = 34 and 28 pC/N, respectively)[23, 24] remain significantly lower than ceramic materials, and they exhibit limited thermal stability at elevated temperatures. Additionally, stabilising the ferroelectric β-phase of PVDF continues to present a considerable challenge[22].

2.6.2 The case for hybrid organic-inorganic piezoelectrics

Consequently, significant efforts have focused on developing a new generation of lead-free materials that combine high piezoelectric coefficients, ease of fabrication, and mechanical flexibility. Among these, hybrid organic-inorganic perovskites and their derivatives have garnered considerable attention due to their exceptional defect tolerance and impressive optoelectronic properties, which have been extensively explored in photovoltaic and other electronic applications [25], whilst ceramics require powder milling processes on the order of days in length, followed by pressing and sintering at around 1000 °C[16, 26], hybrid organic-inorganic materials can be synthesised within a number of hours via solution-processing and thermal annealing at low temperatures ($\sim$ 100 °C), substantially reducing the cost of production.

Notable recent successes include $[(CH_3)_3NCH_2Cl]MnCl_3$ (with d_{33} = 185 pC/N)[27] and $[(CH_3)_3NCH_2F]_x[(CH_3)_3NCH_2Cl]_{1-x}CdCl_3$ (d_{33} = 1540 pC/N) [28] [Table 2.2]. Thus far however, these advances have still relied on toxic and highly-toxic heavy metals, such as Mn and Cd, highlighting the continuing need for low-toxicity ferroelectrics[29–32].

2.6.3 Design principles of organic-inorganic metal halide piezoelectrics

Various design strategies have been proposed and implemented for engineering so-called molecular ferroelectrics, particularly focussed around manipulating their order-disorder phase transitions[33, 34]:

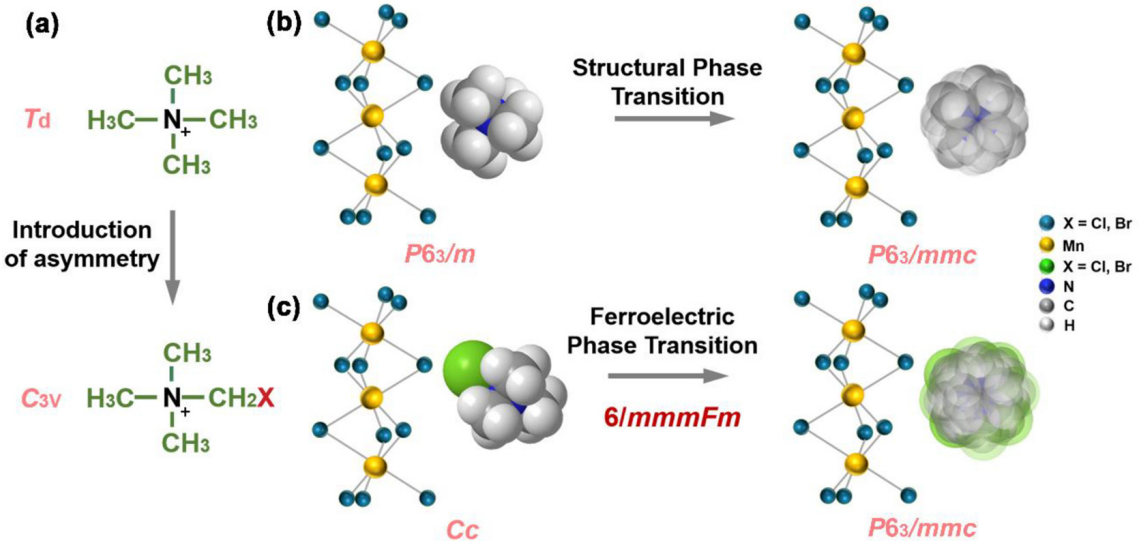


FIGURE 2.9: Application of quasi-spherical theory to the parent structure $[(CH_3)_4]CdCl_3$ to form the ferroelectric $[(CH_3)_3NCH_2Cl]CdCl_3$. Reprinted with permission from Zhang et al. [34]. Copyright 2019 American Chemical Society.

The first of these is *'quasi-spherical theory'*, first proposed in 2019 by Zhang et al[34], which utilises modified 'quasi-spherical' organic cations which exhibit rapid, disordered dynamic motion - typically whole molecule tumbling - above T_c. The high symmetry generated by this motion is lost upon cooling as the asymmetric organic cations become static in the structure, inducing net polarization. In the case of $[(CH_3)_3NCH_2Cl]CdCl_3$, a tetramethylammonium $[(CH_3)_4N]^+$ was modified via the replacement of one methyl group with a chloromethyl group, and inserted into the inorganic cadmium-halide 1D chain. Whilst $[(CH_3)_4]CdCl_3$ crystallizes in the centrosymmetric space groups $P6_3/m$ and $P6_3/mmc$ below and above T_c, respectively; the asymmetry induced by the chloromethyl group leads to $[(CH_3)_3NCH_2Cl]CdCl_3$, with a reduction of symmetry to the polar space group Cc, with C_{3v} symmetry (Figure 2.9). Other examples of modified spherical cations that have been implemented with this theory include 1,4-diazabicyclo[2.2.2]octane (dabco or $N_2(C_2H_4)_3$)[35] and quinuclidine ($HC(C_2H_4)_3N$)[36] to form aspherical cations.

Significant research has also been conducted into inducing ferroelectrics via the introduction of *homochiral* molecules, where the molecules exist in a uniform chirality or 'handed-ness', characterised by a lack of mirror symmetry. There are 11 chiral point groups, denoted in both Hermann-Mauguin (international) and Schoenflies notation[37]: 1 (C_1), 2 (C_2), 222 (D_2), 4 (C_4), 422 (D_4), 3 (C_3), 32 (D_3), 6

(C_6), 622 (D_6), 23 (T) and 432 (O), where the Schoenflies notation (in parentheses) uses C_n for cyclic groups, D_n for dihedral groups, and T and O for tetrahedral and octahedral groups, respectively. Five of these groups are also polar (1, 2, 3, 4, 6); thus there is a higher probability of crystallization in a chiral polar point group compared with achiral molecules. An example of this is ((R/S)-(-/+)-1-cyclohexylethylammonium)PbI_3, where the orientation of the amine groups along one crystal axis were shown to break the inversion symmetry of the structure, giving rise to a polar space group[38].

Additionally, *H-F substitution*, the substitution of an F for an H atom,[39] has been employed as a means to increase the T_c of ferroelectric structures via a raised potential energy barrier for dynamical rotation and tumbling, enhancing their suitability for practical applications. The first example of this was demonstrated via the fluorination of (pyrrolidinium)$MnCl_3$ [40] to (R/S)-3-(Fluoropyrrolidinium)$MnCl_3$[41], leading to an increase of T_c by 38 °C.

Despite these strategies, often the improvements in ferroelectric and piezoelectric characteristics are small; for example despite the superior piezoresponse of $[(CH_3)_3NCH_2F]_x[(CH_3)_3NCH_2Cl]_{1-x}CdCl_3$ (x=0.26) utilising some of these above-mentioned strategies, its low T_c of 100 °C still renders it unsuitable for practical applications.

TABLE 2.2: Comparison of piezoelectric coefficients (d_{ij}) and transition temperatures (T_c) for various piezoelectric materials.

Category	**Material**	d_{ij} **(pC/N)**	T_c **(°C)**	**Ref.**
Ceramic oxides				
	PZT	360	350	[42]
	$BaTiO_3$ (BTO)	191	120	[43]
	$KNbO_3$	80-160	400	[42]
	$NaNbO_3$	52.5	370	[44]
Organic compounds				
	PVDF	34	154	[23]
	DIPAB	11	153	[45]
Cd,Pb, Mn-containing hybrids				
	$(TMCM)MnCl_3$	185	133	[27]
	$(TMBM)MnBr_3$	112	142	[46]
	$(TMCM)CdBr_3$	139	73	[47]
	$(TMFM)_{0.26}(TMCM)_{0.74}CdCl_3$	1540	80-100	[48]
	$(BnNMe_2Me)CdBr_4$	6	162 (melt)	[49]
	$(FMTMA)PbCl_3$	20.6	242	[50]
	$(ATHP)_2PbBr_4$	76	230	[51]
Others				
	$(BTMA)_2CoBr_4$	$d_{32} = 12.4$	140	[52]
	$(MDABCO)NH_4I_3$	14	175	[53]
Halogeno-bismuthates				
	$(TMIM)_3Bi_2I_9$ Chapter 4	**161.5**	**250?**	*
	$(R/S\text{-}1,2\text{-}DAP_2)I_3{\cdot}BiI_5$	$d_{22} = 35$	132	[54]
	$(R/S\text{-}\alpha\text{-}PEA)_4Bi_2I_{10}$	32	197	[55]
	$(Me_2S)_3Bi_2Br_9$	18	-	[56]
	$(Me_2NH_2)_3Bi_2I_9$	8	187	[57]
	$(MePh_3P)_3Bi_2Br_9$	8	55	[58]
	$\{(sCH(MePh)(Me)NH_3)BiBr_5\}_n$	8	55	[59]

2.7 Photovoltaics

Another significant application of hybrid materials is for photovoltaics, namely hybrid organic-inorganic perovskites. In this section, we cover the crystallographic features and phase transitions of halide perovskites and related structures in the context of photovoltaics.

2.7.1 Perovskite structures and their polymorphs

The first perovskite, calcium titanate ($CaTiO_3$), was discovered in the Ural mountains Gustav Rose in 1839[60] and later named after the Russian mineralogist Lev Aleksevich von Perovski. Perovskites adopt a general ABX_3 structure, where A and B are cations and X is an anion. The structure is characterised by an infinite 3D network of corner-sharing BX_6 octahedral units stabilised by the larger A cation. For about 100 years, discovered and synthesised perovskites were generally oxides (ABO_3) such as the ferroelectric $BaTiO_3$, $PbTiO_3$, PZT and $LiNbO_3$, and others like strontium titanate ($SrTiO_3$)[61] and lanthanum ferrite ($LaFeO_3$)[62]. Their discoveries have had far-reaching consequences as capacitors, non-volatile memory storage, catalysts and solid-oxide fuel cells[63–66].

In 1893, H.L. Wells first reported metal halide perovskites of the compositions $CsPbX_3$ (X=Cl,Br,I)[67]. These compounds were later crystallographically characterised by C.K. Møller[68], who also investigated their photoconductive properties. Møller's work marked the first study of the optoelectronic behaviour of metal halide perovskites, igniting the beginning of their promising future development in optoelectronic applications. In 1978, the first hybrid organic-inorganic perovskite methylammonium lead(II) and tin(II) trihalides (methylammonium$^+$ = $CH_3NH_3^+$ or MA^+ were reported by D. Weber[69, 70]. Shortly thereafter in the 1990s, the optoelectronic and luminescent properties and solution processability of halide perovskites began to be intensely studied, particularly by Mitzi and co-workers[71–78].

The birth of the perovskite for photovoltaics subsequently began in 2009, when Miyasaka and co-workers reported the first perovskite-based solar cell using $MAPbI_3$, leading to a power conversion efficiency (PCE) of 3.8%[79].

The rapid development of metal halide perovskites for solar cells has primarily focused on ABX_3 compositions of the following: the A cation contains either a single species or a mixture of methylammonium ($CH_3NH_3^+$, MA^+), formamidinium ($HC(NH_2)_3^+$, FA^+) or Cs^+. The B cation is typically a divalent metal; Pb^{2+} or Sn^{2+}, while the X-site anion is a halide (I^-, Br^- or Cl^-), or a combination thereof. Several conditions must be considered in order for a perovskite structure to be formed. In 1926, V. M. Goldschmidt proposed the tolerance factor t for inorganic perovskite

structures, establishing a criterion for the stability of cubic ABX_3 phases based on the ionic radii of the constituent elements[80, 81]:

$$t = \frac{r_A + r_X}{\sqrt{2}r_B + r_X} \tag{2.34}$$

where materials with $0.8 < t < 1.0$ are required to form a perovskite structure. For $0.9 < t < 1.0$, a cubic structure is expected to form (t =1.0 is geometrically ideal[82]). Outside of these constraints, distortions and non-perovskite structures can form, which are explained in the following text. However, there are many systems with favourable t that do not form perovskite structures. It was realised that the formability of a stable octahedron was important; that is, the B cation must be large enough with respect to the X anion within the octahedron[83]:

$$\mu = \frac{r_B}{r_X} \tag{2.35}$$

where $\mu > 0.414$ is required.

Deviations from these geometrical descriptors can lead to breaking of cubic symmetry, arising from a combination of distortion of the BX_6 octahedral units, B-cation displacements within the octahedra and tilting of the BX_6 octahedra relative to one another, where the latter is the most common distortion[84, 85]. The structures obtained by these deviations were first classified by Glazer[86]. The tilting can be described in Glazer notation, which assigns either an in-phase (+) or out-of-phase (-) rotation of octahedra along each of the three spatial dimensions, x (first position), y (second position), and z (third position). These deviations have important effects on the properties of perovskites such as their electronic properties.

These symmetry-breaking distortions, often caused by octahedral tilts or cation displacements, typically drive phase transitions that reduce crystal symmetry. In such transitions, the lower-symmetry space group is a subgroup of the higher-symmetry phase. Many perovskites exhibit similar phase transition behaviour governed by these octahedral tilt distortions. For example, both $CaTiO_3$ and $MAPbI_3$ undergo

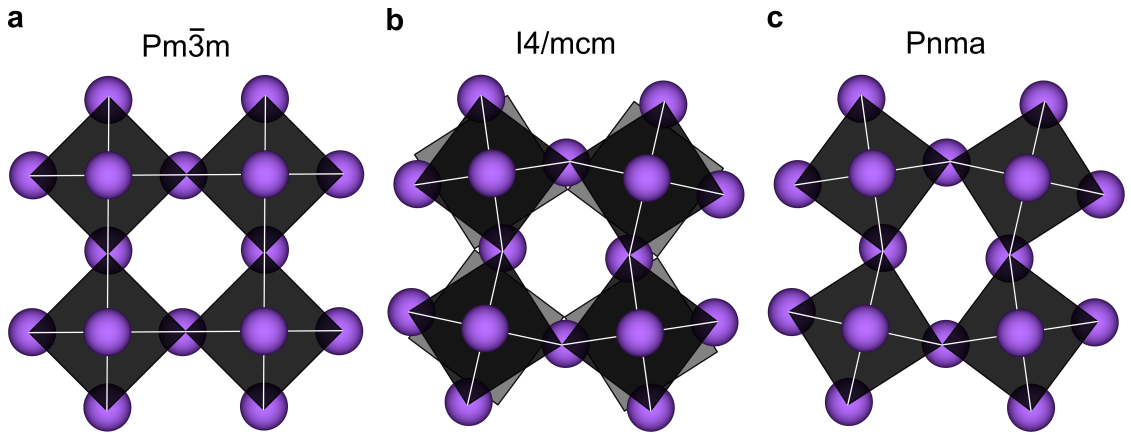


FIGURE 2.10: Visualisation of common structural distortions of perovskites: **a** cubic (α), b tetragonal (β) and c orthorhombic (γ)

analogous transitions from the cubic to tetragonal to orthorhombic with lowering temperature (Figure 2.10), often named the α, β and γ phases. These transitions follow the sequence[87–90]:

$$Pm\bar{3}m(a^0a^0a^0) \rightarrow I4/mcm/P4/mbm \quad (a^0a^0b^-/a^0a^0b^+) \rightarrow Pnma(a^-a^-b^+) \tag{2.36}$$

Among the standard cations, Cs^+ is the smallest ($Cs^+ < MA^+ < FA^+$), resulting in a tolerance factor which is too small, leading to the photo-inactive, yellow δ-$CsBX_3$ (Figure 2.11b). A corner-sharing phase can still be obtained, but typically requires a high temperature ($> 300°C$) annealing step, or modified deposition processes such as low-temperature co-evaporation using a CsI-rich composition[91] in order to kinetically stabilise the 3D corner-sharing phase.

On the other hand, the larger FA^+ cation leads to the easy formation of lower-dimensional, phases formed of face-sharing hexagonal or corner-sharing layers, named the 2H (δ), 4H and 6H polytypes, first reported and characterised by Gratia et al. [92] (Figure 2.11c-e). For example, at room temperature δ-$CsPbI_3$ and 2H-$FAPbI_3$ are thermodynamically stable, requiring thermal annealing in order to be converted and stabilised in the photoactive 3D corner-sharing phases.

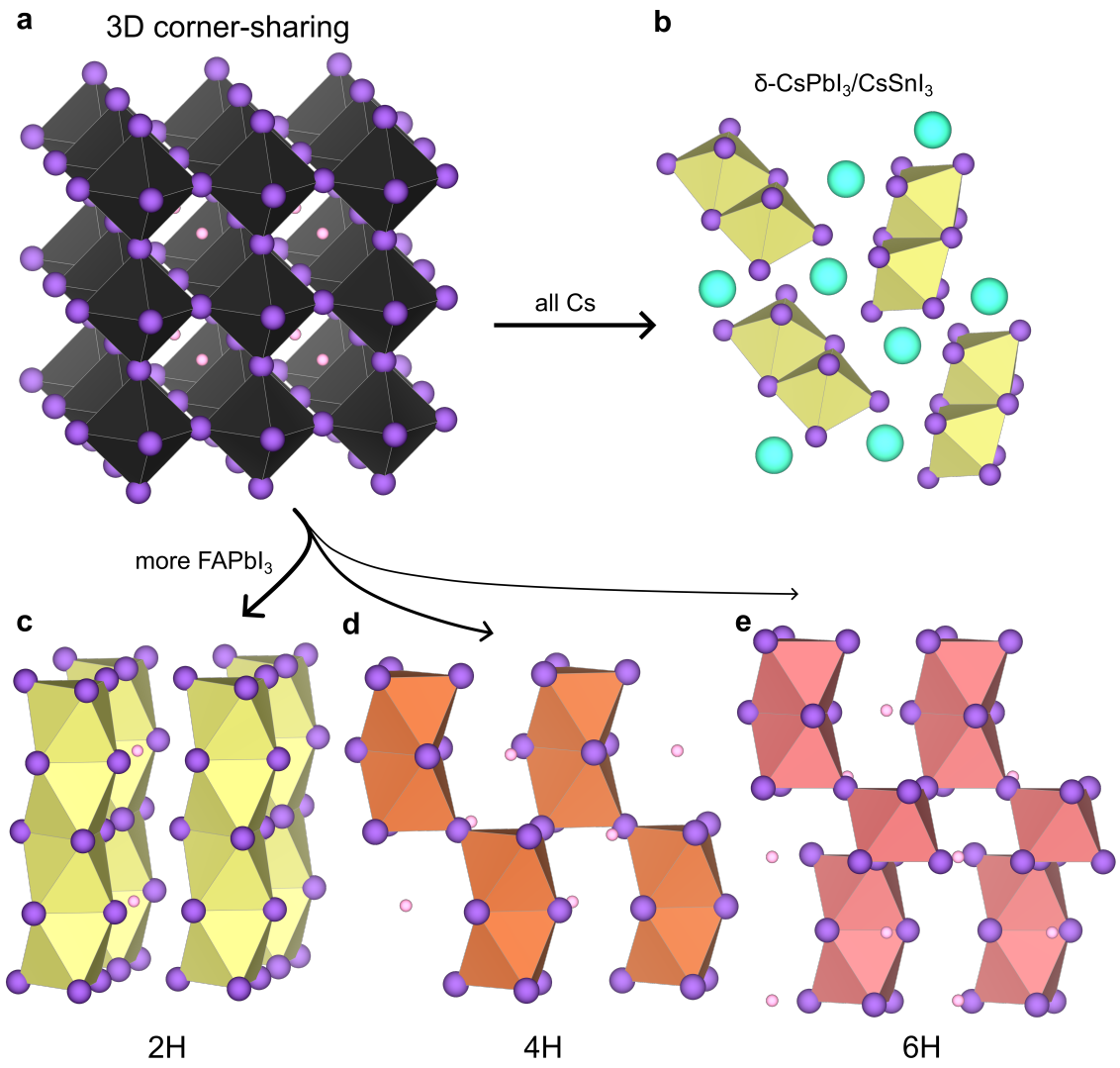


FIGURE 2.11: Transitions to non-perovskite phases from **a** 3D corner-sharing perovskite to **b** δ-$CsMX_3$ (M=Pb,Sn) or **c** 2H, **d** 4H and **e** 6H hexagonal polytypes. Pink spheres represent the A cation

While the Goldschmidt tolerance factor provides a useful geometrical criterion for perovskite formation, it has significant limitations. Whilst it correctly predicts formability of 83% of oxide perovskites, its accuracy is lower for halide perovskites. Overall, it only correctly predicts 74% of materials. These limitations arise because the tolerance factor considers only ionic radii, neglecting other important factors such as the oxidation state of the A cation.

To address these limitations, Bartel et al. proposed a new tolerance factor, τ, that incorporates both geometrical and electronic considerations[93]. This improved

model considers the oxidation state of the A cation (n_A) in addition to the ionic radii, achieving a prediction accuracy of 91% for perovskite formation. The new tolerance factor is given by:

$$\tau = \frac{r_X}{r_B} - n_A \left(n_A - \frac{r_A/r_B}{\ln(r_A/r_B)} \right) \tag{2.37}$$

where n_A is the oxidation state of the A cation. For a compound to form a perovskite structure, τ must be less than 4.18.

2.7.2 Solution processing of perovskites: Crystallization processes

A key advantage of metal halide perovskites is their solution processability, facilitated by the solubility of both metal and organic halides in organic solvents, enabling their ease of processing into thin films at low temperatures. Additionally, their low nucleation and activation energies ($\sim$ 100 kJmol^{-1})[94, 95] allows for simple solution processing techniques such as spin-coating, as well as scalable industrial fabrication methods such as slot-die coating, blade-coating, ink-jet printing and roll-to-roll printing[96]. Perovskite thin films are typically composed of crystal grains varying from sub-100 nanometres to microns in size, where the films themselves are a few hundred nanometres in thickness[97]. Ideally, grain boundaries within the film thickness should be minimised. The thin film processing conditions can have an enormous impact on the homogeneity, quality and nature of the crystal grain growth, which has subsequent effects on their charge transport properties. For example, it has been shown that controlling the orientation of crystal grains such that lattice planes are aligned with respect to the substrate, is important for maximising charge transport[98–100] and even thin film stability[101]. Furthermore, preventing the growth of any undesired amorphous or crystalline non-perovskite phases is important as they may act as sites of degradation.

Briefly, we outline the mechanism of thin film crystallization from one step deposition:

1. Solution deposition

The perovskite precursor materials, typically AX and BX_2 halide salts, are usually dissolved in polar aprotic solvents such as dimethylformamide (DMF) and dimethyl sulfoxide (DMSO) which coordinate strongly with precursors. The perovskite precursor solution can be considered as composed of coordination complexes of the precursors with the solvent molecules, typically of approximately nm in size [102]. At this point, additives such as formamidinium acetate (FAOAc), methylammonium chloride (MACl) are sometimes added into the precursor solution in order to improve final thin film orientation, interfacial contact with other solar cell layers and passivate bulk defects[103–106]. The first stage of thin film formation starts with deposition of the perovskite precursor solution using methods such as spin-coating or blade-coating.

2. Quenching

To initiate the nucleation process in the thin film, the coordinating solvent must be effectively removed. This is typically achieved by introducing an appropriate anti-solvent—such as chlorobenzene, anisole, or diethyl ether—which is miscible with the host solvent but insoluble with the perovskite precursors. During spin-coating, the application of the anti-solvent rapidly induces supersaturation of the precursor solution, triggering homogeneous nucleation and growth of the crystalline phase[107, 108]. Crystallization is covered in more detail in Section 3.1.3.

Alternatively, nitrogen gas quenching to dry and drive out the host solvent, offers greater compatibility with scalable deposition methods such as slot-die coating. In this process, intermediate phases based on PbX_2-AX-solvent are often formed. Controlling this step is crucial for improving the final film quality, particularly in terms of grain size, homogeneity, and crystal grain orientation, all of which significantly influence the resulting optoelectronic properties.

3. Annealing

The thermal annealing step, usually at about 100 °C, is used to drive out the solvent and convert any intermediate phases to the final perovskite phases. For example, in FA-containing perovskites, the photo-inactive, 2H (or δ) - phase is always thermodynamically stable at room temperature, and the annealing step is essential for conversion to the cubic 3C (or α) phase.

2.7.3 Solvent-based intermediate phases of metal halide perovskites

The structural pathways for the formation of halide perovskites are crucial for achieving high-quality films through controlled crystallization kinetics. In particular, the choice of solvent system and precursor composition directly influences the formation of intermediate phases. This is largely dictated by the coordination ability of the metal ion - such as Pb^{2+} - with other complexes in the precursor solution[109, 110]. Solvent strength coordination, commonly quantified by Gutmann's donor number D_N[111], plays a key role in determining the stability of these intermediates[96]. D_N is the negative enthalpy change (in kcal/mol) for the reaction between a solvent molecule and $SbCl_5$ in 1,2-dichloroethane, essentially a measure of the strength of the solvent's coordination ability. However, strongly coordinating solvents such as DMSO and N-methyl-2-pyrrolidone (NMP) can be disadvantageous due to their low vapour pressures and high boiling points. Residual solvent may persist in the perovskite thin film even after annealing, creating defect sites that accelerate degradation.

The formation of intermediate phases is not always beneficial. Bu et al. reported that using a DMF-based solvent system for $FA_{0.83}Cs_{0.17}PbI_3$ led to rough, inhomogeneous and poor-quality films due to the $FA_2Pb_3I_8{\cdot}4DMF$ and $Cs_2Pb_3I_8{\cdot}4DMF$ intermediates[112]. The incorporation of NMP, which has a higher D_N (27.3 kcal/mol)[113] suppressed these intermediates through the formation of a strong $PbI_2{\cdot}NMP$ adduct, leading to denser films and improved photovoltaic performance.

DMSO also has a higher D_N of 30.0 kcal/mol than DMF (26.5 kcal/mol)[114], resulting in a shorter Pb-O bond-length of 2.386 Å compared to 2.431 Å when coordinating with PbI_2[96]. During the processing of $MAPbI_3$, various intermediate phases can form, including $(MA)_2Pb_3I_8{\cdot}2DMF$, $(MA)_2Pb_2I_6{\cdot}2DMF$, $(MA)_3PbI_5{\cdot}2DMF$, $(MA)_2Pb_3I_8{\cdot}2DMSO$ and $(MA)_3PbI_5{\cdot}DMSO$ (Figure 2.12). However, the $(MA)_2Pb_3I_8{\cdot}2DMSO$ adduct preferentially forms when the solvent system contains a mixture of DMF and DMSO[115]. Specifically, $(MA)_2Pb_3I_8{\cdot}2DMSO$ was shown to have a lower, and thus more stable, formation enthalpy of -390.4 kcal/mol compared to -180 kcal/mol for DMSO and DMF, respectively. This more

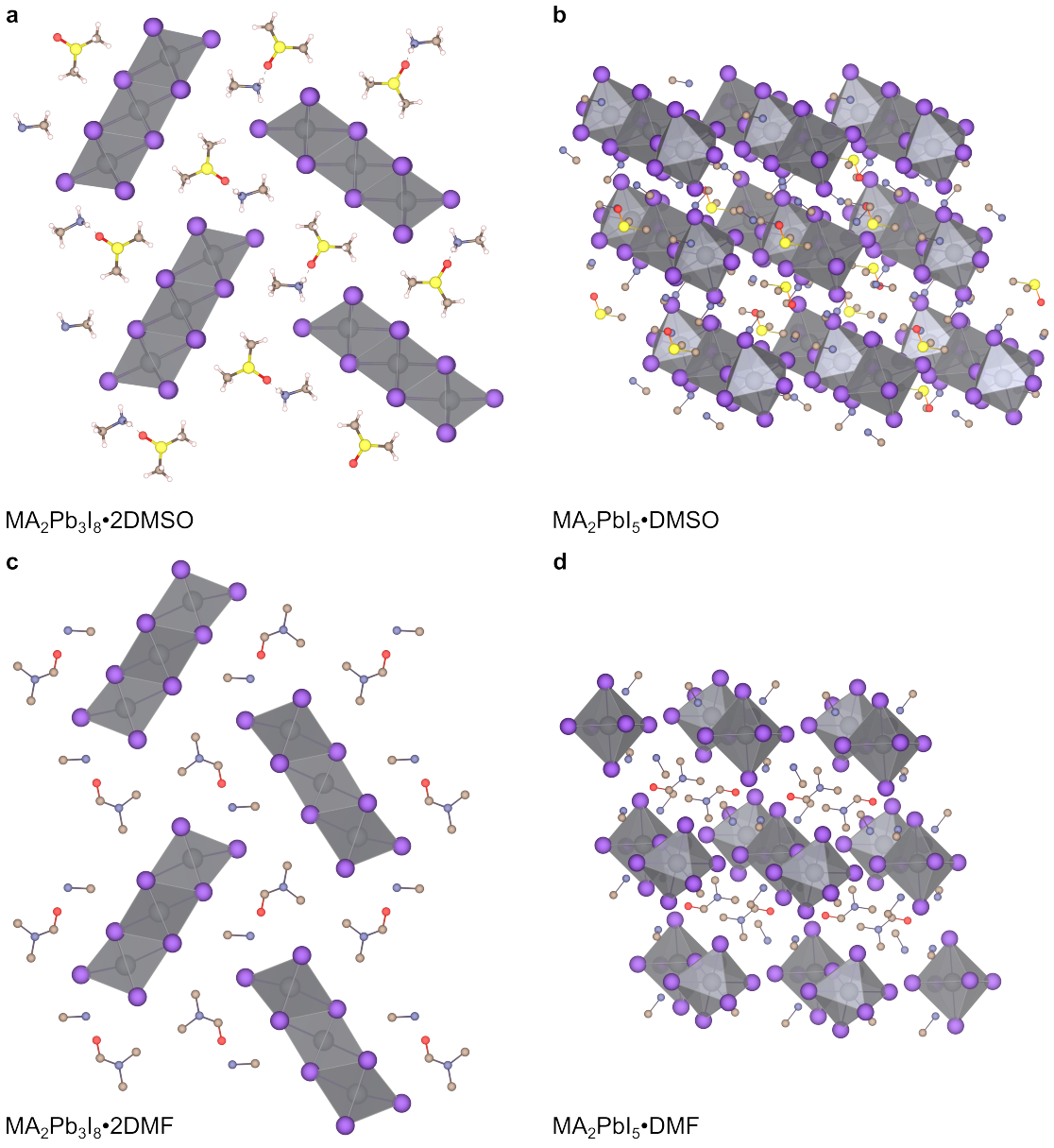


FIGURE 2.12: Crystal structures of known solvent intermediate phases. Crystal structures of $MA_2Pb_3I_8$·2DMF **c** and MA_3PbI_5·DMF **c** were reproduced with permission from reference [115], copyright 2017 American Chemical Society.

stable intermediate means that, a small amount of DMSO incorporation has been shown to lead to higher performing perovskite solar cells[116].

2.8 Chapter Summary

This chapter has provided a theoretical foundation, covering the core principles of crystallography, symmetry, and diffraction. We have established how these concepts dictate the structure-property relationships crucial for understanding phase transitions and thin-film crystallization in functional materials.

Armed with these principles, the following chapters will delve into two primary research directions. We will first explore the design and synthesis of novel organic-inorganic piezoelectric materials, examining their phase transitions through detailed X-ray diffraction analysis. Following this, we will investigate the optimisation of perovskite solar cells, focusing on the control of solution-based crystallization kinetics and intermediate phase formation to enhance device performance.

Bibliography

[1] N. W. Ashcroft and D. Mermin, *Solid State Physics*. Brooks/Cole, revised edition ed., 2020.

[2] M. T. Dove, *Structure and dynamics : an atomic view of materials*. Oxford University Press, 2003.

[3] P. F. Schewe, "Polonium's simple cubic structure," *Physics Today*, vol. 60, pp. 24–24, 2007.

[4] J.-F. Li, *Lead-Free Piezoelectric Materials*. John Wiley & Sons, 2020.

[5] S. Rühle, "Tabulated values of the Shockley-Quisser limit for single junction solar cells," *Solar Energy*, vol. 130, pp. 139–147, 2016.

[6] W. Shockley and H. J. Queisser, "Detailed balance limit of efficiency of p-n junction solar cells," *Journal of Applied Physics*, vol. 32, pp. 510–519, 1961.

[7] T. Tiedje, E. Yablonovitch, G. D. Cody, and B. G. Brooks, "Limiting efficiency of silicon solar cells," *IEEE Transactions on Electron Devices*, vol. 31, pp. 711–716, 1984.

[8] A. Grünebohm, A. Hütten, A. E. Böhmer, J. Frenzel, I. Eremin, R. Drautz, I. Ennen, L. Caron, T. Kuschel, F. Lechermann, D. Anselmetti, T. Dahm, F. Weber, K. Rossnagel, and G. Schierning, "A unifying perspective of common motifs that occur across disparate classes of materials harboring displacive phase transitions," *Advanced Energy Materials*, vol. 13, p. 2300754, 2023.

[9] I. R. Bonilla, A. Holz, and H. N. Rutt, "Theory of the order parameter of $NaNO_2$ in molecular field approximation," *physica status solidi (b)*, vol. 63, pp. 297–305, 1974.

[10] E. K. H. Salje, "Crystallography and structural phase transitions, an introduction*," *Lead Article Acta Cryst*, vol. 47, pp. 453–469, 1991.

[11] V. Jella, S. Ippili, J. H. Eom, S. V. Pammi, J. S. Jung, V. D. Tran, V. H. Nguyen, A. Kirakosyan, S. Yun, D. Kim, M. R. Sihn, J. Choi, Y. J. Kim, H. J. Kim, and S. G. Yoon, "A comprehensive review of flexible piezoelectric generators based on organic-inorganic metal halide perovskites," *Nano Energy*, vol. 57, pp. 74–93, 2019.

[12] J. A. Paradiso and T. Starner, "Energy scavenging for mobile and wireless electronics," *IEEE Pervasive Computing*, vol. 4, pp. 18–27, 2005.

[13] M. H. Bagheri, A. A. Khan, S. Shahzadi, M. M. Rana, M. S. Hasan, and D. Ban, "Advancements and challenges in molecular/hybrid perovskites for piezoelectric nanogenerator application: A comprehensive review," *Nano Energy*, vol. 120, p. 109101, 2024.

[14] M. E. Lines and A. M. Glass, *Principles and applications of ferroelectrics and related materials*. Oxford university press, 2001.

[15] N. Materials, "A century of ferroelectricity," *Nature Materials 2020 19:2*, vol. 19, pp. 129–129, 2020.

[16] G. H. Haertling, "Ferroelectric ceramics: History and technology," *Journal of the American Ceramic Society*, vol. 82, pp. 797–818, 1999.

[17] H. Park, C. Ha, and J. H. Lee, "Advances in piezoelectric halide perovskites for energy harvesting applications," *Journal of Materials Chemistry A*, vol. 8, pp. 24353–24367, 2020.

[18] S. K. Karan, R. Bera, S. Paria, A. K. Das, S. Maiti, A. Maitra, B. B. Khatua, S. K. Karan, R. Bera, S. Paria, A. K. Das, S. Maiti, A. Maitra, and B. B. Khatua, "An approach to design highly durable piezoelectric nanogenerator based on self-poled PVDF/ALO-rGO flexible nanocomposite with high power density and energy conversion efficiency," *Advanced Energy Materials*, vol. 6, p. 1601016, 2016.

[19] Y. Saito, H. Takao, T. Tani, T. Nonoyama, K. Takatori, T. Homma, T. Nagaya, and M. Nakamura, "Lead-free piezoceramics," *Nature*, vol. 432, no. 7013, pp. 84–87, 2004.

[20] B. Carreño-Jiménez, A. Reyes-Montero, and R. López-Juárez, "Complete set of ferro/piezoelectric properties of $BaZrO_3$ and (Ba,Ca)ZrO_3 doped KNLNS-based electroceramics," *Ceramics International*, vol. 48, pp. 21090–21100, 2022.

[21] Y. Abe, M. Kakizaki, T. Hideshima, J. A. Barreras-Uruchurtu, N. Besnard, and C. Paul, "The piezoelectricity of poly(vinylidene fluoride)," *Japanese Journal of Applied Physics*, vol. 8, p. 975, 1969.

[22] P. Costa, J. Nunes-Pereira, N. Pereira, N. Castro, S. Gonçalves, and S. Lanceros-Mendez, "Recent progress on piezoelectric, pyroelectric, and magnetoelectric polymer-based energy-harvesting devices," *Energy technology*, vol. 7, no. 7, p. 1800852, 2019.

[23] O. García-Zaldívar, T. Escamilla-Díaz, M. Ramírez-Cardona, M. A. Hernández-Landaverde, R. Ramírez-Bon, J. M. Yañez-Limón, and F. Calderón-Piñar, "Ferroelectric-paraelectric transition in a membrane with quenched-induced δ-phase of PVDF," *Scientific Reports*, vol. 7, no. 1, pp. 1–8, 2017.

[24] X. Hu, M. You, N. Yi, X. Zhang, and Y. Xiang, "Enhanced piezoelectric coefficient of PVDF-TrFE films via in situ polarization," *Frontiers in Energy Research*, p. 381, 2021.

[25] S. Shahrokhi, W. Gao, Y. Wang, P. R. Anandan, M. Z. Rahaman, S. Singh, D. Wang, C. Cazorla, G. Yuan, J.-M. Liu, T. Wu, S. Shahrokhi, Y. Wang, P. R. Anandan, M. Z. Rahaman, S. Singh, D. Wang, C. Cazorla, T. Wu, W. Gao,

G. Yuan, and J. m Liu, "Emergence of ferroelectricity in halide perovskites," *Small Methods*, vol. 4, p. 2000149, 2020.

[26] L. B. Kong, T. S. Zhang, J. Ma, and F. Boey, "Progress in synthesis of ferroelectric ceramic materials via high-energy mechanochemical technique," *Progress in Materials Science*, vol. 53, pp. 207–322, 2008.

[27] Y. M. You, W. Q. Liao, D. Zhao, H. Y. Ye, Y. Zhang, Q. Zhou, X. Niu, J. Wang, P. F. Li, D. W. Fu, Z. Wang, S. Gao, K. Yang, J. M. Liu, J. Li, Y. Yan, and R. G. Xiong, "An organic-inorganic perovskite ferroelectric with large piezoelectric response," *Science*, vol. 357, 2017.

[28] W. Q. Liao, D. Zhao, Y. Y. Tang, Y. Zhang, P. F. Li, P. P. Shi, X. G. Chen, Y. M. You, and R. G. Xiong, "A molecular perovskite solid solution with piezoelectricity stronger than lead zirconate titanate," *Science*, vol. 363, 2019.

[29] R. Wang, H. Li, and H. Sun, "Bismuth: Environmental pollution and health effects," *Encyclopedia of Environmental Health*, pp. 415–423, 2019.

[30] S. L. O'Neal and W. Zheng, "Manganese toxicity upon overexposure: a decade in review," *Current environmental health reports*, vol. 2, pp. 315–328, 2015.

[31] G. Genchi, M. S. Sinicropi, G. Lauria, A. Carocci, and A. Catalano, "The effects of cadmium toxicity," *International Journal of Environmental Research and Public Health 2020*, vol. 17, p. 3782, 2020.

[32] I. Coondoo, N. Panwar, and A. Kholkin, "Lead-free piezoelectrics: Current status and perspectives," *https://doi.org/10.1142/S2010135X13300028*, vol. 03, p. 1330002, 2013.

[33] H.-Y. Liu, H.-Y. Zhang, X.-G. Chen, and R.-G. Xiong, "Molecular design principles for ferroelectrics: ferroelectrochemistry," *Journal of the American Chemical Society*, vol. 142, no. 36, pp. 15205–15218, 2020.

[34] H. Y. Zhang, Y. Y. Tang, P. P. Shi, and R. G. Xiong, "Toward the targeted design of molecular ferroelectrics: modifying molecular symmetries and homochirality," *Accounts of Chemical Research*, vol. 52, pp. 1928–1938, 2019.

[35] W.-Y. Zhang, Y.-Y. Tang, P.-F. Li, P.-P. Shi, W.-Q. Liao, D.-W. Fu, H.-Y. Ye, Y. Zhang, and R.-G. Xiong, "Precise molecular design of high-Tc 3D organic–inorganic perovskite ferroelectric:[MeHdabco] RbI3 (MeHdabco= N-methyl-1, 4-diazoniabicyclo [2.2. 2] octane," *Journal of the American Chemical Society*, vol. 139, no. 31, pp. 10897–10902, 2017.

[36] D. Fu, Z. Hou, Y. He, J. C. Liu, H. P. Lv, and Y. Y. Tang, "Multiaxial ferroelectricity and ferroelasticity in a chiral perovskite," *Chemistry of Materials*, vol. 34, pp. 3518–3524, 2022.

[37] I. U. o. C. Theo. Hahn, *International tables for crystallography*. Reidel, 1983.

[38] Y. Hu, F. Florio, Z. Chen, W. A. Phelan, M. A. Siegler, Z. Zhou, Y. Guo, R. Hawks, J. Jiang, J. Feng, L. Zhang, B. Wang, Y. Wang, D. Gall, E. F. Palermo, Z. Lu, X. Sun, T. M. Lu, H. Zhou, Y. Ren, E. Wertz, R. Sundararaman, and J. Shi, "A chiral switchable photovoltaic ferroelectric 1D perovskite," *Science Advances*, vol. 6, 2020.

[39] Y. Ai, H. P. Lv, Z. X. Wang, W. Q. Liao, and R. G. Xiong, "H/F substitution for advanced molecular ferroelectrics," *Trends in Chemistry*, vol. 3, pp. 1088–1099, 2021.

[40] Y. Zhang, W. Q. Liao, D. W. Fu, H. Y. Ye, Z. N. Chen, and R. G. Xiong, "Highly efficient red-light emission in an organic-inorganic hybrid ferroelectric: (Pyrrolidinium)$MnCl_3$," *Journal of the American Chemical Society*, vol. 137, pp. 4928–4931, 2015.

[41] Y. Ai, X. G. Chen, P. P. Shi, Y. Y. Tang, P. F. Li, W. Q. Liao, and R. G. Xiong, "Fluorine substitution induced high T_c of enantiomeric perovskite ferroelectrics: (R)- and (S)-3-(Fluoropyrrolidinium)$MnCl_3$," *Journal of the American Chemical Society*, vol. 141, pp. 4474–4479, 2019.

[42] J. Rödel, W. Jo, K. T. Seifert, E. M. Anton, T. Granzow, and D. Damjanovic, "Perspective on the development of lead-free piezoceramics," *Journal of the American Ceramic Society*, vol. 92, pp. 1153–1177, 2009.

[43] J. Gao, D. Xue, W. Liu, C. Zhou, and X. Ren, "Recent progress on $BaTiO_3$-based piezoelectric ceramics for actuator applications," *Actuators 2017*, vol. 6, p. 24, 2017.

[44] L. A. Reznichenko, A. V. Turik, E. M. Kuznetsova, and V. P. Sakhnenko, "Piezoelectricity in $NaNbo_3$ ceramics," *Journal of Physics: Condensed Matter*, vol. 13, p. 3875, 2001.

[45] D.-W. Fu *et al.*, "Diisopropylammonium bromide is a high-temperature molecular ferroelectric crystal," *Science*, vol. 339, pp. 425–428, 2013.

[46] W. Q. Liao, Y. Y. Tang, P. F. Li, Y. M. You, and R. G. Xiong, "Large piezoelectric effect in a lead-free molecular ferroelectric thin film," *Journal of the American Chemical Society*, vol. 139, pp. 18071–18077, 2017.

[47] W. Q. Liao, Y. Y. Tang, P. F. Li, Y. M. You, and R. G. Xiong, "Competitive halogen bond in the molecular ferroelectric with large piezoelectric response," *Journal of the American Chemical Society*, vol. 140, pp. 3975–3980, 2018.

[48] W.-Q. Liao, D. Zhao, Y.-M. Yu, I. Grinberg, A. M. Rappe, K. A. Nelson, J. Li, Y. Ren, P. Wu, K. Yang, J.-L. Liu, P.-F. Li, D.-W. Fu, S. Gao, Z. Wang, and R.-G. Xiong, "A lead-halide perovskite molecular ferroelectric semiconductor," *Nature communications*, vol. 10, no. 1, pp. 1–8, 2019.

[49] Y. Zhang, S. Seo, S. Y. Lim, Y. Kim, S. G. Kim, D. K. Lee, S. H. Lee, H. Shin, H. Cheong, and N. G. Park, "Achieving reproducible and high-efficiency (>21%) perovskite solar cells with a presynthesized $FAPbI_3$ powder," *ACS Energy Letters*, vol. 5, pp. 360–366, 2020.

[50] X. G. Chen, X. J. Song, Z. X. Zhang, P. F. Li, J. Z. Ge, Y. Y. Tang, J. X. Gao, W. Y. Zhang, D. W. Fu, Y. M. You, and R. G. Xiong, "Two-dimensional layered perovskite ferroelectric with giant piezoelectric voltage coefficient," *Journal of the American Chemical Society*, vol. 142, pp. 1077–1082, 2020.

[51] T. M. Guo, Y. J. Gong, Z. G. Li, Y. M. Liu, W. Li, Z. Y. Li, and X. H. Bu, "A new hybrid lead-free metal halide piezoelectric for energy harvesting and human motion sensing," *Small*, 2021.

[52] H. Y. Ye, Y. Y. Tang, P. F. Li, W. Q. Liao, J. X. Gao, X. N. Hua, H. Cai, P. P. Shi, Y. M. You, and R. G. Xiong, "Metal-free three-dimensional perovskite ferroelectrics," *Science*, vol. 361, pp. 151–155, 2018.

[53] C. F. Wang, N. Wang, L. Liu, L. P. Miao, H. Y. Ye, Y. Zhang, and C. Shi, "Enantiomeric hybrid high-temperature multiaxial ferroelectrics with a narrow bandgap and high piezoelectricity," *Chinese Chemical Letters*, vol. 34, p. 108051, 2023.

[54] K. Tao, B. Zhang, Q. Li, Q. Yan, K. Tao, B. Zhang, Q. Li, and Q. Yan, "Centimeter-sized piezoelectric single crystal of chiral bismuth-based hybrid halide with superior electrostrictive coefficient," *Small*, vol. 19, p. 2207663, 2023.

[55] Z. Zhang, Y. Zhang, Y. Zhao, M. Zhao, R. Zhang, J. Guo, F. An, and X. Sun, "Origin of high piezoelectricity of a bismuth-based organic-inorganic hybrid crystal," *Journal of Materials Chemistry C*, vol. 11, pp. 1401–1408, 2023.

[56] Y. Z. Zhang, D. S. Sun, J. X. Gao, X. N. Hua, X. G. Chen, G. Q. Mei, and W. Q. Liao, "A semiconducting organic-inorganic hybrid perovskite-type non-ferroelectric piezoelectric with excellent piezoelectricity," *Chemistry - An Asian Journal*, vol. 14, pp. 1028–1033, 2019.

[57] K. Zhang, B. Ding, C. Wang, P. Shi, X. Zhang, C. Liu, Y. Yang, X. Gao, R. Wang, L. Tao, K. G. Brooks, S. Dai, P. J. Dyson, M. K. Nazeeruddin, and Y. Ding, "Highly efficient and stable $FAPbI_3$ perovskite solar cells and modules based on exposure of the (011) facet," *Nano-Micro Letters*, vol. 15, pp. 1–11, 2023.

[58] S. Deswal, R. Panday, D. R. Naphade, P. Dixit, B. Praveenkumar, J. K. Zaręba, T. D. Anthopoulos, S. Ogale, R. Boomishankar, S. Deswal, R. Panday, R. Boomishankar, D. R. Naphade, T. D. Anthopoulos, J. K. Zaręba, and S. Ogale, "Efficient piezoelectric energy harvesting from a discrete hybrid bismuth bromide ferroelectric templated by phosphonium cation," *Chemistry - A European Journal*, vol. 28, p. e202200751, 2022.

[59] S. Sahoo, N. Deka, and R. Boomishankar, "Piezoelectric energy harvesting of a bismuth halide perovskite stabilised by chiral ammonium cations," *CrystEngComm*, vol. 24, pp. 6172–6177, 2022.

[60] G. Rose, "Beschreibung einiger neuen mineralien des urals," *Annalen der Physik*, vol. 124, pp. 551–573, 1839.

[61] C. E. Ekuma, M. Jarrell, J. Moreno, and D. Bagayoko, "First principle electronic, structural, elastic, and optical properties of strontium titanate," *AIP Advances*, vol. 2, p. 12189, 2012.

[62] K. R. Nagavenkatesh, C. Sambathkumar, M. Murugesan, P. Devendran, N. Nallamuthu, P. Lakshmanan, and A. Shameem, "Review on the recent improvements in lanthanum ferrite perovskites for visible light driven textile dyes degradation and its various hetero-junctions catalysis mechanism," *Journal of Industrial and Engineering Chemistry*, vol. 136, pp. 16–45, 2024.

[63] J. Zhu, H. Li, L. Zhong, P. Xiao, X. Xu, X. Yang, Z. Zhao, and J. Li, "Perovskite oxides: Preparation, characterizations, and applications in heterogeneous catalysis," *ACS Catalysis*, vol. 4, pp. 2917–2940, 2014.

[64] W. J. Yin, B. Weng, J. Ge, Q. Sun, Z. Li, and Y. Yan, "Oxide perovskites, double perovskites and derivatives for electrocatalysis, photocatalysis, and photovoltaics," *Energy & Environmental Science*, vol. 12, pp. 442–462, 2019.

[65] C. Sun, J. A. Alonso, J. Bian, C. W. Sun, J. J. Bian, and J. A. Alonso, "Recent advances in perovskite-type oxides for energy conversion and storage applications," *Advanced Energy Materials*, vol. 11, p. 2000459, 2021.

[66] J. Sunarso, S. S. Hashim, N. Zhu, and W. Zhou, "Perovskite oxides applications in high temperature oxygen separation, solid oxide fuel cell and membrane reactor: A review," *Progress in Energy and Combustion Science*, vol. 61, pp. 57–77, 2017.

[67] H. L. Wells, "über die Casium- und Kalium-Bleihalogenide," *Zeitschrift für anorganische Chemie*, vol. 3, pp. 195–210, 1893.

[68] W. A. Wooster and C. K. M, "Crystal structure and photoconductivity of cæsium plumbohalides," *Nature 1958 182:4647*, vol. 182, pp. 1436–1436, 1958.

[69] D. Weber, "$Ch_3nh_3pbx_3$, ein pb(ii)-system mit kubischer perowskitstruktur," *Zeitschrift fur Naturforschung - Section B Journal of Chemical Sciences*, vol. 33, pp. 1443–1445, 1978.

[70] D. Weber, "$CH_3NH_3SnBr_xI_{3-x}$ (x = 0–3), ein Sn(II)-System mit kubischer Perowskitstruktur," *Zeitschrift fur Naturforschung - Section B Journal of Chemical Sciences*, vol. 33, pp. 862–865, 1978.

[71] A. Vinattieri and G. Giorgi, "Halide perovskites for photonics: Recent history and perspectives," *Halide Perovskites for Photonics*, pp. 1–1–1–28, 2021.

[72] D. B. Mitzi, C. A. Feild, W. T. Harrison, and A. M. Guloy, "Conducting tin halides with a layered organic-based perovskite structure," *Nature 1994 369:6480*, vol. 369, pp. 467–469, 1994.

[73] D. B. Mitzi, K. Chondroudis, and C. R. Kagan, "Organic-inorganic electronics," *IBM Journal of Research and Development*, vol. 45, pp. 29–45, 2001.

[74] D. B. Mitzi, "Templating and structural engineering in organic-inorganic perovskites," *Journal of the Chemical Society, Dalton Transactions*, pp. 1–12, 2001.

[75] K. Liang, D. B. Mitzi, and M. T. Prikas, "Synthesis and characterization of organic-inorganic perovskite thin films prepared using a versatile two-step dipping technique," *Chemistry of Materials*, vol. 10, pp. 403–411, 1998.

[76] D. B. Mitzi, C. A. Feild, Z. Schlesinger, and R. B. Laibowitz, "Transport, optical, and magnetic properties of the conducting halide perovskite $CH_3NH_3SnI_3$," *Journal of Solid State Chemistry*, vol. 114, pp. 159–163, 1995.

[77] T. Kondo, T. Azuma, T. Yuasa, and R. Ito, "Biexciton lasing in the layered perovskite-type material $(C_6H_13NH_3)_2PbI_4$," *Solid State Communications*, vol. 105, pp. 253–255, 1998.

[78] H. Dong, C. Ran, W. Gao, M. Li, Y. Xia, and W. Huang, "Metal halide perovskite for next-generation optoelectronics: progresses and prospects," *eLight 2023 3:1*, vol. 3, pp. 1–16, 2023.

[79] A. Kojima, K. Teshima, Y. Shirai, and T. Miyasaka, "Organometal halide perovskites as visible-light sensitizers for photovoltaic cells," *Journal of the American Chemical Society*, vol. 131, pp. 6050–6051, 2009.

[80] V. M. Goldschmidt, "Die Gesetze der Krystallochemie," *Die Naturwissenschaften*, vol. 14, pp. 477–485, 1926.

[81] V. M. Goldschmidt, "Krystallbau und chemische Zusammensetzung," *Berichte der deutschen chemischen Gesellschaft (A and B Series)*, vol. 60, pp. 1263–1296, 1927.

[82] Z. Li, M. Yang, J. S. Park, S. H. Wei, J. J. Berry, and K. Zhu, "Stabilizing perovskite structures by tuning tolerance factor: Formation of formamidinium and cesium lead iodide solid-state alloys," *Chemistry of Materials*, vol. 28, pp. 284–292, 2016.

[83] C. Li, K. C. K. Soh, and P. Wu, "Formability of ABO_3 perovskites," *Journal of Alloys and Compounds*, vol. 372, pp. 40–48, 2004.

[84] C. J. Howard and H. T. Stokes, "Structures and phase transitions in perovskites - a group-theoretical approach," *urn:issn:0108-7673*, vol. 61, pp. 93–111, 2004.

[85] P. M. Woodwardt, "Octahedral tilting in perovskites. i. geometrical considerations," *Acta Cryst*, vol. 53, pp. 32–43, 1997.

[86] A. M. Glazer, "Simple ways of determining perovskite structures," *Acta Cryst*, vol. 31, p. 756, 1975.

[87] M. Yashima and R. Ali, "Structural phase transition and octahedral tilting in the calcium titanate perovskite $CaTiO_3$," *Solid State Ionics*, vol. 180, pp. 120–126, 2009.

[88] J. S. Bechtel and A. V. D. Ven, "Octahedral tilting instabilities in inorganic halide perovskites," *Physical Review Materials*, vol. 2, p. 025401, 2018.

[89] A. Alaei, A. Circelli, Y. Yuan, Y. Yang, and S. S. Lee, "Polymorphism in metal halide perovskites," *Materials Advances*, vol. 2, pp. 47–63, 2021.

[90] P. S. Whitfield, N. Herron, W. E. Guise, K. Page, Y. Q. Cheng, I. Milas, and M. K. Crawford, "Structures, phase transitions and tricritical behavior of the hybrid perovskite $MAPbI_3$," *Scientific Reports 2016 6:1*, vol. 6, pp. 1–16, 2016.

[91] P. Becker, J. A. Márquez, J. Just, A. Al-Ashouri, C. Hages, H. Hempel, M. Jošt, S. Albrecht, R. Frahm, and T. Unold, "Low temperature synthesis of stable γ-$CsPbI_3$ perovskite layers for solar cells obtained by high throughput experimentation," *Advanced Energy Materials*, vol. 9, p. 1900555, 2019.

[92] P. Gratia, I. Zimmermann, P. Schouwink, J. H. Yum, J. N. Audinot, K. Sivula, T. Wirtz, and M. K. Nazeeruddin, "The many faces of mixed ion perovskites: Unraveling and understanding the crystallization process," *ACS Energy Letters*, vol. 2, pp. 2686–2693, 2017.

[93] C. J. Bartel, C. Sutton, B. R. Goldsmith, R. Ouyang, C. B. Musgrave, L. M. Ghiringhelli, and M. Scheffler, "New tolerance factor to predict the stability of perovskite oxides and halides," *Science Advances*, vol. 5, 2019.

[94] D. T. Moore, H. Sai, K. W. Tan, D. M. Smilgies, W. Zhang, H. J. Snaith, U. Wiesner, and L. A. Estroff, "Crystallization kinetics of organic-inorganic trihalide perovskites and the role of the lead anion in crystal growth," *Journal of the American Chemical Society*, vol. 137, pp. 2350–2358, 2015.

[95] C. Lu, Y. Wang, R. Zhang, and S. Xu, "Demystifying phase transformations in metal halide perovskites," *Matter*, vol. 4, pp. 2627–2629, 2021.

[96] W. Xiang, J. Zhang, S. F. Liu, S. Albrecht, A. Hagfeldt, and Z. Wang, "Intermediate phase engineering of halide perovskites for photovoltaics," *Joule*, vol. 6, pp. 315–339, 2022.

[97] H. Fan, F. Li, P. Wang, Z. Gu, J. H. Huang, K. J. Jiang, B. Guan, L. M. Yang, X. Zhou, and Y. L. Song, "Methylamine-assisted growth of uniaxial-oriented perovskite thin films with millimeter-sized grains," *Nature Communications 2020 11:1*, vol. 11, pp. 1–10, 2020.

[98] J. Li, N. Yan, Z. Fang, and S. F. Liu, "Alkyl diamine-induced (100)-preferred crystal orientation for efficient Pb-Sn perovskite solar cells," *ACS Applied Energy Materials*, vol. 5, pp. 6936–6942, 2022.

[99] Y. Sun, S. Yang, Z. Pang, Y. Quan, R. Song, Y. Chen, W. Qi, Y. Gao, F. Wang, X. Zhang, Y. Sun, J. Yang, L. Yang, and F. Rosei, "Preferred film orientation to achieve stable and efficient Sn-Pb binary perovskite solar cells," *ACS Applied Materials and Interfaces*, vol. 13, pp. 10822–10836, 2021.

[100] Z. Wu, Y. Zhao, C. Wang, T. Ma, C. Chen, Y. Liu, T. Jia, Y. Zhai, C. Chen, C. Zhang, G. Cao, Z. Yang, D. Zhao, X. Li, Z. Wu, Y. Zhao, C. Wang, T. Ma, C. Chen, Y. Liu, T. Jia, Y. Zhai, C. Zhang, G. Cao, Z. Yang, X. Li, and D. Zhao, "Enhancing photovoltaically preferred orientation in wide-bandgap perovskite for efficient all-perovskite tandem solar cells," *Advanced Materials*, vol. 37, p. 2412943, 2025.

[101] C. Ma, F. T. Eickemeyer, S. H. Lee, D. H. Kang, S. J. Kwon, M. Grätzel, and N. G. Park, "Unveiling facet-dependent degradation and facet engineering for stable perovskite solar cells," *Science*, vol. 379, pp. 173–178, 2023.

[102] M. E. O'Kane, J. A. Smith, R. C. Kilbride, E. L. Spooner, C. P. Duif, T. E. Catley, A. L. Washington, S. M. King, S. R. Parnell, and A. J. Parnell, "Exploring nanoscale structure in perovskite precursor solutions using neutron and light scattering," *Chemistry of Materials*, vol. 34, pp. 7232–7241, 2022.

[103] J. Zhang, Z. Wang, A. Mishra, M. Yu, M. Shasti, W. Tress, D. J. Kubicki, C. E. Avalos, H. Lu, Y. Liu, B. I. Carlsen, A. Agarwalla, Z. Wang, W. Xiang, L. Emsley, Z. Zhang, M. Graetzel, W. Guo, and A. Hagfeldt, "Intermediate phase enhances inorganic perovskite and metal oxide interface for efficient photovoltaics," *Joule*, vol. 4, pp. 222–234, 2020.

[104] M. Kim, G. H. Kim, T. K. Lee, I. W. Choi, H. W. Choi, Y. Jo, Y. J. Yoon, J. W. Kim, J. Lee, D. Huh, H. Lee, S. K. Kwak, J. Y. Kim, and D. S. Kim, "Methylammonium chloride induces intermediate phase stabilization for efficient perovskite solar cells," *Joule*, vol. 3, pp. 2179–2192, 2019.

[105] P. W. Liang, C. Y. Liao, C. C. Chueh, F. Zuo, S. T. Williams, X. K. Xin, J. Lin, and A. K. Jen, "Additive enhanced crystallization of solution-processed perovskite for highly efficient planar-heterojunction solar cells," *Advanced Materials*, vol. 26, pp. 3748–3754, 2014.

[106] Q. Zhang, Q. Zhao, H. Wang, Y. Yao, L. Li, Y. Wei, R. Xu, C. Zhang, E. O. Shalenov, Y. Tu, K. Wang, and M. Xiao, "Tuning isomerism effect in organic bulk additives enables efficient and stable perovskite solar cells," *Nano-Micro Letters*, vol. 17, pp. 1–13, 2025.

[107] A. D. Taylor, Q. Sun, K. P. Goetz, Q. An, T. Schramm, Y. Hofstetter, M. Litterst, F. Paulus, and Y. Vaynzof, "A general approach to high-efficiency perovskite solar cells by any antisolvent," *Nature Communications 2021 12:1*, vol. 12, pp. 1–11, 2021.

[108] Y. Li, J. Wang, Y. Yuan, X. Dong, and P. Wang, "Anti-solvent dependent device performance in $CH_3NH_3PbI_3$ solar cells: the role of intermediate phase content in the as-prepared thin films," *Sustainable Energy & Fuels*, vol. 1, pp. 1041–1048, 2017.

[109] J. C. Hamill, J. Schwartz, and Y. L. Loo, "Influence of solvent coordination on hybrid organic-inorganic perovskite formation," *ACS Energy Letters*, vol. 3, pp. 92–97, 2018.

[110] O. Shargaieva, H. N. asström, J. A. Smith, D. Többens, R. Munir, and E. Unger, "Hybrid perovskite crystallization from binary solvent mixtures: interplay of evaporation rate and binding strength of solvents," *Materials Advances*, vol. 1, pp. 3314–3321, 2020.

[111] V. Gutmann, "Solvent effects on the reactivities of organometallic compounds," *Coordination Chemistry Reviews*, vol. 18, pp. 225–255, 1976.

[112] T. Bu, J. Li, H. Li, C. Tian, J. Su, G. Tong, L. K. Ono, C. Wang, Z. Lin, N. Chai, X. L. Zhang, J. Chang, J. Lu, J. Zhong, W. Huang, Y. Qi, Y. B. Cheng, and F. Huang, "Lead halide-templated crystallization of methylamine-free perovskite for efficient photovoltaic modules," *Science*, vol. 372, pp. 1327–1332, 2021.

[113] S. H. Lee, S. Hong, and H. J. Kim, "Selection of a suitable solvent additive for 2-methoxyethanol-based antisolvent-free perovskite film fabrication," *ACS Applied Materials and Interfaces*, vol. 14, pp. 39132–39140, 2022.

[114] M. Katayama, M. Shinoda, K. Ozutsumi, S. Funahashi, and Y. Inada, "Reevaluation of donor number using titration calorimetry," *Analytical Sciences*, vol. 28, pp. 103–106, 2012.

[115] A. A. Petrov, I. P. Sokolova, N. A. Belich, G. S. Peters, P. V. Dorovatovskii, Y. V. Zubavichus, V. N. Khrustalev, A. V. Petrov, M. G. atzel, E. A. Goodilin, and A. B. Tarasov, "Crystal structure of DMF-intermediate phases uncovers the link between $CH_3NH_3PbI_3$ morphology and precursor stoichiometry," *Journal of Physical Chemistry C*, vol. 121, pp. 20739–20743, 2017.

[116] J. Chen, Y. Xiong, Y. Rong, A. Mei, Y. Sheng, P. Jiang, Y. Hu, X. Li, and H. Han, "Solvent effect on the hole-conductor-free fully printable perovskite solar cells," *Nano Energy*, vol. 27, pp. 130–137, 2016.

Chapter 3

Materials and Methods

In this chapter, the experimental techniques used in this thesis are described. First, the fabrication protocols used to synthesise single crystals, powders and thin films are described. Secondly, X-ray diffraction has been used extensively in this work, and so the basic principles of these techniques are outlined.

3.1 Fabrication

3.1.1 Materials

The following liquid state chemicals were purchased from Sigma Aldrich: acetone($\geq$ 99.5%), 2-propanol (IPA, anhydrous, $\geq$99.5%), ethanol (EtOH, anhydrous, $\geq$99.5%), methanol (MeOH, anhydrous, $\geq$99.8%), dimethyl sulfoxide (DMSO, anhydrous, $\geq$99.8%), dimethylformamide (DMF, anhydrous, $\geq$99.8%), dichloromethane (DCM, $\geq$99.9%), dibromomethane (DBM, stabilised for synthesising), chlorobenzene (CB, $\geq$99.5%), diethyl ether (DEE, anhydrous, $\geq$99.0%), hydrobromic acid (HBr, 48 wt% in H_2O, $\geq$99.99%), Fomblin (Sigma Aldrich). 2M trimethylamine in tetrahydrofuran (THF) was purchased from Fluorochem and trimethylamine (33%(wt/wt) in Ethanol) was purchased from Thermo Scientific Chemicals and silver paint from RS pro.

Of the solid state chemicals: (iodomethyl)trimethylammonium iodide ((TMIM)I, $\geq$ 98 %), bismuth chloride ($BiCl_3$, 99.999 %), antimony(III) bromide ($SbBr_3$, 99.5 %) were purchased from Thermo Scientific Chemicals. (ferrocenyl)trimethylammonium iodide (FMTMAI, $\geq$ 97 %) was purchased from BLD Pharm. Bismuth iodide (BiI_3, 99.999 %), bismuth bromide ($BiBr_3$, 99.0 %), antimony(III) iodide (SbI_3, 98 %) and caesium iodide (CsI, 99.9 %) were purchased from Alfa Aesar. Lead(II) iodide (PbI_2, $\geq$ 99.99 %, metals basis) was purchased from Tokyo Chemical Industries. Tin(II) iodide (SnI_2, beads, $\geq$ 99.99 %, trace metals basis), tin(II) fluoride (SnF_2, $\geq$ 99.99 %, trace metals basis), Sn(0) powder ($\leq$ 45 μm particle size, 99.8 %), and dimethylammonium chloride (DMACl, 98 %) were purchased from Sigma Aldrich.

All non-aqueous chemicals were stored in a N_2 environment in a glovebox. All chemicals were used without further purification,

Fluorine-doped tin oxide (FTO) coated glass substrates ($15\Omega sq^{-1}$, 100μm thickness) were purchased from Latech Scientific Supply Pte. Ltd.

3.1.2 Synthesis of (TMCM)Cl and (TMBM)Br

(chloromethyl)trimethylammonium chloride ((TMCM)Cl) and (bromomethyl)trimethylammonium bromide ((TMBM)Br) were synthesised in the following way via a S_N2 nucleophilic substitution reaction. 200 mmol of the constituents were reacted in the following way:

200 mL of trimethylamine in THF (or 47.3 mL of trimethylamine in ethanol), and 64 mL of DCM (or 69.5 mL DBM) were added to a round-bottom glass flask and stirred under a nitrogen environment via a Schlenk line for 5 days, after which white powder precipitated out. At least five times excess of the dihalomethane was used to ensure complete reaction. The powder was extracted using a gravity filter and dried under N_2 at room temperature for 1 day, and then transferred to a N_2-filled glovebox for storage.

The synthesis of (TMCM)Cl via trimethylamine in THF and dichloromethane led to a 65.3% yield whilst the synthesis of (TMBM)Br via trimethylamine in ethanol and dibromomethane led to a $\sim$20% yield.

3.1.3 Single crystal growth

The controlled growth of high-quality organic-inorganic hybrid metal halide single crystals is paramount for research in energy applications. Single crystals reflect, as close as possible, the intrinsic properties of a semiconductor. Furthermore, attaining high-quality crystals is crucial for effective measurements of their properties via characterisation techniques.

Commonly, single crystal growth from solution occurs from controlled supersaturation of a precursor solution. This is when the solution contains more solute than the equilibrium solubility allows, given the conditions of the system, such as temperature and pressure. Crystallization kinetics are governed by the rate of nucleation and the rate of crystal growth, which can be carefully controlled by conditions such as the temperature, solvent and the rate of change of these conditions[1].

As the metastable point of supersaturation is reached, nucleation occurs. At low supersaturation, growth kinetics dominate crystallization, while at high supersaturation, nucleation becomes dominant. For the work of this thesis, three main methods were used to grow single crystals: antisolvent vapour diffusion, slow-cooling, and layered diffusion. In antisolvent vapour diffusion, a solution containing the host solute and solvent is exposed to a miscible antisolvent, reducing solubility and inducing crystallization. The layered diffusion technique follows a similar principle, where layered miscible solvents containing solutes gradually interdiffuse, creating supersaturation at their interface. The slow-cooling method decreases solute solubility through controlled temperature reduction, causing crystallization.

3.1.3.1 Antisolvent vapour diffusion

Single crystals of $(TMIM)_3Bi_2I_9$ (Chapter 4), $(TMIM)_3BiBr_6$, $(TMIM)_3Bi_2Cl_9$, $(TMIM)_3Bi_2Cl_9$, $(TMCM)_3Bi_2I_9$, $(TMCM)_3Bi_2Br_9$ and the$(FMTMA)_3Bi_2X_9$ (X = I, Cl, Br) series (Chapter 6) were grown in this way. 1.5 mmol of the organic precursor ((TMIM)I: 490.4 mg, (TMBM)Br: 315.34 mg, (TMCM)Cl: 216.06 mg, (FMTMA)I: 577.6 mg) was dissolved with 1 mmol of BiX_3 (BiI_3: 589.7 mg, $BiBr_3$: 448.7 mg, $BiCl_3$: 315.3 mg) in up to 5 mL of DMSO, in an 8 mL glass vial, and stirred using a magnetic stirrer for $\sim$ 2 hours. The open glass vial was placed in a larger 40 mL vial

containing ∼2-4 mL of MeOH or EtOH, which was sealed. This system was placed in a minimally-disturbed fumehood. After a time period of days to a few weeks, 0.05 - 0.4 mm crystals were obtained. $(TMIM)_3Bi_2I_9$ crystals typically grew within 2-3 days. The obtained crystals were separated and rinsed with DEE or CB, and dried on a hotplate at 30 °C for 15 minutes. DEE and CB were selected as suitable solvents miscible with the host solvent that would not dissolve the crystals.

Note: single crystals of $(TMIM)_3Bi_2I_9$ grown via the slow-cooling method in HI aqueous solution below were the primary crystals used for measurements in Chapter 4.

3.1.3.2 Slow-cooling

Single crystals of $(TMIM)_3Bi_2I_9$, $(TMIM)_3Sb_2I_9$, $(TMIM)_3Sb_2Br_9{\cdot}Br_2$ and $(TMCM)_3Sb_2I_9{\cdot}I_2$ were grown via this method. 1.5 mmol of the (TMXM)Cl precursor was dissolved with 1 mmol of MX_3 (X = Cl, Br, I and M = Bi, Sb) in hydrohalic acids as follows:

For $(TMIM)_3Bi_2I_9$ and $(TMIM)_3Sb_2I_9$: 490.4 mg of (TMIM)I and 589.7 mg of BiI_3 (or 502.47 mg of SbI_3) were dissolved in 10 mL of HI and stirred vigorously at 90 °C for 4 h. The solution was then gradually cooled by 5 °C per day down to room temperature. The obtained crystals were separated, rinsed with DEE or CB, and dried on a hotplate at 30 °C for 15 minutes, resulting in dark red $(TMIM)_3Bi_2I_9$ (red-brown $(TMIM)_3Sb_2I_9$) crystals with sizes ranging from 0.1 to 0.5 mm. The crystal growth for $(TMIM)_3Sb_2I_9$ typically yielded slightly smaller crystals.

For $(TMIM)_3Sb_2Br_9{\cdot}Br_2$ (and $(TMCM)_3Sb_2I_9{\cdot}I_2$): 490.4 mg of (TMIM)I (216.06 mg of (TMCM)Cl) and 589.7 mg of $BiBr_3$ (or 361.472 mg of $SbBr_3$) were dissolved in 10 mL of HBr (HI) and stirred vigorously at 90 °C for 1 h. The solution was then gradually cooled by 15 °C per hour down to room temperature. The obtained crystals were separated, rinsed with DEE or CB, and dried on a hotplate at 30 °C for 15 minutes, resulting in black crystals with sizes ranging from 0.05 to 0.3 mm.

3.1.3.3 Layered diffusion

Due to the room temperature solubility of the precursors, the slow-cooling method was not used for the growth of $(TMCM)_3Bi_2Cl_9$ and $(TMBM)_3Bi_2Br_9$.

Single crystals of $(TMCM)_3Bi_2Cl_9$ and $(TMBM)_3Bi_2Br_9$ were grown via this method. 1.5 mmol of the (TMXM)Cl precursor (349.41 mg (TMBM)Br or 216.06 mg (TMCM)Cl) was dissolved in 2 mL of methanol in a vial. 1 mmol of BiX_3 (448.69 mg of $BiBr_3$ or 315.34 mg of $BiCl_3$) was dissolved in the corresponding hydrohalic acid in a separate vial. Both solutions were filtered through a μm PTFE membrane filter with a 0.25 (0.45 for the BiX_3 solution) μm pore size prior to use.

0.5 mL of the BiX_3 solution was placed into the bottom of a thin NMR tube, followed by $\sim$ 0.1 mL of neat HX, and finally 0.5 mL of the (TMXM)X solution is carefully placed on top using a syringe and needle. The NMR tube is then sealed with a cap and placed in an undisturbed fumehood. After 3 days, small crystals grow on the interface between the two layers. The solution is then allowed to sit undisturbed for a further 3 days, during which time the solution becomes saturated with crystals. The solution is then carefully removed and the crystals are collected into a glass vial.

3.1.3.4 Single crystal growth of $CsSnI_3{\cdot}3DMSO$

In a N_2-filled glovebox, 519.6 mg CsI, 745.0 mg SnI_2 and 10 mg Sn powder were dissolved in 2 mL of DMSO and stirred overnight. The solution was then filtered through a PTFE membrane filter with a 0.45 μm pore size, and 200 μL of the solution was transferred to a 4 mL glass vial with a screw cap septum. In a fumehood, this vial was connected to a Schlenk line and placed under a low nitrogen flow, with a secondary needle inserted into the vial via the septum to outgas. The solution was then allowed to sit undisturbed for 3 days, during which time a number of clear-looking crystals formed. The vial was removed from the Schlenk line and Fomblin was added into the vial. Under the microscope, the crystals dispersed in Fomblin were observed to be of the form shown in Figure 3.1; purple squares identified to be CsI crystals. After one day, the mixture on the slide darkened and the crystals observed to be of the form shown in Figure 3.2; the red colour indicates oxidation

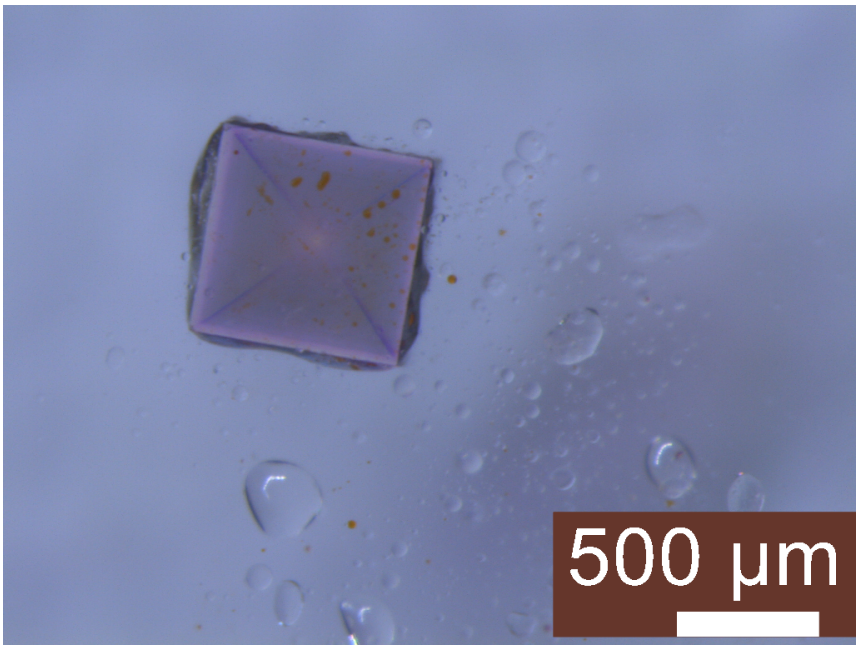


FIGURE 3.1: Microscope image of the single crystal growth of $CsSnI_3$·3DMSO. The purple squares identified to be CsI crystals.

of the Sn^{2+} ions present in the solution. The otherwise transparent crystals in this mixture are measured to be $CsSnI_3$·3DMSO as discussed in Chapter 7.

All weighing of precursor powders was performed in a N_2-filled glovebox.

3.1.4 Thin film processing

3.1.4.1 Thin films of $(TMIM)_3Bi_2I_9$

490.4 mg of (TMIM)I and 589.7 mg of BiI_3 were dissolved in 2.5 mL DMSO and the resulting solution was stirred vigorously for 2 h before being filtered through a PTFE membrane filter with a 0.45 μm pore size prior to thin film deposition. FTO-coated glass substrates were sequentially cleaned in ultrasonic baths for ten minutes each in the following solutions: deionised water with 4% v/v solution of Decon 90 cleaning detergent, deionised water, acetone and isopropanol (IPA). Substrates were then dried with a stream of compressed nitrogen gas and subjected to UV-ozone treatment for 20 minutes before deposition. 100 μL of the $(TMIM)_3Bi_2I_9$ precursor solution was then statically dispensed onto the substrates and spun at 4000 rpm

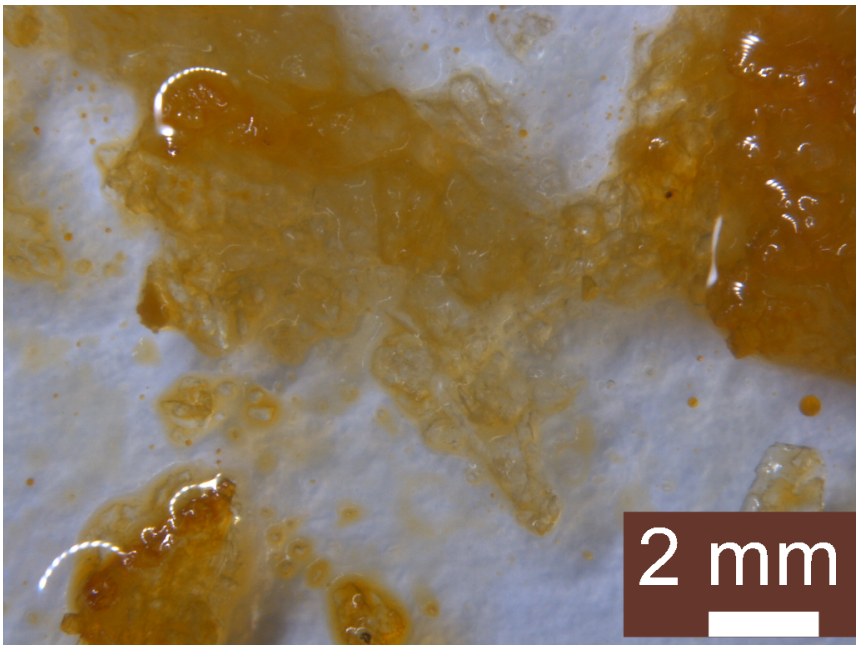


FIGURE 3.2: Microscope image of the single crystal growth of $CsSnI_3 \cdot 3DMSO$. The mixture on the slide after 1 day.

(4000 rpm s^{-1}) for 30 seconds. 15 seconds into this protocol, 170 μL of IPA was dispensed onto the substrate to assist with the extraction of the solvent, DMSO, from the as-deposited thin film ("anti-solvent quench"). The films were then annealed at 100 °C for 30 minutes on a hotplate. All spin-coating and annealing was conducted inside a N_2-filled glovebox. The obtained films are approximately 100 nm thick.

3.1.5 Powders

Microcrystalline, mechanosynthesised powders of $(TMIM)_3Bi_2I_9$, $(TMBM)_3Bi_2Br_9$, $(TMCM)_3Bi_2Cl_9$ and $(TMIM)_3Sb_2I_9$ were prepared in this way. 1.5 mmol of the (TMXM)Cl precursor and 1 mmol of BiX_3 (weights given above) were weighed out into a Teflon grinding jar (14 mL) containing a zirconia ball bearing (10 mm) and ground in an electric ball mill (VWR Beater Mixer Mill) for 30 minutes at a vibration frequency of 15 Hz to produce a microcrystalline powder. The resulting powder was then transferred to a glass vial and annealed for 30 minutes in an oven at 100 °C.

3.2 Blade-coated thin films for *in situ* GIWAXS

3.2.1 Solution preparations

The compositions $FA_{0.6}MA_{0.4}PbI_3$ (FAI: 371.5 mg, MAI: 228.9 mg), $FA_{0.6}MA_{0.3}Cs_{0.1}PbI_3$ (FAI: 317.94 mg, MAI: 171.7 mg, CsI: 93.5 mg), $FA_{0.83}Cs_{0.17}PbI_3$ (FAI: 513.8 mg, CsI: 159.0 mg) were prepared by dissolving the organic precursors with 4 mmol of PbI_2 (829.8 mg) in 2 mL of a 4:1 ratio of DMF and DMSO (1.6 mL DMF, 0.4 mL DMSO).

The compositions $FA_{0.6}MA_{0.4}Pb_{0.5}Sn_{0.5}I_3$, $FA_{0.6}MA_{0.3}Cs_{0.1}Pb_{0.5}Sn_{0.5}I_3$, $FA_{0.83}Cs_{0.17}Pb_{0.5}Sn_{0.5}I_3$, $FA_{0.7}Cs_{0.3}Pb_{0.5}Sn_{0.5}I_3$ (FAI: 433.4 mg, CsI: 280.6 mg) and $CsPb_{0.5}Sn_{0.5}I_3$ (CsI: 935.3 mg) were prepared in the same way as the pure-Pb compositions, but with 2 mmol of SnI_2 (670.54 mg), 2 mmol of PbI_2 (829.8 mg), 28.2 mg of SnF_2 and 10 mg of Sn powder for 10 mol% SnF_2 and 5 mg/mL Sn concentrations, respectively.

The compositions $MASnI_3$, $FASnI_3$ in neat DMF or DMSO solutions were prepared by dissolving 2 mmol of the corresponding precursors (MAI: 343.94 mg, FAI: 317.94 mg, SnI_2: 745.04 mg) with 10 mg of Sn powder in 2 mL of DMF and DMSO, respectively.

The $CsSnI_3$ composition was prepared by dissolving 2 mmol of CsI (519.62 mg) and 2 mmol of SnI_2 (745.04 mg) with 10 mg of Sn powder in 1 mL of DMSO.

For the DMACl-containing compositions, 513.85 mg of FAI, 159 mg of CsI, 829.8 mg of PbI_2, 670.54 mg of SnI_2, 28.2 mg of SnF_2 and 10 mg of Sn powder were dissolved in 1 mL of DMSO, and then stirred overnight. The appropriate amount of DMACl powder was then added to the solution to give the desired composition. The preparation of the DMACl-containing compositions was done by Dr. M. Farrar and Dr. J.A. Smith.

All solutions were magnetically stirred for $\sim$2 hours and then filtered through a PTFE membrane filter with a 0.45 μm pore size prior to thin film deposition.

3.3 Characterisation

3.3.1 Single crystal X-ray diffraction (SCXRD)

Single-crystal X-ray diffraction (SCXRD) is a powerful technique for determining the atomic structure of crystalline materials. It provides key structural information, including unit cell dimensions, bond lengths, and space group symmetry, making it essential for characterising novel compounds. As a fully 3D technique, SCXRD scans across a wide range of angles, enabling comprehensive exploration of reciprocal space. By analysing thousands of unique Bragg reflections captured on a 2D detector, the complete crystal structure can be accurately determined.

First, the appropriate selection of a single crystal for XRD is a crucial stage for a successful measurement. This requires selecting an individual crystal without twins, an appropriate size (typically around 100 μm), depending on the size of the beam.

Initial selection of the crystals is performed using an optical microscope. Single crystals were dispersed in Fomblin on a microscope slide, and 100 μm-sized crystals were selected under a microscope and mounted on a 0.2 mm diameter Mitegen microloop which was then transferred to the goniometer.

Laboratory SCXRD data was obtained using an Agilent Supernova diffractometer with Mo-Kα radiation. Synchrotron SCXRD data was taken at the I19 beamline at Diamond Light Source, using a beam energy of 25 keV, under sessions cy36669-1 and cy38552-1 in hutches EH2 and EH1 respectively. The histogram for the pixel count-rate limit was readily monitored over consecutive exposures in order to assess for beam damage.

3.3.1.1 Data processing

SCXRD data typically consists of a large number of diffraction images collected at varying angles to comprehensively sample reciprocal space. The exposure time of each image is typically 0.1 - 2 seconds, and the total number of images taken is typically 800-1800.

Once the data has been collected, Bragg spots are identified and indexed using the known experimental geometry in order to identify the unit cell. Next, the indexed peaks are fitted in order to identify the unit cell dimensions. After this, the possible Bravais lattices are determined. The next step is integration, which performs 3D profile fitting of indexed peaks. After integration, further assessments of the crystal symmetry are made using the intensity values of the indexed peaks; determining the Laue group symmetry and analysing absent reflections in order to determine the space group symmetry. Next, the intensity values are scaled in order to correct for any experimental effects such as absorption and radiation damage which may result in symmetry-inequivalent reflections having unequal measured intensities. Finally, the resulting data is merged and reduced to produce outputs suitable for structure solution.

Synchrotron diffraction data was indexed, integrated and reduced using *xia2* for small molecules with additional DIALS commands[2] to input the unit cell and space group and a resolution cut-off of 0.7 Å. Lab-based diffraction data was indexed, integrated and reduced using Rigaku CrysAlisPro v171.43.90[3].

For $(TMIM)_3Bi_2I_9$: Structures were solved using SHELXT and refined anisotropically (except where stated, below) by full-matrix least-squares on F^2 using SHELXL in *OLEX2-1.3*[4, 5]. For diffraction data taken at temperatures above 60 °C, $(TMIM)^+$ groups were modelled using Fragment DB, using the 0 °C model[6]. SADI restraints were used on the N-C distances in the $(TMIM)^+$ cations to enable a stable refinement. DELU restraints were used on most of the anisotropically refined carbon and nitrogen positions. For all structures, all non-hydrogen and non-cationic atoms were refined anisotropically. For the data taken at 140 °C, the disorder of the cationic units as well as low reflection intensities made it necessary to refine carbon positions of $(TMIM)^+$ isotropically. Hydrogen atoms were assigned to idealised rotating CH_3 geometric positions and idealised non-rotating CH_3 geometric positions, where the latter was used to enable stable refinement. For temperatures 130 °C (403 K) and 140 °C (413 K), hydrogen atoms were either partially or not assigned due to the disorder in the structure.

Crystal structures were visualised and XRD patterns simulated using the 3D visualisation program VESTA[7].

3.3.2 Powder or thin-film X-ray Diffraction

The 1D-XRD patterns were obtained with a Panalytical X'Pert Pro and Empyrean X-Ray diffractometers with $CuK_{\alpha}1$ (1.54060 Å) source.

3.3.2.1 Data processing

Fitting of the XRD patterns was performed using the Pawley fit[8], which requires only the unit cell dimensions and space groups to obtain fitted lattice parameters. Rietveld refinement takes into account the composition of the system as well as the space group symmetry, and thus models the predicted peak intensities and positions for a given composition and space group[9]. Several materials in this work displayed poor-quality single-crystal diffraction data characterised by low resolution limits, broad peaks, and diffuse scattering, indicating substantial structural disorder that precluded complete crystal structure determination. Moreover, these materials produced poor-quality XRD data. Consequently, Rietveld refinements were not viable, and Pawley fits were employed as an alternative approach. All XRD fitting was conducted using Topas Academic[10].

3.3.3 Grazing incidence wide-angle scattering

Grazing incidence X-ray diffraction (GIXRD) offers distinct advantages over conventional Bragg-Brentano geometry. In GIXRD, the incident beam strikes the sample at a fixed shallow angle α_i (typically 0.1-5°) while the detector scans through the scattering angle 2θ (Figure 3.3). This configuration is particularly powerful for studying thin films and surfaces, as it enhances surface sensitivity and allows access to in-plane structural information that remains inaccessible in Bragg-Brentano geometry. When combined with a 2D detector, the technique—known as grazing incidence wide-angle X-ray scattering (GIWAXS)—can simultaneously probe both in-plane and out-of-plane crystallographic orientations, making it ideal for investigating textured or oriented crystallites. GIWAXS is especially valuable at synchrotron facilities, where the high-brilliance X-ray beam enables rapid data collection. This speed, coupled with the technique's versatility, makes it well-suited for *in*

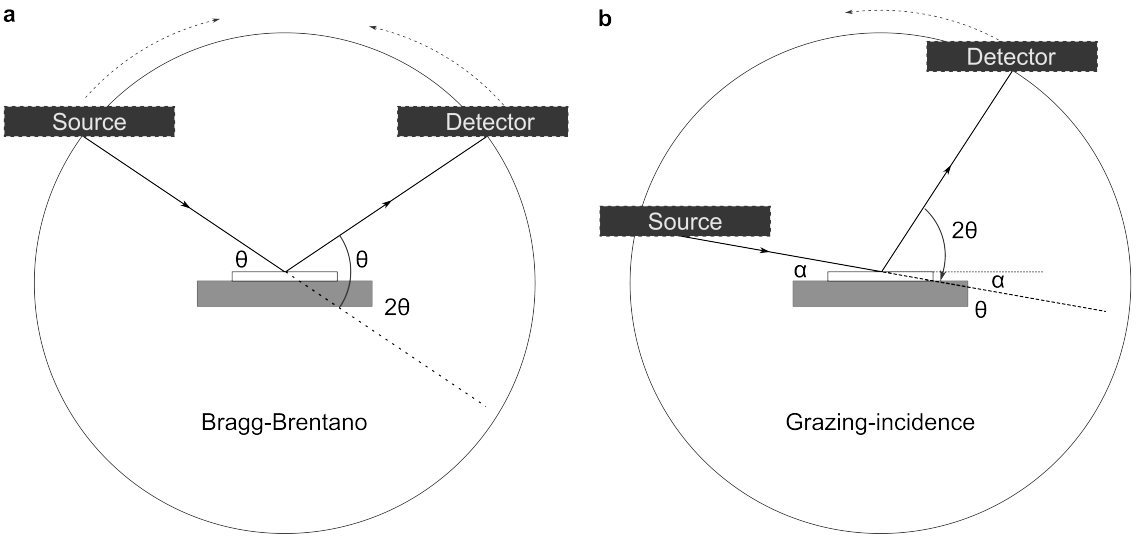


FIGURE 3.3: Comparison of **a** Bragg-Brentano and **b** grazing incidence X-ray diffraction geometries. In grazing incidence, the incident beam angle α_i remains fixed while the detector scans through 2θ.

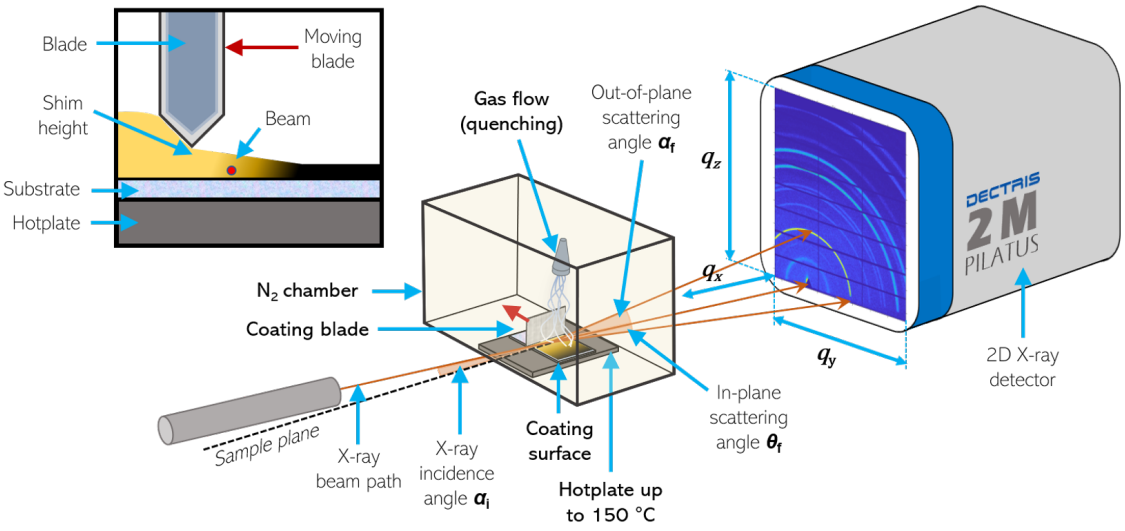


FIGURE 3.4: Schematic diagram of the GIWAXS experimental setup showing the key components: X-ray source, sample stage, and 2D detector. The incident beam strikes the sample at a shallow angle α_i, and scattered X-rays are collected on the 2D detector. This image was produced and provided by Dr. J.A. Smith.

situ and *operando* experiments, including studies of coating processes, environmental responses, and reactions in specialised chambers under controlled temperature, pressure, or atmospheric conditions[11]. An example of a 2D GIWAXS configuration is shown in Figure 3.4.

3.3.3.1 Synchrotron grazing incidence wide angle scattering measurements

Grazing-incidence wide-angle X-ray scattering (GIWAXS) data was acquired at the I07 beamline at Diamond Light Source. X-rays with energy 10 keV were incident on the samples at a grazing incidence angle α_i = 0.1-3°, with scattering collected by a Pilatus 2M (DECTRIS) hybrid photon-counting detector with a sample-to-detector distance (SDD) of 443 mm, with the geometry calibrated using an LaB6 and AgBe standard. *In situ* GIWAXS data was measured using the same configuration. Solutions were deposited using an *in situ* blade coater contained in an N_2 environment incorporating a syringe driver, motorised blade, integrated hotplate and an N_2 outlet directed at the sample acting as an air knife. Solutions were deposited via a microfluidic tube adjacent to the measured area, and coated perpendicular to the beam with the blade set at a shim height of 200 μm and the same coating speed as with the bar coating process, with gas quenching applied continuously from 30 s for 10 s, and measured with a grazing incidence angle of 1.5°. 2D detector images were acquired every 0.1 s for the first 150 s, then every 1 s for the next 1500 s with a lower transmission.

3.3.3.2 Data processing: an overview

The processing of GIWAXS data typically requires the following processes: (i) Calibration, (ii) detector and polarization corrections, (iii) masking and (iv) GIWAXS geometry correction and (iv) data reduction.

(i) Calibration Each pixel on the 2D raw detector image contains in-plane (q_{xy}) and out-of-plane (q_z) scattering vector components. It is critical to calibrate the scattering vector correctly for each instrumental configuration using the known radiation wavelength or energy, sample-to-detector distance (SDD), typically 100 - 500 nm for synchrotron measurements, and a well-scattering calibration standard such as AgBe or lanthanum hexaboride (LaB_6). The well-known d-spacing of the scattering standard is used to calibrate the data and map the 2D detector pixels onto a q range, normally producing a point-of-normal-incidence (PONI) and calibration file.

(ii) Detector and polarization corrections Intensity corrections on the data must be made based on the detector parameters and experimental setup; the pixel size, detector absorber attenuation coefficient, absorber layer thickness of the detector and the polarization (typically horizontally polarized light for synchrotron radiation).

(iii) Masking The data must be masked in order to remove faulty pixels (e.g., anomalously intense hot or close-to-zero-intensity dead pixels) and features arising from the direct beam.

(iv) Grazing incidence geometry corrections In 3D, Bragg peaks arise when the Ewald sphere intersects with the reciprocal lattice of the material being measured, which produces a curved surface which is projected onto a flat 2D detector. Due to the shallow incidence angle ($\alpha_i < 1°$) employed in grazing incidence geometry, the full scattering vector k_f is not captured. In particular, for large q_z, there is always a non-zero q_x such that the in-plane scattering component $q_r = \sqrt{q_x^2 + q_y^2} \neq 0$. This leads to an α_i-dependent 'missing wedge' in the data which must be accounted for via the means of 'reshaping' in order to acquire accurate quantitative information in real space.

Data reduction Most commonly, radial integration and azimuthal (along the radial direction) integration data reduction processes are performed following the previous processes. Radial integration produces a 1D intensity profile as a function of q or 2θ which is comparable to powder or thin-film XRD in Bragg-Brentano geometry. Unlike Bragg-Brentano XRD, which only probes the out-of-plane scattering, this radial integration includes contributions from both in-plane and out-of-plane scattering. Furthermore, 'radial cake cuts' can be performed in order to obtain information corresponding to specific scattering directions.

On the other hand, azimuthal profiles provide insights into the orientation and crystallographic texture of specific lattice planes. Preferred orientations of crystallites or grains along certain directions can be identified through variations in intensity as a function of azimuthal angle, aiding in texture analysis.

For *in situ* measurements, a series of 2D images can be processed in these ways to produce 'waterfall' plots over time in order to understand phase and texture evolution processes.

3.3.3.3 GIWAXS data processing protocols used

In the work covered in this thesis, calibration of the SDD and scattering vector was performed on the data using the pyFAI pyFAI-calib2 graphical user interface (GUI) on AgBe and LaB_6 standards.

Further intensity and geometry corrections, and data reduction processes were performed using code based on the pyFAI and pygix libraries, developed with Dr. J.A. Smith.

3.3.4 Solid state nuclear magnetic resonance (NMR) spectroscopy

All measurements were conducted by Dr. B.M. Gallant and E.Y.H. Hung, and data analysis was done by Dr. B.M. Gallant and Dr. D.J. Kubicki. All measurements were conducted at the UK solid state NMR facility.

Solid-state NMR spectroscopy is a powerful technique to probe atomic-level microstructure and structural dynamics in hybrid organic-inorganic metal halides. Amongst metal halide perovskites, NMR spectroscopy has been shown to effectively probe local atomic structure and bonding, as well as the orientational dynamics of the organic components and their timescales[12, 13].

This technique uses a large magnetic field to probe the intrinsic spin properties of nuclei, by exciting spin transitions between energy levels. All nuclei with a non-zero spin have a magnetic moment μ, given by:

$$\mu = \gamma I, \tag{3.1}$$

where γ is the gyromagnetic ratio, a proportionality constant dependent on the nuclei of choice, and I is the angular momentum quantum number. By applying

various pulse sequences under a magnetic field B_0, the nuclear spin associated with the nuclei can be excited to different energy levels, and in the example of spin 1/2 nuclei, this is given by:

$$E = -m\hbar\gamma B_0, \tag{3.2}$$

where m is the magnetic quantum number ($m = \pm 1/2$ for spin 1/2 nuclei), $\hbar$ is the reduced Planck constant. For the case of quadrupolar nuclei, this is more complicated. The local environment of the nucleus due to, for example local electronic interactions, affects the magnetic field experienced by the nucleus, which causes shifts in the energy levels. By Fourier transforming the signal, a spectrum of peaks can be produced, corresponding to the chemical environments associated with the nuclei of choice[14, 15]. By using a large magnetic field, the energy difference between the spin states can be increased, allowing for improved sensitivity and resolution of the spectra.

3.3.4.1 Solid state NMR spectroscopy measurements

All solid-state nuclear magnetic resonance (NMR) spectroscopy was carried out using a Bruker Avance Neo 20.0 T spectrometer on mechanosynthesised samples packed into 4 mm zirconia rotors. The temperature of the NMR rotors was varied from −40 °C to 150 °C and calibrated using the variation in ^{79}Br shift of KBr[16]. ^{1}H and ^{13}C NMR spectra were recorded under magic-angle spinning (MAS), using a Hahn echo pulse sequence. All rotors were spun using dry nitrogen gas. Radiofrequency pulses of 76 kHz (^{1}H) and 57 kHz (^{13}C) were used. The recycle delay for ^{1}H and ^{13}C measurements was varied as a function of temperature to maintain a value of approximately 1.3 times the measured T_1. ^{1}H and ^{13}C spectra were referenced to solid adamantane (1.91 and 38.48 ppm, respectively). ^{209}Bi spectra were acquired on static (non-spinning) samples using an RF pulse of 100 kHz. The transverse relaxation time constant (T_2^*) was found to be very short for ^{209}Bi, prohibiting the use of wideband excitation approaches. Therefore, a variable-offset cumulative-spectrum (VOCS) method was employed, whereby the frequency of the transmitter was varied systematically over a wide frequency range and a series of subspectra were recorded. These subspectra were added to produce the final ^{209}Bi spectra shown at each temperature. Typically, between 5 and 30 subspectra were recorded, spanning a range of

0.5 to 3 MHz. A Hahn echo pulse sequence was employed (RF pulse, 124 kHz), with a short (25 μs) echo delay and a recycle delay of 5 ms. For ^{14}N spectra, two different pulse sequences were employed, depending on the width of the ^{14}N spectral envelope observed. At low temperatures (broad spectral envelope; slow $(TMXM)^+$ (X=Cl, Br, I) tumbling regime), a static wideband uniform-rate smooth truncation quadrupolar Carr-Purcell Meiboom-Gill (WURST-QCPMG) approach was employed, based on a previously reported method[17]. At high temperatures (narrow spectral envelope; fast $(TMXM)^+$ tumbling regime), ^{14}N spectra were recorded via a Hahn echo pulse sequence (RF pulse, 70 kHz) under 4 kHz MAS. In the case of $(TMIM)_3Bi_2I_9$, this allowed differentiation of spectral features corresponding to $(TMIM)^+$ in the halobismuthate phase and the nitrogen-containing thermal degradation product observed. A recycle delay of 150 ms was used for all ^{14}N spectra. ^{14}N spectra were referenced to NH_4Cl (0 ppm).

3.3.5 Piezoresponse force microscopy

Piezoresponse force microscopy (PFM) is a form of contact-mode atomic force microscopy (AFM) that measures the piezoelectric response of a material. Essentially, a cantilever tip is brought into contact with the surface of the material, and a small AC voltage is applied to the tip as it scans the surface of the sample at a certain frequency of tapping. The resulting cantilever deflection is measured using photodiodes, and the resulting signal is used to map the piezoelectric response of the sample. Importantly, the phase response of the sample with respect to the applied voltage is also measured, which allows determination of piezoelectric domains oriented parallel and anti-parallel to the applied field.

PFM measurements were conducted using a Dimension Icon AFM system with a Nanoscope 6 controller. A conductive probe was utilised of spring constant and tip radius 0.1 N/m and 25 nm respectively. With the tip grounded a 4 V alternating bias signal (V_{ac}) was applied to the sample. This was driven at the contact resonance of the first eigenmode of the cantilever with the tip in contact with the film. In this way magnitude of sample surface displacement and directionality were measured concurrent with topography through the amplitude and phase response of the cantilever for sample imaging.

To measure voltage-dependent behaviour in the piezoelectric response of the material, force feedback was maintained at a constant tip contact force whilst a DC bias voltage was swept from -3 V to +3 V. Amplitude and Phase response in the cantilever were therefore acquired relative to applied bias. From the gradient obtained from the linear fit (visualised in Figure 4.12) of the acquired curves the d_{33} coefficient could therefore be calculated with an equation of the form $z = z_0 + d_{33,eff}V_{dc}$. Phase-voltage loops were taken in locations crossing domains which presented different responses during PFM imaging of the surface.

PFM measurements were also conducted using a Multi-Mode VIII AFM system with Nanoscope V controller. The same procedures were followed to generate correlative images of film piezo response in ambient environment.

Images were processed using the plane leveling function in Gwyddion in order to remove the background.

All AFM and PFM measurements were conducted by Dr. R. Harniman, and data analysis was done by E.Y.H. Hung.

3.3.5.1 Piezoelectric measurements

The Berlincourt method works by subjecting a piezoelectric crystal to low frequency, oscillating force, and measuring the resulting charge generated.

Piezoelectric coefficient measurements were conducted using an APC International Ltd YE2730A Berlincourt meter. The instrument was calibrated using a PZT pC N^{-1} standard (d_{33} = 367 pm V^{-1}).

3.3.6 Second harmonic generation (SHG)

The phenomenon of second harmonic generation (SHG) is a nonlinear optical process where a single photon is converted into two photons of twice the frequency.

In order to avoid exciting any other optoelectronic properties of these compounds, a laser wavelength of 1400 nm was used, with a power of 400 μW. ~100 fs pulses

were used at 5 kHz repetition rate, sampled in 5-20K steps. A set of reference measurements were also taken using $LiNbO_3$ crystals. These measurements were conducted by F.M. Adamczyk, M. Stein and A. Kapp, under the supervision of Prof. S. Chatterjee.

3.3.7 Density functional theory (DFT) calculations

3.3.7.1 Electrostatic potential calculations

Electrostatic potential (ESP) maps for $TMIM^+$ and $(TMIM)_3Bi_2I_9$ were computed using DFT as implemented in the Amsterdam Density Functional (ADF) module of the Amsterdam Modelling Suite (AMS 2023.104)[18, 19]. Single-point energy calculations were carried out on fixed geometries obtained from the crystal structures. For $TMIM^+$, in the form of a singly charged cation, the r^2SCAN-3c composite method was used[20]. This method combines the r^2SCAN meta-GGA exchange-correlation functional with a tailor-made triple-ζ polarized basis set (mTZ2P), and includes a D4 dispersion correction, geometrical counterpoise (gCP) correction for basis set superposition error, and additional short-range basis set incompleteness corrections. No frozen core approximation was used. The numerical integration quality was set to "good", and the default Becke fuzzy cell integration grid was used. For $(TMIM)_3Bi_2I_9$, in the form of a neutral molecular cluster, the BP86 generalised-gradient approximation (GGA) functional was used in combination with the TZP basis set and no frozen core approximation. Numerical integration quality was set to "normal", and the default Becke fuzzy cell integration grid was used. ESP maps were visualised using ADF's built-in tools by colouring electron density isosurfaces according to the SCF-derived electrostatic (Coulomb) potential. This approach gives a qualitative picture of the spatial charge distribution.

ESP calculations for the work covered in Chapter 4 were performed by Dr. D.J. Kubicki.

3.3.7.2 DFT and polarization calculations of $(TMIM)_3Bi_2I_9$ and $[(CH_3)_4N]_3Bi_2I_9$

First principles modelling of structures based on $(TMIM)_3Bi_2I_9$ and $[(CH_3)_4N]_3Bi_2I_9$ was carried out via plane-wave density functional theory (DFT), as implemented in the Quantum ESPRESSO-6.5 package[21, 22]. We use the generalised gradient approximation, within the Perdew-Burke-Ernzerhof parametrisation (DFT-PBE)[23]. All calculations use the scalar relativistic Optimised Norm Conserving Vanderbilt pseudopotentials[24], as collected in the Pseudo-Dojo database[25]. We used a kinetic energy cutoff of 70 Ry with gamma-centred k-point mesh of $6 \times 4 \times 2$ for all calculations.

To calculate the polarization vector of different structures, we used the Berry phase implementation of the Quantum ESPRESSO code[26–29]. On top of gamma-centred k-point grid of $6 \times 4 \times 2$ for scf calculations, we used $8 \times 4 \times 2$, $6 \times 8 \times 2$ and $6 \times 4 \times 5$ k-point grid for the calculations of polarization vectors along [100] (P_x), [010] (P_y) and [001] (P_z) directions, respectively.

Calculations were performed using the experimental crystal structure of $(TMIM)_3Bi_2I_9$, obtained at 293 K (orthorhombic space group $Pna2_1$). $TMIM^+$ cations in this model were replaced with by $[(CH_3)_4N]^+$ by replacing the iodine in the $[(CH_3)_3CH_2NI]^+$ ($TMIM^+$) cation with H and relaxing these H atoms only. $Cs_3Bi_2I_9$ was obtained by replacing N of the TMIM cation with Cs and removing rest of the organic atoms of $TMIM^+$. We found that there was little difference in the polarization by interchanging Cs^+ and $[(CH_3)_4N]^+$ (Supplementary Table 2), so calculations were also performed on the composition $Cs_3Bi_2I_9$ in the space group $P3_1c$ by modifying $[(CH_3)_4N]_3Bi_2I_9$ shown in Fig. 1b and swapping $[(CH_3)_4N]^+$ with Cs^+, in order to calculate its polarization[30].

DFT calculations for the work covered in Chapter 4 were performed by Dr. S. Saha and Dr. M. Filip.

3.3.7.3 DFT relaxations

DFT relaxations allow the crystal structure to adjust to its most stable configuration, minimising its energy. First, the known perovskite polymorphs were relaxed. Then, a similar approach was applied to Sn-based structures, systematically replacing Pb with Sn and repeating the variable cell relaxations. By comparing the energies of the different polymorphs relative to the 2H polymorph, one can determine their relative stability.

Density functional theory (DFT) calculations were performed with xDM van der Waals (vdW) corrections[31] using the Quantum ESPRESSO package[21]. DFT is a computational method used to model the electronic structure of materials, allowing us to calculate their energy and other properties. Van der Waals corrections are included to account for weak forces between atoms that are not directly bonded, which can be important in these materials.

For each polymorph, variable cell relaxation was conducted using the Quantum ESPRESSO code[21] with a plane wave basis set with a 60 Ry kinetic energy cutoff and a 480 Ry density cutoff using PAW pseudopotentials[32] and ensuring 0.05 spacing between reciprocal K-points.

DFT calculations for the work covered in Chapter 7 were performed by Dr. P. Ahlawat.

3.3.8 Molecular dynamics simulations using machine learning potentials

It is important to acknowledge that DFT calculations, while powerful, have limitations. In particular, the formamidinium (FA) cations within the perovskite structure can rotate, and during the structural relaxation process at 0 K, these rotations can sometimes lead to the system getting trapped in a local energy minimum, rather than finding the true global minimum. As a result, the DFT energies should be considered qualitative.

The simulations were performed using the state-of-the-art GRACE-2L machine learning potentials[33, 34]. Machine learning potentials provide an efficient way to approximate the DFT level interactions between atoms, enabling simulation of much larger systems than would be possible with DFT.

Supercells of various polymorphs (2H, 4H, 6H, 8H, 10H, 12H, and 3R) were prepared, each containing up to 5000 atoms. These simulations were performed at 300 K (room temperature) in the isothermal-isobaric (NPT) ensemble. The NPT ensemble maintains constant temperature and pressure, allowing the system to equilibrate under realistic conditions. Temperature was controlled using a velocity rescaling thermostat[34], and pressure was controlled using a Martyna-Tobias-Klein (MTK) barostat[35]. The MD simulations were carried out using the LAMMPS (Large-scale Atomic/Molecular Massively Parallel Simulator) package[35], a widely used software for atomistic simulations.

All MD simulations were performed by Dr. P. Ahlawat.

3.3.9 Polarization analysis

To investigate the influence of the $TMIM^+$ cations and isolate the effect of the distorted inorganic framework on the polarization, we first replaced the $TMIM^+$ cations with $[(CH_3)_4N]^+$. This substitution yielded a net polarization of 2.31 $\mu C/cm^2$ along the crystallographic c axis. In contrast, $[(CH_3)_4N]_3Bi_2I_9$ (Fig. 1b) exhibited a significantly lower polarization of 0.35 $\mu C/cm^2$. This six-fold increase in polarization demonstrates the crucial role of the distorted inorganic framework in $(TMIM)_3Bi_2I_9$ compared to its non-halogenated counterpart. When considering the complete system including the $TMIM^+$ cation, the overall polarization for $(TMIM)_3Bi_2I_9$ was calculated to be 3.57 $\mu C/cm^2$, which is an order of magnitude higher than that of $[(CH_3)_4N]_3Bi_2I_9$. This finding is consistent with our point charge model calculations. Additional calculations were performed by replacing $TMIM^+$ with Cs^+, which resulted in a polarization similar to that observed with the high-symmetry, non-polar $[(CH_3)_4N]^+$ cation. The substantial polarization observed in $(TMIM)_3Bi_2I_9$, particularly its significant enhancement compared to the non-halogenated system, suggests strong piezoelectric properties that could be valuable for applications in energy harvesting and sensing devices.

Bibliography

[1] J. Nývlt, "Kinetics of nucleation in solutions," *Journal of Crystal Growth*, vol. 3-4, pp. 377–383, 1968.

[2] G. Winter, D. G. Waterman, J. M. Parkhurst, A. S. Brewster, R. J. Gildea, M. Gerstel, L. Fuentes-Montero, M. Vollmar, T. Michels-Clark, I. D. Young, N. K. Sauter, and G. Evans, "DIALS: implementation and evaluation of a new integration package," *research papers Acta Cryst*, vol. 74, pp. 85–97, 2018.

[3] Agilent, "CrysAlis PRO," *Agilent Technologies Ltd*, 2014.

[4] G. M. Sheldrick, "A short history of SHELX," *Journal of Applied Crystallography*, vol. 64, pp. 112–122, 2007.

[5] G. M. Sheldrick, "SHELXT- integrated space-group and crystal-structure determination," *Journal of Applied Crystallography*, vol. 71, pp. 3–8, 2015.

[6] D. Kratzert, J. J. Holstein, and I. Krossing, "DSR: Enhanced modelling and refinement of disordered structures with SHELXL," *Journal of Applied Crystallography*, vol. 48, pp. 933–938, 2015.

[7] K. Momma and F. Izumi, "VESTA: a three-dimensional visualization system for electronic and structural analysis," *Journal of Applied Crystallography*, vol. 41, pp. 653–658, 2008.

[8] G. S. Pawley, "Unit-cell refinement from powder diffraction scans," *Journal of Applied Crystallography*, vol. 14, pp. 357–361, 1981.

[9] H. M. Rietveld, "Line profiles of neutron powder-diffraction peaks for structure refinement," *Journal of Applied Crystallography*, vol. 22, pp. 151–152, 1967.

[10] A. A. Coelho, "TOPAS and TOPAS-Academic: an optimization program integrating computer algebra and crystallographic objects written in C++," *Journal of Applied Crystallography*, vol. 51, pp. 210–218, 2018.

[11] J. A. Steele, E. Solano, D. Hardy, D. Dayton, D. Ladd, K. White, P. Chen, J. Hou, H. Huang, R. A. Saha, L. Wang, F. Gao, J. Hofkens, M. B. Roeffaers, D. Chernyshov, and M. F. Toney, "How to GIWAXS: Grazing incidence wide

angle X-ray scattering applied to metal halide perovskite thin films," *Advanced Energy Materials*, vol. 13, p. 2300760, 2023.

[12] D. J. Kubicki, S. D. Stranks, C. P. Grey, and L. Emsley, "Nmr spectroscopy probes microstructure, dynamics and doping of metal halide perovskites," *Nature Reviews Chemistry 2021 5:9*, vol. 5, pp. 624–645, 2021.

[13] R. E. Wasylishen, O. Knop, and J. B. Macdonald, "Cation rotation in methylammonium lead halides," *Solid State Communications*, vol. 56, pp. 581–582, 1985.

[14] A. ur Rahman, "Nuclear magnetic resonance," *Nuclear Magnetic Resonance*, 1986.

[15] J. B. Lambert, *Nuclear magnetic resonance spectroscopy : an introduction to principles, applications, and experimental methods*. Pearson/Prentice Hall, 2004.

[16] R. N. Purusottam, G. Bodenhausen, and P. Tekely, "Determination of sample temperature in unstable static fields by combining solid-state 79Br and 13C NMR," *Journal of Magnetic Resonance*, vol. 246, pp. 69–71, 2014.

[17] L. A. O'Dell, R. W. Schurko, K. J. Harris, J. Autschbach, and C. I. Ratcliffe, "Interaction tensors and local dynamics in common structural motifs of nitrogen: A solid-state 14N NMR and DFT study," *Journal of the American Chemical Society*, vol. 133, pp. 527–546, 2011.

[18] V. Universiteit, "Adf 2025.1, scm, theoretical chemistry„" 2025.

[19] E. J. Baerends, N. F. Aguirre, N. D. Austin, J. Autschbach, F. M. Bickelhaupt, R. Bulo, C. Cappelli, A. C. van Duin, F. Egidi, C. F. Guerra, A. Förster, M. Franchini, T. P. Goumans, T. Heine, M. Hellström, C. R. Jacob, L. Jensen, M. Krykunov, E. van Lenthe, A. Michalak, M. M. Mitoraj, J. Neugebauer, V. P. Nicu, P. Philipsen, H. Ramanantoanina, R. Rüger, G. Schreckenbach, M. Stener, M. Swart, J. M. Thijssen, T. Trnka, L. Visscher, A. Yakovlev, and S. van Gisbergen, "The Amsterdam Modeling Suite," *Journal of Chemical Physics*, vol. 162, p. 162501, 2025.

[20] T. Gasevic, J. B. Stückrath, S. Grimme, and M. Bursch, "Optimization of the r2SCAN-3c composite electronic-structure method for use with slater-type orbital basis sets," *Journal of Physical Chemistry A*, vol. 126, pp. 3826–3838, 2022.

[21] P. Giannozzi, S. Baroni, N. Bonini, M. Calandra, R. Car, C. Cavazzoni, D. Ceresoli, G. L. Chiarotti, M. Cococcioni, I. Dabo, A. D. Corso, S. D. Gironcoli, S. Fabris, G. Fratesi, R. Gebauer, U. Gerstmann, C. Gougoussis, A. Kokalj, M. Lazzeri, L. Martin-Samos, N. Marzari, F. Mauri, R. Mazzarello, S. Paolini, A. Pasquarello, L. Paulatto, C. Sbraccia, S. Scandolo, G. Sclauzero, A. P. Seitsonen, A. Smogunov, P. Umari, and R. M. Wentzcovitch, "QUANTUM ESPRESSO: a modular and open-source software project for quantumsimulations of materials," *Journal of Physics: Condensed Matter*, vol. 21, p. 395502, 2009.

[22] P. Giannozzi, O. Andreussi, T. Brumme, O. Bunau, M. B. Nardelli, M. Calandra, R. Car, C. Cavazzoni, D. Ceresoli, M. Cococcioni, N. Colonna, I. Carnimeo, A. D. Corso, S. D. Gironcoli, P. Delugas, R. A. Distasio, A. Ferretti, A. Floris, G. Fratesi, G. Fugallo, R. Gebauer, U. Gerstmann, F. Giustino, T. Gorni, J. Jia, M. Kawamura, H. Y. Ko, A. Kokalj, E. Kücükbenli, M. Lazzeri, M. Marsili, N. Marzari, F. Mauri, N. L. Nguyen, H. V. Nguyen, A. Otero-De-La-Roza, L. Paulatto, S. Poncé, D. Rocca, R. Sabatini, B. Santra, M. Schlipf, A. P. Seitsonen, A. Smogunov, I. Timrov, T. Thonhauser, P. Umari, N. Vast, X. Wu, and S. Baroni, "Advanced capabilities for materials modelling with QUANTUM ESPRESSO," *Journal of Physics: Condensed Matter*, vol. 29, p. 465901, 2017.

[23] J. P. Perdew, K. Burke, and M. Ernzerhof, "Generalized Gradient Approximation made simple," *Physical Review Letters*, vol. 77, p. 3865, 1996.

[24] D. R. Hamann, "Optimized norm-conserving Vanderbilt pseudopotentials," *Physical Review B - Condensed Matter and Materials Physics*, vol. 88, p. 085117, 2013.

[25] M. J. van Setten, M. Giantomassi, E. Bousquet, M. J. Verstraete, D. R. Hamann, X. Gonze, and G. M. Rignanese, "The PseudoDojo: Training and grading a 85 element optimized norm-conserving pseudopotential table," *Computer Physics Communications*, vol. 226, pp. 39–54, 2018.

[26] R. Resta, "Theory of the electric polarization in crystals," *Ferroelectrics*, vol. 136, pp. 51–55, 1992.

[27] R. Resta, "Macroscopic polarization in crystalline dielectrics: the geometric phase approach," *Reviews of Modern Physics*, vol. 66, p. 899, 1994.

[28] R. D. King-Smith and D. Vanderbilt, "Theory of polarization of crystalline solids," *Physical Review B*, vol. 47, p. 1651, 1993.

[29] D. Vanderbilt, "Berry-phase theory of proper piezoelectric response," *Journal of Physics and Chemistry of Solids*, vol. 61, pp. 147–151, 2000.

[30] C. Feldmann, "Crystal structure of tris(tetramethylammonium) dibismuth nonaiodide, $[N(CH_3)_4]_3Bi_2I_9$," *Zeitschrift fur Kristallographie - New Crystal Structures*, vol. 216, pp. 487–488, 2001.

[31] A. Otero-De-La-Roza and E. R. Johnson, "Van der waals interactions in solids using the exchange-hole dipole moment model," *Journal of Chemical Physics*, vol. 136, p. 174109, 2012.

[32] A. D. Corso, "Pseudopotentials periodic table: From H to Pu," *Computational Materials Science*, vol. 95, pp. 337–350, 2014.

[33] A. Bochkarev, Y. Lysogorskiy, and R. Drautz, "Graph Atomic Cluster Expansion for Semilocal Interactions beyond Equivariant Message Passing," *Physical Review X*, vol. 14, p. 021036, 2024.

[34] G. Bussi, D. Donadio, and M. Parrinello, "Canonical sampling through Velocity Rescaling," *Journal of Chemical Physics*, vol. 126, p. 22, 2007.

[35] G. J. Martyna, D. J. Tobias, and M. L. Klein, "Constant pressure molecular dynamics algorithms," *The Journal of Chemical Physics*, vol. 101, pp. 4177–4189, 1994.

Chapter 4

Tailoring a novel, lead-free organic-inorganic halobismuthate for large piezoelectricity

4.1 Abstract

Molecular piezoelectrics are a potentially disruptive technology, enabling a new generation of self-powered electronics that are flexible, high-performance, and inherently low-toxicity. Although significant efforts have been made towards understanding their structural design by targeted manipulation of their phase transition behaviour, the resulting achievable piezoresponse remains limited. In this work, we use a low-symmetry, 0D inorganic framework alongside a carefully selected 'quasi-spherical' organic cation to manipulate organic-inorganic interactions, and form the hybrid, piezoelectric material $[(CH_3)_3NCH_2I]_3Bi_2I_9$. Using variable-temperature single crystal X-ray diffraction and solid state nuclear magnetic resonance spectroscopy we demonstrate that this material simultaneously exhibits an order-disorder and displacive symmetry-breaking phase transition. This phase transition is mediated by halogen bonding between the organic and inorganic frameworks, and results in a large piezoelectric response, d_{33} = 161.5 pm V^{-1}. This value represents a four-fold

improvement on previously reported halobismuthate piezoelectrics and is comparable to those of commercial inorganic piezoelectrics, thus offering a new pathway towards low-cost, low-toxicity mechanical-energy harvesting and actuating devices.

4.2 Introduction

Piezoelectric materials possess the ability to generate electrical polarization in response to mechanical stress, and vice versa, owing to their lack of inversion symmetry. Amongst these, ferroelectrics tend to be the best-performing as they exhibit spontaneous polarization, which can be switched by an external electric field to produce a stronger piezoelectric response, described by the piezoelectric coefficients d_{ij}. High performance ferroelectrics such as lead zirconium titanate (PZT) ceramics are extensively used in devices like sensors, actuators, and energy harvesting systems, however consist of more than 60% lead by weight[1], raising significant environmental and regulatory concerns as global restrictions on toxic substances continue to tighten[2]. Furthermore, ceramic oxides are highly brittle and require rigorous compositional control throughout production, alongside expensive high temperature and pressure processing[3], rendering them unsuitable for inexpensive internet-of-things (IoT) and flexible applications despite their high d_{ij}s.

Consequently, significant efforts have focused on developing a new generation of lead-free materials that combine high piezoelectric coefficients, ease of fabrication, and mechanical flexibility. Among these, hybrid organic-inorganic perovskites and their derivatives have garnered considerable attention[3] due to their exceptional defect tolerance and impressive optoelectronic properties, which have been extensively explored in photovoltaic and other electronic applications. Notable successes include $[(CH_3)_3NCH_2Cl]MnCl_3$ (d_{33} = 185 pC/N)[4] and $[(CH_3)_3NCH_2F]_x[(CH_3)_3NCH_2Cl]_{1-x}CdCl_3$ (d_{33} = 1540 pC/N)[5]. Thus far however, these advances have still relied on toxic and highly-toxic heavy metals, such as Mn and Cd, highlighting the continuing need for low-toxicity ferroelectrics[3].

Inspired by these ideas and those outlined in Section 2.6.3, we select 'quasi-spherical' $[(CH_3)_3NCH_2I]^+$ (trimethyl(iodomethyl)ammonium = $TMIM^+$) as the cation in a

non-toxic, 0D iododobismuthate material and synthesise $(TMIM)_3Bi_2I_9$, which remains polar until its decomposition temperature at 250 °C and exhibits record-breaking piezoelectricity for a halobismuthate when processed as a thin film. We synthesise $(TMIM)_3Bi_2I_9$ not only via thin film solution processing, but also as single crystals by a solution crystallization method and as microcrystalline powders via mechanosynthesis, demonstrating the broad and facile processability of this material. By conducting in-depth variable temperature structural analysis combining single crystal X-ray diffraction (SCXRD) using synchrotron radiation with high magnetic field solid-state nuclear magnetic resonance (NMR) spectroscopy and DFT calculations, we establish the structural origins of the phase transition behaviour of $(TMIM)_3Bi_2I_9$. In particular, we experimentally detail how the halogen bonding between the $[TMIM]^+$ cation and $[Bi_2I_9]^{3-}$ governs the phase transition behaviour for the first time.

4.3 Results and Discussion

4.3.1 Designing halobismuthates for high piezoresponse

Dark red single crystals of $(TMIM)_3Bi_2I_9$ are synthesised by slow cooling of a HI aqueous solution (see Methods). Structural analyses of single crystal X-ray diffraction (SCXRD) data (**Figure 4.1a**) show that $(TMIM)_3Bi_2I_9$ crystallizes in the orthorhombic polar space group $Pna2_1$ at 20 °C. Notably, this is a non-centrosymmetric space group, satisfying the fundamental structural criterion for a piezoelectric material.

In comparison to the polar phase of its organohalide-free counterpart, $[(CH_3)_4N]_3Bi_2I_9$ (**Fig. 4.1b**), we observe several features desirable for high piezoresponse in $(TMIM)_3Bi_2I_9$. First, the $[Bi_2I_9]^{3-}$ dimers are oriented at ± 26.5° with respect to the longest crystallographic (a) axis, towards the c axis, and nearly perpendicular ± 88.8° to the b axis. This degree of asymmetry in the dimer is unusual for $A_3B_2X_9$ structures, where the $[Bi_2X_9]^{3-}$ (X=I,Br,Cl) dimers are aligned close to or parallel to the long crystallographic axes[6–10]. As a result, this distortion leads to a

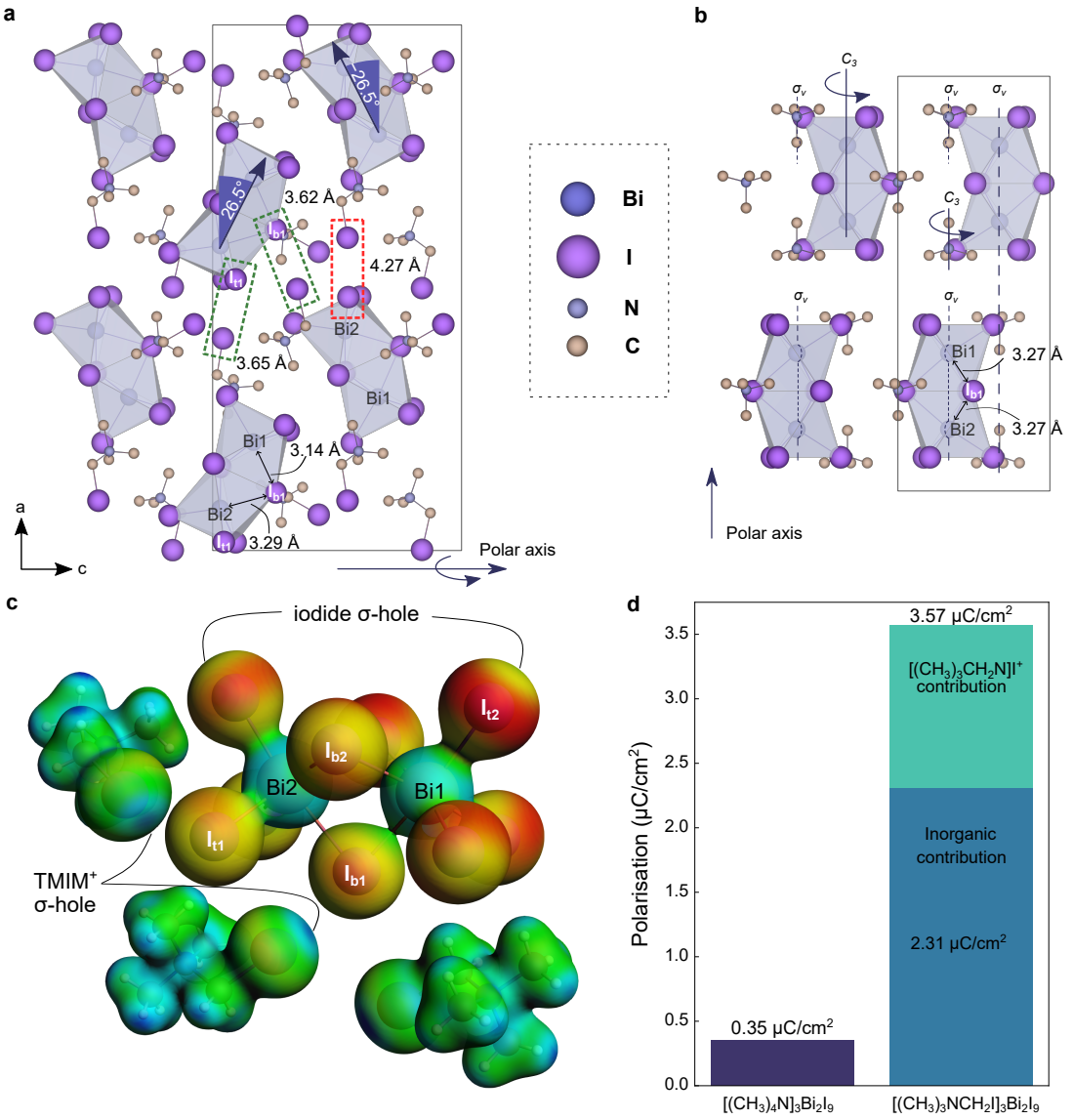


FIGURE 4.1: Inducing non-centrosymmetry for high piezoresponse. **a** Room temperature crystal structure of $[(CH_3)_3CH_2NI]_3Bi_2I_9$, or $(TMIM)_3Bi_2I_9$. **b** Crystal structure of $[(CH_3)_4N]_3Bi_2I_9$, reproduced from ICSD code 170840. Hydrogen atoms are omitted for clarity. **c** Electrostatic potential (ESP) surface of $(TMIM)_3Bi_2I_9$, where the colour scheme represents electrostatic potential from red (more negative) to blue (more positive), where the sigma hole on the iodine (blue region) is shown oriented as being oriented towards the inorganic framework. **d** Calculated net polarization for $[(CH_3)_4N]_3Bi_2I_9$ and $[(CH_3)_3CH_2NI]_3Bi_2I_9$. The electrostatic potential calculations were performed by Dr. D.J.Kubicki, and the polarization calculations were performed by Dr. S. Saha

reduced-symmetry-doubling of the unit cell compared to $[(CH_3)_4N]_3Bi_2I_9$[11]. Additionally, we observe a pronounced distortion in the $[Bi_2X_9]^{3+}$ dimer of $(TMIM)_3Bi_2I_9$, originating from asymmetry in the Bi1-I_{b1}-Bi2 bond distances for one of the bridging iodides (I_{b1}): the Bi1-I_{b1} distance is 3.14 Å, while the Bi2-I_{b1} distance is 3.29 Å. The $[Bi_2I_9]^{3+}$ dimer in $(TMIM)_3Bi_2I_9$ also lacks rotational symmetry about the Bi$\cdots$Bi axis. In contrast, the $[Bi_2X_9]^{3+}$ dimers in $[(CH_3)_4N]_3Bi_2I_9$ are nearly symmetric in the face-sharing plane of μ_2-bridging iodides, as well as exhibiting both three-fold rotational (C_3) and vertical mirror plane (σ_v) site symmetry (**Fig. 4.1b**).

By adopting a point charge model for polarization that considers only the inorganic components, the tilted and distorted dimers in $(TMIM)_3Bi_2I_9$ result in an order-of-magnitude increase in polarization along the polar 2_1 screw axis compared to that along the 3_1 axis of $[(CH_3)_4N]_3Bi_2I_9$ (Appendix A.1). Moreover, the tilting of the dimer in $(TMIM)_3Bi_2I_9$ leads to increased voids between the dimers along its polar (c) axis compared to the polar (long) axis in $[(CH_3)_4N]_3Bi_2I_9$, which may allow for increased displacement of ions and enhance polarization.

Since the inorganic $[Bi_2I_9]^{3-}$ dimer is compositionally unchanged compared to $[(CH_3)_4N]_3Bi_2I_9$, the distortion of the inorganic framework in $(TMIM)_3Bi_2I_9$ must arise from the asymmetric, polar $[TMIM]^+$ cations and their interaction with the $[Bi_2I_9]^{3-}$ dimers. In the room temperature structure, determined by SCXRD, the $[TMIM]^+$ cations exhibit well-defined positions with pronounced asymmetry around each dimer. Specifically, all three organic cations associated with each dimer are positioned such that their iodomethyl groups orient toward different I^- ions within the same BiI_6 octahedron ($Bi2$, in **Fig. 4.1a**). This asymmetric arrangement contrasts with the high-symmetry positioning of $[(CH_3)_4N]^+$ cations in $[(CH_3)_4N]_3Bi_2I_9$, where their contribution is nearly equal in magnitude and antiparallel to the contribution from the $[Bi_2I_9]^{3+}$ dimers, resulting in near-to-total cancelling out of the net polarization (Appendix A.1). Therefore, the ordered $[TMIM]^+$ cations disrupt this cancellation and contribute to a higher net polarization in $(TMIM)_3Bi_2I_9$.

Importantly, we identify that the I$\cdots$I$^-$ distances between two of these cations and their nearest neighbour iodides in the $[Bi_2I_9]^{3-}$ dimer (green dashed boxes, **Fig. 4.1a**), 3.62 Å and 3.65 Å, are substantially less than the sum of the van der Waals radius of iodine and the Shannon ionic radius of iodide (4.18 Å). This suggests the presence of a bonding interaction between the organic and inorganic

components; one between a $[TMIM]^+$ cation and a bridging iodide (I_{b1}) and another between a second $[TMIM]^+$ cation and a terminal iodide (I_{t1}). The C-I$\cdots$I$^-$ bond angles corresponding to these interactions (172.0° and 163.2°) are consistent with the presence of halogen bonds, in which iodide serves as the electron donating species.

To investigate the presence of these interactions, we calculate the electrostatic potential (ESP) surface surrounding the $[(CH_3)_3NCH_2I]^+$ cation and observe a significant positive electrostatic well localised on the iodine atom and antiparallel to the C-I bond (Supplementary Fig. 2). This electrostatic potential motif is commonly described as a "σ-hole" in the electron density surrounding the iodine and is essential for effective halogen bonding[12–14]. The positively charged quaternary ammonium substituent on the iodomethyl group of $[TMIM]^+$ acts as a highly effective electron-withdrawing group, directing positive charge into the σ-hole. We next calculate the electrostatic potential ESP across the $(TMIM)_3Bi_2I_9$ structure (**Fig. 4.1c**). For the two short I$\cdots$I$^-$ distances identified, the σ-hole of $[TMIM]^+$ is directed toward the adjacent iodide, consistent with halogen bond formation. However, the ESP map shows only a small amount of shared electron density between the two atoms (Figure 4.2). This suggests a high degree of ionicity in this bond, as expected for a halogen-halide interaction between two ions.

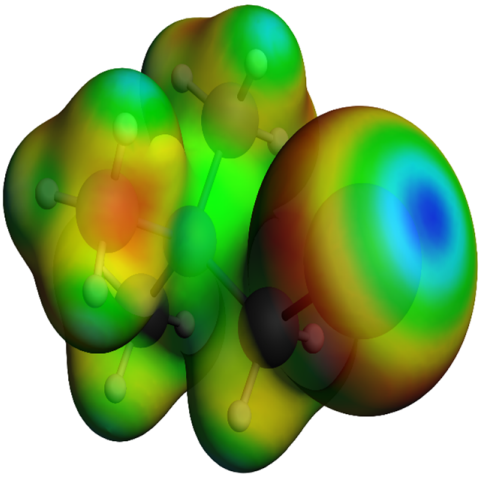


FIGURE 4.2: Electrostatic potential (ESP) map of $TMIM^+$. The colour map represents the distribution of charge across the cation; red and blue correspond to regions of lesser and greater positive charge, respectively. The ESP map was calculated by Dr. D.J. Kubicki.

The ESP map also reveals a second type of σ-hole in the $(TMIM)_3Bi_2I_9$ structure, located on the iodide ions, and particularly pronounced on terminal iodides not involved in halogen bonding, e.g. I_{t2}. This feature originates from the covalent nature of the Bi-I bonds, which leads to regions of relative electropositivity on the iodide antiparallel to the Bi-I bond axis. The presence of this σ-hole is important in rationalising the observed geometry in the room temperature structure of $(TMIM)_3Bi_2I_9$. For instance, the near-perpendicular Bi2-$I_{t1}\cdots$I bond angle of 93.1° arises to minimise electrostatic repulsion between the σ-holes of $[TMIM]^+$ and I_{t1} (**Fig. 4.1c**). The iodide σ-hole formation similarly governs the orientation of the halogen bond to I_{b1}, where a Bi2-$I_{b1}\cdots$I bond angle of 94.1° is observed. Critically, this geometry leads to a nearly-linear Bi1-$I_{b1}\cdots$I bond angle of 176.3°, which appears to unfavourably orient the $[TMIM]^+$ σ-hole directly toward an I_{b1} σ-hole. However, analysis of the electron density distribution across the non-halogen-bonded I_{b2}, suggests that σ-hole formation on μ_2-bridging iodides is not as pronounced as on terminal iodides due to the orthogonal arrangement of the two Bi-I bonds (**Fig. 4.1c**). Thus, the I_{b1} halogen bond orientation may not be as energetically unfavourable as expected.

The influence of the halogen bond on the Bi1-I_{b1} bond distance is also particularly striking. As noted above, the Bi1-I_{b1} bond is unexpectedly shorter than the Bi2-I_{eq1} bond (**Fig. 4.1a**). Typically, the donation of electron density from I_{b1} toward the σ-hole of $[TMIM]^+$ might be expected to weaken and lengthen the Bi1-I_{b1} bond. Instead, the observed bond shortening suggests that the donation of electron density originates from a molecular orbital of the $[Bi_2I_9]^{3-}$ dimer which is antibonding in nature; the depopulation of this orbital serves to strengthen the Bi1-I_{b1} bond. Furthermore, the energetic benefit of this bond strengthening likely contributes to the otherwise unfavourable head-on orientation of the iodide (I_{b1}) and $[TMIM]^+$ σ-holes.

Crucially, this halogen bond-induced shortening of the Bi1-I_{eq1} bond drives the desymmetrisation of the $[Bi_2I_9]^{3-}$ dimer. Similarly, the orientation of this halogen bond (176.3° and 94.1° to the Bi1-I_{b1} and Bi2-I_{b1} bonds, respectively) – determined by the interaction between the σ-holes of $[TMIM]^+$ and I_{b1} – anchors the $[TMIM]^+$ cations in their highly asymmetric arrangement around the dimer, highlighted above in contrast to the symmetric positioning of the organics in $[(CH_3)_4N]_3Bi_2I_9$. Taken together with the asymmetric tilting of the dimers away from the crystallographic axes, these halogen bond-induced structural phenomena are expected to contribute

to significant polarization across the overall $(TMIM)_3Bi_2I_9$ structure and thus enhance its piezoelectric responsivity.

To verify these structural findings, we calculate the polarization vectors of $(TMIM)_3Bi_2I_9$ and $[(CH_3)_4N]_3Bi_2I_9$ using the Berry phase approach in plane-wave density functional theory (DFT) (**Fig. 4.1d**)[15–20]. To isolate the contribution of the tilted and distorted inorganic framework from that of the $[TMIM]^+$, we first replace the $[TMIM]^+$ cations with $[(CH_3)_4N]^+$ while preserving the inorganic framework geometry of $(TMIM)_3Bi_2I_9$. This substitution yields a net polarization of 2.31 $\mu C/cm^2$ along the crystallographic c axis. By contrast, conducting the same calculation using the true, undistorted $[(CH_3)_4N]_3Bi_2I_9$ structure yields a significantly lower polarization of 0.35 $\mu C/cm^2$. This six-fold increase demonstrates the crucial role of the distorted inorganic framework in $(TMIM)_3Bi_2I_9$ in the overall polarization of the structure. When considering the complete system including the $[TMIM]^+$ cation, the overall polarization for $(TMIM)_3Bi_2I_9$ is calculated to be 3.57 $\mu C/cm^2$, an order of magnitude higher than that of $[(CH_3)_4N]_3Bi_2I_9$. This relative increase in polarization is consistent with our point charge model calculations, and comparable or larger than that of other organic-inorganic metal-halide ferroelectrics[4, 21–23]. Additional calculations were performed by replacing $[TMIM]^+$ with Cs^+, which resulted in a polarization similar to that observed with the high-symmetry, non-polar $[(CH_3)_4N]^+$ cation (Appendix Table **??**).

Importantly, we have demonstrated through both experimental structural analysis and theoretical calculations that introducing intermolecular interactions - in this case halogen bonding - induces structural tilting, distortion and increased asymmetry in $(TMIM)_3Bi_2I_9$. This leads to a significant enhancement in polarization compared to the non-halogenated system, demonstrating the potential to leverage intermolecular interactions for tuneable and optimised piezoelectric properties.

4.3.2 Phase transition behaviour: Differential scanning calorimetry

The phase transition behaviour of $(TMIM)_3Bi_2I_9$ at elevated temperature is first studied by conducting differential scanning calorimetry (DSC, **Fig. 4.3**). Upon

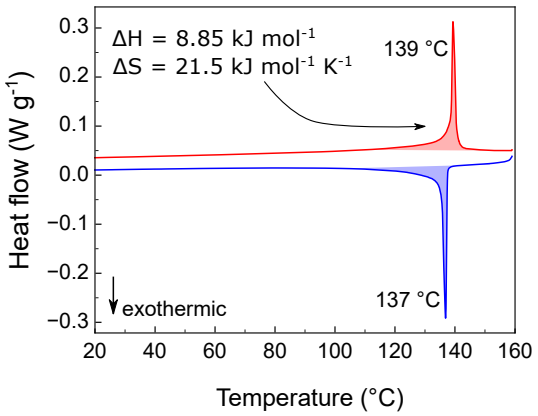


FIGURE 4.3: Differential scanning calorimetry (DSC) trace of $(TMIM)_3Bi_2I_9$. DSC measurements were done by Dr. N. Hawkins, and analysed by E.Y.H. Hung

heating, an endothermic event at 139 °C is observed, which is reversible with an exotherm at 137 °C upon cooling, indicating a transition temperature at 138 °C. The sharp, well-defined peaks observed in both heating and cooling cycles suggest that this transition is first-order in nature. The calculated molar enthalpy change (ΔH) and molar entropy change (ΔS) for this transition are +8.85 kJ mol^{-1} and +21.5 J mol^{-1} K^{-1}, respectively. This value of ΔS is larger than those reported previously for order-disorder transitions in hybrid organic-inorganic halides (∼5-15 J mol^{-1} K^{-1})[24, 25], and more comparable to molecular ferroelectrics[26, 27]. Using $\Delta S = R\ln N \approx 21.5$ J mol^{-1} K^{-1} (where R is the molar gas constant and N the ratio of the number of geometrically distinguishable orientations between the two phases) we find N = 13, suggesting the onset of high-symmetry orientational reconfiguration upon phase transition.

4.3.3 Phase transition behaviour: Variable temperature SCXRD

We determine the structural evolution of $(TMIM)_3Bi_2I_9$ with temperature using variable temperature (VT) SCXRD (Figure 4.4) and identify a polar-to-polar structural phase transition occurring at 140 °C, from the room temperature (RT) $Pna2_1$ to high temperature (HT) $Pmn2_1$. This structural transition is associated with a gain in translational symmetry along the a_{LT} (b_{HT}) axes leading to an approximate halving of the unit cell volume ($b_{HT} = \frac{1}{2} a_{LT}$), evident in the $(hk0)_{LT}$ and $(0kl)_{HT}$

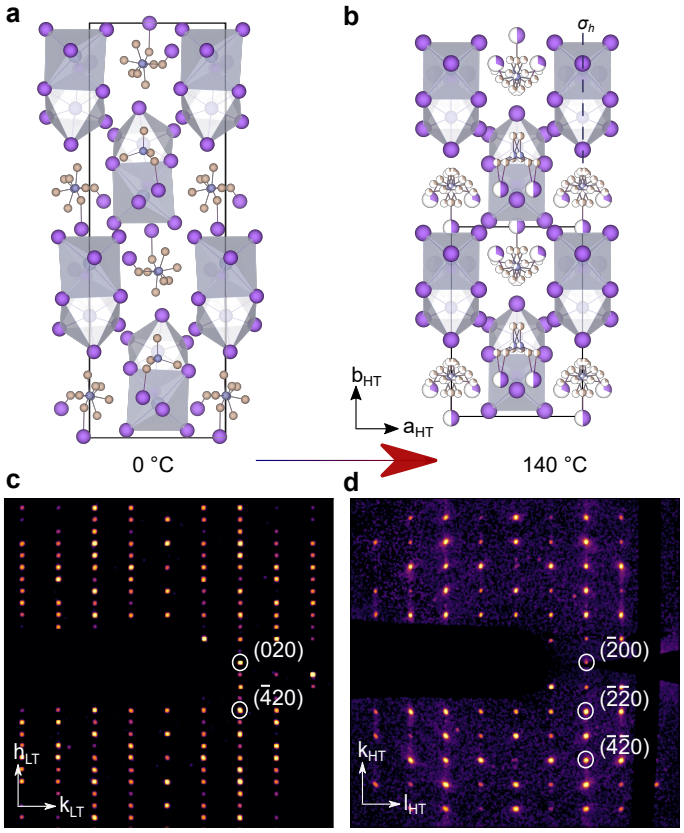


FIGURE 4.4: Crystal structures and (hk0) reciprocal space reconstructions of $(TMIM)_3Bi_2I_9$ at 0 and 130 °C, respectively. The reciprocal space reconstructions have been plotted on a logarithmic intensity scale to enhance the visibility of diffuse scattering features.

reciprocal space reconstructions, indicated by doubling of the Bragg peak spacing along $(h00)_{LT}$ and $(0k0)_{HT}$ (**Fig. 4.4c,d**). Temperature-induced, rod-like diffuse scattering is also observed in the HT reciprocal space reconstruction, signifying deviations or disorder relative to the average structure derived from long-range Bragg scattering.

Analysis of the HT structure with increasing temperature shows that the $[Bi_2I_9]^{3-}$ dimer moves from general Wyckoff positions from the LT phase to a special position with σ_h symmetry in the HT phase. This shift is accompanied by a linear change in the tilt of the inorganic dimer with temperature towards the a_{LT} axis from ± 26.5 to 26.0 ° just before the phase transition; upon the phase transition it discontinuously tilts back to ± 26.3 ° (**Fig. 4.5**). Furthermore, the positions of the $[TMIM]^+$ cations with respect to the dimer change by up to 0.74 Å (Table 4.1), indicating a displacive

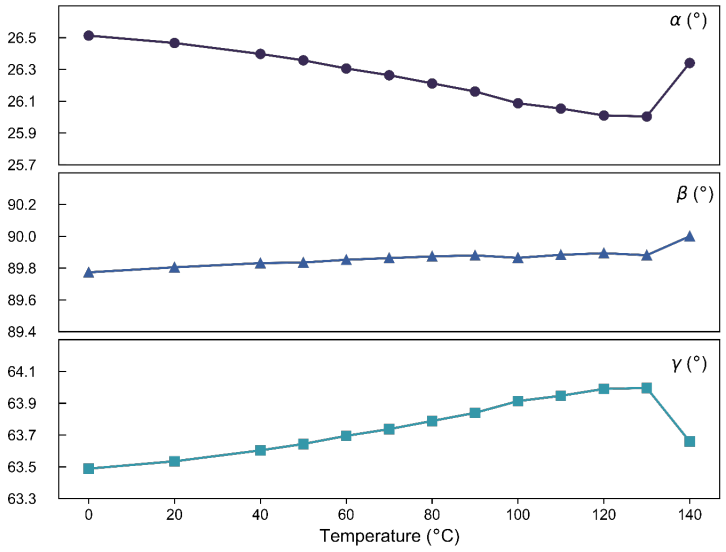


FIGURE 4.5: Tilting of $(Bi_2I_9)^{3-}$ dimer with temperature. α, β and γ refer to the angle with respect to the a, b and c-axis, respectively.

transition. The retention of the tilting of the dimer indicates that the polar, non-centrosymmetric nature of $(TMIM)_3Bi_2I_9$ is preserved in the HT phase even if the disordered organic component is ignored.

TABLE 4.1: N$\cdots$Bi distances (error) in $(TMIM)_3Bi_2I_9$ at room temperature and 140 °C, from SCXRD data analysis.

Distances (Å)	0 °C	140 °C
N1-Bi1	13.333 (12)	12.749 (14)
N2-Bi1	10.687 (15)	10.87 (3)
N3-Bi1	9.434 (12)	9.29 (5)
N1-Bi2	10.099 (12)	9.359 (14)
N2-Bi2	6.528 (15)	6.69 (3)
N3-Bi2	6.637 (13)	6.54 (5)

The $[TMIM]^+$ cations undergo more significant change in the HT phase transitioning from an ordered and distinct arrangement to exhibiting two-fold orientational disorder across a mirror plane (σ_h, **Fig. 4.4b**). In the difference Fourier map in the HT phase, only the positions of the nitrogen and (disordered) iodine atoms of the cation are discernible, suggesting that $[TMIM]^+$ undergoes reorientation in this phase. During the peak indexing process for data reduction (via *xia2*)[28], diffuse

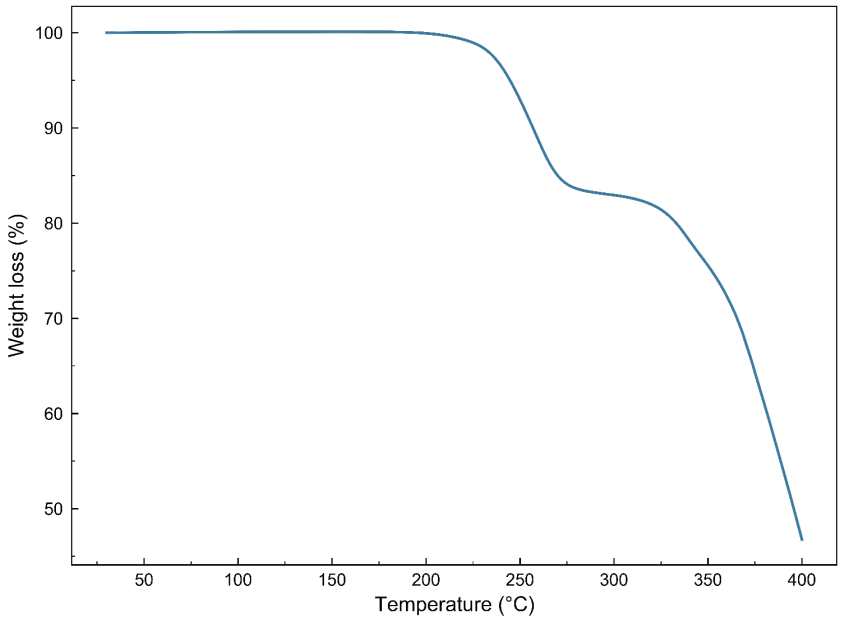


FIGURE 4.6: Thermogravimetric analysis (TGA) of $(TMIM)_3Bi_2I_9$.

scattering is discarded, resulting in a slight loss of electron density in the HT difference Fourier map compared to the RT structure. This leads to less than 100% refined occupancy of the $[TMIM]^+$ cations in the HT phase: one $[TMIM]^+$ is refined to 63% occupancy split across two positions, one refined to 48% occupancy over two positions, and one to 100% occupancy split equally across two positions. The residual electron density map shows weak residual density surrounding these $[TMIM]^+$ cations. The observed diffuse scattering is thus attributed to the dynamic molecular behaviour of the organic component. Notably, $(TMIM)_3Bi_2I_9$ retains a polar and non-centrosymmetric phase up to its decomposition temperature (250 °C, **Fig. 4.6**), demonstrating significant advantage over other hybrid materials for applications across a wide temperature range[4, 9, 10].

The crystallographic data and ORTEP diagrams for $(TMIM)_3Bi_2I_9$ from 0 to 140 °C are given in Tables A.8 - A.11 and A.11 - A.13, respectively.

4.3.4 Phase transition behaviour: Variable temperature solid-state NMR spectroscopy

To gain deeper insight into the phase transition between the two phases of $(TMIM)_3Bi_2I_9$, variable-temperature multinuclear solid-state nuclear magnetic resonance (VT NMR) spectroscopy is employed. VT NMR is a uniquely powerful tool to investigate the evolution in both local structure and dynamic motion within solid materials. For experimental convenience, we conduct all NMR measurements on $(TMIM)_3Bi_2I_9$ synthesised via mechanosynthesis as a microcrystalline powder.

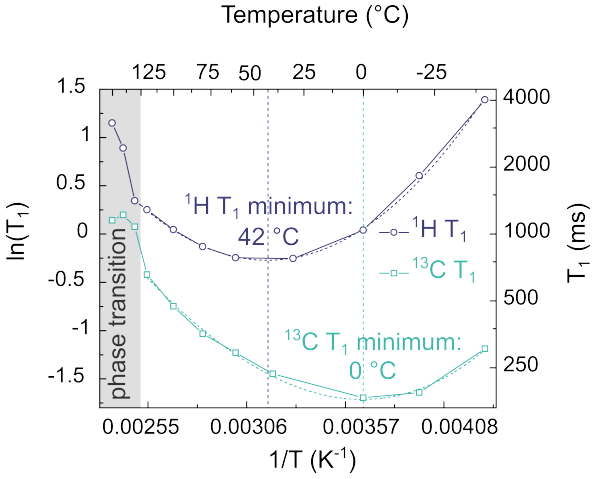


FIGURE 4.7: Temperature dependence of ^{1}H and ^{13}C NMR spin-lattice relaxation times, T_1 observed for $(TMIM)_3Bi_2I_9$. Dotted lines joining the points represent the quadratic fit used to fit the region at temperatures below the phase transition. The NMR measurements were conducted in collaboration with Dr. B.M. Gallant, and the analysis was performed by Dr. B.M. Gallant.

First, we measure the ^{1}H and ^{13}C spin-lattice relaxation time constant (T_1) as a function of temperature (Figure 4.7). T_1 relaxation in solids is driven by local fluctuations in magnetic field, typically induced in organic molecules by dynamic motion including methyl group rotations or whole molecule tumbling, or the presence of nearby quadrupolar nuclei such as ^{127}I. We find that the ^{1}H and ^{13}C T_1 minima occur at 42 °C and 0 °C, respectively; unusually low values for solids and most likely attributable to a strong ^{127}I-^{1}H/^{13}C scalar coupling effect[29]. Notably, however, the distribution of T_1 values surrounding these minima is described by a quadratic, unless structural changes cause new T_1 relaxation mechanisms to become active as temperature increases. Fitting of the T_1 curves shows that there are substantial

deviations in T_1 away from the expected quadratic distribution at temperatures above 125 °C, indicating a change in either the local environment or dynamic motion of the organic cation at this temperature, confirming that the $[TMIM]^+$ cations play an integral role in the structural phase change at this temperature.

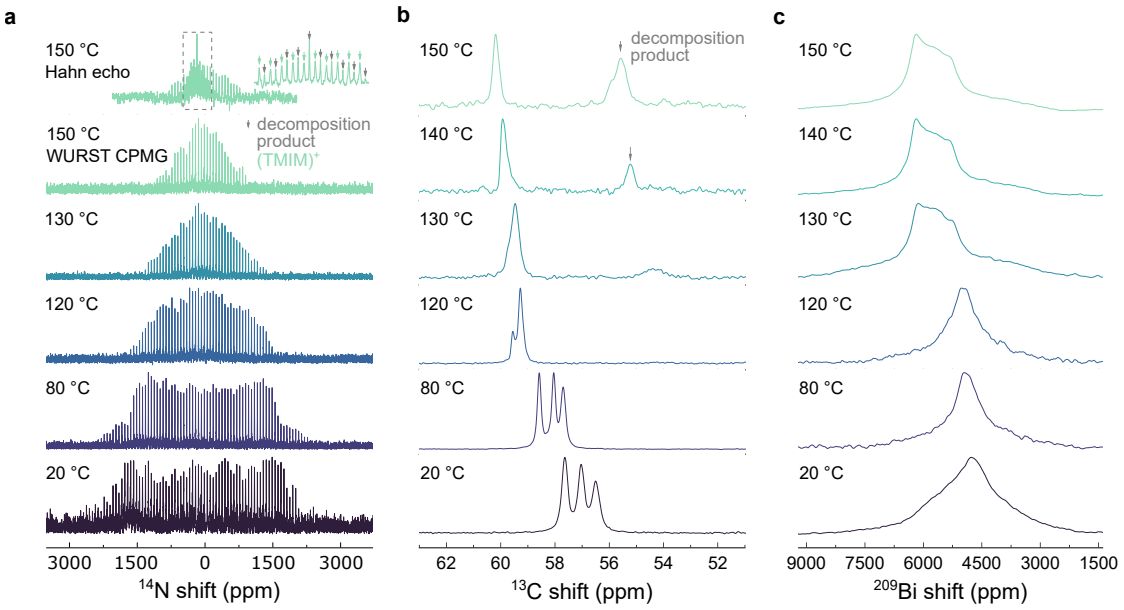


FIGURE 4.8: Variable-temperature **a** ^{14}N **b** ^{13}C and **c** ^{209}Bi solid state nuclear magnetic resonance (NMR) spectra. The NMR measurements were conducted in collaboration with Dr. B.M. Gallant, and the analysis was performed by Dr. B.M. Gallant and Dr. D.J. Kubicki.

To isolate the role of $[TMIM]^+$ reorientation from other motions we conduct static VT ^{14}N NMR at 20.0 T (**Fig. 4.8a**). The static nature of this measurement gives rise to the spikelets observed in the ^{14}N NMR spectra; separated in frequency by that corresponding to the echo train collected by the measurement. ^{14}N is a quadrupolar spin $I = 1$ nucleus and its lineshapes are highly sensitive to local symmetry and dynamics[30, 31]. In $[(CH_3)_3NCH_2I]^+$ the inequivalent substituents generate a substantial electric field gradient (EFG) across the ^{14}N nucleus, leading to a large quadrupole coupling constant (C_Q) which determines the line width of $[TMIM]^+$ in the absence of reorientation. However, as reported for $[CH_3NH_3]^+$ and $[(NH_2)_2CH]^+$ cations in photovoltaic halide perovskites, rapid whole molecule reorientation, with correlation times comparable to or shorter than $1/C_Q$ act to dynamically average the EFG[30, 31]. In the regime of fast EFG reorientation, the width of the spectral

envelope is dictated by the cation's local environment rather than its intrinsic symmetry, leading to a reduced C_Q and spectral narrowing. Since the EFG is located on the nitrogen, it can only change due to a whole-body reorientation of the organic cation. The broad (330 kHz) ^{14}N signal envelope remains unchanged between RT and 100 °C, and narrows significantly between 120 and 150 °C, coinciding with the phase transition temperature. The three-fold reduction in linewidth observed demonstrates that $[TMIM]^+$ becomes appreciably dynamic at the phase transition temperature, reorienting with correlation times comparable to the inverse of the static C_Q, estimated at 1-2 MHz, i.e. on the microsecond time scale. The onset of such motion is consistent with halogen bonds breaking at elevated temperatures, resulting in an order-disorder phase transition.

In order to resolve the individual temperature-dependent behaviour of the three structurally inequivalent $[TMIM]^+$ in $(TMIM)_3Bi_2I_9$, we conduct VT ^{1}H-^{13}C cross-polarization (CP) magic angle spinning (MAS). **Fig. 4.8b** shows the ^{13}C region corresponding to the iodomethyl group of $[TMIM]^+$. At room temperature, three distinct signals appear reflecting the presence of three inequivalent $[TMIM]^+$ cations in the unit cell. As temperature increases, all three signals shift to higher frequency. By 120 °C, two merge into a single narrow peak (full-width-half-maximum, FWHM = 35 Hz), and by 140 °C all three merge. This result indicates that the three $[TMIM]^+$ cations progressively become magnetically equivalent and indistinguishable with increasing temperature, owing to their tumbling.

To isolate the role of the inorganic sublattice of $(TMIM)_3Bi_2I_9$ in the phase transition, we perform static ^{209}Bi NMR (**Fig. 4.8c**). ^{209}Bi is a highly quadrupolar nucleus ($I = 9/2$), typically leading to large C_Q values and broad NMR signals[32]. While we do not observe clearly resolved quadrupolar lineshapes at any temperature, likely due to signal overlap from two structurally inequivalent Bi^{3+} and additional line broadening due to nearby quadrupolar ^{127}I nuclei[33], we see a substantial change in the ^{209}Bi spectrum on crossing the phase transition temperature. This result is consistent with the pronounced reorientation of the $[Bi_2I_9]^{3-}$ dimers at the phase transition observed via SCXRD and confirms a displacive component of the transformation. Since SCXRD shows that bond length and angle changes within the dimer above and below the phase transition are negligible, we attribute the decisive change in the ^{209}Bi lineshape to the release of halogen bonding interactions between

the organic and inorganic components, altering the local environment of the $[Bi_2I_9]^{3-}$ dimers.

Together, the VT SCXRD, ^{13}C NMR and ^{209}Bi NMR measurements show that a substantial rearrangement of both the inorganic dimers and organic cations, independently and relative to each other, takes place during the phase transition. ^{14}N NMR and VT SCXRD, supported by ^{13}C NMR and DSC analysis, confirms the simultaneous onset of rapid, microsecond timescale, organic cation tumbling within the structure at the phase transition. Importantly, these findings therefore confirm that symmetry breaking at the high temperature phase transition of $(TMIM)_3Bi_2I_9$ involves contributions from both order-disorder (organic cation tumbling) and displacive (structural rearrangement) components, both enabled by the release of C-I$\cdots$I$^-$ halogen bonds between the organic and inorganic components.

4.3.5 Piezoelectric response

Having established the origins of symmetry breaking between the two phases of $(TMIM)_3Bi_2I_9$, we measure the piezoelectric response at room temperature. Generally, piezoelectric response is comprised of intrinsic (lattice displacement) and extrinsic (movement of domain walls) contributions[34]. Although accurately distinguishing their relative contributions is experimentally challenging, the intrinsic piezoresponse can be quantified with *in situ* electric field SCXRD measurements.

To directly measure lattice parameter strain under applied electric field, we carry out *in situ* SCXRD measurements using a method developed by Saunders et al[35]. Here, DC-voltage is applied to a crystal while it is mounted on the diffractometer and held at constant temperature in a cryostream. SCXRD measurements are recorded at different applied electric field strengths, from positive to negative 4 kV/mm across the *c*-axis (as determined by crystal morphology simulation[36] (**Fig. 4.9b**)). The evolution of refined lattice parameters is shown in **Fig. 4.9c**. Over this range, the *a* and *b* lattice parameters linearly decrease by 0.01% and 0.007% respectively, whilst a larger linear increase of the *c* lattice parameter by 0.035% is observed, leading to an overall increase in unit cell volume. The absolute change in individual lattice parameters under applied field (0.001 Å at 1 kV/mm) is comparable to values previously reported for high performance piezoelectrics PZT and PMN-PT[37, 38].

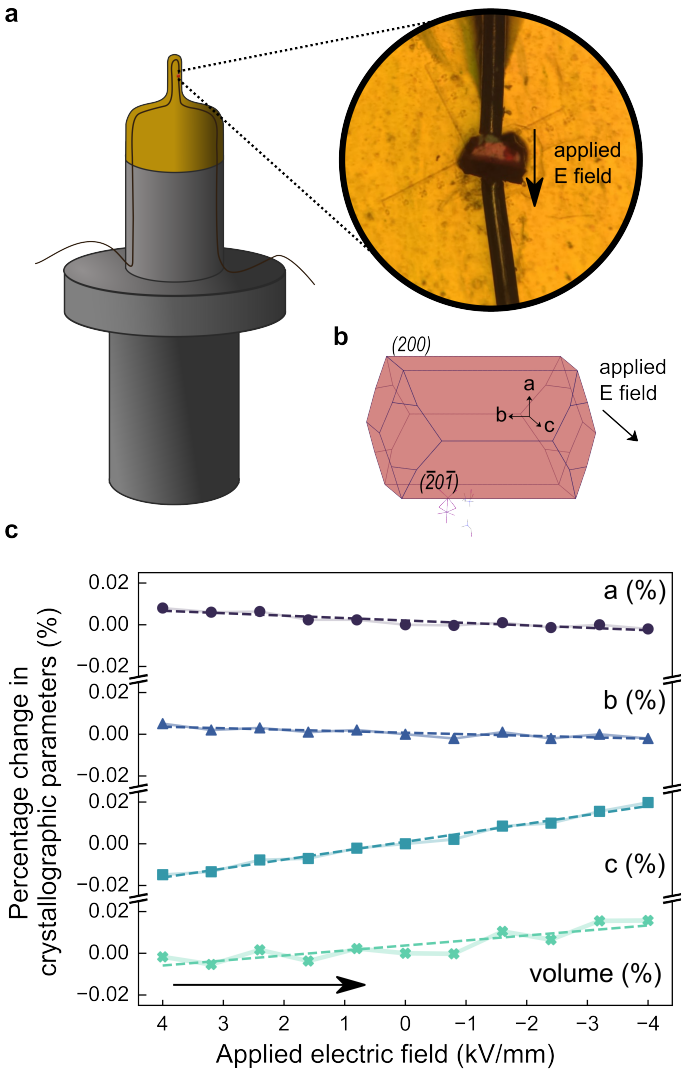


FIGURE 4.9: Intrinsic piezoresponse via *in situ* electric field measurements. **a** Left: Visualisation of crystal mounted on Kapton, connected to copper electrodes. Right: microscope image of crystal connected to electrodes. **b** Crystal growth morphology of $(TMIM)_3Bi_2I_9$, simulated using the Bravais Friedel Donnay Harker (BFDH) method in Mercury. **c** Percentage change of lattice parameters and unit cell volume with applied electric field, where field is swept from positive to negative. The error bands on each measurement are indicated by the shaded region about each point.

The electrical dependencies can be used to extract information about the intrinsic piezoelectric coefficients:

$$d_{kij} = \frac{\partial \epsilon_{ij}}{\partial E_k}$$

where ϵ_{ij} is the strain tensor relating to the change in the lattice parameters, and E_k are the components of the electric field.

Using the off-field lattice parameters a_0, b_0, c_0 = 29.9188, 9.8303, 14.1641 Å respectively and the linear regression coefficients for Figure 4.9c, the piezoelectric tensor coefficients d_{31}, d_{32} and d_{33} are calculated to be 11.7, 0.7 and -42.8 pC N^{-1} respectively. Single crystals frequently contain nanoscale domains that fall below the detection limits of SCXRD, yielding diffraction patterns that represent a coherent average across all domains. Therefore, the derived piezoelectric coefficients from lattice parameter variations reflect domain-averaged values, which are expected to be lower than those of individual domains.

For practical applications such as energy harvesters, sensors and actuators, piezoelectric materials processed into thin films are often preferred[39]. Therefore, we next develop $(TMIM)_3Bi_2I_9$ into a thin film to investigate its piezo- and ferroelectric properties.

TABLE 4.2: Pawley fit parameters for the XRD patterns of the mechanosynthesised powder, thin film on plain glass and thin film on FTO.

Sample	*a* (Å)	*b* (Å)	*c* (Å)
Mechanosynthesised powder	29.93090 (17)	9.83970 (6)	14.18660 (8)
Thin film on plain glass	29.896 (2)	9.829 (1)	14.200 (3)
Thin film on FTO	29.771 (8)	9.794 (3)	14.109 (6)

First, we deposit a thin film of $(TMIM)_3Bi_2I_9$ onto a fluorine-doped tin oxide (FTO) coated glass substrate using a dynamic spin-coating method, as detailed in Section 3. Photos of the thin film are shown in Figure 4.10a. XRD patterns of the mechanosynthesised powder, thin film on plain glass and thin film on FTO are shown in Figure 4.10b. The thin film XRD patterns are fitted using a Pawley fit, with the parameters given in Table 4.2. The rough agreement between the lattice

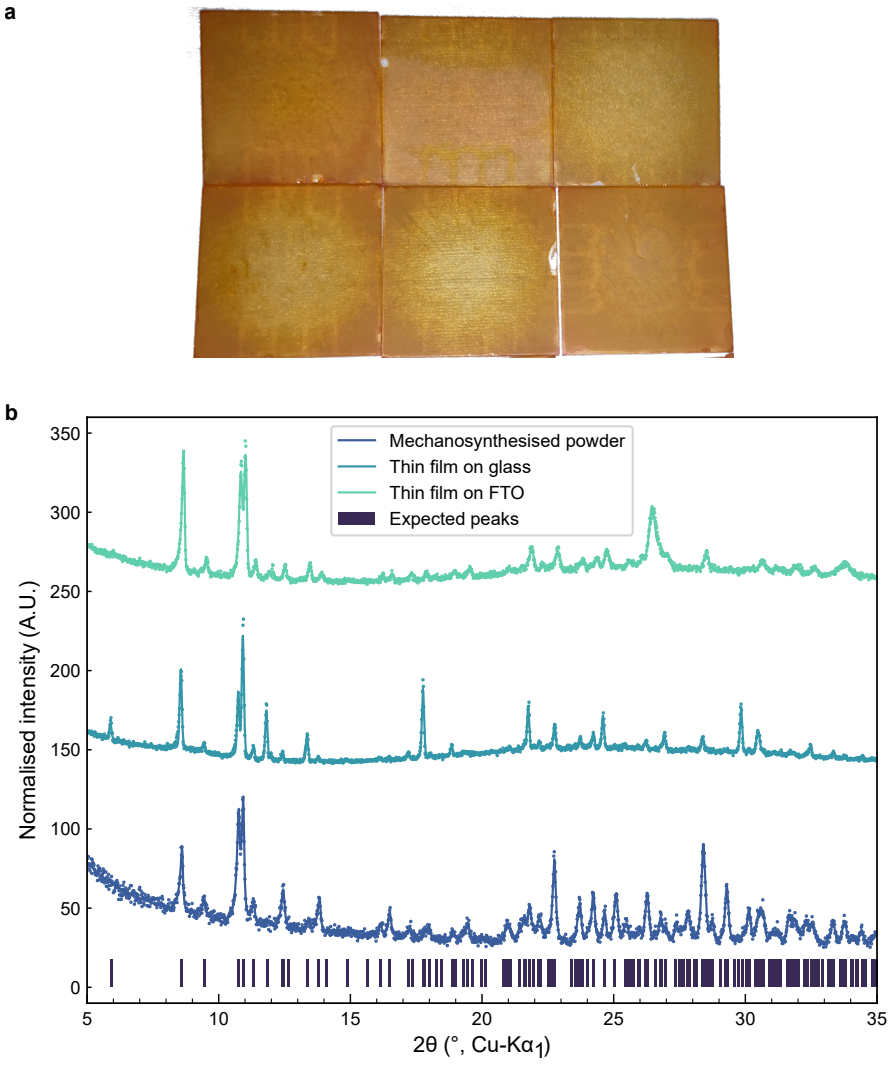


FIGURE 4.10: Thin films of $(TMIM)_3Bi_2I_9$. **a** Images of thin films on FTO-coated glass. **b** XRD patterns and simulated peak positions based on the single crystal data. XRD is fitted using a Pawley fit, with the fitted parameters shown in Table 4.2.

parameters across the three samples indicates their phase purity and agreement with the single crystal structure.

Following this, piezoresponse force microscopy (PFM) is used to investigate the piezoelectric properties of the thin film. **Fig. 4.11a-c** presents the topography, piezoelectric amplitude and phase response, where we identify the presence of piezoelectric domains with 180° phase difference, indicating oppositely oriented polarizations. We observe these domains spanning multiple crystal grains, confirming that the signal originates from the polarization state rather than topographical artefacts.

To investigate the polarization switching behaviour and piezoresponse, we measure the amplitude and phase response at different locations on the thin film whilst sweeping the cantilever tip DC voltage between -3 and 3 V, with a superimposed AC voltage. Representative phase-bias and amplitude-bias loops are shown in **Fig. 4.11d** and **e** respectively, and show clear 180° polarization switching. The individual measurement points are shown in **Fig. 4.12**. The effective piezoelectric coefficient ($d_{33,\text{eff}}$) can be determined using the gradient of the linear fit of the amplitude-bias loops. A boxplot of calculated values from different sample locations is shown in **Fig. 4.11f**, yielding a median d_{33} of 92.0 pm/V and a peak value of 161.5 pm/V. We note that measurements in regions with a higher calculated $d_{33,\text{eff}}$ exhibit more pronounced fluctuations around the linear fit (**Fig. 4.11e**). This is attributed to the stronger electromechanical responsivity of these regions, which amplifies the effects of local material inhomogeneities and instrumental noise. The distribution of the piezoelectric coefficients can be attributed to the multi-oriented and multi-domain nature of the thin film.

We further confirm the piezoelectric behaviour via the Berlincourt method on single crystals, which uses the direct piezoelectric effect[40]. As the crystals do not exhibit a natural face corresponding to a (00l) plane, piezoelectric measurements were measured over multiple orientations of the crystal. Therefore, the measured $d_{33,\text{eff}}$ in **Fig. 4.11g** correspond to a distribution over the natural crystal faces. This yielded an average $d_{33,\text{eff}}$ of 63 pC N^{-1}, with a peak value of 163.4 pC N^{-1}, in agreement with the peak value obtained from PFM (we note that pC N^{-1} is equivalent to the unit pm V^{-1}). The values obtained from the Berlincourt method and PFM are much greater than that obtained from the lattice strain measurements, which we attribute to the former more likely representing a combination of extrinsic and

intrinsic piezoelectric contributions. To the best of our knowledge, this value (161.5 pC N^{-1}) is the highest reported for any halobismuthate, representing a nearly four-fold enhancement as compared to published literature[41], as shown in Table 2.2 and **Fig. 4.11h**. Moreover, the piezoelectric performance of $(TMIM)_3Bi_2I_9$ is comparable to that of both $BaTiO_3$ (d_{33} = 191 pm V^{-1}[42]) and other higher-toxicity hybrid materials, whilst also demonstrating more advantageous phase transition characteristics (**Fig. 4.11i**), maintaining a polar, non-centrosymmetric structure up to its decomposition temperature.

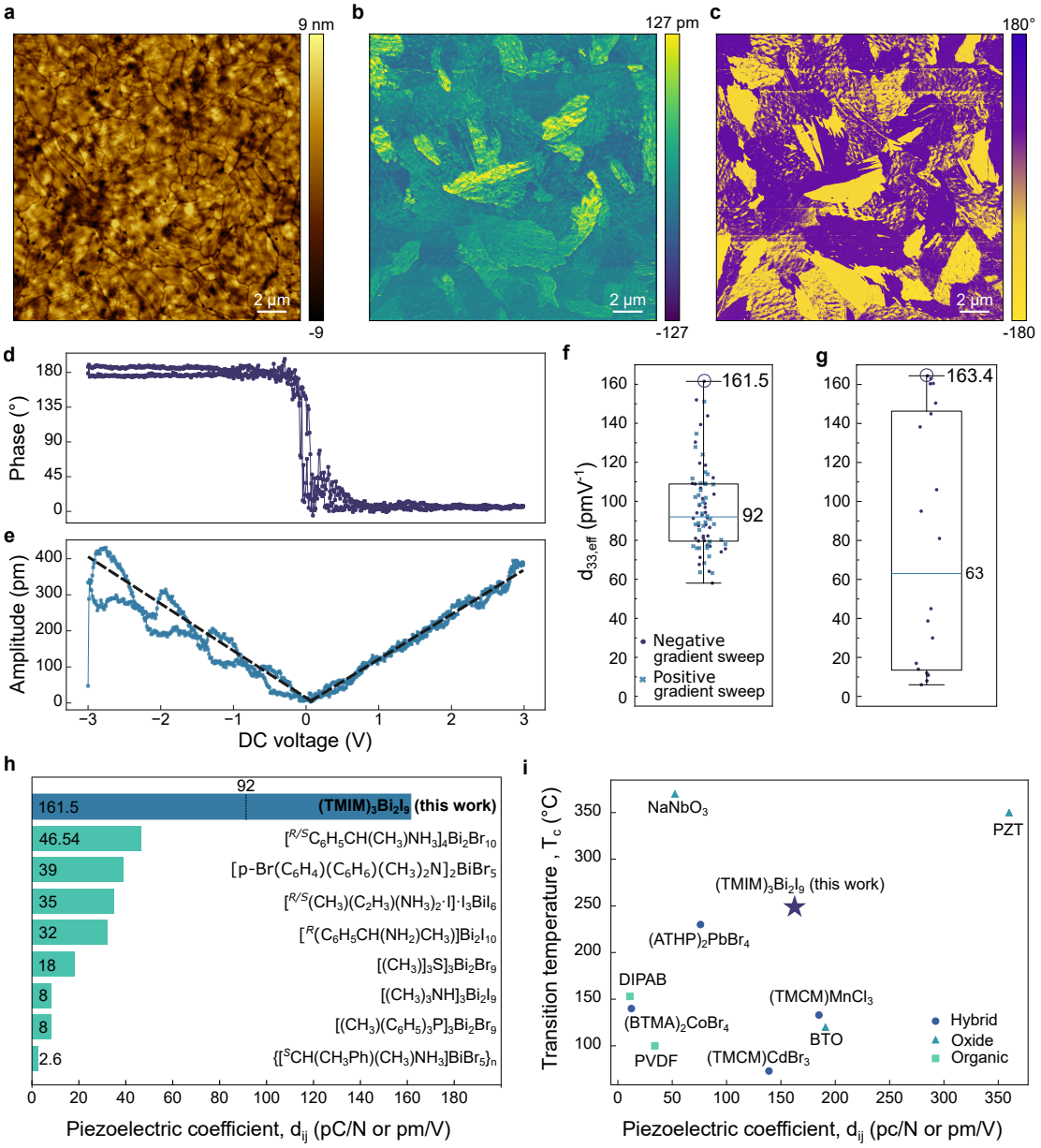


FIGURE 4.11: Highest piezoelectric response for a halobismuthate. Piezoresponse force microscopy: **a** Topography, **b** piezoelectric amplitude and **c** phase images. Switching spectroscopy PFM measurements: **d** Phase-voltage (top) and **e** Amplitude-voltage (bottom) loops, where the dashed line indicates the linear fit used to calculate the piezoelectric coefficient. Box plots showing $d_{33,\text{eff}}$ values calculated from **f** amplitude-voltage loops from PFM, and **g** single crystals respectively where the whiskers show the entire range of data. Champion values for each measurement are circled. For the piezoelectric coefficients calculated from PFM, the absolute values obtained from the negative and positive gradient are indicated. **h** Comparison of piezoelectric coefficients d_{ij} with previously reported piezoelectric halobismuthates, where the median value from PFM measurements is indicated for $(TMIM)_3Bi_2I_9$[4, 41–50]. **i** Comparison of phase transition temperature and piezoelectric coefficients with previously reported piezoelectric materials, where the decomposition temperature is used when no piezo-to-non-piezoelectric transition temperature is reported. Full data shown in Table 2.2. The PFM measurements were conducted in collaboration with Dr. R. Harniman and Dr. K. Kaja and analysed by E.Y.H. Hung.

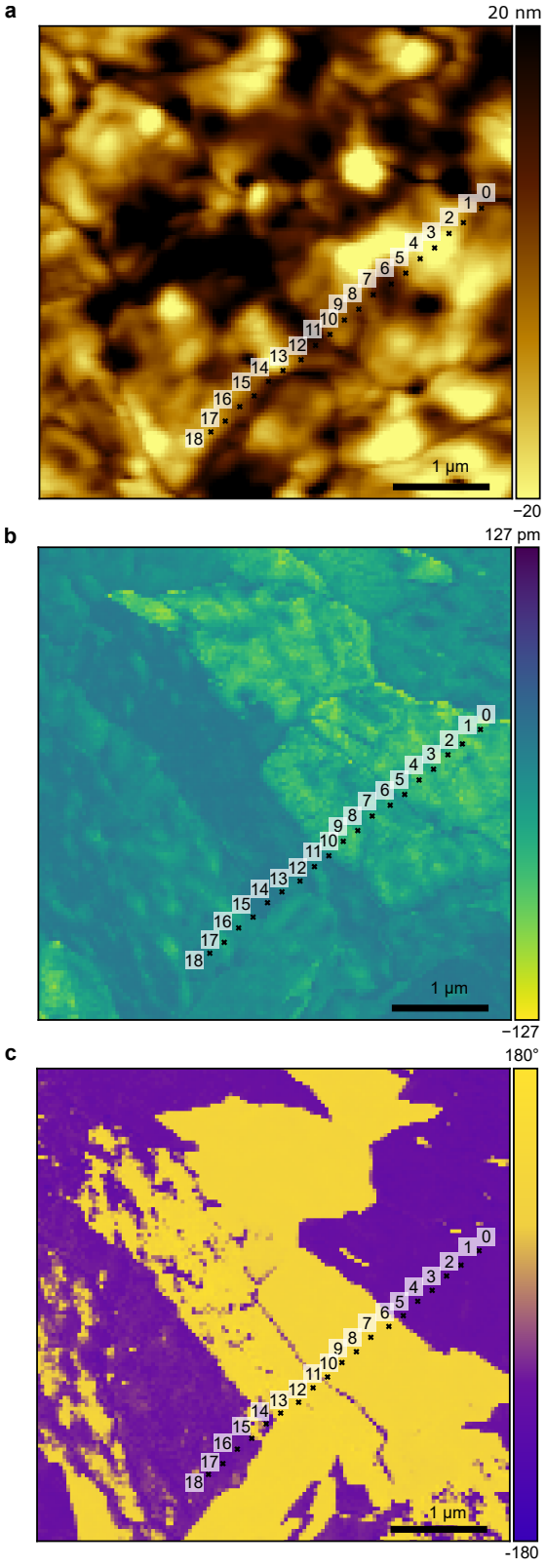


FIGURE 4.12: The corresponding points used for phase-voltage and amplitude-voltage loop measurements: **a** Topography, **b** PFM amplitude and **c** PFM Phase

4.4 Summary

Our work shows that strategic design of organic-inorganic intermolecular interactions can yield high-performance hybrid piezoelectric materials. In the case of $[(CH_3)_3CH_2NI]_3Bi_2I_9$, the introduction of halogen bonding induces not only asymmetric positioning of the molecular components, but also structural distortion within the inorganic framework, ultimately resulting in a low-symmetry structure optimised for enhanced non-centrosymmetry and polarization. As a result, $[(CH_3)_3CH_2NI]_3Bi_2I_9$ demonstrates a piezoresponse close to that of $BaTiO_3$, the highest reported for a halobismuthate (**Fig. 4.11h-i**). Moreover, we demonstrate that the breaking of the halogen bonding also dictates the $(TMIM)_3Bi_2I_9$ exhibits a polar-to-polar phase transition with simultaneous order-disorder and displacive symmetry breaking at a high critical temperature (138 °C). These findings provide strong experimental and theoretical evidence for the tunability of structural distortion and symmetry via careful manipulation of intermolecular interactions, thus validating and expanding on previous theories proposed for inducing symmetry-breaking in hybrid metal halides. This work establishes both a guiding design framework and a promising material system for developing low-toxicity, high-performing piezoelectrics, enabling the next generation of sustainable, self-powered technologies.

Bibliography

[1] Y. Saito, H. Takao, T. Tani, T. Nonoyama, K. Takatori, T. Homma, T. Nagaya, and M. Nakamura, "Lead-free piezoceramics," *Nature*, vol. 432, no. 7013, pp. 84–87, 2004.

[2] B. Carreño-Jiménez, A. Reyes-Montero, and R. López-Juárez, "Complete set of ferro/piezoelectric properties of $BaZrO_3$ and $(Ba,Ca)ZrO_3$ doped KNLNS-based electroceramics," *Ceramics International*, vol. 48, pp. 21090–21100, 2022.

[3] H. Park, C. Ha, and J. H. Lee, "Advances in piezoelectric halide perovskites for energy harvesting applications," *Journal of Materials Chemistry A*, vol. 8, pp. 24353–24367, 2020.

[4] Y. M. You, W. Q. Liao, D. Zhao, H. Y. Ye, Y. Zhang, Q. Zhou, X. Niu, J. Wang, P. F. Li, D. W. Fu, Z. Wang, S. Gao, K. Yang, J. M. Liu, J. Li, Y. Yan, and R. G. Xiong, "An organic-inorganic perovskite ferroelectric with large piezoelectric response," *Science*, vol. 357, 2017.

[5] W.-Q. Liao, D. Zhao, Y.-M. Yu, I. Grinberg, A. M. Rappe, K. A. Nelson, J. Li, Y. Ren, P. Wu, K. Yang, J.-L. Liu, P.-F. Li, D.-W. Fu, S. Gao, Z. Wang, and R.-G. Xiong, "A lead-halide perovskite molecular ferroelectric semiconductor," *Nature Communications*, vol. 10, no. 1, pp. 1–8, 2019.

[6] R. L. Hoye, R. E. Brandt, A. Osherov, V. Stevanović, S. D. Stranks, M. W. Wilson, H. Kim, A. J. Akey, J. D. Perkins, R. C. Kurchin, *et al.*, "Methylammonium bismuth iodide as a lead-free, stable hybrid organic–inorganic solar absorber," *Chemistry–A European Journal*, vol. 22, no. 8, pp. 2605–2610, 2016.

[7] P. Szklarz, A. Gagor, R. Jakubas, P. Zielinski, A. Piecha-Bisiorek, J. Cichos, M. Karbowiak, G. Bator, and A. Cizman, "Lead-free hybrid ferroelectric material based on formamidine: $[NH_2\ CHNH_2]_3\ Bi_2\ I_9$," *Journal of Materials Chemistry C*, vol. 7, no. 10, pp. 3003–3014, 2019.

[8] P. Szklarz, R. Jakubas, W. Medycki, A. Gągor, J. Cichos, M. Karbowiak, and G. Bator, "$(C_3N_2H_5)_3Sb_2I_9$ and $(C_3N_2H_5)_3Bi_2I_9$: ferroelastic lead-free hybrid perovskite-like materials as potential semiconducting absorbers," *Dalton Transactions*, vol. 51, pp. 1850–1860, 2022.

[9] Q. Wang, Y. W. Zhang, W. Y. Zhang, P. P. Shi, Q. Ye, and D. W. Fu, "A high-temperature multiaxial precision time-delayed dielectric switch crystal triggered by linear/propeller/ball three-form motion," *Journal of Materials Chemistry C*, vol. 7, pp. 2994–3002, 2019.

[10] Z. X. Zhang, C. Y. Su, J. Li, X. J. Song, D. W. Fu, and Y. Zhang, "Ferroelastic hybrid bismuth bromides with dual dielectric switches," *Chemistry of Materials*, vol. 33, pp. 5790–5799, 2021.

[11] C. Feldmann, "Crystal structure of tris(tetramethylammonium) dibismuth nonaiodide, $[N(CH_3)_4]_3Bi_2I_9$," *Zeitschrift fur Kristallographie - New Crystal Structures*, vol. 216, pp. 487–488, 2001.

[12] T. Clark, M. Hennemann, J. S. Murray, and P. Politzer, "Halogen bonding: the sigma-hole. Proceedings of "Modeling interactions in biomolecules II", Prague, September 5th-9th, 2005," *Journal of molecular modeling*, vol. 13, pp. 291–296, 2007.

[13] G. R. Desiraju, P. S. Ho, L. Kloo, A. C. Legon, R. Marquardt, P. Metrangolo, P. Politzer, G. Resnati, and K. Rissanen, "Definition of the halogen bond (IUPAC recommendations 2013)," *Pure and Applied Chemistry*, vol. 85, pp. 1711–1713, 2013.

[14] G. Cavallo, P. Metrangolo, R. Milani, T. Pilati, A. Priimagi, G. Resnati, and G. Terraneo, "The halogen bond," *Chemical Reviews*, vol. 116, pp. 2478–2601, 2016.

[15] N. A. Spaldin, "A beginner's guide to the modern theory of polarization," *Journal of Solid State Chemistry*, vol. 195, pp. 2–10, 2012.

[16] P. Umari and A. Pasquarello, "Ab initio molecular dynamics in a finite homogeneous electric field," *Physical Review Letters*, vol. 89, p. 157602, 2002.

[17] I. Souza, J. Íñiguez, and D. Vanderbilt, "First-principles approach to insulators in finite electric fields," *Physical Review Letters*, vol. 89, p. 117602, 2002.

[18] P. Hohenberg and W. Kohn, "Inhomogeneous electron gas," *Physical Review*, vol. 136, p. B864, 1964.

[19] W. Kohn and L. J. Sham, "Self-consistent equations including exchange and correlation effects," *Physical Review*, vol. 140, p. A1133, 1965.

[20] J. P. Perdew, K. Burke, and M. Ernzerhof, "Generalized gradient approximation made simple," *Physical Review Letters*, vol. 77, p. 3865, 1996.

[21] W. Q. Liao, Y. Y. Tang, P. F. Li, Y. M. You, and R. G. Xiong, "Large piezoelectric effect in a lead-free molecular ferroelectric thin film," *Journal of the American Chemical Society*, vol. 139, pp. 18071–18077, 2017.

[22] Z. Wu, S. Li, Y. M. Yousry, W. P. Wong, X. Wang, T. Ma, Z. Chen, Y. Shao, W. H. Liew, K. Yao, F. Pan, and K. P. Loh, "Intercalation-driven ferroelectric-to-ferroelastic conversion in a layered hybrid perovskite crystal," *Nature Communications 2022 13:1*, vol. 13, pp. 1–8, 2022.

[23] C. Jiang, N. Zhong, C. Luo, H. Lin, Y. Zhang, H. Peng, and C. G. Duan, "(Diisopropylammonium)$_2$MnBr$_4$: a multifunctional ferroelectric with efficient green-emission and excellent gas sensing properties," *Chemical Communications*, vol. 53, pp. 5954–5957, 2017.

[24] N. Onoda-Yamamuro, O. Yamamuro, T. Matsuo, and H. Suga, "p-T phase relations of $CH_3NH_3PbX_3$ (X = Cl, Br, I) crystals," *Journal of Physics and Chemistry of Solids*, vol. 53, pp. 277–281, 1992.

[25] W. Wei, W. Li, K. T. Butler, G. Feng, C. J. Howard, M. A. Carpenter, P. Lu, A. Walsh, and A. K. Cheetham, "An unusual phase transition driven by vibrational entropy changes in a hybrid organic-inorganic perovskite," *Angewandte Chemie International Edition*, vol. 57, pp. 8932–8936, 2018.

[26] P. F. Li, W. Q. Liao, Y. Y. Tang, W. Qiao, D. Zhao, Y. Ai, Y. F. Yao, and R. G. Xiong, "Organic enantiomeric high-T_c ferroelectrics," *Proceedings of the National Academy of Sciences of the United States of America*, vol. 116, pp. 5878–5885, 2019.

[27] Z. H. Wei, Z. T. Jiang, X. X. Zhang, M. L. Li, Y. Y. Tang, X. G. Chen, H. Cai, and R. G. Xiong, "Rational design of ceramic-like molecular ferroelectric by quasi-spherical theory," *Journal of the American Chemical Society*, vol. 142, pp. 1995–2000, 2020.

[28] G. Winter, D. G. Waterman, J. M. Parkhurst, A. S. Brewster, R. J. Gildea, M. Gerstel, L. Fuentes-Montero, M. Vollmar, T. Michels-Clark, I. D. Young, N. K. Sauter, and G. Evans, "DIALS: implementation and evaluation of a new integration package," *research papers Acta Cryst*, vol. 74, pp. 85–97, 2018.

[29] D. J. Kubicki, D. Prochowicz, E. Salager, A. Rakhmatullin, C. P. Grey, L. Emsley, and S. D. Stranks, "Local structure and dynamics in methylammonium, formamidinium, and cesium tin(II) mixed-halide perovskites from 119Sn solid-state NMR," *Journal of the American Chemical Society*, vol. 142, pp. 7813–7826, 2020.

[30] D. J. Kubicki, S. D. Stranks, C. P. Grey, and L. Emsley, "NMR spectroscopy probes microstructure, dynamics and doping of metal halide perovskites," *Nature Reviews Chemistry 2021 5:9*, vol. 5, pp. 624–645, 2021.

[31] D. J. Kubicki, D. Prochowicz, A. Hofstetter, P. Péchy, S. M. Zakeeruddin, M. G. atzel, and L. Emsley, "Cation dynamics in mixed-cation $(MA)_x(FA)_1$-$x$$PbI_3$ hybrid perovskites from solid-state NMR," *Journal of the American Chemical Society*, vol. 139, pp. 10055–10061, 2017.

[32] H. Hamaed, M. W. Laschuk, V. V. Terskikh, and R. W. Schurko, "Application of solid-state 209Bi NMR to the structural characterization of bismuth-containing materials," *Journal of the American Chemical Society*, vol. 131, pp. 8271–8279, 2009.

[33] L. Piveteau, V. Morad, and M. V. Kovalenko, "Solid-state NMR and NQR spectroscopy of lead-halide perovskite materials," *Journal of the American Chemical Society*, vol. 142, pp. 19413–19437, 2020.

[34] N. Zhang, S. Gorfman, H. Choe, T. Vergentev, V. Dyadkin, H. Yokota, D. Chernyshov, B. Wang, A. M. Glazer, W. Ren, and Z. G. Ye, "Probing the intrinsic and extrinsic origins of piezoelectricity in lead zirconate titanate single crystals," *Journal of Applied Crystallography*, vol. 51, pp. 1396–1403, 2018.

[35] L. K. Saunders, H. H.-M. Yeung, M. R. Warren, P. Smith, S. Gurney, S. F. Dodsworth, I. J. Vitorica-Yrezabal, A. Wilcox, P. V. Hathaway, G. Preece, P. Roberts, S. A. Barnett, and D. R. Allan, "An electric field cell for performing in situ single-crystal synchrotron X-ray diffraction," *Journal of Applied Crystallography*, vol. 54, pp. 1349–1359, 2021.

[36] C. F. MacRae, I. Sovago, S. J. Cottrell, P. T. Galek, P. McCabe, E. Pidcock, M. Platings, G. P. Shields, J. S. Stevens, M. Towler, and P. A. Wood, "Mercury 4.0: from visualization to analysis, design and prediction," *Journal of Applied Crystallography*, vol. 53, pp. 226–235, 2020.

[37] T. Vergentev, I. Bronwald, D. Chernyshov, S. Gorfman, S. H. Ryding, P. Thompson, and R. J. Cernik, "A rapid two-dimensional data collection system for the study of ferroelectric materials under external applied electric fields," *Journal of Applied Crystallography*, vol. 49, pp. 1501–1507, 2016.

[38] G. Tan, K. Maruyama, Y. Kanamitsu, S. Nishioka, T. Ozaki, T. Umegaki, H. Hida, and I. Kanno, "Crystallographic contributions to piezoelectric properties in PZT thin films," *Scientific Reports 2019 9:1*, vol. 9, pp. 1–6, 2019.

[39] Z. Song, R. Hou, and F. Jiang, "Recent progress in piezoelectric thin films as self-powered devices: material and application," *Frontiers in Materials*, vol. 11, p. 1373040, 2024.

[40] M. G. Cain, "Characterisation of ferroelectric bulk materials and thin films," *Springer*, vol. 2, 2014.

[41] Z. Zhang, Y. Zhang, Y. Zhao, M. Zhao, R. Zhang, J. Guo, F. An, and X. Sun, "Origin of high piezoelectricity of a bismuth-based organic-inorganic hybrid crystal," *Journal of Materials Chemistry C*, vol. 11, pp. 1401–1408, 2023.

[42] J. Gao, D. Xue, W. Liu, C. Zhou, and X. Ren, "Recent progress on $BaTiO_3$-based piezoelectric ceramics for actuator applications," *Actuators 2017, Vol. 6, Page 24*, vol. 6, p. 24, 2017.

[43] N. Meena, S. Sahoo, N. Deka, J. K. Zaręba, and R. Boomishankar, "Ferroelectric organic-inorganic hybrid ammonium halogenobismuthate(III) for piezoelectric energy harvesting," *Inorganic Chemistry*, vol. 63, pp. 9245–9251, 2024.

[44] C. F. Wang, N. Wang, L. Liu, L. P. Miao, H. Y. Ye, Y. Zhang, and C. Shi, "Enantiomeric hybrid high-temperature multiaxial ferroelectrics with a narrow bandgap and high piezoelectricity," *Chinese Chemical Letters*, vol. 34, p. 108051, 2023.

[45] K. Tao, B. Zhang, Q. Li, Q. Yan, K. Tao, B. Zhang, Q. Li, and Q. Yan, "Centimeter-sized piezoelectric single crystal of chiral bismuth-based hybrid halide with superior electrostrictive coefficient," *Small*, vol. 19, p. 2207663, 2023.

[46] Y. Z. Zhang, D. S. Sun, J. X. Gao, X. N. Hua, X. G. Chen, G. Q. Mei, and W. Q. Liao, "A semiconducting organic-inorganic hybrid perovskite-type non-ferroelectric piezoelectric with excellent piezoelectricity," *Chemistry - An Asian Journal*, vol. 14, pp. 1028–1033, 2019.

[47] J. Zhang, S. Han, C. Ji, W. Zhang, Y. Wang, K. Tao, Z. Sun, and J. Luo, "$[(CH_3)_3NH]_3Bi_2I_9$: A polar lead-free hybrid perovskite-like material as a potential semiconducting absorber," *Chemistry - A European Journal*, vol. 23, pp. 17304–17310, 2017.

[48] S. Deswal, R. Panday, D. R. Naphade, P. Dixit, B. Praveenkumar, J. K. Zaręba, T. D. Anthopoulos, S. Ogale, R. Boomishankar, S. Deswal, R. Panday, R. Boomishankar, D. R. Naphade, T. D. Anthopoulos, J. K. Zaręba, and S. Ogale, "Efficient piezoelectric energy harvesting from a discrete hybrid bismuth bromide ferroelectric templated by phosphonium cation," *Chemistry - A European Journal*, vol. 28, p. e202200751, 2022.

[49] S. Sahoo, N. Deka, and R. Boomishankar, "Piezoelectric energy harvesting of a bismuth halide perovskite stabilised by chiral ammonium cations," *CrystEngComm*, vol. 24, pp. 6172–6177, 2022.

[50] Y. J. Gong, L. C. An, Y. Zhang, C. Zhao, Z. G. Li, T. M. Guo, M. He, J. Yu, W. Li, and X. H. Bu, "Utilizing shear piezoelectricity of chiral lead-free metal halides for electromechanical sensing," *Advanced Functional Materials*, vol. 34, p. 2402649, 2024.

gensymb

Chapter 5

Tuning polar order in $(TMXM)_3M_2X_9$ materials via structural modifications

5.1 Introduction

Organic-inorganic hybrid halide perovskites have garnered significant research interest due to their remarkable power conversion efficiency in photovoltaic devices and their promising potential in optoelectronic applications. These materials uniquely integrate the design versatility of organic compounds with the high charge carrier mobility and stability of inorganic materials, making them highly attractive for next-generation energy and electronic technologies.

Following up from work detailed in Chapter 4, we explore the properties and implications of structural modifications to the 'parent' $(TMIM)_3Bi_2I_9$ and broaden the studies to the wider $(TMXM)_3M_2X_9$ family (X = Cl, Br; M = Sb). Given the implications of organic-inorganic interactions and their impact on crystal symmetry, as learned in Chapter 4, understanding the fuller implications of halogen and halide substitution may lead to a more complete understanding of induction of polar order in this family of materials.

The relationship between structural modifications and symmetry changes in hybrid organic-inorganic materials has been studied in several material families. For instance, in the $[(CH_3)_3NCH_2X]PbI_3$ family (X=H,F,Cl,Br,I)[1], an increase in phase transition or 'Curie' temperature was observed from the lighter to heavier halogen atoms, concurrent with the induction of room-temperature non-centrosymmetry in the crystal structure. Specifically, the structure changes from hexagonal space groups $P6_3/m$ or $P6_3/mmc$ for X= H,F,Cl,Br to monoclinic C_2 for X=I.

In contrast, the $[(CH_3)_3NCH_2X]ZnCl_3$ family exhibits different behaviour[2]. Here, halogen substitution induces a non-centrosymmetric structure for all X = H, F, Cl, Br, I, with minimal effect on phase transition temperatures. The key structural difference lies in the inorganic frameworks: while $[(CH_3)_3NCH_2X]PbI_3$ features 1D octahedral $[PbI_6]^{4-}$ chains, $[(CH_3)_3NCH_2X]ZnCl_3$ contains lower-symmetry 1D tetrahedral $[ZnCl_3]^-$ chains.

Further evidence of the importance of inorganic framework dimensionality comes from the $[(CH_3)_3NCH_2X]FeBr_4$ family[3], where every structure is polar with lowering symmetry for X=H, F, Cl, Br, I. In this case, the inorganic framework consists of discrete or '0D' $[FeBr_4]^-$ tetrahedrons, suggesting that the dimensionality of the inorganic framework plays a crucial role in determining the material's symmetry properties.

Building upon these insights, this chapter investigates the combined effects of structural modifications in both the organic cation and inorganic framework. We specifically examine:

- The replacement of iodine ions with smaller chlorine and bromine atoms
- The full metal substitution of Bi^{3+} with electronically equivalent Sb^{3+}

Through these modifications, we synthesise and characterise three compounds: $(TMCM)_3Bi_2Cl_9$, $(TMBM)_3Bi_2Br_9$, and $(TMIM)_3Sb_2I_9$. These materials are prepared both as single crystals grown from solution (Section 3.1) and as mechanosynthesised powders (Figure 5.1).

To understand the structural modifications and phase transitions in these materials, we employ a comprehensive suite of characterisation techniques, including Differential Scanning Calorimetry (DSC), Variable Temperature Solid-State Nuclear Magnetic Resonance (VT ssNMR), Variable Temperature Single-Crystal X-Ray Diffraction (VT SCXRD), and Second Harmonic Generation (SHG) measurements.

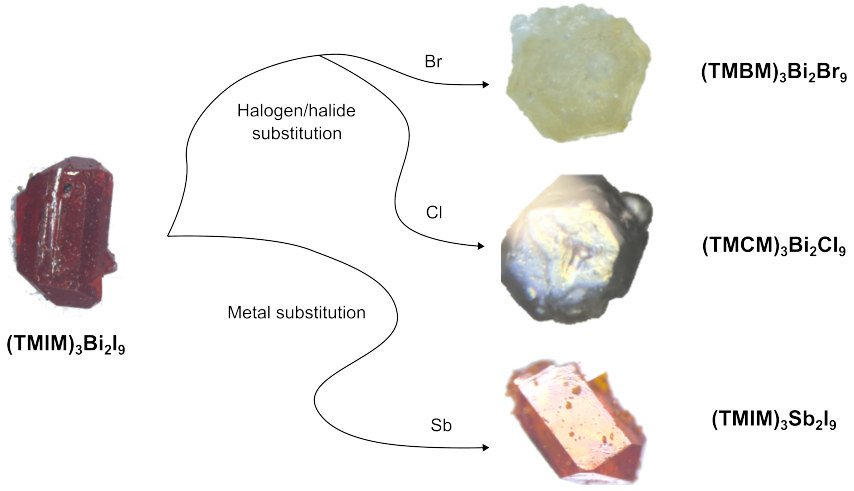


FIGURE 5.1: Microscope images of single crystals of $(TMBM)_3Bi_2Br_9$, $(TMCM)_3Bi_2Cl_9$ and $(TMIM)_3Sb_2I_9$ obtained as structural modifications to $(TMIM)_3Bi_2I_9$.

5.2 Results and Discussion

5.2.1 Thermal analysis

TABLE 5.1: Thermodynamic parameters. The phase transition temperatures given are the average between the heating and cooling loop for each pair of endo- and exo-therms. R is the molar gas constant.

Material	Temp (°C)	ΔH (kJ mol^{-1})	ΔS (J $mol^{-1}K^{-1}$)	N (ΔS = RlnN)
$(TMBM)_3Bi_2Br_9$ (i)	12.0	3.78247	13.27371	4.94
$(TMBM)_3Bi_2Br_9$ (ii)	36.2	2.01344	6.51088	2.19
$(TMCM)_3Bi_2Cl_9$	-1.85	5.62375	20.74038	12.13
$(TMIM)_3Sb_2I_9$	126.5	5.10416	12.77484	4.65

First, we study the thermal phase transition behaviour of each compound via differential scanning calorimetry (DSC) measurements (Figure 5.2a) on microcrystalline

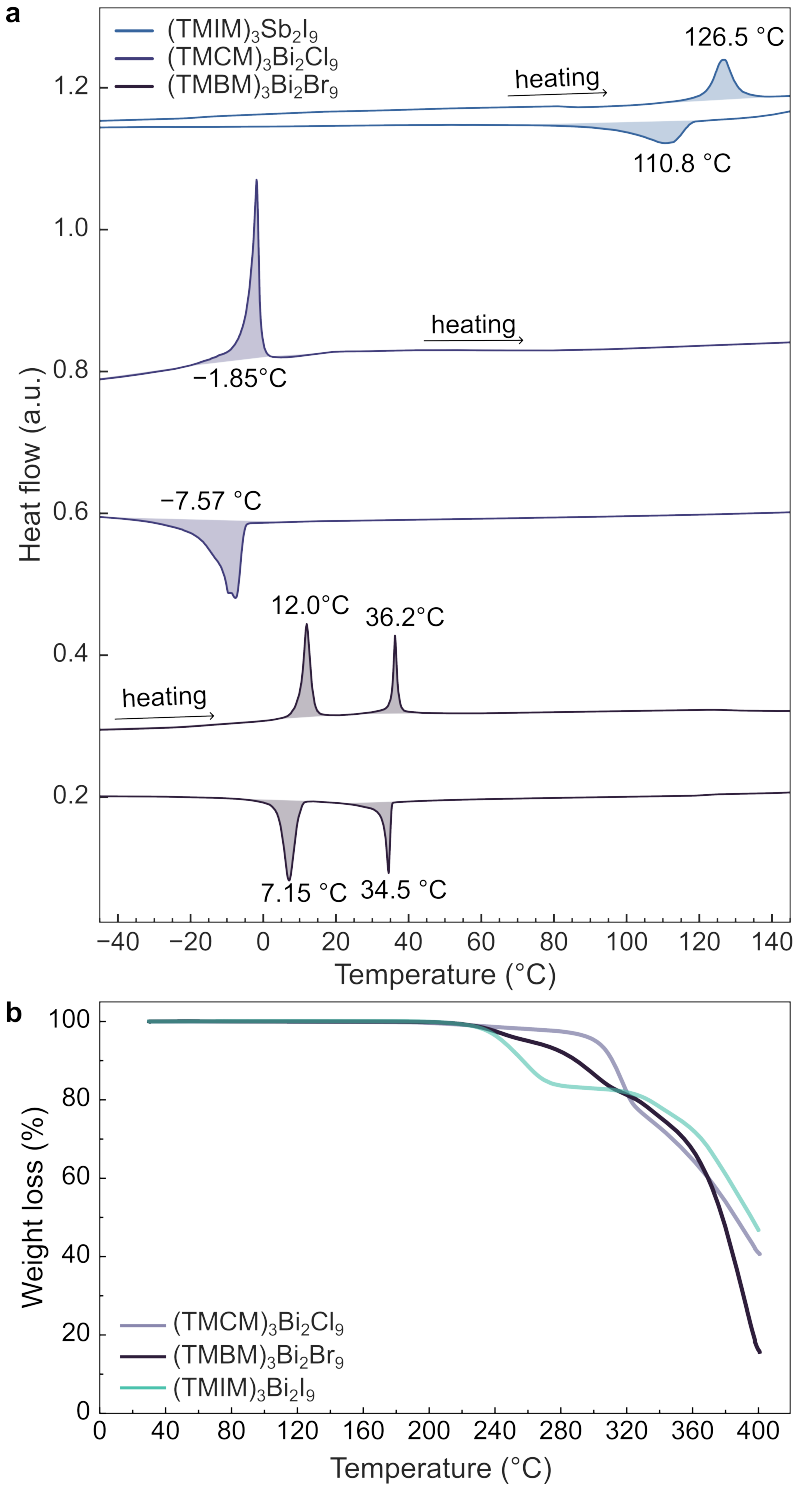


FIGURE 5.2: Thermal analysis of microcrystalline, mechanosynthesised powders of $(TMBM)_3Bi_2Br_9$, $(TMCM)_3Bi_2Cl_9$, and $(TMIM)_3Sb_2I_9$: **a** Differential scanning calorimetry (DSC), where the peak areas used to calculate the molar enthalpy (ΔH) and entropy (ΔS) change are marked. **b** Thermogravimetric analysis (TGA) measurements, where the data for $(TMIM)_3Bi_2I_9$ is plotted for comparison. TGA data was not taken for $(TMIM)_3Sb_2I_9$. DSC measurements were conducted by N. Hawkins and analysed by E.Y.H. Hung. TGA measurements were conducted by B.M. Gallant.

powders, where their fitted thermodynamic parameters are shown in Table 5.1. All three compounds exhibit endothermic events upon heating, which are reversible with exotherms upon cooling.

First, we observe that $(TMBM)_3Bi_2Br_9$ has two phase transitions at 12 °C and 36.2 °C, while $(TMCM)_3Bi_2Cl_9$ has only one phase transition, at -1.85 °C, all with relatively small thermal hysteresis ($\sim$ 5 °C). We note that these phase transitions occur at much lower temperatures than the pure-iodo and iodide counterpart $(TMIM)_3Bi_2I_9$ (Figure 5.2a), and that of $(TMIM)_3Sb_2I_9$. $(TMIM)_3Sb_2I_9$ exhibits greater thermal hysteresis ($\sim$ 16 °C), suggesting the existence of additional structural relaxation processes upon cooling compared with $(TMBM)_3Bi_2Br_9$ and $(TMCM)_3Bi_2Cl_9$. For example, large thermal hysteresis in organic-inorganic metal halides has previously been tentatively attributed to the displacement of isolated metal halide polyhedra[4, 5].

The lack of existence of phase transitions at higher (> 100 °C) temperatures for both $(TMBM)_3Bi_2Br_9$ and $(TMCM)_3Bi_2Cl_9$ indicates that at close to room temperature, these compounds adopt their highest-symmetry configuration. On the other hand, $(TMIM)_3Sb_2I_9$ exhibits phase transition characteristics with great similarity to its pure-Bi counterpart; albeit with a lower phase transition temperature at 126.5 °C compared to 138 °C.

The values of the change in enthalpy (ΔH), the change in entropy (ΔS) and orientation number (N) for the phase transitions of all three compounds of ($\Delta H \sim 5$ kJ mol^{-1}, $\Delta S \sim 15$ J mol^{-1} K^{-1} and $N \sim 5$) are comparable to that reported for order-disorder-type ferroelectrics[6], except for phase transition (ii) of $(TMBM)_3Bi_2Br_9$ with much smaller values.

Thermogravimetric analysis (TGA) (Figure 5.2b) shows that for the $(TMXM)_3Bi_2X_9$ series, the onset of decomposition increases from X = I ($\sim$250 °C), to X=Br ($\sim$ 270 °C) to X = Cl ($\sim$ 320 °C).

5.2.2 Single crystal structural analysis

In order to understand the structural nature of these phase transitions, we perform single-crystal X-ray diffraction measurements on $(TMBM)_3Bi_2Br_9$,

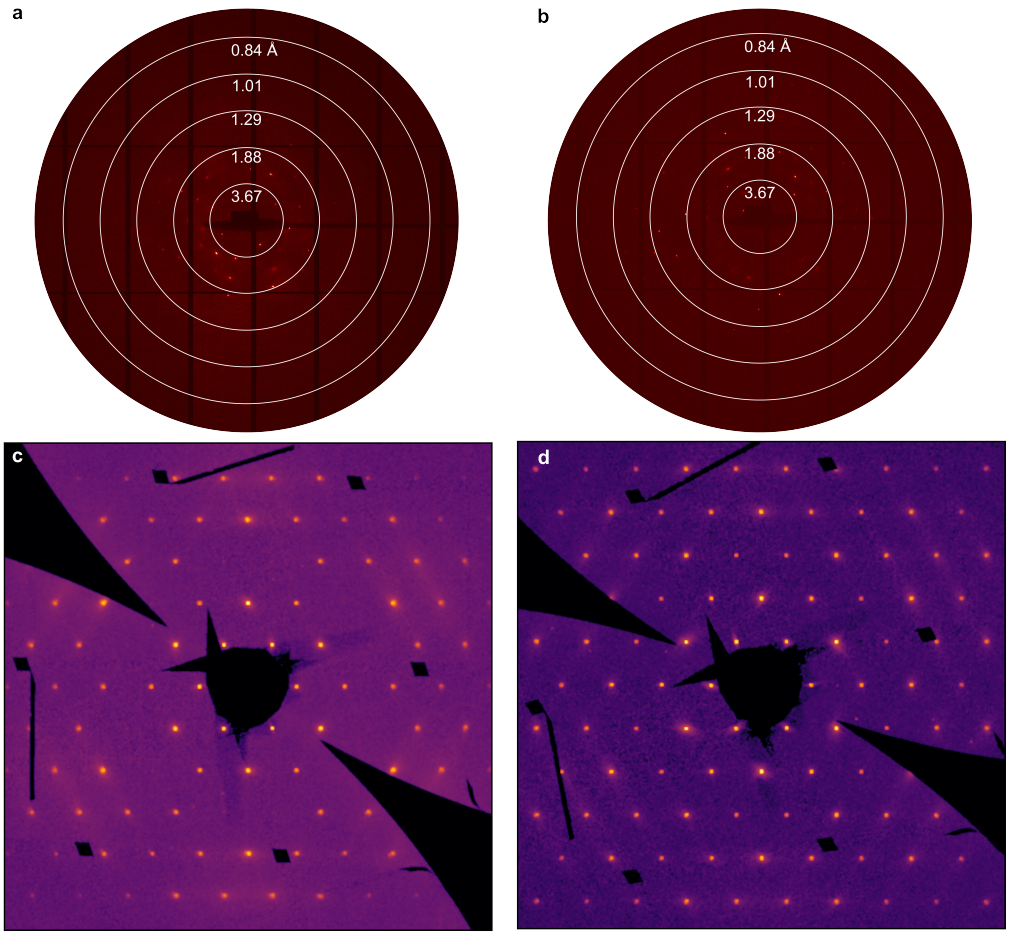


FIGURE 5.3: Single raw diffraction image with resolution rings overlaid **a**, **b** and (hk0) Miller plane reconstructions **c**, **d** of $(TMBM)_3Bi_2Br_9$ and $(TMCM)_3Bi_2Cl_9$ respectively.

$(TMCM)_3Bi_2Cl_9$ and $(TMIM)_3Sb_2I_9$ across the temperature range where phase transitions are observed in DSC measurements (Figure 5.2). For $(TMBM)_3Bi_2Br_9$ and $(TMCM)_3Bi_2Cl_9$, despite using synchrotron radiation and collecting a full sphere of data, we observe an absence of Bragg peaks beyond 1.0 Å resolution (Figure 5.3a,b). This is accompanied with weak diffuse scattering about the Bragg peaks (Figure 5.3c,d), suggesting a high degree of dynamic disorder in these materials, particularly in the organic cation components, which persists across the phase transition temperatures.

Peak indexing and analysis of systematic absences lead to the deductions of unit cell dimensions belonging to the hexagonal space groups $P6_3mc$ from temperatures from 250 - 320 K. $(TMBM)_3Bi_2Br_9$ generally takes a larger unit cell than $(TMCM)_3Bi_2Cl_9$

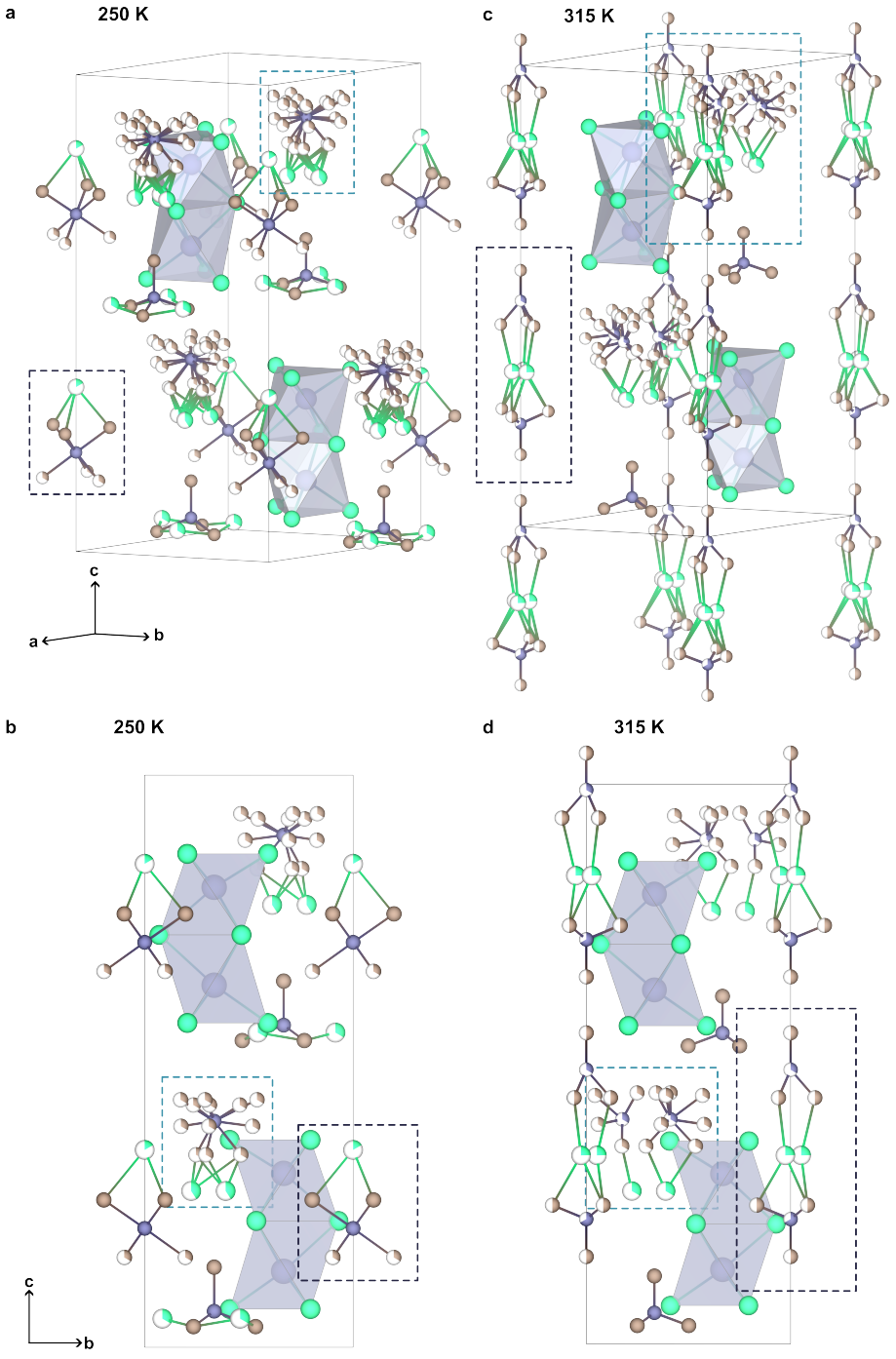


FIGURE 5.4: Crystal structure of $(TMCM)_3Bi_2Cl_9$ at 250 K **a**, **b** and 315 K **c**, **d**.

at all temperatures, as expected with the larger Br ion. For example, at room temperature (300 K or 27 °C), $(TMBM)_3Bi_2Br_9$ has cell dimensions of a, c = 9.8298, 23.1945 Å compared with a, c = 9.4731, 22.5275 Å for $(TMCM)_3Bi_2Cl_9$.

Analysis of the difference Fourier map reveals that $(TMBM)_3Bi_2Br_9$ and

$(TMCM)_3Bi_2Cl_9$ are isostructural. The $(Bi_2X_9)^{3-}$ anions are well-ordered, while the organic cations show significant dynamic disorder, with only the nitrogen atoms being clearly resolved. This disorder is further evidenced by Flack parameters close to 0.5, suggesting a twinned acentric structure, incorrect space group assignment or multi-domain structures. However, careful analysis of the lattice centrings indicates their acentric nature.

We examine $(TMCM)_3Bi_2Cl_9$ at temperatures above and below its transition point (Figure 5.4). At 250 K, the $[TMCM]^+$ cations are disordered about fixed positions, with one cation exhibiting three-fold orientational disorder (Figure 5.4a, dotted blue rectangle). Above the transition temperature, the cations show translational disorder, particularly along the long (c) axis. It should be noted that the structural model's accuracy is limited by the lack of measured data resolution beyond 1.0 Å.

For comparison, Figure 5.5a-d presents the room temperature crystal structures of $(TMBM)_3Bi_2Br_9$, $(TMCM)_3Bi_2Cl_9$, $(TMIM)_3Bi_2I_9$, and $(TMIM)_3Sb_2I_9$. The halogen and halide substitutions lead to significant structural changes from the parent compound $(TMIM)_3Bi_2I_9$. Both $(TMBM)_3Bi_2Br_9$ and $(TMCM)_3Bi_2Cl_9$ adopt higher symmetry hexagonal structures, in contrast to the orthorhombic system of the parent compound. Notably, the $(Bi_2X_9)^{3-}$ anions in these compounds show minimal distortion, aligning completely parallel to the long (c) crystallographic axis.

In contrast, $(TMIM)_3Sb_2I_9$ crystallizes in the space group $Pna2_1$ with unit cell dimensions of a,b,c = 29.7698, 9.8747, and 14.0032 Å, which are slightly smaller than those of $(TMIM)_3Bi_2I_9$. Despite the significant difference in ionic radii between Sb^{3+} (0.76 pm) and Bi^{3+} (1.03 pm)[7], both compounds maintain the same crystal structure. This structural similarity between Sb and Bi compounds is consistent with previous reports of $A_3M_2X_9$ compounds (A = Cs^+, MA^+; M = Sb^{3+}, Bi^{3+})[8–12], which exhibit isostructural crystallization in the hexagonal space group $P6_3/mmc$.

In the room temperature phase, we observe C-I$\cdots$I distances of 3.6238(11), 3.6427(13) 4.4896(14) Å, the former two of which are substantially less than the sum of the van der Waals radius of iodine and the Shannon ionic radius of iodine (4.18 Å), indicative of the presence of a bonding interaction between the organic and inorganic components, analogously to the C-I$\cdots$I interactions in $(TMIM)_3Bi_2I_9$. Where this

was clearly advantageous for the resulting piezoelectric properties in $(TMIM)_3Bi_2I_9$, we expect that this will also be the case for $(TMIM)_3Sb_2I_9$.

Upon heating, the crystal structure of $(TMIM)_3Sb_2I_9$ undergoes a polar-to-polar structural phase transition at 130 °C (Figure 5.6) to a structure with half the unit cell size of the room temperature structure, with the organic cations disordered about fixed positions as determined by freely refining the electron densities for each cationic $TMIM^+$ unit. We observe that, like for $(TMIM)_3Bi_2I_9$ in Chapter 4, the organic cations are disordered about fixed positions, with an increase in symmetry seen from the change in the tilt of the inorganic $(Sb_2I_9)^{3-}$ anions to align parallel to the long crystallographic axis (Figure 5.6b).

5.2.3 Second harmonic generation

In order to verify the non-centrosymmetry of these compounds, particularly where there is significant orientational disorder of the organic cation in the measured crystal structure, we employ temperature-dependent second harmonic generation measurements (Figure 5.7, 5.8), including on the parent compound $(TMIM)_3Bi_2I_9$.

Whilst $(TMCM)_3Bi_2Cl_9$ exhibits frequency-doubling characteristics from below its first phase transition point, up to 460 K (Figure 5.7a,b), confirming its non-centrosymmetry even at elevated temperatures, $(TMBM)_3Bi_2Br_9$ loses its SHG signal at 280 K, indicating that above this temperature, the structure becomes centrosymmetric. Therefore, we confirm that the phase transition of $(TMBM)_3Bi_2Br_9$ is associated with a change in symmetry, unresolved by our SCXRD measurements.

For $(TMIM)_3Bi_2I_9$ and $(TMIM)_3Sb_2I_9$ (Figure 5.8), SHG signal is also observed from room temperature until 420 K (147 °C), past their known phase transition temperatures, confirming their non-centrosymmetry even at elevated temperatures.

5.2.4 Probing molecular dynamics with NMR

For practical applications, powders are often preferred forms for piezoelectric materials. Therefore, we produce microcrystalline powders of the three compounds

via mechanosynthesis. XRD patterns of $(TMBM)_3Bi_2Br_9$, $(TMCM)_3Bi_2Cl_9$ and $(TMIM)_3Sb_2I_9$ are obtained (Figure 5.9). Due to the lack of fully solved structure for $(TMBM)_3Bi_2Br_9$ and $(TMCM)_3Bi_2Cl_9$, and the poor powder diffraction data for TISI, we are unable to perform Rietveld refinement. Therefore, we fit the XRD patterns using a Pawley fit. The fitted lattice parameters are given in Table 5.2.

TABLE 5.2: Fitted lattice parameters from Pawley fits of powder XRD data.

Material	a (Å)	b (Å)	c (Å)
$(TMBM)_3Bi_2Br_9$	9.623 (2)	9.623 (2)	22.101 (5)
$(TMCM)_3Bi_2Cl_9$	9.389 (3)	9.389 (3)	22.315 (9)
$(TMIM)_3Sb_2I_9$	29.719 (8)	9.931 (3)	14.011 (4)

To complement our structural analysis from SCXRD, we employ variable temperature multinuclear solid-state nuclear magnetic resonance (VT NMR) spectroscopy on mechanosynthesised microcrystalline powders of the three compounds. This technique provides unique insights into the local molecular dynamics and structural changes that occur during phase transitions, particularly those involving organic cation motion and inorganic framework distortions that may be too subtle or dynamic to be resolved by SCXRD alone. By probing different nuclei (^{1}H, ^{13}C, ^{14}N, and ^{209}Bi), we can separately track the behaviour of both the organic and inorganic components across the phase transitions, offering a more complete picture of the structural evolution.

First, we measure the ^{1}H and ^{13}C spin-lattice relaxation time constant (T_1) as a function of temperature (Figure 5.10). For $(TMBM)_3Bi_2Br_9$ the ^{1}H T_1 minimum is at 7.9 °C, where discontinuities are observed at 30 °C and 10 °C, close to the phase transition temperatures observed in DSC measurements (Figure 5.2a). The most significant change is observed for the lower temperature phase transition ($\Delta t \sim 75$ ms). For $(TMCM)_3Bi_2Cl_9$, the ^{1}H T_1 changes continuously with temperature until a jump-discontinuity followed by a step-change discontinuity ($\Delta t \sim 600$ ms) is observed at -7.5 °C (Figure 5.10b).

In contrast, $(TMIM)_3Sb_2I_9$ exhibits more subtle dynamic changes (Figure 5.10c), with a modest increase in ^{1}H T_1 relaxation time of approximately 100 ms occurring at 125 °C. This temperature coincides precisely with the deviation of ^{13}C T_1 measurements as noted previously. The simultaneous changes in both ^{1}H and ^{13}C relaxation behaviour at this temperature indicate a structural transition associated with

the organic cation, though with less pronounced effects compared to the bismuth analogue $(TMIM)_3Bi_2I_9$ in Chapter 4. The relaxation behaviour of $(TMIM)_3Sb_2I_9$ mirrors that of $(TMIM)_3Bi_2I_9$, with T_1 minima occurring at 40 °C for ^{1}H and X °C for ^{13}C, closely matching the values observed for $(TMIM)_3Bi_2I_9$ (42 °C and 0 °C, respectively). These unusually low temperatures for T_1 minima in solids can be attributed to the strong scalar coupling between the ^{127}I nuclei and the organic cation's ^{1}H/^{13}C nuclei[13], which enhances the relaxation pathways available to these nuclei. This similarity in relaxation behaviour between the two compounds suggests comparable local magnetic environments and dynamic processes within their organic components.

Next, in order to further probe the local dynamics of the organic cations in these compounds, we conduct VT static ^{14}N NMR at 20.0 T across the phase transition temperatures (Figure 5.11). The ^{14}N NMR lineshapes in these compounds are governed by the interplay between the nuclear quadrupolar moment, the electric field gradient (EFG) tensor, and the correlation time of molecular motion, as discussed in Section 4.3.4[14].

Across all three compounds, we observe a clear evolution in the ^{14}N NMR spectral envelopes with temperature: broad lineshapes at low temperatures progressively narrow as temperature increases, reflecting changes in the orientational dynamics of the organic cations. For $(TMBM)_3Bi_2Br_9$, the ^{14}N NMR lineshape at 0 °C closely resembles that of $[(CH_3)NH_3]PbI_3$ in its low-temperature tetragonal phase (Figure 5.11a)[14]. The broad linewidths observed in all three compounds at low temperatures stem from the large EFG at the ^{14}N sites in the $[(CH_3)_3NCH_2X]^+$ cations, indicating static or nearly-static cation disorder. As temperature increases, the spectra gradually narrow, with $(TMBM)_3Bi_2Br_9$ showing distinct lineshapes at 0, 20, and 60 °C, and $(TMCM)_3Bi_2Cl_9$ exhibiting similar behaviour between −20 and 0 °C. The incomplete narrowing of these lineshapes reveals restricted cation reorientation, with $(TMBM)_3Bi_2Br_9$ displaying two distinct regimes of motion.

In contrast to $(TMBM)_3Bi_2Br_9$ and $(TMCM)_3Bi_2Cl_9$, $(TMIM)_3Sb_2I_9$ shows a dramatic narrowing of its ^{14}N NMR spectral envelope between 120 and 130 °C. This pronounced narrowing, resulting from rapid whole-molecule tumbling that effectively averages the EFG tensor, indicates an order-disorder transition characterised by the onset of near-isotropic cation motion rather than restricted reorientation.

Following this, we conduct VT ^{1}H-^{13}C cross-polarization (CP) magic angle spinning (MAS) NMR with ^{1}H decoupling (20.0 T, 10 kHz) (Figure 5.12). As temperature increases, all signals shift to higher frequency. For $(TMBM)_3Bi_2Br_9$ and $(TMCM)_3Bi_2Cl_9$ (Figure 5.12a,b) at all temperatures, we observe two distinct signals corresponding to the halomethyl group of the two symmetry inequivalent $[TMBM]^+$ and $[TMCM]^+$ respectively (70-73 ppm and 61-64 ppm respectively), where at low temperature the signals become progressively broader and unresolvable. The lower chemical shift regions correspond to the CH_3 methyl groups. In contrast, from 20-100 °C in $(TMIM)_3Sb_2I_9$, we observe three distinct and well-resolved ^{13}C signals (Figure 5.12c) reflecting the three symmetry inequivalent $[TMIM]^+$ cations. The ^{13}C NMR spectra show a progressive coalescence of signals with increasing temperature: at 120 °C, two signals merge into a single narrow peak, and by 140 °C, all three signals coalesce. This behaviour, analogous to that observed in $(TMIM)_3Bi_2I_9$, indicates the emergence of chemically equivalent environments for the cations. Supported by the ^{14}N NMR results, we attribute this coalescence to the onset of isotropic cation tumbling averaging the environments of the three iodomethyl groups.

5.2.5 An aside: Unusual phase transition behaviour - reversible cyclic twinning

In order to study for potential phase transitions below room temperature, we measure SCXRD of $(TMBM)_3Bi_2Br_9$ from RT down to 140 K (Figure 5.13). Whilst the hexagonal unit cell is maintained, the a (b) lattice parameter and unit cell volume linearly decreases, in line with thermal expansion but across two regimes. However, the c lattice parameter increases with approximate linear behaviour, and then decreases.

In one experiment, we directly placed a crystal from room temperature into the cryostream set at 250 K (−23 °C) rather than the gradual cooling procedure used for the data in Figure 5.13. Here, we observed a structural phase with a three-fold domain nature with a quadrupled unit cell spacing (Figure 5.14). These three domains are offset from each other by 120 °, indicative of cyclic twinning[15]. The peaks can be fit to three main domain components of 27.1, 24.1 and 14.0 % (Figure 5.14), with initial unit cell dimensions given in Table 5.3. Twin domain components of less

than 10% are disregarded. Peak profile fitting and data reduction leads to a unit cell for domain 1 with dimensions a, b and c of 9.6103 (14), 22.815 (2) and 34.502 (19) Å and near-perpendicular angles (89.935(7),89.968(8) and 89.933(10) °), where a and b correspond to the short and long unit cell lengths of the room-temperature, hexagonal phase. The third unit cell dimension of 34.5 Å is in line with an approximate quadrupling of the unit cell size compared with before the transition.

Often, the impact of flash cooling can thermally stress a single crystal, causing mechanical twinning. However, we unusually find that this transition is fully reversible (Figure 5.15), indicating that this transition is not due to mechanical twinning. We find that the highest temperature that the crystal of $(TMBM)_3Bi_2Br_9$ can be flash-cooled to, to observe this phase transition is 265 K (Figure 5.15e-h). Reconstructions of the Miller planes show that the unit cell changes occur along the a and b axis of the room temperature phase, and that the cyclic twinning occurs about the [001] or c axis of the room temperature phase; there are no changes along the l axis. Due to the likely overlapping intensities of peaks from the three domains, we are unable to determine a single crystal structure for this phase.

Cyclic twinning is often observed as a natural phenomenon in natural minerals such as chrysoberyl[16, 17] and aragonite[18], which exhibit pseudo-hexagonal symmetry arising from the intergrowth of three crystals or misoriented subgrains at 120 ° to each other. However, in the case of $(TMBM)_3Bi_2Br_9$, the cyclic twinning arises from the flash cooling process, rather than any crystal growth mechanisms. To our knowledge, this behaviour has not been previously observed in a system, least of all for a hybrid organic-inorganic metal halide.

The formation of a reversible, twinned superstructure upon flash-cooling strongly suggests an order-disorder phase transition. We propose that the high-temperature hexagonal phase is a dynamic average over multiple local structural configurations that become 'frozen' into a long-range ordered state at low temperature. This process breaks the parent symmetry and introduces local variations in bond lengths and angles that are absent in the time-averaged high-temperature structure.

TABLE 5.3: Unit cell parameters for the three domain components.

Twin (% of peaks)	a (Å)	b (Å)	c (Å)	α, β, γ (°)
#1 (27.1%)	9.610 (1)	22.814 (2)	34.502 (2)	89.935 (7), 89.968 (8), 89.933 (10)
#2 (24.1%)	9.610 (1)	22.815 (2)	34.502 (2)	89.935 (7), 89.967 (7), 89.933 (10)
#3 (14.0%)	9.6010 (1)	22.816 (2)	34.500 (4)	90.06 (1), 90.00 (1), 90.00 (2)

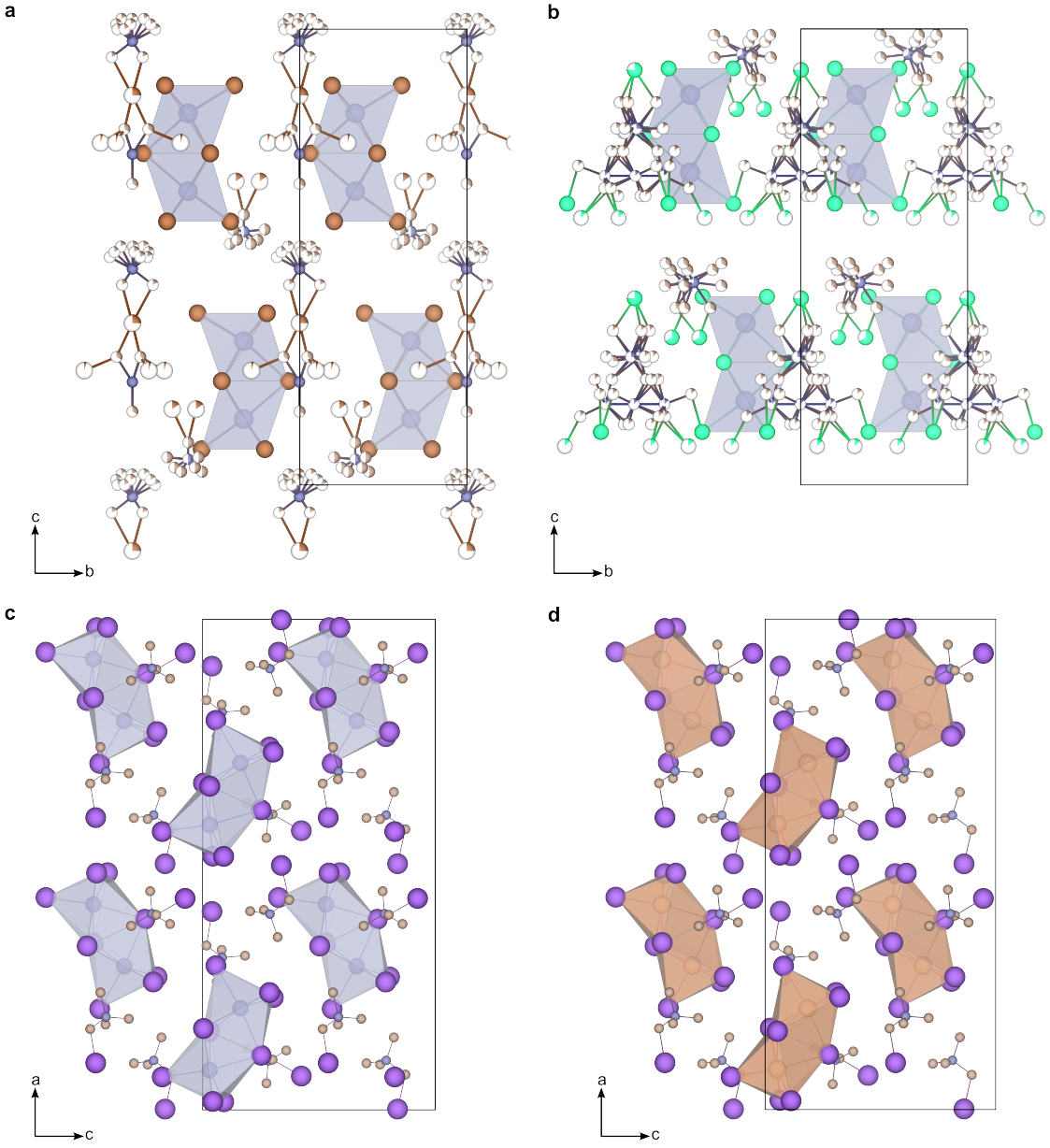


FIGURE 5.5: Room temperature crystal structures of **a** $(TMBM)_3Bi_2Br_9$, **b** $(TMCM)_3Bi_2Cl_9$, **c** $(TMIM)_3Bi_2I_9$ and **d** $(TMIM)_3Sb_2I_9$. The structures are solved by first assigning the atoms of the inorganic framework (larger electron density in the Fourier map) before seeking to identify the locations of the organic cations. For the more disordered structures, only the nitrogen atoms can be clearly resolved.

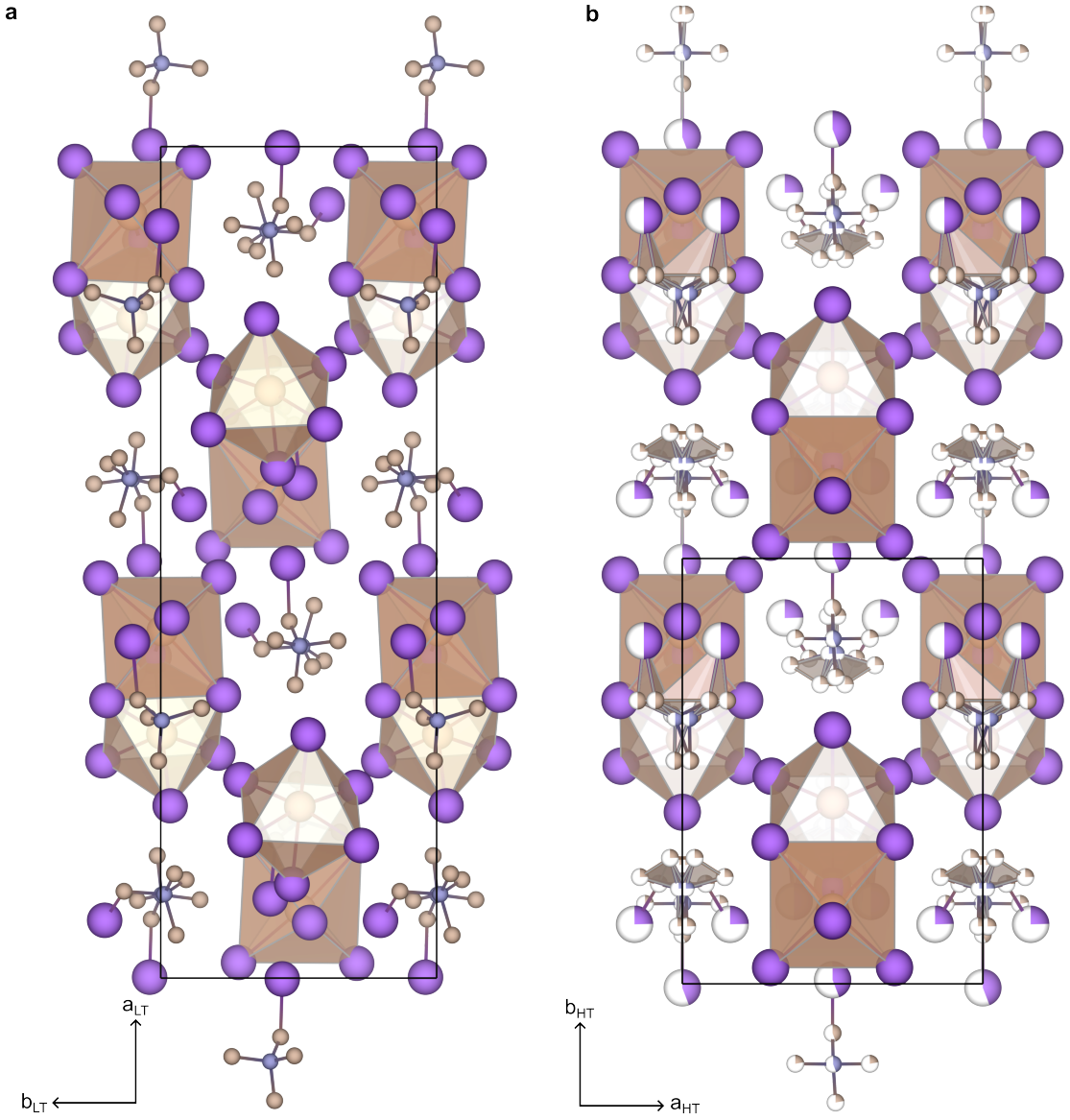


FIGURE 5.6: Room temperature (20 °C) **a** and high temperature (130 °C) **b** crystal structure of $(TMIM)_3Sb_2I_9$. Crystallographic data for $(TMIM)_3Sb_2I_9$ is given in Appendix B, Table B.2.

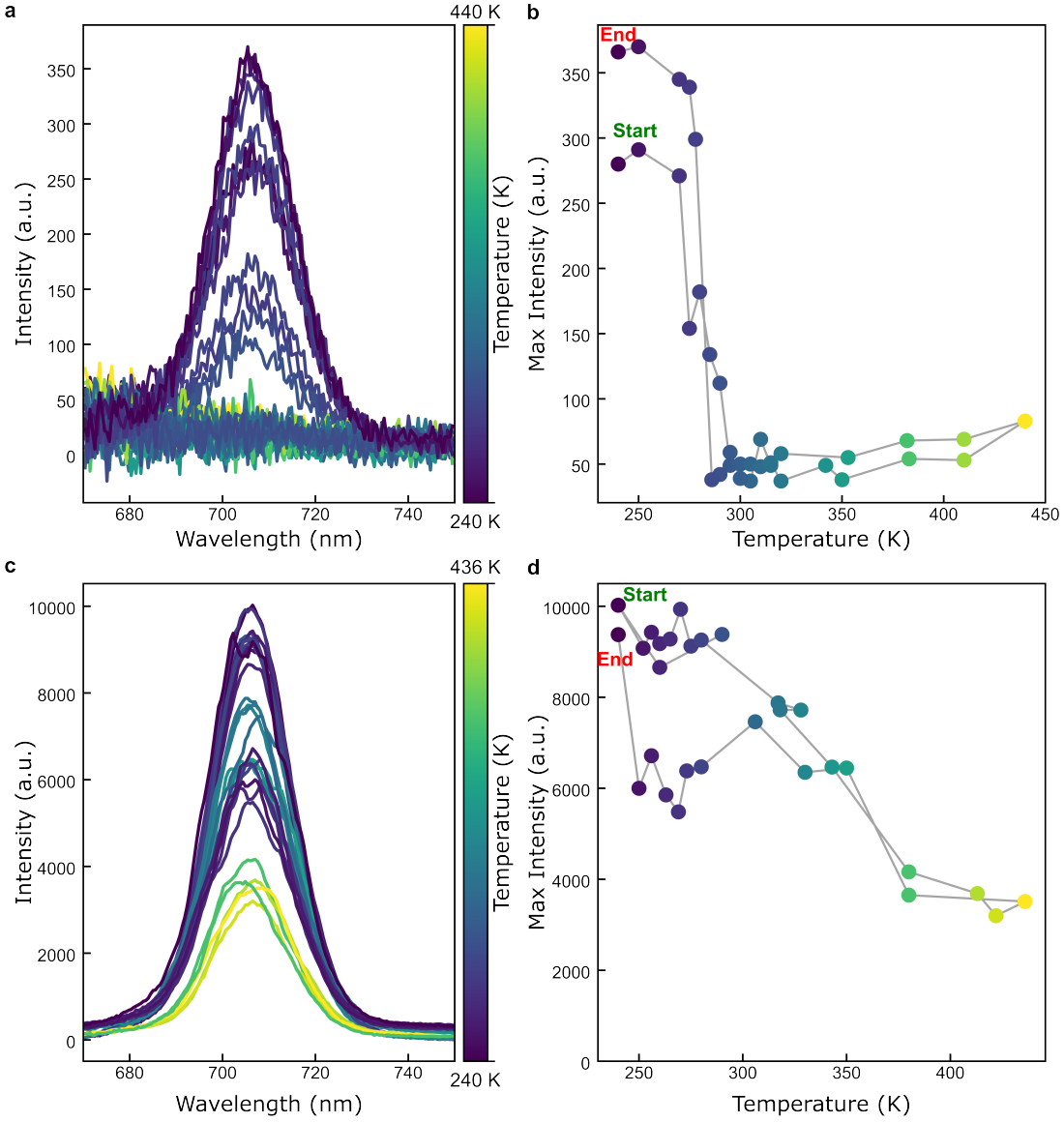


FIGURE 5.7: Temperature-dependent second harmonic generation (SHG) measurements of **a,b** $(TMBM)_3Bi_2Br_9$ and **c,d** $(TMCM)_3Bi_2Cl_9$. The SHG peak intensity values with varying temperature are plotted in **b,d**, to show more clearly the trend with temperature. The change in shape and width of the peaks is affected by the size of the crystal and small changes in the orientation of illumination.

These measurements were conducted by F.M. Adamczyk and M. Stein.

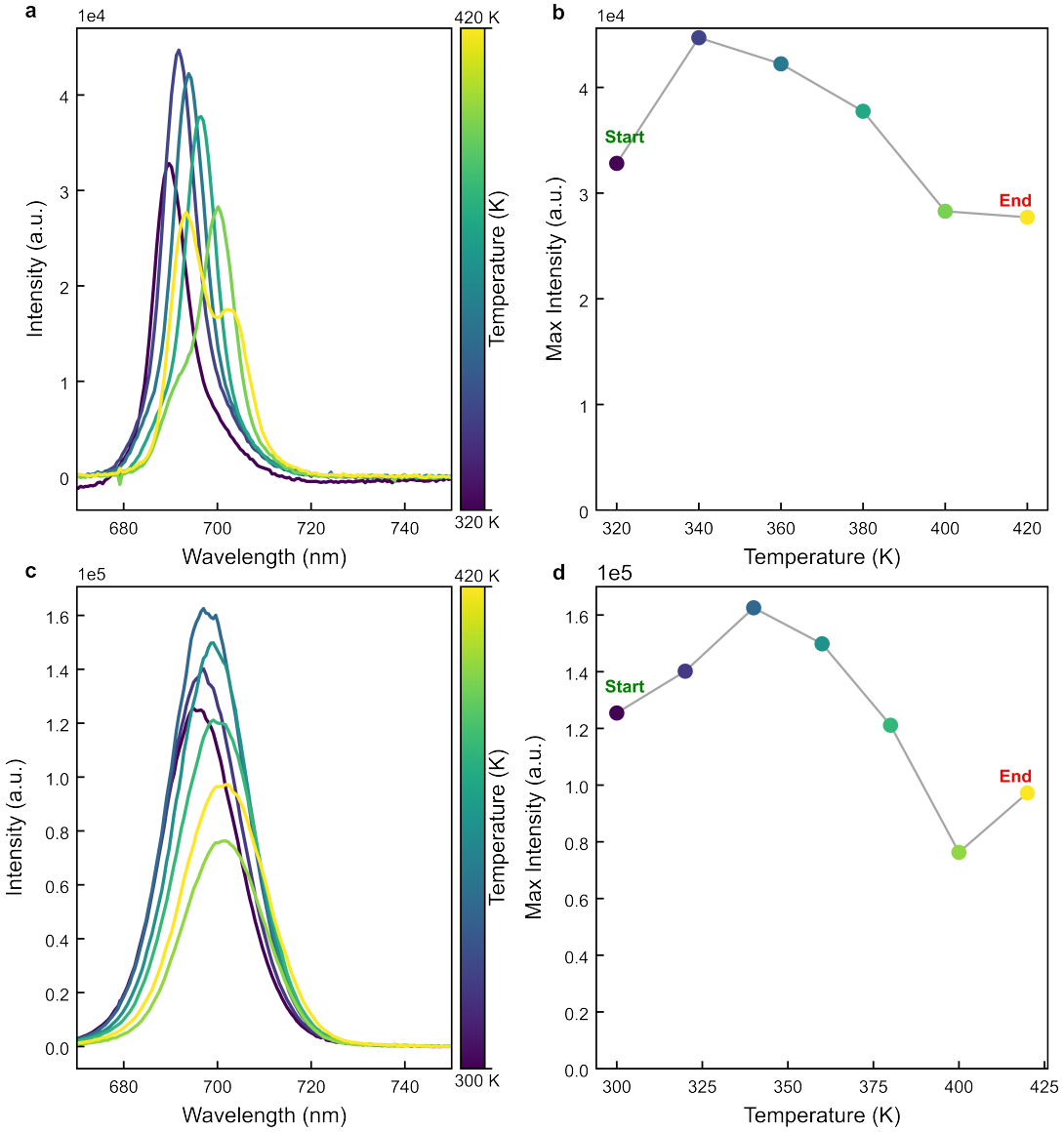


FIGURE 5.8: Temperature-dependent second harmonic generation (SHG) measurements of **a,b** $(TMIM)_3Bi_2I_9$ and **c,d** $(TMIM)_3Sb_2I_9$. The SHG peak intensity values with varying temperature are plotted in **b,d**, to show more clearly the trend with temperature. The change in shape and width of the peaks is affected by the size of the crystal and small changes in the orientation of illumination. These measurements were conducted by F.M. Adamczyk and M. Stein.

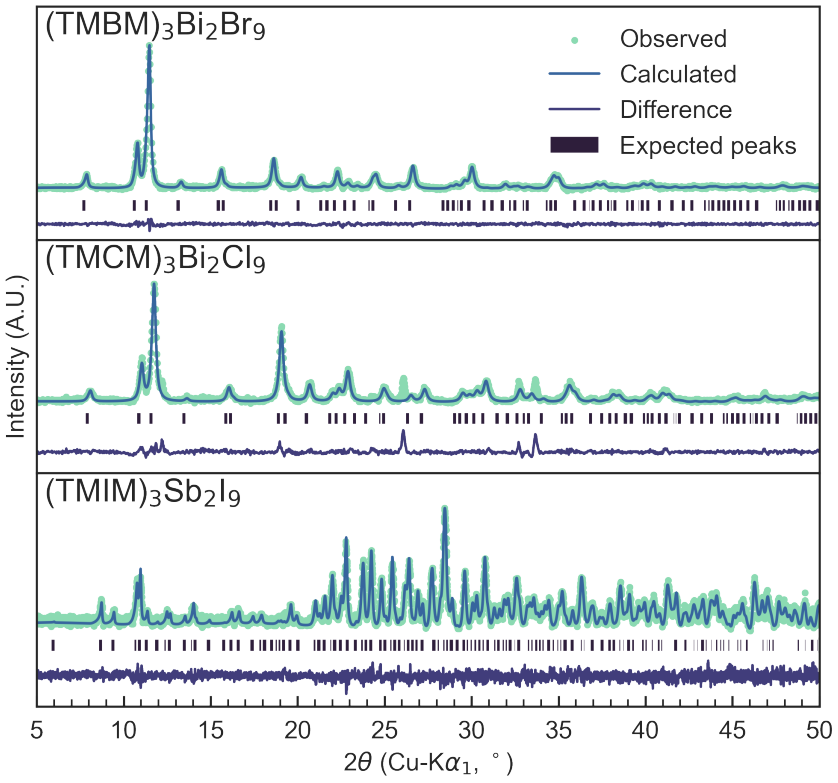


FIGURE 5.9: XRD measurements of $(TMBM)_3Bi_2Br_9$, $(TMCM)_3Bi_2Cl_9$ and $(TMIM)_3Sb_2I_9$. We note that the XRD pattern for $(TMCM)_3Bi_2Cl_9$ contains peaks which have not been indexed to the space group $P6_3mc$, and has not been otherwise identified as belonging to any other phase.

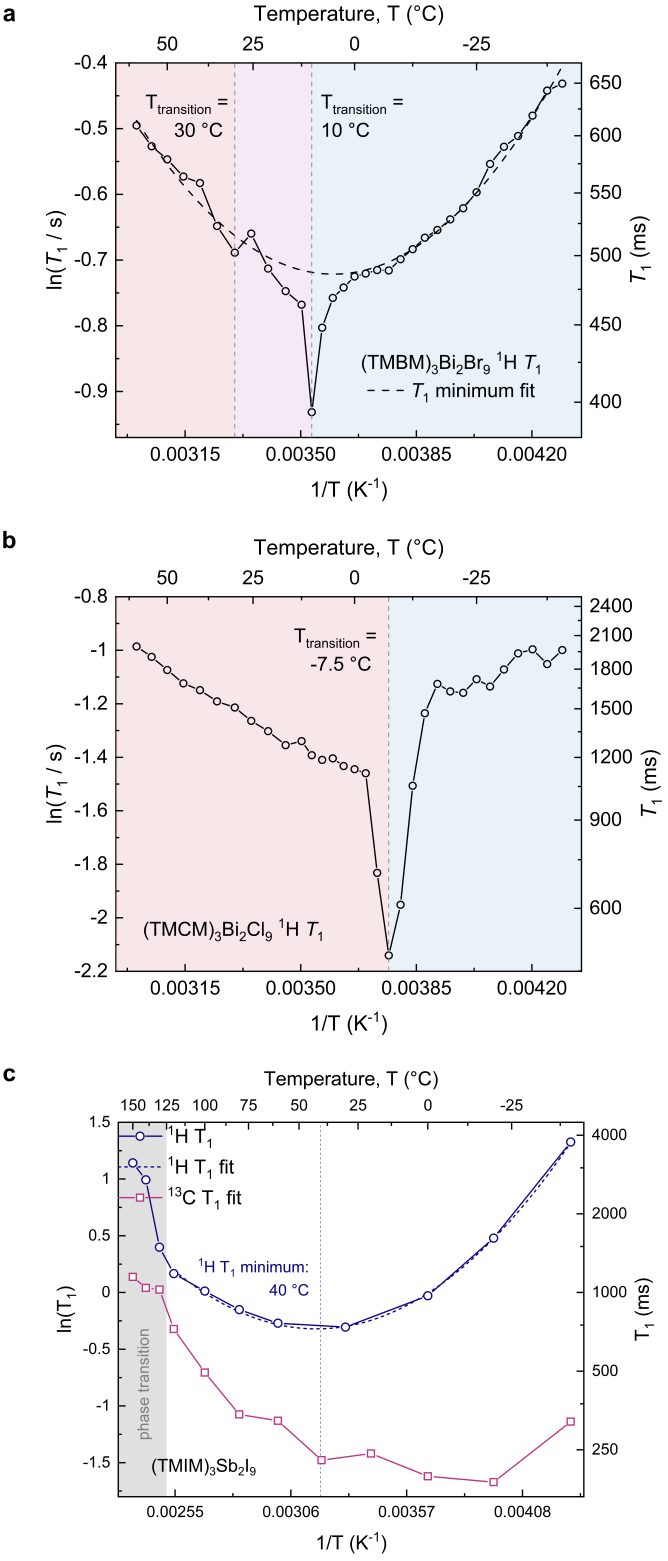


FIGURE 5.10: ^{1}H and ^{13}C spin-lattice relaxation (T_1) measurements for **a** $(TMBM)_3Bi_2Br_9$, **b** $(TMCM)_3Bi_2Cl_9$ and **c** $(TMIM)_3Sb_2I_9$. These measurements were conducted in collaboration with Dr. B.M. Gallant, and the analysis was performed by Dr. B.M. Gallant.

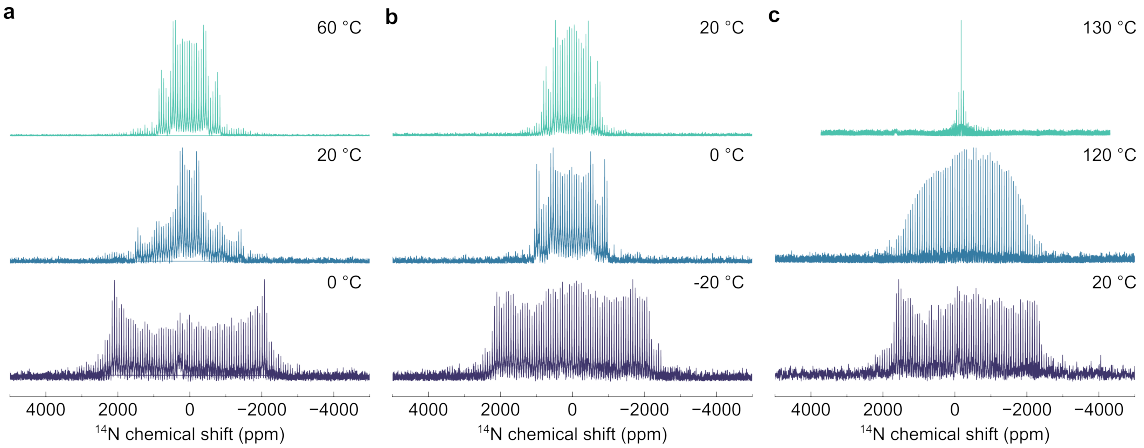


FIGURE 5.11: Variable temperature NMR spectra: Variable temperature solid state NMR spectra of ^{14}N in **a** $(TMBM)_3Bi_2Br_9$, **b** $(TMCM)_3Bi_2Cl_9$ and **c** $(TMIM)_3Sb_2I_9$. The NMR measurements were conducted in collaboration with Dr. B.M. Gallant, and the analysis was performed by Dr. B.M. Gallant.

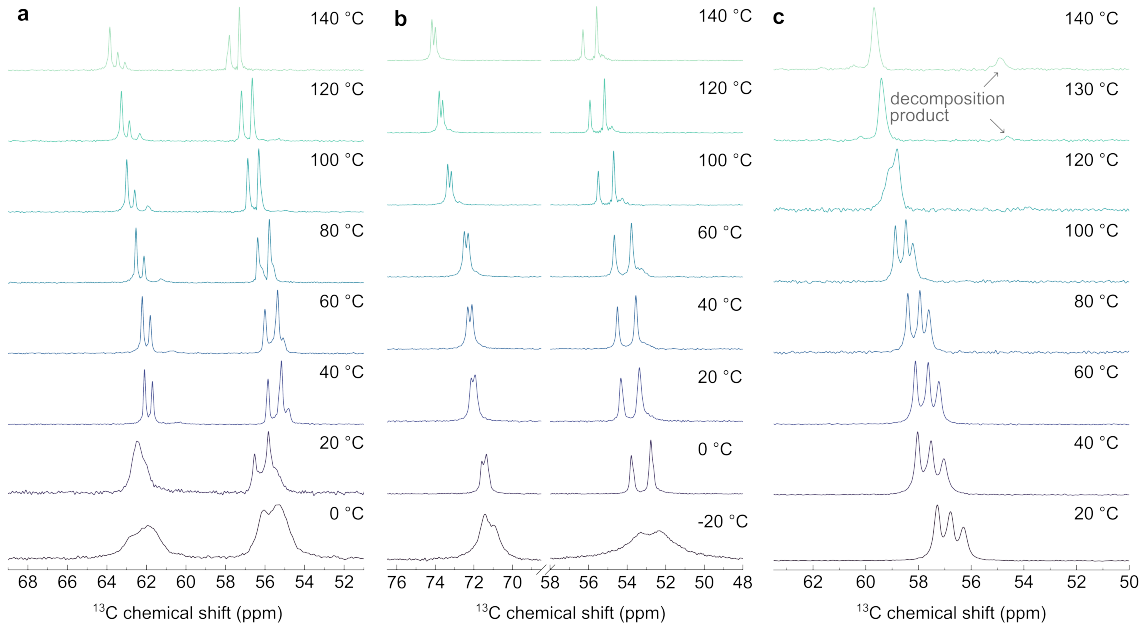


FIGURE 5.12: Variable temperature NMR spectra: Variable temperature solid state NMR spectra of ^{13}C in **a** $(TMBM)_3Bi_2Br_9$, **b** $(TMCM)_3Bi_2Cl_9$ and **c** $(TMIM)_3Sb_2I_9$. For $(TMIM)_3Sb_2I_9$, the signals (at lower chemical shifts) corresponding to the CH_3 methyl groups are very weak, and thus are not shown here. The NMR measurements were conducted in collaboration with Dr. B.M. Gallant, and the analysis was performed by Dr. B.M. Gallant.

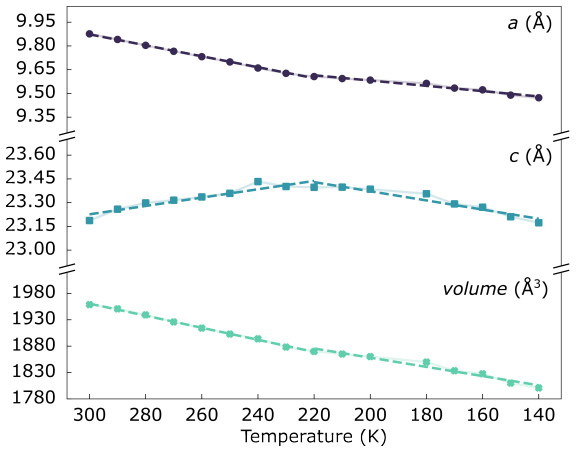


FIGURE 5.13: Lattice parameter changes of $(TMBM)_3Bi_2Br_9$ while cooling.

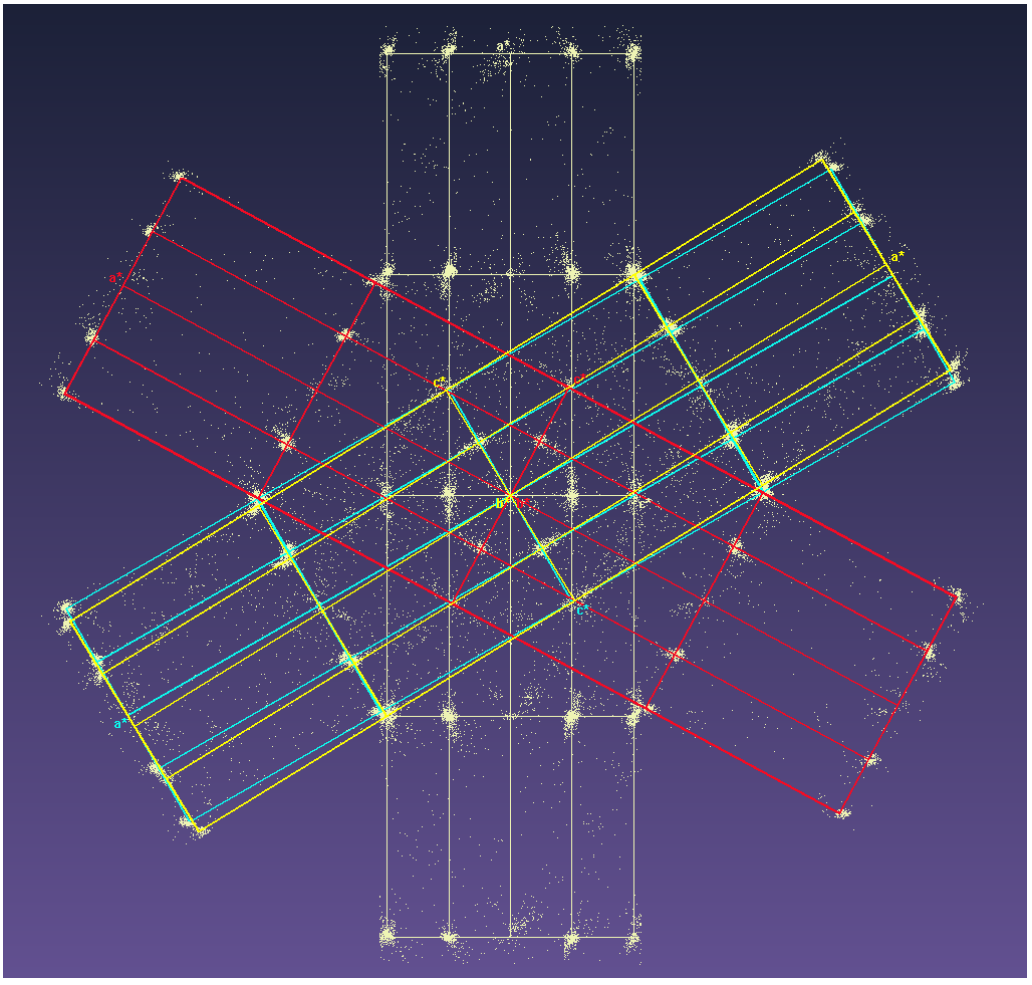


FIGURE 5.14: Fitting of the indexed peaks of the low-temperature phase of $(TMBM)_3Bi_2Br_9$ after flash cooling.

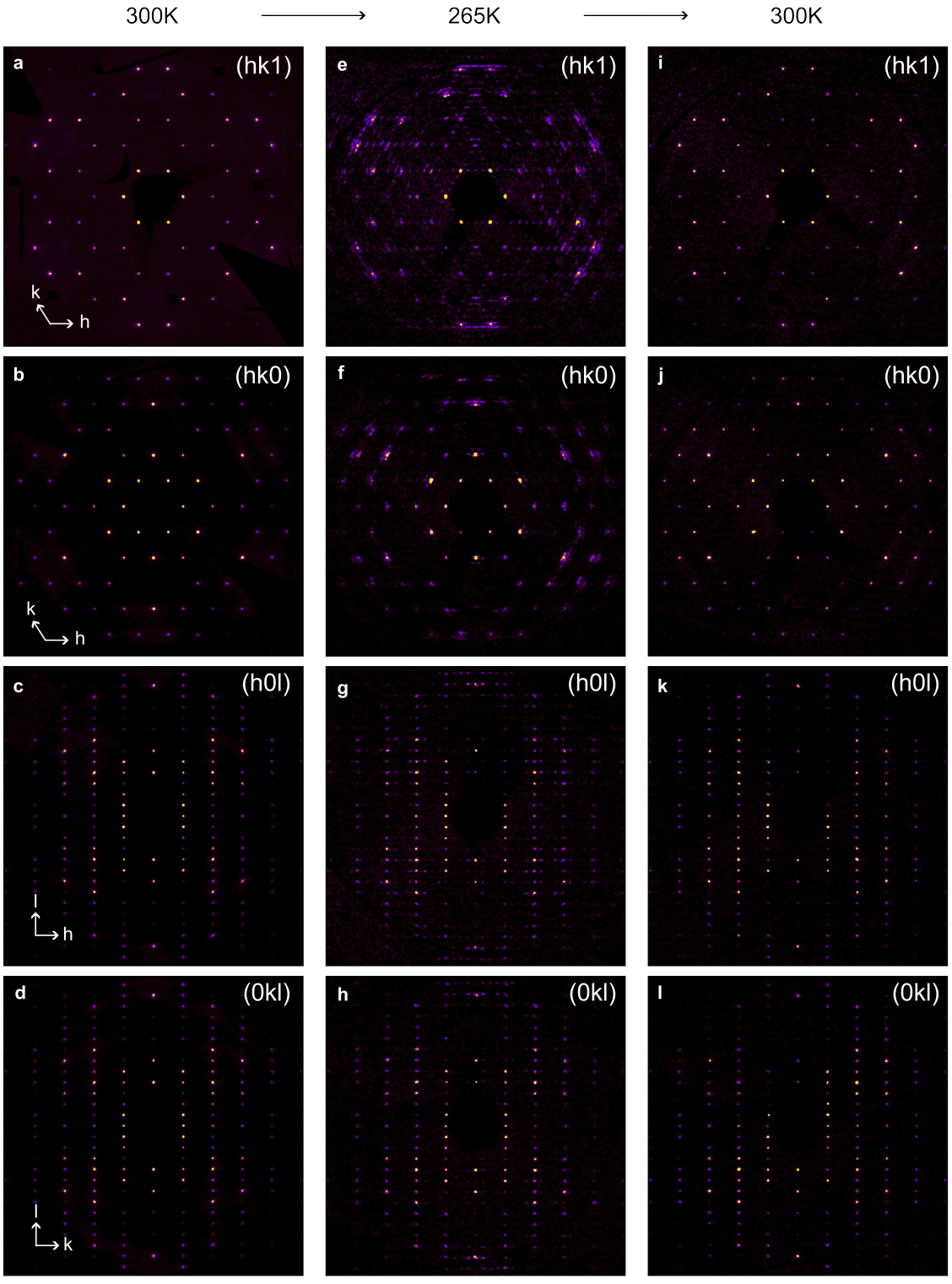


FIGURE 5.15: Unusual phase behaviour: $(TMBM)_3Bi_2Br_9$ reciprocal space reconstructions of the (hk1), (hk0), (h0l) and (0kl) Miller planes at 300 K (**a-d**), 265 K (**e-h**) and upon heating back up to 300 K (**i-l**).

5.3 Conclusion

In this chapter, we have systematically investigated the impact of halogen and halide substitutions on the structural and dynamic properties of the $(TMXM)_3M_2X_9$ family of hybrid organic-inorganic metal halides, using a series of variable temperature techniques. Through the synthesis and comprehensive characterisation of three new compounds - $(TMBM)_3Bi_2Br_9$, $(TMCM)_3Bi_2Cl_9$, and $(TMIM)_3Sb_2I_9$ - we have revealed several key findings.

First, we have shown that all three compounds maintain polar, non-centrosymmetric structures, as confirmed by SCXRD and second harmonic generation measurements. Halogen and halide substitutions in $(TMBM)_3Bi_2Br_9$ and $(TMCM)_3Bi_2Cl_9$ lead to significant structural changes from the parent $(TMIM)_3Bi_2I_9$ compound, including the adoption of higher symmetry hexagonal structures, minimal distortion of the inorganic framework, and weaker C-X$\cdots$X-Bi interactions between organic and inorganic components. On the other hand, the Sb-substituted compound $(TMIM)_3Sb_2I_9$ exhibits analogous structural features and phase transition characteristics to $(TMIM)_3Bi_2I_9$, despite the significant difference in ionic radii between Sb^{3+} and Bi^{3+}. VT NMR spectroscopy reveals that all three compounds exhibit phase transitions of order-disorder character.

The structural and dynamic properties of these materials have important implications for their potential applications in piezoelectric and ferroelectric devices. While $(TMBM)_3Bi_2Br_9$ and $(TMCM)_3Bi_2Cl_9$ are polar in nature, their piezoelectric response may be limited by the orientational disorder of the organic cations. In contrast, $(TMIM)_3Sb_2I_9$ shows promise for enhanced piezoelectric properties due to the strong halogen bonding that pins the organic cations in place, potentially leading to greater local polarizability and unit cell polarization. However, further investigation is needed to confirm this hypothesis, via direct measurement of ferroelectric and piezoelectric properties.

These findings contribute to the growing understanding of structure-property relationships in hybrid organic-inorganic materials and provide valuable insights for the design of new functional materials with tailored properties.

Bibliography

[1] X. N. Hua, W. Q. Liao, Y. Y. Tang, P. F. Li, P. P. Shi, D. Zhao, and R. G. Xiong, "A room-temperature hybrid lead iodide perovskite ferroelectric," *Journal of the American Chemical Society*, vol. 140, pp. 12296–12302, 2018.

[2] L. Chen, W. Q. Liao, Y. Ai, J. Li, S. Deng, Y. Hou, and Y. Y. Tang, "Precise molecular design toward organic-inorganic zinc chloride ABX_3 ferroelectrics," *Journal of the American Chemical Society*, vol. 142, pp. 6236–6243, 2020.

[3] Y. Zhang, X. J. Song, Z. X. Zhang, D. W. Fu, and R. G. Xiong, "Piezoelectric energy harvesting based on multiaxial ferroelectrics by precise molecular design," *Matter*, vol. 2, 2020.

[4] W. J. Wei, H. Q. Gao, Y. Yang, M. Fang, X. D. Wang, X. Chen, W. L. Qin, G. Q. Chen, R. X. Li, Y. Z. Tang, and Y. Wei, "Zero-dimensional molecular ferroelectrics with significant nonlinear effect and giant entropy," *Chemistry of Materials*, vol. 34, pp. 6323–6330, 2022.

[5] L. S. Li, Y. H. Tan, W. J. Wei, H. Q. Gao, Y. Z. Tang, and X. B. Han, "Chiral switchable low-dimensional perovskite ferroelectrics," *ACS Applied Materials and Interfaces*, vol. 13, pp. 2044–2051, 2021.

[6] C. C. Fan, C. D. Liu, B. D. Liang, W. Wang, M. L. Jin, C. Y. Chai, C. Q. Jing, T. Y. Ju, X. B. Han, and W. Zhang, "Tuning ferroelectric phase transition temperature by enantiomer fraction," *Nature Communications 2024 15:1*, vol. 15, pp. 1–9, 2024.

[7] R. D. Shannon, "Revised effective ionic radii and systematic studies of interatomic distances in halides and chalcogenides," *Journal of Applied Crystallography*, vol. 32, pp. 751–767, 1976.

[8] B. Saparov, F. Hong, J. P. Sun, H. S. Duan, W. Meng, S. Cameron, I. G. Hill, Y. Yan, and D. B. Mitzi, "Thin-film preparation and characterization of $Cs_3Sb_2I_9$: A lead-free layered perovskite semiconductor," *Chemistry of Materials*, vol. 27, pp. 5622–5632, 2015.

[9] M. Leng, Z. hengwu Chen, Y. ing Yang, Z. Li, K. Zeng, K. anghua Li, G. Niu, Y. He, Q. ingchao Zhou, J. Tang, M. Y. Leng, Z. W. Chen, Y. Yang, D. Li,

K. Zeng, K. H. Li, D. DNiu, Y. S. He, J. Tang, and Q. C. Zhou, "Lead-free, blue emitting bismuth halide perovskite quantum dots," *Angewandte Chemie International Edition*, vol. 55, pp. 15012–15016, 2016.

[10] S. V. Mel'nikova and A. I. Zaĭtsev, "Ferroelectric phase transition in $Cs_3Bi_2I_9$," *Physics of the Solid State*, vol. 39, pp. 1652–1654, 1997.

[11] K. Eckhardt, V. Bon, J. Getzschmann, J. Grothe, F. M. Wisser, and S. Kaskel, "Crystallographic insights into $(CH_3NH_3)_3Bi_2I_9$: a new lead-free hybrid organic-inorganic material as a potential absorber for photovoltaics," *Chemical Communications*, vol. 52, pp. 3058–3060, 2016.

[12] B. Chabot and E. Parthé, "$Cs_3Sb_2I_9$ and $Cs_3Bi_2I_9$ with the hexagonal $Cs_3Cr_2Cl_9$ structure type," *Journal of Applied Crystallography*, vol. 34, pp. 645–648, 1978.

[13] D. J. Kubicki, D. Prochowicz, E. Salager, A. Rakhmatullin, C. P. Grey, L. Emsley, and S. D. Stranks, "Local structure and dynamics in methylammonium, formamidinium, and cesium tin(II) mixed-halide perovskites from 119Sn solid-state NMR," *Journal of the American Chemical Society*, vol. 142, pp. 7813–7826, 2020.

[14] A. Senocrate, I. Moudrakovski, and J. Maier, "Short-range ion dynamics in methylammonium lead iodide by multinuclear solid state NMR and 127I NQR," *Physical Chemistry Chemical Physics*, vol. 20, pp. 20043–20055, 2018.

[15] L. Han, N. Fujit, H. Chen, C. Jin, O. Terasaki, and S. Che, "Crystal twinning of bicontinuous cubic structures," *IUCrJ*, vol. 7, pp. 228–237, 2020.

[16] H. Tabata, E. Ishii, and H. Okuda, "Growth and morphology of chrysoberyl single crystals," *Journal of Crystal Growth*, vol. 24-25, pp. 656–660, 1974.

[17] S. Drev, M. Komelj, M. Mazaj, N. Daneu, and A. Rečnik, "Structural investigation of (130) twins and rutile precipitates in chrysoberyl crystals from Rio das Pratinhas in Bahia (Brazil)," *American Mineralogist*, vol. 100, pp. 861–871, 2015.

[18] P. N. Gavryushkin, A. Rečnik, K. G. Donskikh, M. V. Banaev, N. E. Sagatov, S. Rashchenko, S. Volkov, S. Aksenov, D. Mikhailenko, A. Korsakov, N. Daneu, and K. D. Litasov, "The intrinsic twinning and enigmatic twisting of aragonite

crystals," *Proceedings of the National Academy of Sciences of the United States of America*, vol. 121, p. e2311738121, 2024.

Chapter 6

Unfinished business: Yet more crystal structures

6.1 Background and introduction

During our investigations of novel, lead-free hybrid piezoelectrics, we tested synthesising a range of compounds. Crystal growth from solution is not always straightforward; whilst stoichiometric quantities of reactants are dissolved, the growth of single crystals of the desired composition is not guaranteed. In this chapter, first we explore synthesis of other compositions of the $(TMXM)_3M_2X'_9$ family, where M = Bi, Sb, and X' = I, Br, Cl. During our synthesis attempts of members in this family, we also synthesise compositions of the form $(TMXM)_3M_2X'_9{\cdot}X_2$, where X = Br, I.

As part of our studies and search for non-centrosymmetric compounds of the $A_3B_2X_9$ family, we investigate the use of a large cation, $[(CH_3)_3Fe(C_5H_5)_2N]^+$ (ferrocenylmethyl)trimethylammonium ($FMTMA^+$), as a component of the A-site in the $A_3B_2X_9$ structure. Amongst previously reported hybrid ferro- and piezoelectrics, Zhang et al. reported the synthesis of the piezoelectric series $(FMTMA)PbX_2I$ (X = I, Br, Cl)[1]. In this series, the $[FMTMA]^+$ cation aligns along the b axis, leading to the polar c axis. The PbX_6 octahedra within these structures were shown to become more distorted from X = I to Br to Cl, correlating with the increasing piezoelectric

coefficients (d_{33}) of 10.6, 15.4 to 20.6 pC/N. Therefore, we investigate the structural impact of this cation in a series of $(FMTMA)_3Bi_2X_9$ (X = I, Br, Cl) compounds.

6.2 Results and discussion

6.2.1 Extending the $(TMXM)_3Bi_2X_9$ family

From single crystal growth, we were able to grow a range of centrosymmetric compounds. The refined crystal structures (Figure 6.1) and parameters for these compounds are given in Table 6.1.

First, by attempting to modify $(TMIM)_3Bi_2I_9$ by replacing the halide ions with Br, we grow orange single crystals of $(TMIM)_3BiBr_6$ (Figure 6.1a) from solution. As a result, the orthorhombic structure is retained, but the nature of the structure is different; $(TMIM)_3BiBr_6$ is composed of isolated $[BiBr_6]^{3-}$ anions rather than the $[Bi_2Br_9]^{3-}$ anions in $(TMIM)_3Bi_2I_9$ and the compounds in Chapter 5, likely owing to the crystallization kinetics and likely weaker Bi-Br bonding from solution.

However, by inserting $(TMIM)^+$ into a (Bi-Cl) framework, we were able to grow single crystals of $(TMIM)_3Bi_2Cl_9$ (Figure 6.1b). This compound adopts a hexagonal $P6_3mc$ structure, isostructural with the $(TMBM)_3Bi_2Br_9$ and $(TMCM)_3Bi_2Cl_9$ from Chapter 5.

On the other hand, by inserting $(TMCM)^+$ cations into iodobismuthate or bromobismuthate frameworks, whilst also isostructural in orientation to $(TMCM)_3Bi_2Cl_9$ ($P6_3mc$), they crystallize in the centrosymmetric $P6_3/mmc$ structure (Figure 6.1c and d). We note that due to the poor quality of the data, the space group assignment is not certain.

6.2.2 $(TMXM)_3Bi_2X_9{\cdot}X_2$ family

We also grew compounds of the form $(TMXM)_3Sb_2X_9{\cdot}X_2$ (Figure 6.2): **a** $(TMIM)_3Sb_2Br_9{\cdot}Br_2$, **b** $(TMCM)_3Sb_2I_9{\cdot}I_2$. Crystal structure parameters for these compounds are given in Table 6.2. We observe that in both compounds, molecular

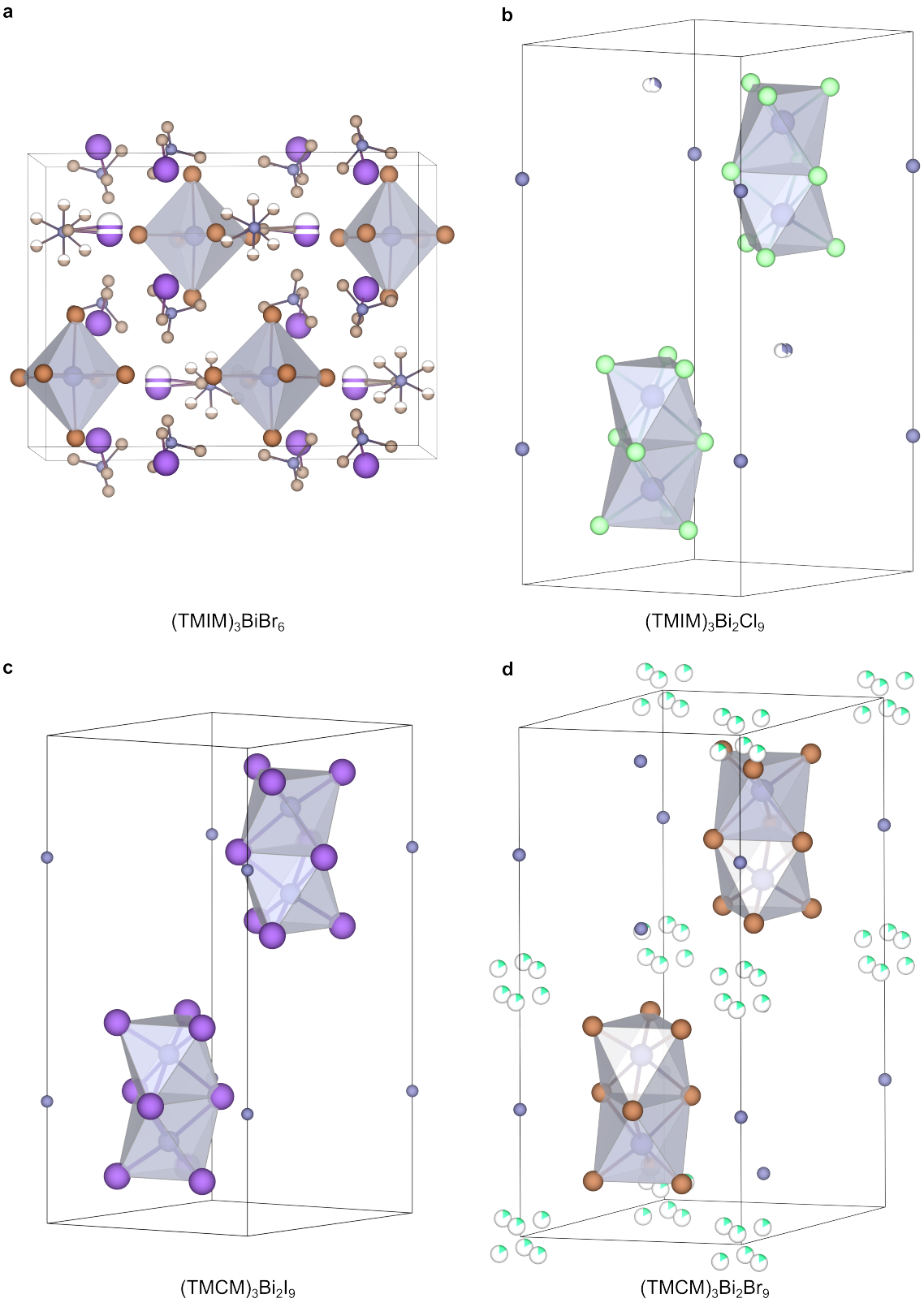


FIGURE 6.1: $(TMXM)_3Bi_2X_9$ family of compounds. **a** $(TMIM)_3BiBr_6$, **b** $(TMIM)_3Bi_2Cl_9$, **c** $(TMCM)_3Bi_2I_9$, **d** $(TMCM)_3Bi_2Br_9$. For **b-d**, significant diffuse scattering is present in the raw-diffraction pattern, paired with a lack of Bragg peaks beyond 1.0 Å resolution. We attribute this to significant disorder of the organic cations which means we are unable to resolve their positions in the crystal structures. Mostly only the nitrogen atoms are discernible. These measurements were taken on a lab-based diffractometer.

TABLE 6.1: Crystal structure parameters for $(TMXM)_3Bi_2X_9$ compounds.

Compound	Space Group	Cell Dimensions (a, b, c) Å	$\angle$ (α, β, γ) °
$(TMIM)_3BiBr_6$	$Pnma$	19.0047(5), 14.2596(4), 12.0057(4)	90, 90, 90
$(TMIM)_3Bi_2Cl_9$	$P6_3mc$	9.4058(5), 9.4058(5), 22.3681 (15)	90, 90, 120
$(TMCM)_3Bi_2I_9$	$P6_3/mmc$	10.6074(8), 10.6074(8), 23.3209(12)	90, 90, 120
$(TMCM)_3Bi_2Br_9$	$P6_3/mmc$	9.8026(10), 9.8026(10), 22.8055(17)	90, 90, 120

bromine and iodine are present in the crystal structure, accompanied by $(SbX_9)^{3-}$ anions (X=Br or I) which are aligned parallel to the long axes of the unit cell, unlike for $(TMIM)_3Sb_2I_9$ (Chapter 5). The growth of these structures was likely enabled by their growth in hydrohalic acids.

The crystal structure of $(TMIM)_3Sb_2Br_9{\cdot}Br_2$ (Figure 6.2a) displays two defining characteristics. Firstly, the intercalated Br_2 molecules display positional disorder, distributed with partial (50%) occupancy over two distinct crystallographic sites along the *b*-axis (for visual clarity, only one site is observable in Figure 6.2a). Secondly, the $(SbBr_9)^{3-}$ anions form a superstructure arising from their specific arrangement. The anions are organised into rows that group into pairs; while these pairs maintain a consistent overall orientation, the constituent rows within each pair are slightly rotated relative to one another. This rotational modulation is responsible for the doubling of the unit cell compared to that of the analogous $(TMCM)_3Sb_2I_9{\cdot}I_2$ compound.

For $(TMCM)_3Sb_2I_9{\cdot}I_2$ (Figure 6.2b), the structural analysis reveals that the $(TMCM)^+$ cations are disordered, occupying two distinct positions within the crystal structure. The $(SbI_9)^{3-}$ anions are well-ordered, with the anions aligned parallel to the long axes of the unit cell.

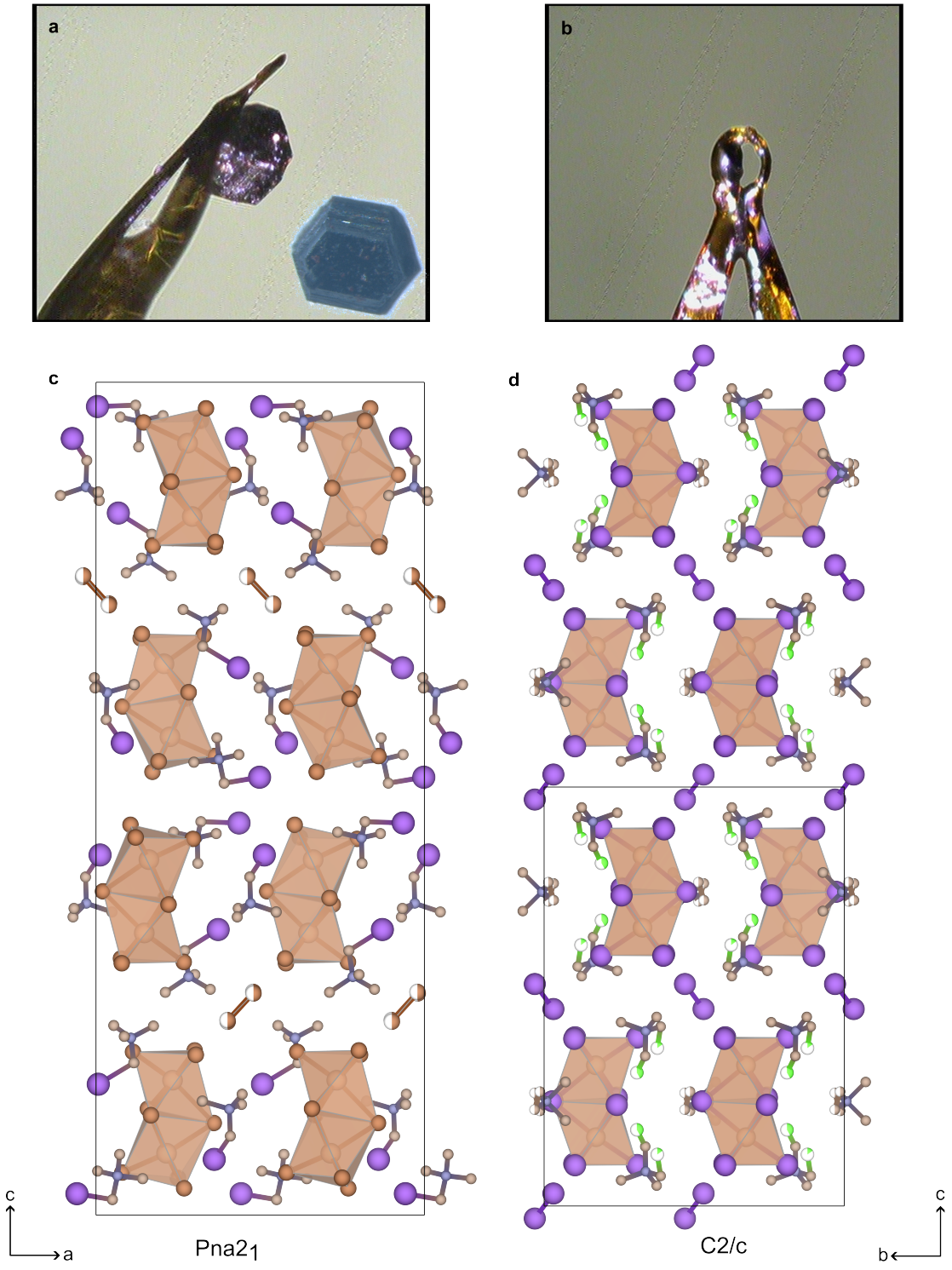


FIGURE 6.2: $(TMXM)_3Sb_2X_9{\cdot}X_2$ family of compounds.

TABLE 6.2: Crystal structure parameters for $(TMXM)_3Sb_2X_9{\cdot}X_2$ compounds.

Compound	Space Group	Cell Dimensions (a, b, c) Å	$\angle$ (α, β, γ) °
$(TMIM)_3Sb_2Br_9{\cdot}Br_2$	$Pnma$	17.9969 (3), 9.7455(2), 45.6606(10)	90, 90, 120
$(TMCM)_3Sb_2I_9{\cdot}I_2$	$C2/c$	10.5698(3), 17.2432(4), 24.1802(6)	90, 95.527 (2), 90

6.2.3 $(FMTMA)_3Bi_2X_9$ family

In one case, we investigated using a large cation, (ferrocenylmethyl)trimethylammonium ($FMTMA^+$), as a component of the A-site in the $A_3B_2X_9$ structure. By dissolving stoichiometric quantities of (ferrocenylmethyl)trimethylammonium iodide (FMTMAI) and bismuth halide salts (BiX_3), we were able to grow single crystals of $(FMTMA)_3Bi_2X_9$ (Figure 6.3). Their refined crystal structure parameters are given in Table 6.3. We find that all three compounds adopt centrosymmetric structures, and thus are not piezoelectric. As a result, their electrical characterisations are not conducted.

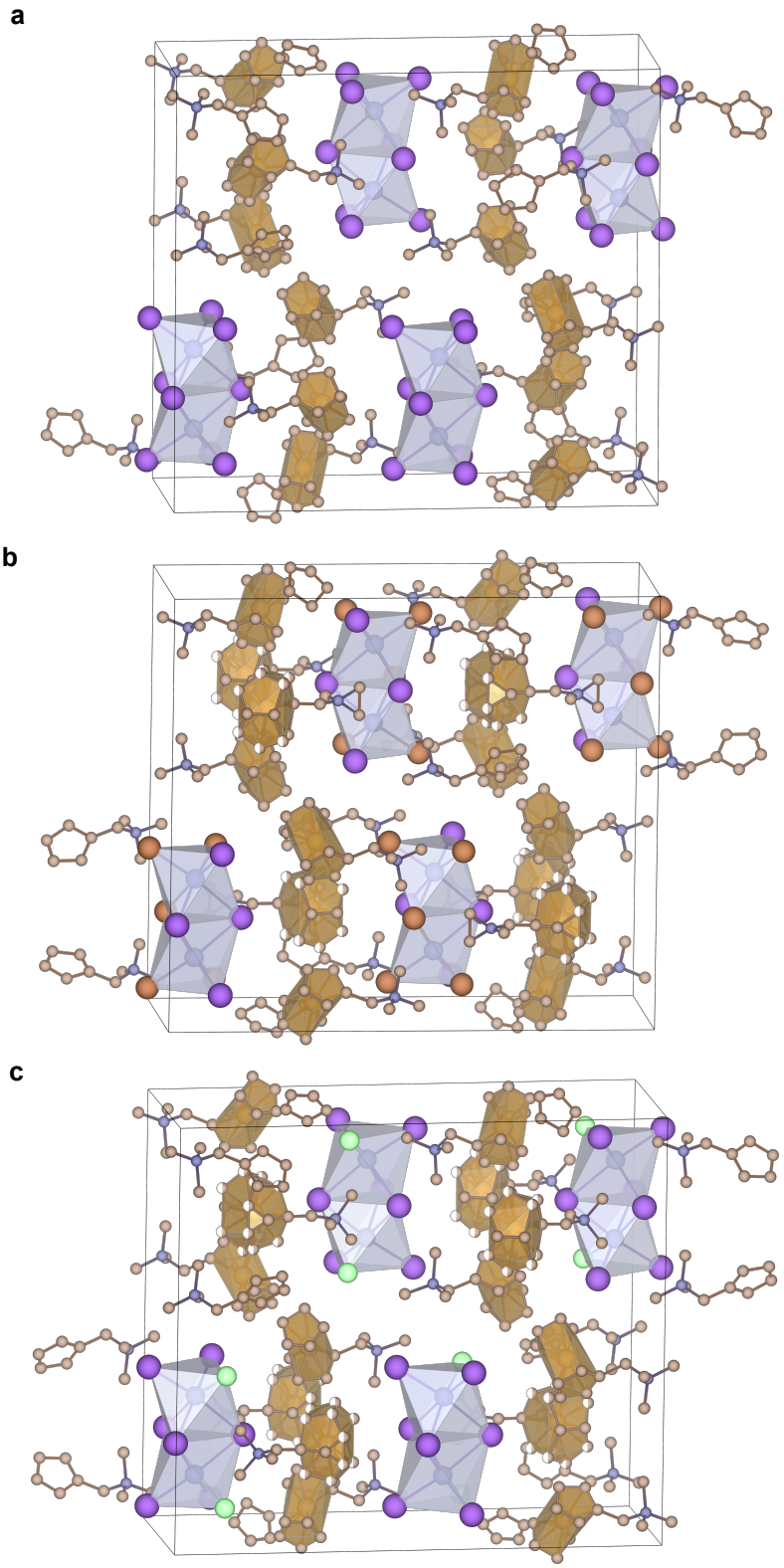


FIGURE 6.3: Crystal structures of **a** $(FMTMA)_3Bi_2I_9$, **b** $(FMTMA)_3Bi_2Br_5I_4$ and **c** $(FMTMA)_3Bi_2I_7Cl_2$.

TABLE 6.3: Crystallographic data for the three compounds $(FMTMA)_3Bi_2I_9$, $(FMTMA)_3Bi_2Br_5I_4$ and $(FMTMA)_3Bi_2I_7Cl_2$ at 100 K

Empirical formula	$C_{42}H_{60}Bi_2Fe_3I_9N_3$	$C_{42}H_{32}Bi_2Br_5Fe_3I_4N_3$	$C_{43}H_{51}Bi_2Cl_2Fe_3I_7N_3$
Formula weight	2334.54	2071.36	2154.57
Crystal system	monoclinic	orthorhombic	orthorhombic
Space group	$P2_1/n$	$Pnma$	$Pnma$
a,b,c (Å)	10.15700(8), 25.35390(19), 22.9747(2)	24.7810(2), 22.1106(3), 10.09670(9)	25.2354(6), 22.0725(5), 10.0719(2)
α, β, γ (°)	90, 91.3010(8), 90	90, 90, 90	90, 90, 90
Volume (Å^3)	5914.91(8)	5532.21(10)	5610.1(2)
Z	4	4	4
ρ_{calc} (g/cm^3)	2.622	2.487	2.551
μ (mm^{-1})	4.215	4.793	4.071
F(000)	4216.0	3744.0	3916.0
Crystal size (mm^3)	0.06 x 0.05 x 0.02	0.144 x 0.14 x 0.083	0.07 x 0.06 x 0.04
Radiation	Synchrotron (λ = 0.4859)	Synchrotron (λ = 0.4859)	Synchrotron (λ = 0.4859)
2Θ range (°)	2.424 to 40	2.248 to 40	3.232 to 40
Index ranges	-14 ≤ h ≤ 14, -35 ≤ k ≤ 35, -32 ≤ l ≤ 32	-34 ≤ h ≤ 34, -31 ≤ k ≤ 31, -14 ≤ l ≤ 14	-35 ≤ h ≤ 26, -24 ≤ k ≤ 31, -11 ≤ l ≤ 14
Reflections collected	114498	104731	13325
Independent reflections	17266 [R_{int} = 0.0833, R_{sigma} = 0.0656]	8282 [R_{int} = 0.0936, R_{sigma} = 0.0416]	7448 [R_{int} = 0.0989, R_{sigma} = 0.1533]
Data/restraints/parameters	17266/40/541	8282/0/312	7448/133/300
Goodness-of-fit on F^2	0.890	1.044	0.918
Final R indices [I≥2σ(I)]	R_1 = 0.0402,	R_1 = 0.0737,	R_1 = 0.0985,
	wR_2 = 0.1094	wR_2 = 0.2588	wR_2 = 0.2679
Final R indices [all data]	R_1 = 0.0597,	R_1 = 0.0982,	R_1 = 0.1604,
	wR_2 = 0.1243	wR_2 = 0.2816	wR_2 = 0.2962
Largest diff. peak/hole (eÅ^{-3})	3.01/-2.88	4.05/-5.86	2.85/-3.80

6.3 Conclusion

In this chapter, we have successfully synthesised and characterised a diverse range of novel lead-free hybrid metal halides, expanding our understanding of structure-property relationships in these materials. First, we demonstrate a significantly altered structure for $(TMIM)_3BiBr_6$ compared with the expected $(Bi_2Br_9)^{3-}$ framework, signifying a deviation from the common $(Bi_2X_9)^{3-}$ framework upon Br substitution. We also observe that cation choice plays a crucial role in determining the symmetry of the resulting structure. While $(TMIM)_3Bi_2Cl_9$ adopts the polar $P6_3mc$ space group, the analogous $(TMCM)_3Bi_2I_9$ and $(TMCM)_3Bi_2Br_9$ crystallize in the centrosymmetric $P6_3/mmc$ structure, highlighting the subtle influence of organic cation size and shape on structural symmetry. The incorporation of molecular halogens (Br_2 or I_2) in the Sb-based compounds $(TMIM)_3Sb_2Br_9{\cdot}Br_2$ and $(TMCM)_3Sb_2I_9{\cdot}I_2$ introduces additional structural complexity, though these materials may face stability challenges due to the volatile nature of the molecular halogens. Finally, the use of the large $(FMTMA)^+$ cation leads to the formation of large centrosymmetric structures, suggesting that cation size may be a critical parameter in controlling structural symmetry in these hybrid materials.

These findings provide valuable initial insights into the potential pathways for the design of lead-free hybrid metal halides with tailored structural and functional properties.

Bibliography

[1] Z. X. Zhang, H. Y. Zhang, W. Zhang, X. G. Chen, H. Wang, and R. G. Xiong, "Organometallic-based hybrid perovskite piezoelectrics with a narrow band gap," *Journal of the American Chemical Society*, vol. 142, pp. 17787–17794, 2020.

Chapter 7

Understanding and engineering the intermediate phase behaviour in PbSn perovskites

7.1 Abstract

The crystallization dynamics of Sn-containing perovskites occur on significantly faster timescales, leading to poorly-controlled crystallization and posing challenges for their synthesis. Despite the similarity in perovskite formability between Pb and Sn perovskites according to the Bartel tolerance factor, Sn-based compositions more readily form 3D, corner-sharing architectures. Moreover, intermediate phases - such as solvates and hexagonal polytypes - that are often observed in Pb-based systems are typically absent during the processing of Sn-containing perovskites. In this work, we investigate the crystallization kinetics of blade-coated, pure-Pb and mixed PbSn perovskite solutions using *in situ* GIWAXS. Whilst typical crystalline intermediates are observed for pure Pb compositions, none are observed for PbSn compositions apart from high Cs compositions. This indicates stronger Sn-halide bonding networks and an inherent preference for corner-sharing architectures in Sn-containing compositions. Reactive force-field machine learning simulations further support this, revealing a suppression of non-corner-sharing Sn phases. To overcome this, we introduce a larger cation; DMA^+ into the lattice to modulate crystallization,

promoting a transient 2H polytype that facilitates formation of the desired, final 3D perovskite phase. This leads to the growth of larger crystal grains, demonstrating a viable pathway to control the crystallization of Sn-containing perovskites through engineered intermediate phases.

The experimental results in this chapter were performed and analysed by E. Hung, unless otherwise stated in the figure captions.

7.2 Introduction

Metal halide perovskites (MHPs) have attracted substantial research and development interest for photovoltaic applications owing to their defect tolerance, long charge-carrier diffusion lengths, tuneable bandgaps, low defect density and solution processability. Pure-lead halide perovskites are however limited by having bandgaps only larger than 1.45 eV. Tin ions have a comparable ionic radius to lead (Pb^{2+}: 119 pm, Sn^{2+}: 115 pm)[1, 2], and their partial substitution into the lead perovskite structure, typically at a 50% ratio, can reduce the bandgap to around 1.2 eV[3]. This brings MHPs closer to the optimal range for photovoltaic applications and crucially - for achieving higher efficiencies in all-perovskite tandem solar cells.

However, tin-based perovskites face certain challenges in their synthesis. First, their stability; Sn^{2+} readily oxidises into Sn^{4+} due to the more reactive lone pair of electrons on the 5s orbital, resulting in Sn^{4+} having a more stable electronic configuration - in contrast to the 6s orbital in Pb which is considered an 'inert pair'[4]. Additionally, the strong self p-doping nature of Sn perovskites significantly limits their charge carrier dynamics[5–7]. Efforts to reduce the oxidation have included the incorporation of SnF_2 to decrease the number of tin vacancies in the structure, structural doping (trivalent cation doping) and additives to control the oxidation[7–9]. Secondly, controlling the crystallization process of a Pb-Sn perovskite film is challenging. Sn-based perovskites generally crystallize much more readily than their Pb-based counterparts. This can result in a narrow processing window and variety of undesirable effects, such as challenges with morphology control. In mixed Sn-Pb perovskites, this disparity in crystallization dynamics leads to inhomogeneous metal distribution throughout the film, affecting its morphology and stability[10–14].

The crystallization of Sn-Pb films is still less-studied and understood than that of Pb-based perovskites[15, 16]. Due to the lower formation energy of Pb compared with Sn perovskites, significant efforts have been made to retard the crystallization to the 3D perovskite phase. One approach to enhancing crystallization control involves adjusting deposition protocols, such as two-step processing[17], vacuum-drying, and gas-quenching[18]. Additionally, incorporating additives like methylammonium thiocyanate (MASCN) can form ligands with the perovskite precursors, thereby reducing reaction activity and stabilising crystallization[17, 19, 20]. Another effective technique is the templated growth of the final desired 3D Pb-Sn phase using a 2D Ruddlesden-Popper intermediate, which has been shown to improve crystallization kinetics, growth, and crystal grain orientation[21, 22].

In the solution processing of Pb-based perovskites, intermediate phases frequently form, highly dependent on the choice of A cation. These intermediates often consist of perovskite precursors coordinated with solvent molecules, such as $MA_3Pb_2I_8{\cdot}2DMSO$ and $FA_3Pb_2I_8{\cdot}2DMSO$[23]. Additionally, composition-dependent hexagonal polytypes are commonly observed, as discussed in Section 2.7.1 (Figure 2.11). While the presence of hexagonal polytypes is typically viewed as undesirable due to their tendency to cause trap-assisted performance losses and photoinstabilities[24, 25], careful control of these phases can be leveraged to modulate crystallization. For instance, McMeekin et al. demonstrated that introducing dimethylammonium chloride (DMACl) can facilitate a controlled phase transition from hexagonal polytypes to corner-sharing perovskites, resulting in improved grain size, texturing, and orientation[26].

On the other hand, crystalline intermediates - both solvent complexes or hexagonal polytypes - are rarely observed in the processing of Sn-containing perovskites. Zhang et al. (2022) observed the formation of a crystalline intermediate in $Cs_{0.25}FA_{0.75}Pb_{0.6}Sn_{0.4}I_3$ films and linked it to development of heterogeneous nucleation sites and aggregate crystallization - its suppression allowed the formation of a homogeneous, unwrinkled perovskite film surface[27]. For Sn-containing perovskites, hexagonal polymorphs are not observed unless larger cations such as ethylammonium (EA), guanidinium (GA), acetamidinium (ACA) and imidazolium (IM) are used (Figure 7.1)[28]. As demonstrated in Pb-based perovskites, intermediate phases can be beneficial rather than detrimental. The key insight is that controlling

their formation and properties can lead to enhanced thin film device performance. This presents a significant opportunity for Sn-containing perovskites, where similar control strategies could unlock improved device characteristics.

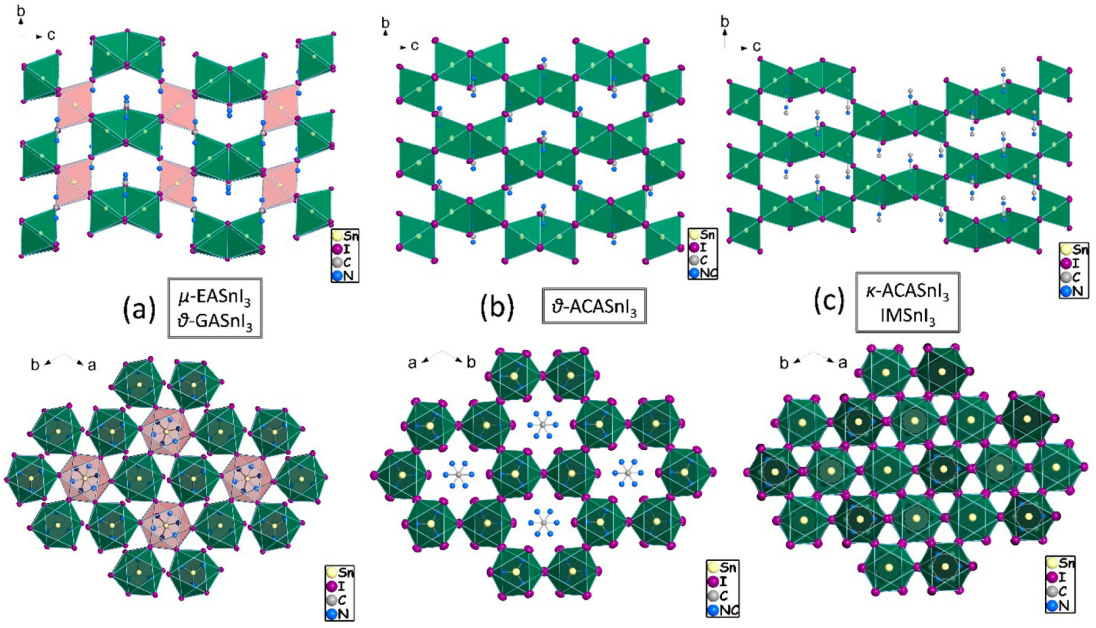


FIGURE 7.1: Crystal structures of the hexagonal polytypes. **a** (bottom) Parallel and (top) perpendicular views of the crystal structures of μ-$EASnI_3$ and θ-$GASnI_3$ (only the latter is shown) crystallizing in the 6H type. **b** (bottom) Parallel and (top) perpendicular views of the crystal structure of θ-$ACASnI_3$ crystallizing in the 4H type. **c** (bottom) Parallel and (top) perpendicular views of the crystal structures of κ-$EASnI_3$ and $IMSnI_3$ (only the latter is shown) crystallizing in the 9R type. Reprinted with permission from Stoumpos et al.[28]. Copyright 2017 American Chemical Society.

In this work, we seek to understand the intermediate phase behaviour of standard Sn-containing perovskite compositions using *in situ* GIWAXS with blade-coated solutions, and molecular dynamics simulations. First, we find that, unlike pure-Pb perovskites, mixed Pb-Sn perovskites bypass any crystalline intermediates across various cation stoichiometries - until the Cs content is increased. Using reactive ML force-field modelling, we show that there is a strong preference for Sn to form corner-sharing phases, outcompeting other possible intermediate phases using commonly-used cations. Therefore, we introduce a new, 'sacrificial' cation, dimethylammonium$^+$ (DMA^+) and show that we can manipulate the crystallization of a 3D, corner-sharing Pb:Sn perovskite to occur via hexagonal polytype phases, leading to improved film quality and stability of the final phase.

7.3 Results and Discussion

7.3.1 Intermediate phases in pure-Pb perovskites

We use a one-step blade-coating technique to fabricate a series of perovskite compositions prepared from a solution of dimethylformamide (DMF) and dimethyl sulfoxide (DMSO): (i) $FA_{0.6}MA_{0.4}PbI_3$, (ii) $FA_{0.6}MA_{0.3}Cs_{0.1}PbI_3$ and (iii) $FA_{0.83}Cs_{0.17}PbI_3$ (FA^+ = formamidinium$^+$, MA^+ = methylammonium$^+$). Following deposition, the solutions are gas quenched with nitrogen gas and then annealed, where the temperature is quickly ramped to 100 °C. Since the choice of A-site cation composition significantly influences the crystallization process, it is essential to compare a range of these compositions. Samples (i) and (ii) are identical, except for the inclusion of Cs in (ii), where the triple-cation formulation enhances stability and efficiency. Composition (iii) is without MA^+, and the cation ratio is selected for its favourable phase stability.

First, in all films (Figure 7.2a-c), we observe broad diffuse scattering features between 0.30-0.75 Å^{-1} and 1.60-2.25 Å^{-1}, associated with the non-crystalline solvate phases in the precursor solution. These quickly convert into crystalline peaks upon gas quenching (Figure 7.2d-f), where we observe crystallization into 3D perovskite through a combination of intermediate phases. One of these is characterised by peaks at 0.47, 0.51, and 0.65 Å^{-1} - consistent with the well-documented $MA_3Pb_2I_8{\cdot}2DMSO$ complex (Figure 7.2g). DMSO, a strongly coordinating solvent (more so than DMF), commonly leads to the formation of $MAPbI_3$-DMSO complexes via the PbI_2-DMSO adduct[29]. The reasoning for the appearance of a (MAPI-solvent) coordination may be attributed to the well-reported stronger MA-I bonds facilitated by hydrogen bonding[30, 31]. Additional peaks at 0.84, 1.18 and 1.87 Å^{-1} correspond to the 2H hexagonal polytype phase (Figure 7.2h), which is thermodynamically stable at room temperature[32, 33].

However, the crystallization pathways vary significantly across compositions. In $FA_{0.6}MA_{0.4}PbI_3$, $MA_3Pb_2I_8{\cdot}2DMSO$ is the dominant intermediate and the first to crystallize (Figure 7.2d). Its intensity peaks at around 180 seconds, coinciding with a local minimum of the 2H phase. Both phases gradually disappear as the 3D perovskite phase continues to form. The dip in 2H intensity at 180s indicates its

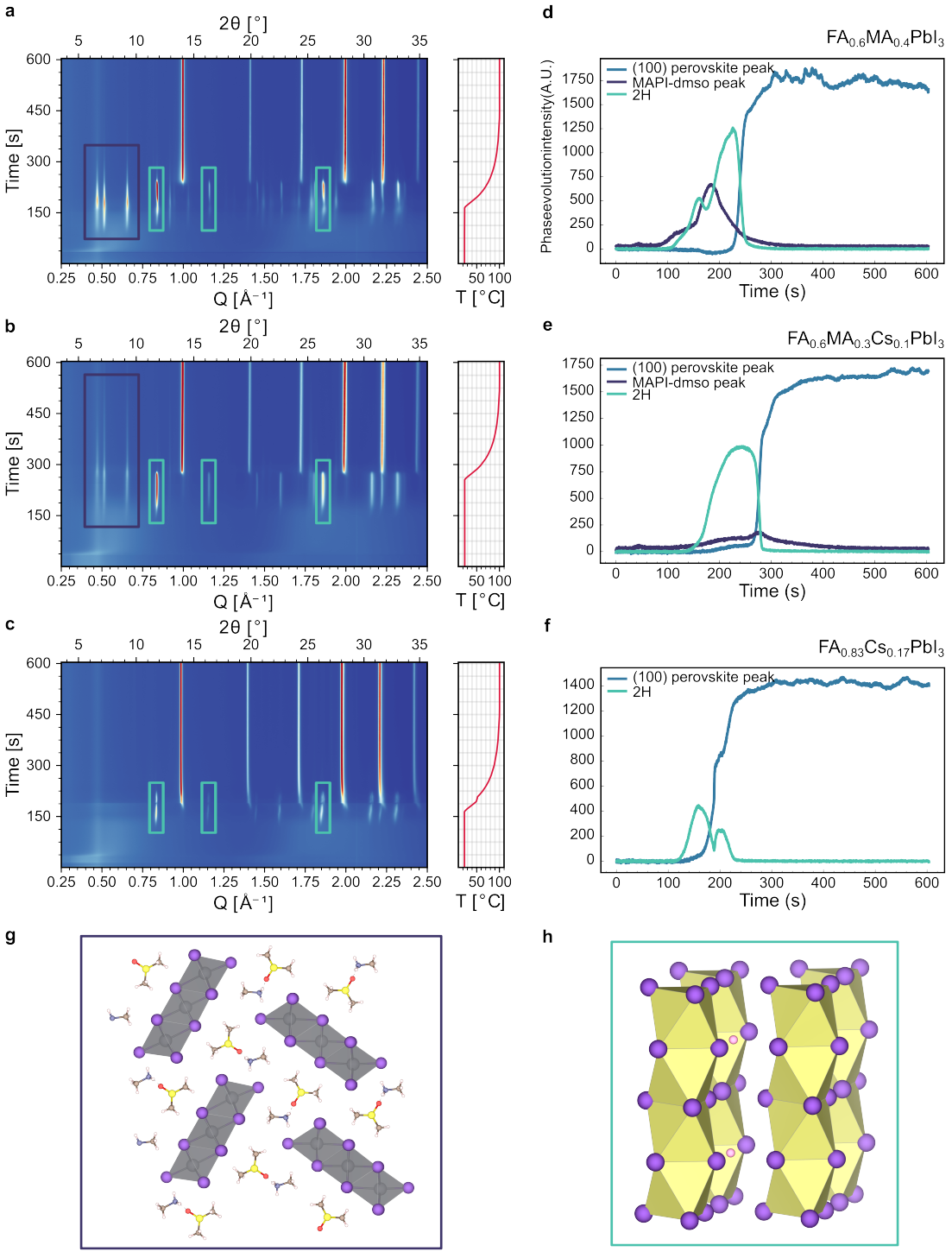


FIGURE 7.2: *In situ* GIWAXS. 1D azimuthal integration **a-c**, and phase evolution behaviour **d-f** of $FA_{0.6}MA_{0.4}PbI_3$, $FA_{0.6}MA_{0.3}Cs_{0.1}PbI_3$ and $FA_{0.83}Cs_{0.17}PbI_3$ (FA^+ = formamidinium$^+$, MA^+ = methylammonium$^+$) respectively. Diffuse scattering at 0.25 - 0.75 Å^{-1}, and 1.60-2.25 Å^{-1} indicative of non-crystalline solute phases. Crystal structures of **g** 2(DMSO)-$MA_3Pb_2I_8$ and **h** 2H (δ)-$FAPbI_3$. The *in situ* GIWAXS measurements were performed in collaboration with Dr. J. Smith, and analysed by E. Hung.

temporary dissolution and conversion to $MA_3Pb_2I_8{\cdot}2DMSO$, which subsequently transforms back into 2H.

In contrast, the 2H phase is the dominant intermediate and crystallizes first in the reduced-MA composition, $FA_{0.6}MA_{0.3}Cs_{0.1}PbI_3$ composition (Figure 7.2b,e) with a slower transition to the 3D phase. The introduction of a small amount of Cs significantly suppressed the $MA_3Pb_2I_8{\cdot}2DMSO$ phase. The MA-free $FA_{0.83}Cs_{0.17}PbI_3$ composition exhibits no crystalline solvent intermediate, transitioning directly to the 3D perovskite phase via the 2H phase (Figure 7.2c,f). This composition exhibits the weakest intermediate signature and crystallizes the fastest of the three compositions. The significantly weaker presence of the 2H phase aligns with previous explanations asserting the incorporation of $CsPbI_3$ leading to reduced tolerance factor compared with $FAPbI_3$, promoting the more stable crystallization of the black corner-sharing phase[34].

7.3.2 Mixed Pb:Sn perovskites

Next, we perform the same depositions and measurements with the same A cation stoichiometries, except this time with a 50:50 ratio of Pb:Sn as the metal ion (Figure 7.3a-c).

First, we find that in all three compositions, there is some spontaneous crystallization into the 3D perovskite phase even whilst still at room temperature, with no evidence of non-perovskite intermediates (Figure 7.3a–d). For the highest MA-containing composition, this is observed most distinctly, with perovskite peaks forming roughly 120 seconds before the temperature ramping is started. This is in agreement with literature reports of the faster reactivity of MAI compared to FAI, with SnI_2. This spontaneous crystallization occurs more weakly in $FA_{0.6}MA_{0.3}Cs_{0.1}Pb_{0.5}Sn_{0.5}I_3$ (Figure 7.3b), and significantly more weakly still in MA-free $FA_{0.83}Cs_{0.17}Pb_{0.5}Sn_{0.5}I_3$. The retarded crystallization upon 10% incorporation of Cs is in agreement with reports elsewhere[35]. The no-MA composition $FA_{0.83}Cs_{0.17}Pb_{0.5}Sn_{0.5}I_3$ composition exhibits the slowest crystallization, yet exhibits the quickest 'ripening' of the perovskite phase, evident by the plateauing of the (100) perovskite peak (Figure 7.3c,d).

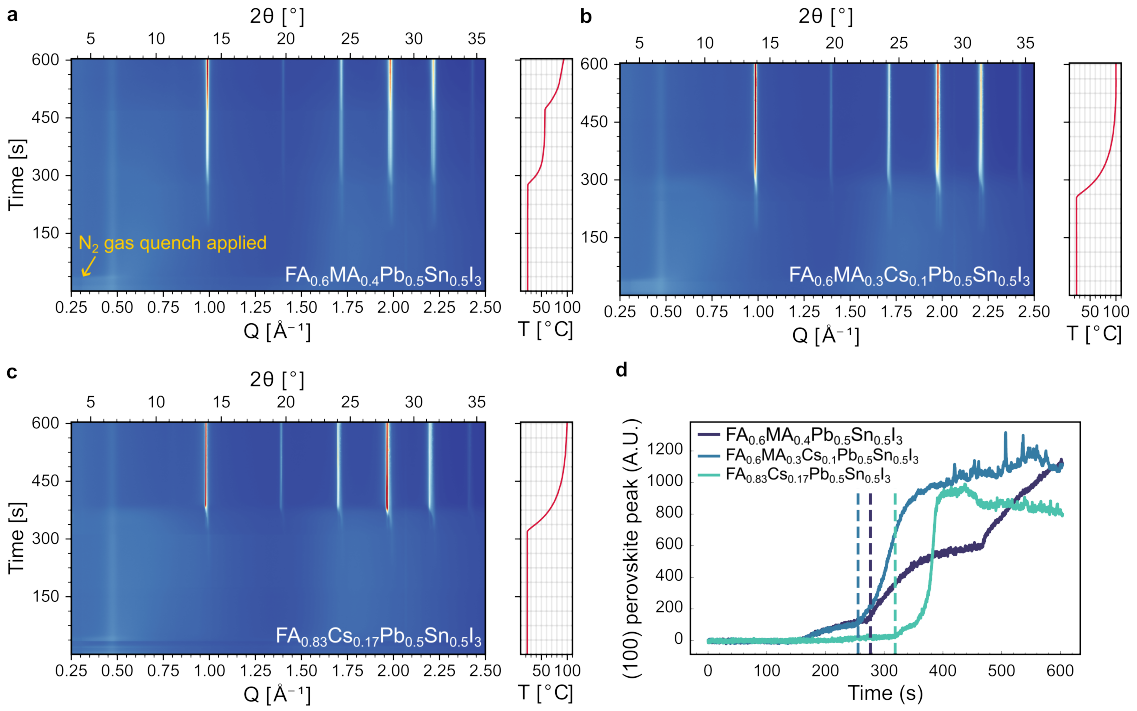


FIGURE 7.3: Pb:Sn: *In situ* GIWAXS. 1D azimuthal integration **a-c** of $FA_{0.6}MA_{0.4}Pb_{0.5}Sn_{0.5}I_3$, $FA_{0.6}MA_{0.3}Cs_{0.1}Pb_{0.5}Sn_{0.5}I_3$ and $FA_{0.83}Cs_{0.17}Pb_{0.5}Sn_{0.5}I_3$ respectively, and **d** corresponding (100) perovskite peak intensity with time. Vertical line indicates beginning of temperature ramp. In all samples, gas quenching is applied from 30 seconds. The *in situ* GIWAXS measurements were performed in collaboration with J.A. Smith, and analysed by E. Hung.

The stark lack of crystalline intermediate phase formation upon partial substitution of Pb with Sn may be attributed to a few things: first, the mixed metal ion composition may lead to competition between the formation of Pb- and Sn-intermediates. However, we investigate the pure Sn compositions $FASnI_3$ and $MASnI_3$ to verify this (Figure 7.4a-b) and observe that, even with pure FA^+ - which readily forms face-sharing hexagonal polytype structures in pure-Pb perovskites - no Sn-equivalent structure emerges, despite the similarity in the tolerance factors of $FASnI_3$ and $FAPbI_3$ (Table 7.1) for perovskite formability.

Therefore, the geometrical Goldschmidt and revised Bartel tolerance factors are insufficient for accurately describing the structural stability of corner-sharing perovskites, in the case of Sn-containing compositions. Comparing the structures of MX_2-solvate intermediates between M = Pb and Sn, there is a significant disparity in their structural arrangements. For instance, PbI_2-solvent adducts, such as

TABLE 7.1: Comparison of tolerance factors for $FASnI_3$ and $FAPbI_3$, indicating similar perovskite formability. Calculated using references [1, 2, 36–38] and Equations 2.35, 2.34, 2.37. Ionic radii of Sn^{2+} and Pb^{2+} used for this calculation are 1.15 and 1.18 Å respectively. For the Bartel tolerance factor, the ideal range is $\tau < 4.18$.

Material	**Octahedral factor** μ (ideally $0.414 < \mu < 0.732$)	**Goldschmidt tolerance factor** (ideally $0.825 < t < 1.059$)	**Bartel tolerance factor** τ
$FAPbI_3$	0.541	0.987	3.667
$FASnI_3$	0.523	0.998	3.703

PbI_2·DMSO, PbI_2·2DMSO and PbI_2·DMF, typically feature edge-sharing $[PbX_6]$ (where X = halide or solvent) clusters and chains. In contrast, Sn(II) solvates predominantly consist of isolated, non-sharing SnX_4 and SnX_5 complexes (Figure 7.5d-f). The lack of existence of $[SnX_6]$-structured solvate complexes with extended corner, edge or face-sharing suggests that these are inherently unstable.

Recently, Zhang et al. (2024) proposed that the cohesive energy of SnI_2-DMSO is lower than that of PbI_2-DMSO, indicating that Sn-perovskite crystallization occurs with a lower activation barrier[13]. This finding implies that Sn-halide bonds may be stronger than Sn-solvent interactions, which could inhibit the formation of solvent intermediates and promote the development of larger colloids. Consequently, this leads to more rapid crystallization towards a corner-sharing phase, explaining why crystallization to the corner-sharing $FASnI_3$ phase occurs more readily than for $FAPbI_3$.

Furthermore, Yang et al. (2025) reported that the slower crystallization of Pb-perovskites can be attributed to the edge-sharing $[PbI_6]^{4-}$ intermediates, which require a Pb-I bond breakage process for the organic cation to enter and form the final 3D perovskite phase[11]. In contrast, the non-sharing $[SnI_5]^{3-}$ intermediate frameworks can spontaneously transition to a corner-sharing $[SnI_6]^{4-}$ framework through electrostatic interactions.

Therefore, while the A-site cation stoichiometry significantly influences the crystalline intermediate phases observed in Pb perovskites, in mixed Pb:Sn perovskites, the Sn component appears to dominate the kinetics of the crystallization process.

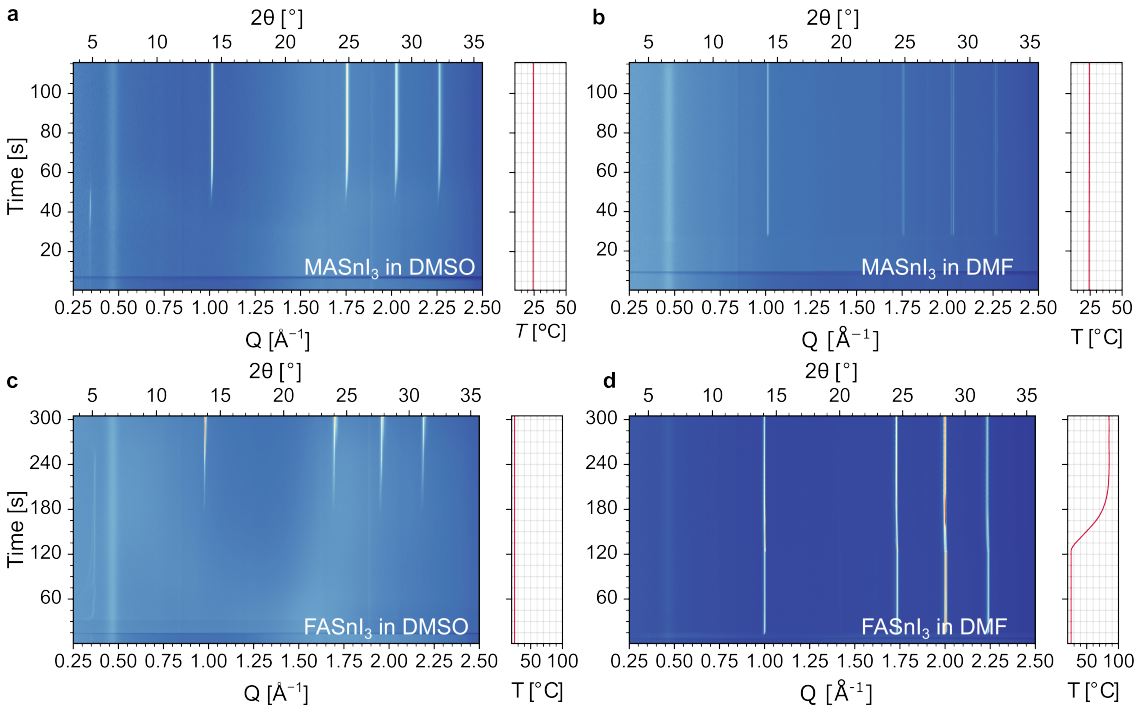


FIGURE 7.4: Pure Sn perovskite compositions. 1D azimuthal integration of *in situ* GIWAXS patterns of **a**, **b**$MASnI_3$ and **c**, **d** $FASnI_3$ compositions from pure DMSO and DMF precursor solutions, respectively. The *in situ* GIWAXS measurements were performed in collaboration with J.A. Smith, and analysed by E. Hung.

7.3.3 Solvent-based Cs-induced Intermediate Phase

In order to understand whether Pb-Sn intermediates are suppressed for all A-site cation stoichiometries, we study the effect of increased Cs incorporation on the crystallization process. We find that with caesium content greater than 30%, peaks form prior to the perovskite phase at 0.47, 0.55, 0.72 and 0.82, 0.94 $Å^{-1}$ (or 2θ = 6.7°, 7.7°, 10.11°, 11.5° and 13.2°), with several further peaks between 1.80-2.00 $Å^{-1}$ (Figure 7.6a-c), which become more prominent with increased Cs ($CsPb_{0.5}Sn_{0.5}I_3$, Figure 7.6b). To specifically identify the intermediate, we coated solutions with pure $CsSnI_3$ in DMF and DMSO, and found identical peaks to the lower Cs compositions in DMSO ($CsSnI_3$, Figure 7.6c).

For $CsPb_{0.5}Sn_{0.5}I_3$, this intermediate is coincident with the main perovskite phase crystallization (Figure 7.6d) for some time and in $CsSnI_3$ it converts directly to the 3D perovskite phase. We observe that the crystallized 3D $CsSnI_3$ phase exhibits

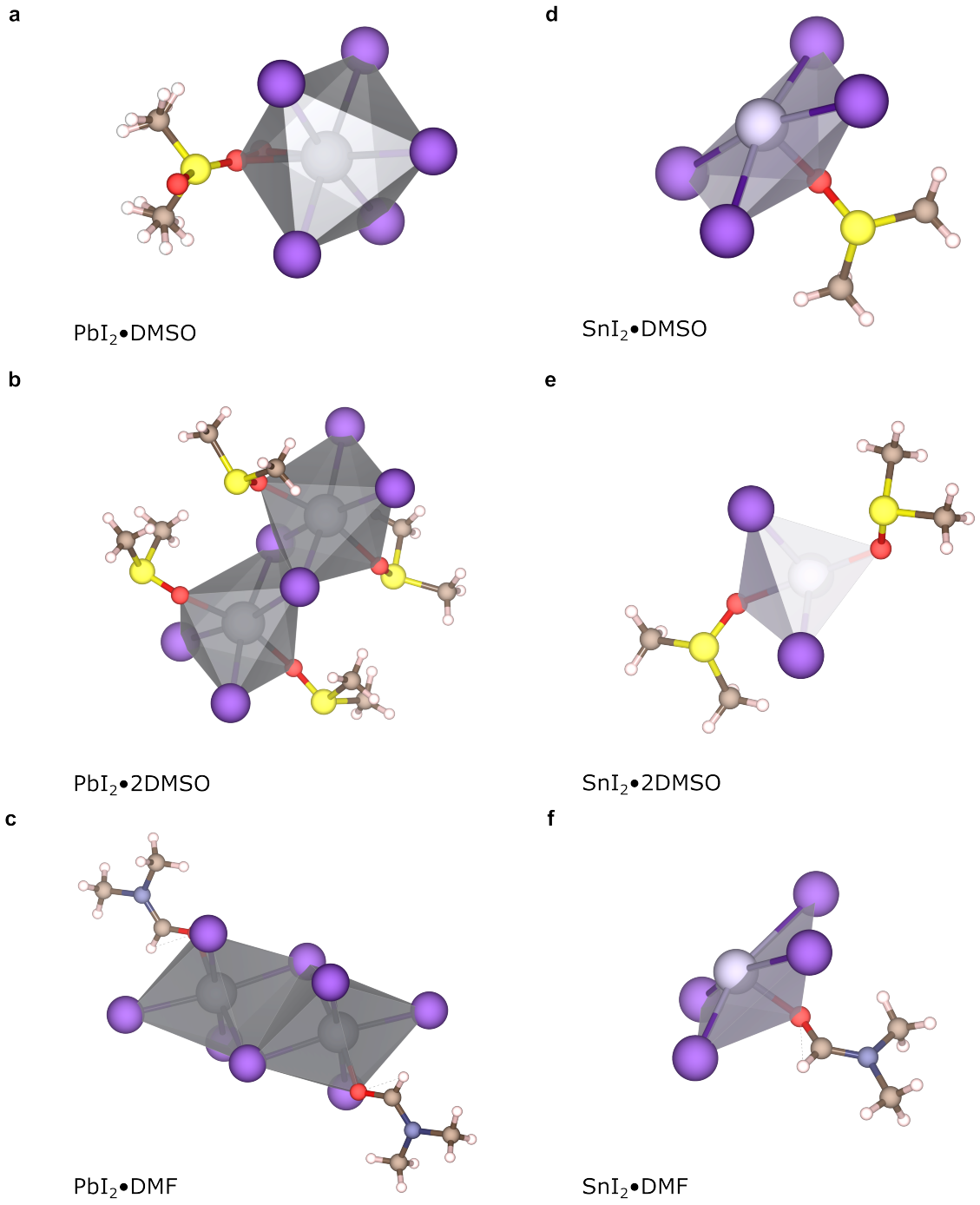


FIGURE 7.5: Visualisation of MX_2 adducts: **a** PbI_2·DMSO **b** PbI_2·2DMSO **c** PbI_2·DMF **d** SnI_2·DMSO **e** SnI_2·2DMSO **f** SnI_2·DMF. Hydrogen atoms omitted for clarity. The crystallographic data from **a-c** are reproduced with permission from Cao et al. Copyright 2016 American Chemical Society[39]. The crystallographic data for **d-f** are reproduced from the Cambridge Crystallographic Data Centre (CCDC) with reference numbers 1558257, 1558258, and 1558255 respectively.

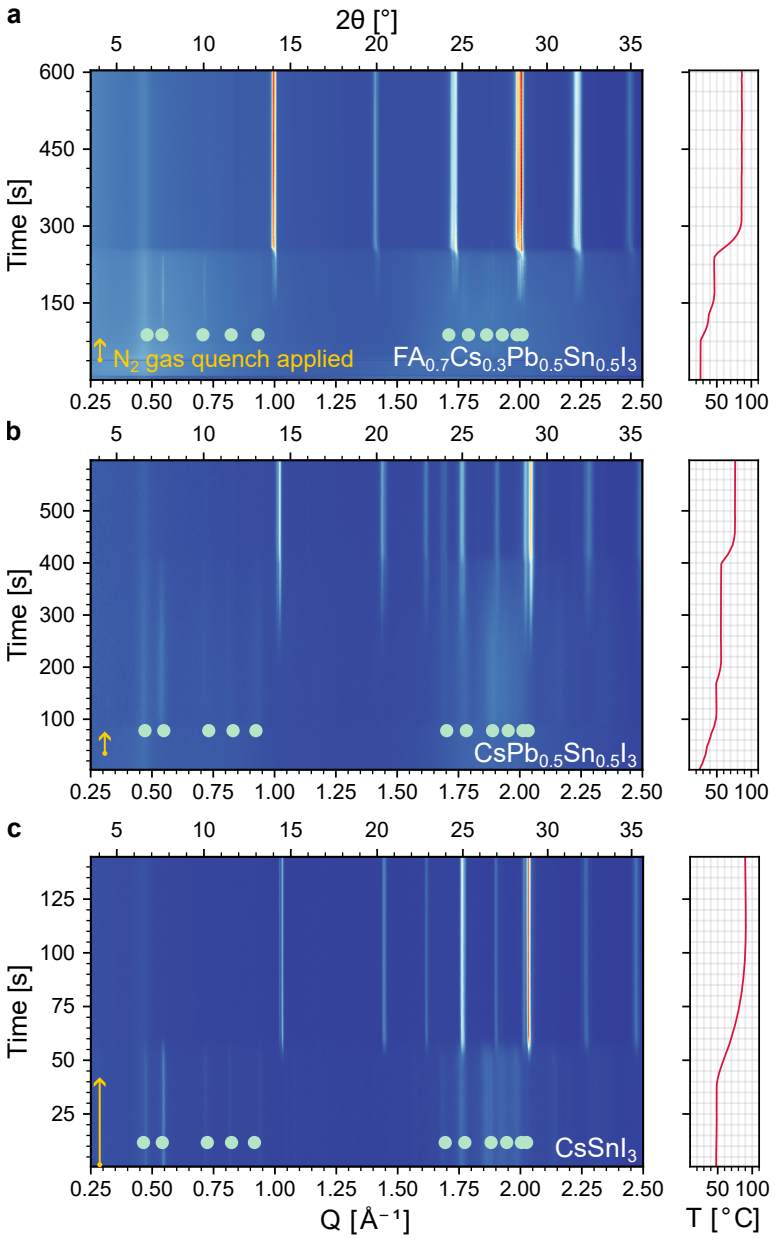


FIGURE 7.6: Caesium-induced Sn-containing intermediate phase: 1D azimuthally integrated GIWAXS patterns for **a** $FA_{0.7}Cs_{0.3}Pb_{0.5}Sn_{0.5}I_3$, **b** $CsPb_{0.5}Sn_{0.5}I_3$, and **c** $CsSnI_3$. In **c**, the data is shown from the onset of crystallization to clearly highlight the intermediate phase peaks. For all three compositions, the temperature ramp was initiated immediately upon detection of the perovskite phase formation.

weak, doubled peaks at 1.03, 1.77 and 2.04; indicative of the crystallization of the orthorhombic $CsSnI_3$ phase[40].

These peak positions do not appear in positions that might be consistent with any perovskite polymorph, nor MX_2-solvent intermediates, thus we can infer that this intermediate phase must be a coordination between the highly-coordinating host solvent (DMSO), Sn and Cs. This set of peaks do not match any previously reported intermediate phase structure to the best of our knowledge[27].

Previously, work by Moot et al. reported that in the processing of Pb-perovskite, CsI-DMSO adducts in fact dominate solution interactions for $CsPbI_3$ perovskites and slowed down nucleation of these phases[41]. Therefore, we postulate that there is a similar effect occurring in the compositions reported here.

In efforts to identify this intermediate phase, we try a slow evaporation technique for growing single crystals of a $CsSnI_3$-DMSO adduct. Structural analyses of the SCXRD data confirm this phase to be $CsSnI_3{\cdot}2DMSO$, comprised of isolated, octahedral SnI_3^- coordinated to 3 DMSO molecules (Figure 7.7, crystallographic data in Table C.1) with an orthorhombic structure. We observe several features which are unusual for Sn-based perovskites and SnI_2-solvates. First, the Sn-I and Sn-O bond lengths (2.68 - 2.81 Å, and 2.10 - 2.16 Å, respectively) are noticeably shorter than that reported for cubic-$CsSnI_3$, $SnI_2{\cdot}DMSO$, $SnI_2{\cdot}2DMSO$ and $SnI_2{\cdot}3DMSO$ (Figure 7.8). Further, one of the I-Sn-I bond angles exhibit a deviation by 10° from octahedral angles, significantly more than other I-Sn-I bond angles reported. This indicates that there are likely to be stronger bonding interactions compared with other solvate phases and 3D $CsSnI_3$. Importantly, we notice that like with the SnI_2-solvent structures, this $CsSnI_3$-solvate phase also features non-sharing frameworks. On the other hand, reported $MAPX_3$-solvent phases tend to feature corner- and edge-sharing characteristics. Despite our success in synthesising a $CsSnI_3$-solvate phase, simulation of the powder XRD pattern shows that this does not correspond with the observed intermediate during the *in situ* GIWAXS measurement. Nevertheless, this is the first report, to the best of our knowledge, of the crystal structure of a Sn-perovskite-solvent phase.

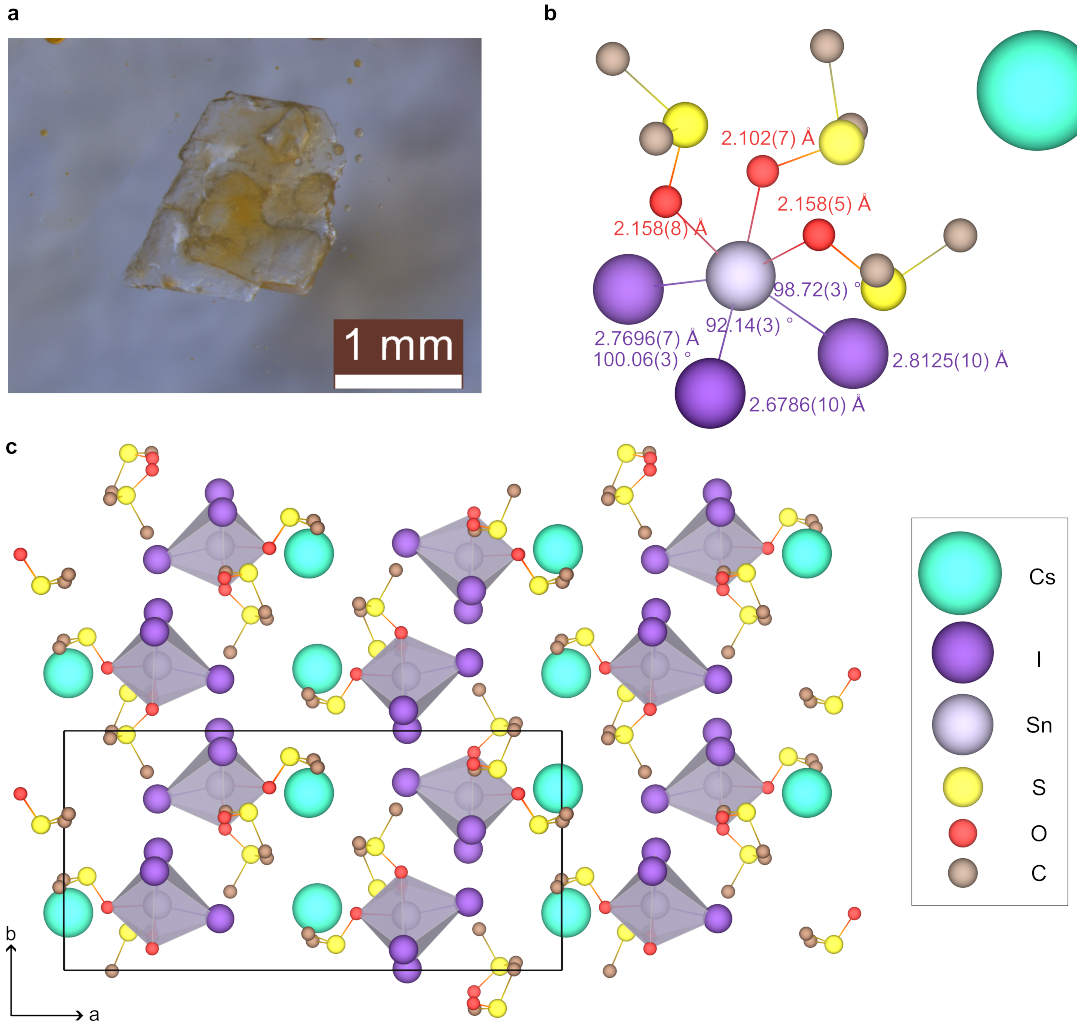


FIGURE 7.7: A novel, Cs and Sn-containing perovskite-solvate phase: $CsSnI_3 \cdot 3DMSO$. **a** Microscope image and **b**, **c** solved crystal structure. Hydrogen atoms are omitted for clarity.

7.3.4 Hexagonal polymorphs in Pb-Sn perovskites: Theoretical investigations

Given the lack of experimental observation of a hexagonal phase equivalent to the 2H phase, we turn to theoretical investigations of the relative thermodynamic stability of lead (Pb) and tin (Sn)-based phases. As observed in Figure 7.3, the 2H phase is the most thermodynamically stable and tends to dominate the crystallization process. However, other polymorphs can also form, and these may exhibit different properties or introduce defects into the material. Therefore, understanding the relative stability

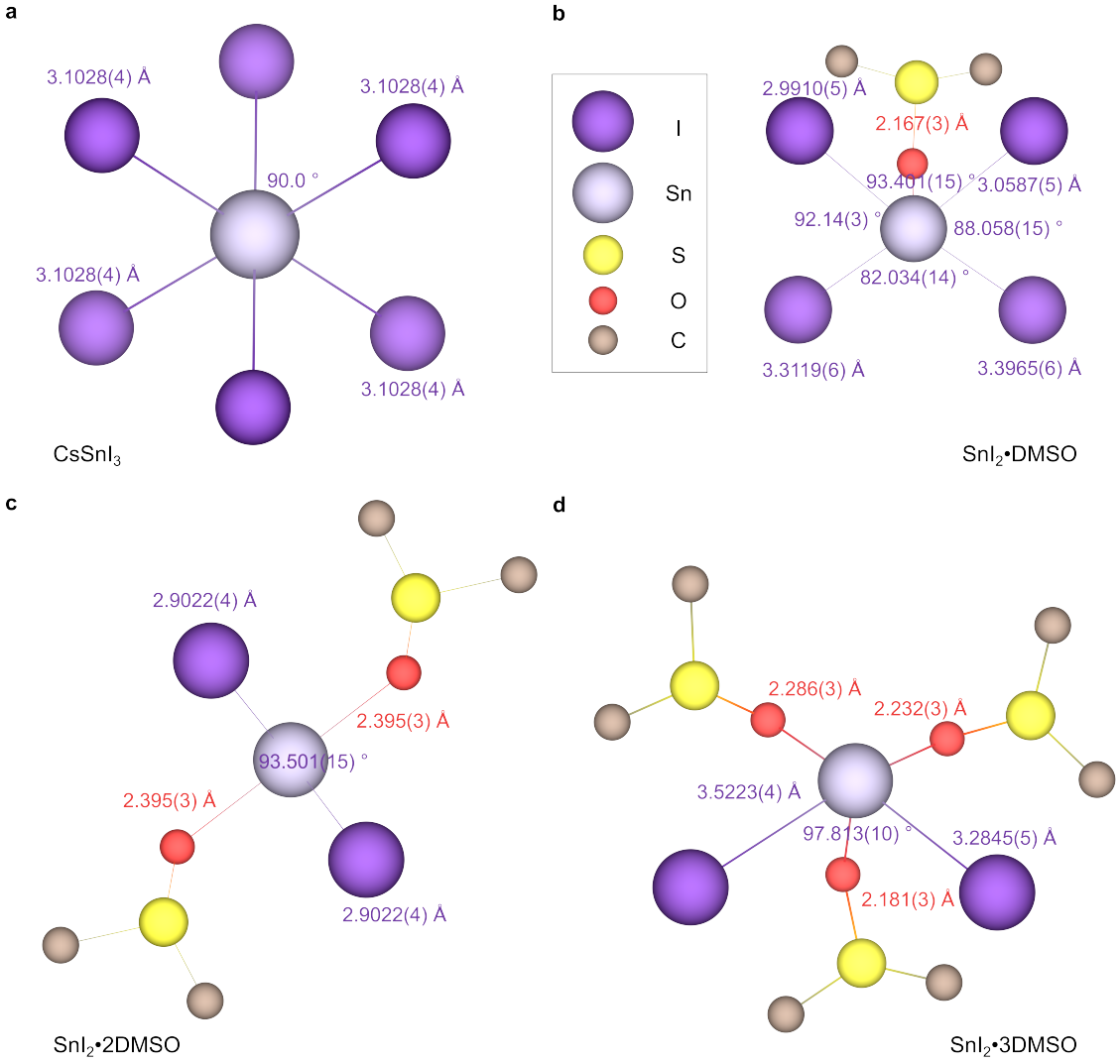


FIGURE 7.8: Visualisations of coordination connectivity with Sn in **a** cubic-$CsSnI_3$, **b** SnI_2·DMSO, **c** SnI_2·2DMSO and **d** SnI_2·3DMSO. Hydrogen atoms are omitted for clarity. **a** is reproduced from the Inorganic Crystal Structure Database (ICSD) with collection code 262924. The crystallographic data for **b-c** are reproduced from the Cambridge Crystallographic Data Centre (CCDC) with reference numbers 1558257 and 1558258, respectively. **d** is reproduced with permission from Hao et al. Copyright 2015 American Chemical Society[42]

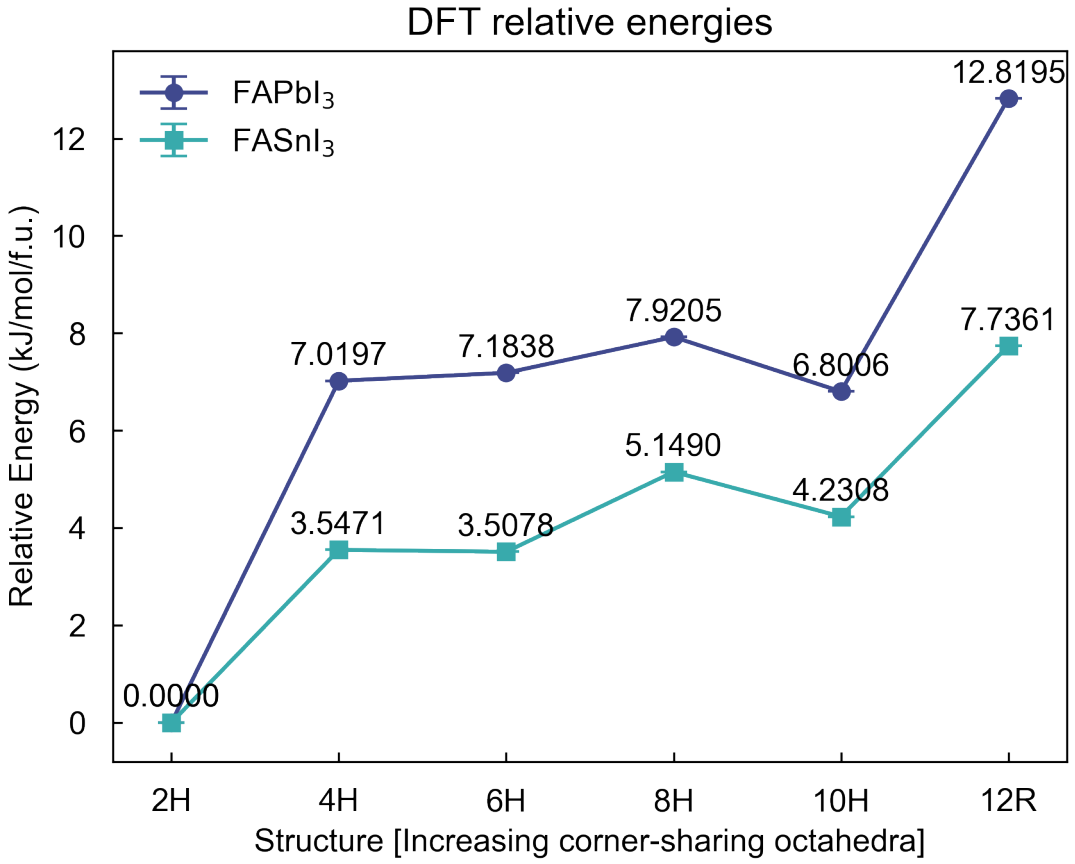


FIGURE 7.9: DFT-calculated relative energies of $FAPbI_3$ and $FASnI_3$ polymorphs with respect to their 2H polymorph. Energies are shown in kJ/mol per formula unit. The x-axis indicates the structure type, with increasing corner-sharing octahedra from left to right. Error bars represent the standard deviation of the energy, typically of size ± 0.0003 kJ/mol/f.u.. These calculations were performed by P. Ahlawat.

of these different polymorphs is crucial for controlling the formation of high-quality perovskite films, which are essential for efficient solar cells.

We employ a multiscale approach to understand their thermodynamic stability. We begin by calculating the relative energies of various polymorphs[28, 43, 44] in their increasing corner-sharing structures (2H, 4H, 6H, 8H, 10H, and 3R) using density functional theory (DFT) with xDM van der Waals (vdW) corrections[45]. By comparing the relaxed energies of the different polymorphs relative to the 2H polymorph, we can determine their relative stability. A key insight from these calculations is

that substituting Pb for Sn increases the thermodynamic stability of corner-sharing structures.

In perovskites, the metal cations (Pb or Sn) are located at the centre of octahedra formed by the halide anions (iodide in this case). These octahedra can connect in different ways: face-sharing (where two octahedra share a triangular face), edge-sharing (sharing an edge), or corner-sharing (sharing only a corner). Corner-sharing structures are generally preferred for optoelectronic applications, as they facilitate efficient charge transport. The DFT results suggest that Sn substitutions can promote the formation of these corner-sharing structures.

In order to address the limitations of DFT calculations, which are only qualitative here, we also perform large-scale finite-temperature molecular dynamics (MD) simulations, which provide a more realistic representation of the system at experimental conditions.

These simulations model the behaviour of a system of atoms over time, allowing us to study its thermodynamic properties. We use the state-of-the-art GRACE-2L machine learning potentials[46, 47] to perform these simulations. The results of the MD simulations are shown in Figure 7.10.

The large-scale MD simulations corroborate the DFT results, confirming that Sn incorporation into Pb-based perovskites enhances the formation of corner-sharing structures. This promotes crystallization of a complete, defect-free perovskite phase while reducing defective hexagonal face-sharing structures that can compromise device performance. In essence, Sn substitution guides the perovskite crystallization process towards a more thermodynamically favourable, corner-sharing arrangement, corroborating the experimental observations.

7.3.5 Hexagonal polymorphs in Pb-Sn perovskites: DMA-induced phase control

While we have demonstrated experimentally and theoretically that Sn-containing perovskites do not typically form hexagonal phases, previous work by Stoumpos et al. demonstrated that larger cations like ethylammonium (EA), guanidinium (GA),

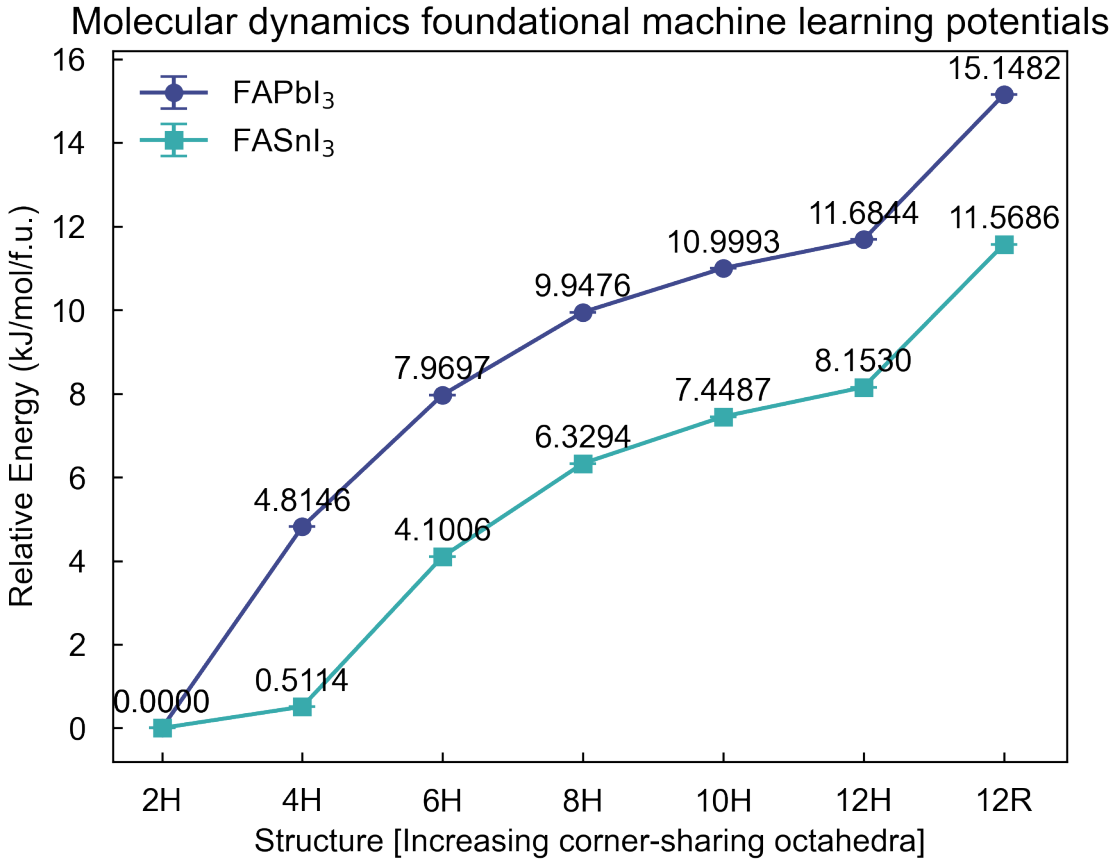


FIGURE 7.10: Relative energies of $FAPbI_3$ and $FASnI_3$ polymorphs from molecular dynamics simulations using machine learning potentials. Energies are shown in kJ/mol per formula unit. The x-axis indicates the structure type, with increasing corner-sharing octahedra from left to right. Error bars represent the standard deviation of the energy. These calculations were performed by P. Ahlawat.

and acetamidinium (ACA) can induce hexagonal polytype formation in Sn-based perovskites[28]. Building on this observation, we hypothesise that introducing a sacrificial, larger cation could similarly control the crystallization pathway in mixed Pb-Sn perovskites. This approach is inspired by McMeekin et al.'s work, where they demonstrated controlled crystallization of pure lead $FA_{0.83}CsPb(I_{0.6}Br_{0.4})_3$ perovskites by replacing DMSO with dimethylammonium chloride (DMACl)[26]. Their work showed that DMACl addition led to the formation of hexagonal polytypes that subsequently transformed into the desired 3D corner-sharing perovskite phase. Following this strategy, we introduce dimethylammonium (DMA^+) via DMACl as an additive to modulate the crystallization pathway and induce hexagonal intermediate

phases in our Pb-Sn perovskite system. Furthermore, previous reports have shown that DMSO can accelerate the oxidation of Sn^{2+} to Sn^{4+}[48, 49]. Thus, the partial replacement of DMSO with DMACl might not only control crystallization but also increase the stability of the resulting perovskite.

First, different precursor solutions of the $FA_{0.83}Cs_{0.17}Pb_{0.5}Sn_{0.5}I_3$ perovskite composition are prepared with varying DMACl content. The SEM images of the thin films deposited from these different precursor solutions are shown in Figure 7.11, where it can be seen that the introduction of DMACl leads to much larger grains compared with mixed DMF:DMSO and neat DMF precursor solutions. The films made with 40 mol% DMACl addition show the largest grain sizes with the best homogeneity. Therefore, the 40 mol% DMACl composition is selected as the optimum composition based on its film morphology.

The larger grains for the DMACl-containing system are likely due to a change in the crystallization kinetics; nucleation has been inhibited, allowing for growth to dominate the crystallization process. In order to investigate this further, we perform *in situ* GIWAXS measurements of the crystallization process of the $FA_{0.83}Cs_{0.17}Pb_{0.5}Sn_{0.5}I_3$ composition from three different precursor solutions: mixed DMF:DMSO, neat DMF, and neat DMF with 40 mol% DMACl addition (Figure 7.12). For the neat DMF precursor solution, we observe rapid crystallization of the perovskite phase during gas quenching, at room temperature, compared with the mixed DMF:DMSO solvent system (Figure 7.12a,b) which requires the thermal annealing step in order to form the perovskite phase. For the DMACl-containing system, during gas quenching at 70s, we observe characteristic hexagonal phase peaks (marked with yellow asterisks) at $Q = 0.83$, 1.14, 1.54, 1.84 and 2.13 $Å^{-1}$ ($2\theta = 11.77$, 16.06, 21.76, 26.06 and 30.26 °), which closely match the (100), (101), (002), (201) and (112) reflections of 2H-$DMAPbI_3$ (CCDC code 1570129 [50])(Figure 7.12c). The slight shift to higher Q values indicates a reduced unit cell volume due to the smaller ionic radius of the likely partially-incorporated Sn^{2+} compared to Pb^{2+}, or the inclusion of Cl^-. Given the reported presence of hexagonal polytype frameworks using larger cations such as GUA^+ and EA^+, we rationalise that a 2H-$DMASnI_3$ phase can be formed.

Shortly after the onset of this 2H phase, we observe the formation of a 3D perovskite phase (10s later, Q=1$Å^{-1}$), which remains weaker in intensity until ∼190s, at which

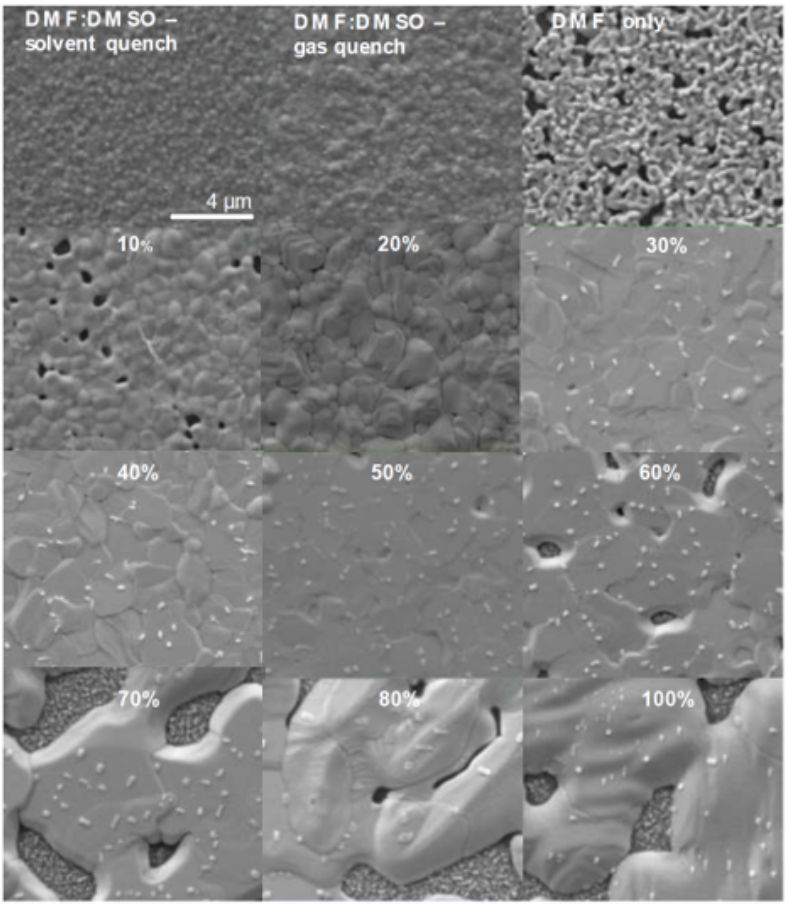


FIGURE 7.11: Scanning electron microscopy (SEM) images of thin films deposited via spin-coating, from different precursor solution compositions. The white particulates in the images are likely to be SnF_2 particles. Both the sample preparation and the SEM measurements were taken by M. Farrar.

point it begins to grow more rapidly and dominates the diffraction pattern. At this point, an unknown intermediate (blue dots, phase I) appears with peaks at $Q \sim$ 0.44, 0.48, 0.63 and 0.89 $Å^{-1}$, coinciding with a reduction in intensity of the 2H phase. This indicates a partial conversion from the 2H phase to the desired 3D perovskite phase partially via the intermediate phase I. Whilst the peak at 0.48 $Å^{-1}$ appears first, this could be an intermediate which reorients during the crystallization process, leading to the domination by the other peaks. We hypothesise this phase to be a DMA-PbSn-X coordination, or a DMA-PbSn-solvent coordination phase.

We also note a small positive shift in the final perovskite peak positions ($\sim$0.2°), which might indicate induction of lattice strain caused by this crystallization pathway, or perhaps partial Cl incorporation. This composition requires annealing at

higher temperature (∼150°C) in order to volatilise the DMA^+ cation and remove the 2H-perovskite intermediate.

The conversion to and ripening of the final 3D perovskite phase occurs significantly more slowly in the DMACl-containing system (∼600s) compared with the mixed DMF:DMSO system (∼375s) and neat DMF system (∼60s). This likely allows for a domination of the growth process instead of nucleation, leading to the larger grains observed in the SEM images.

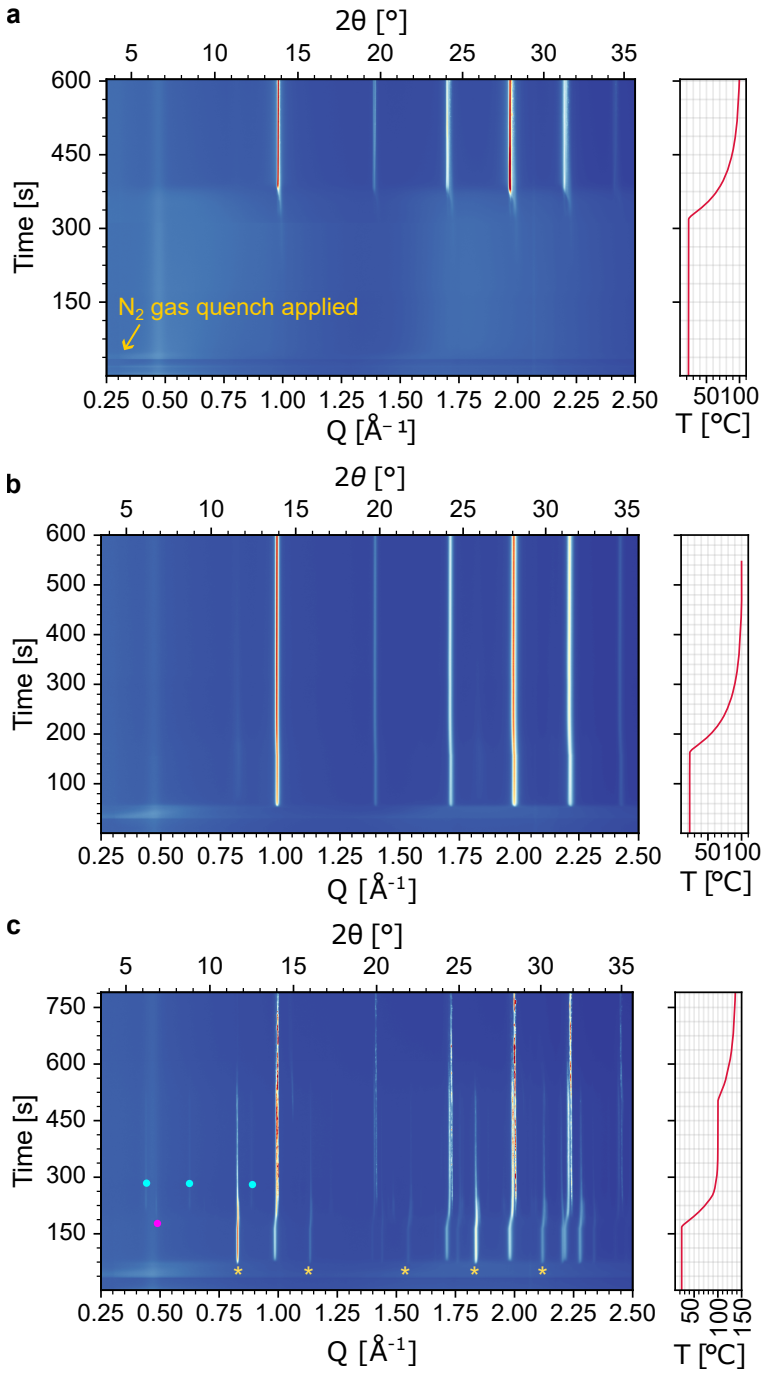


FIGURE 7.12: *In situ* GIWAXS measurements of the formation of hexagonal phases with DMACl addition. **a** DMF:DMSO 3:1 (reproduced from Figure 7.3c for comparison), **b** DMF, **c** DMF and 40 mol% DMACl. 2H-perovskite peaks are indicated by the yellow asterisks. Unknown phases are indicated by the blue and purple circles. In the deposition of all 3 compositions, nitrogen gas quenching was applied at 30s. For the neat-DMF-based and DMF:DMACl compositions, gas quenching was applied for 120s and 270s, respectively. These measurements were taken by J.A. Smith and analysed by E.Y.H. Hung

7.4 Conclusion

Our investigation of Pb-Sn perovskites using *in situ* GIWAXS, DFT, and MD simulations with machine learning potentials reveals that Sn incorporation fundamentally alters the crystallization behaviour compared to pure-Pb compositions. Whilst A-site cations strongly influence crystallization pathways in pure-Pb perovskites, Sn incorporation typically dominates the crystallization kinetics, favouring direct formation of 3D corner-sharing perovskite phases. However, we identified two notable exceptions where A-site cation effects remain significant: (1) the emergence of a Cs-induced solvent-based intermediate phase in high-Cs compositions, and (2) the formation of a hexagonal phase when DMACl is present. In the first case, the strong coordination between Cs^+ and DMSO molecules outcompetes Sn-I bonding, enabling the formation of a novel Cs-DMSO-SnI_3 intermediate phase. In the second case, the larger DMA^+ cation induces a metastable 2H-DMA(Pb,Sn)I_3 phase that serves as a template for the subsequent growth of the final 3D perovskite phase, ultimately leading to improved film morphology and crystallinity. These findings demonstrate that Sn-containing perovskites exhibit fundamentally different crystallization kinetics compared to pure-Pb perovskites, necessitating novel approaches to control their crystallization pathways. This understanding is critical for developing high-quality perovskite films with optimal optoelectronic properties and device performance, where the deliberate induction of certain polytype phases or solvent intermediates can be used to influence the final film structure stability and grain size.

Bibliography

[1] R. D. Shannon, "Revised effective ionic radii and systematic studies of interatomic distances in halides and chalcogenides," *Journal of Applied Crystallography*, vol. 32, pp. 751–767, 1976.

[2] W. Travis, E. N. Glover, H. Bronstein, D. O. Scanlon, and R. G. Palgrave, "On the application of the tolerance factor to inorganic and hybrid halide perovskites: a revised system," *Chemical Science*, vol. 7, pp. 4548–4556, 2016.

[3] F. Hao, C. C. Stoumpos, R. P. Chang, and M. G. Kanatzidis, "Anomalous band gap behavior in mixed Sn and Pb perovskites enables broadening of absorption spectrum in solar cells," *Journal of the American Chemical Society*, vol. 136, pp. 8094–8099, 2014.

[4] F. Yang and K. Zhu, "Advances in mixed Tin-Lead narrow-bandgap perovskites for single-junction and all-perovskite tandem solar cells," *Advanced Materials*, vol. 36, p. 2314341, 2024.

[5] C. Frasca, P. Alippi, R. Schwiddessen, K. Prashanthan, G. Nasti, S. Zuo, M. O. U. Rehman, M. H. Aldamasy, N. T. P. Hartono, A. Musiienko, and A. Abate, "Mitigation of self-p-doping and off-centering effect in tin perovskite via strontium doping," *ACS Energy Letters*, vol. 10, pp. 526–533, 2025.

[6] D. Ricciarelli, D. Meggiolaro, F. Ambrosio, and F. D. Angelis, "Instability of tin iodide perovskites: Bulk p-doping versus surface tin oxidation," *ACS Energy Letters*, vol. 5, pp. 2787–2795, 2020.

[7] D. Meggiolaro, D. Ricciarelli, A. A. Alasmari, F. A. Alasmary, and F. D. Angelis, "Tin versus lead redox chemistry modulates charge trapping and self-doping in tin/lead iodide perovskites," *Journal of Physical Chemistry Letters*, vol. 11, pp. 3546–3556, 2020.

[8] M. Xiao, S. Gu, P. Zhu, M. Tang, W. Zhu, R. Lin, C. Chen, W. Xu, T. Yu, and J. Zhu, "Tin-based perovskite with improved coverage and crystallinity through tin-fluoride-assisted heterogeneous nucleation," *Advanced Optical Materials*, vol. 6, p. 1700615, 2018.

[9] Z. Zhang, Y. Huang, J. Jin, Y. Jiang, Y. Xu, J. Zhu, and D. Zhao, "Mechanistic understanding of oxidation of tin-based perovskite solar cells and mitigation strategies," *Angewandte Chemie International Edition*, vol. 62, p. e202308093, 2023.

[10] S. Hu, J. Thiesbrummel, J. Pascual, M. Stolterfoht, A. Wakamiya, and H. J. Snaith, "Narrow bandgap metal halide perovskites for all-perovskite tandem photovoltaics," *Chemical Reviews*, vol. 124, pp. 4079–4123, 2024.

[11] X. Yang, T. Ma, H. Hu, W. Ye, X. Li, M. Li, A. Zhang, C. Ge, X. Sun, Y. Zhu, S. Yan, J. Yan, Y. Zhou, Z. Li, C. Chen, H. Song, and J. Tang, "Understanding and manipulating the crystallization of Sn-Pb perovskites for efficient all-perovskite tandem solar cells," *Nature Photonics 2025*, pp. 1–8, 2025.

[12] A. R. Bowman, M. T. Klug, T. A. Doherty, M. D. Farrar, S. P. Senanayak, B. Wenger, G. Divitini, E. P. Booker, Z. Andaji-Garmaroudi, S. Macpherson, E. Ruggeri, H. Sirringhaus, H. J. Snaith, and S. D. Stranks, "Microsecond carrier lifetimes, controlled p-doping, and enhanced air stability in low-bandgap metal halide perovskites," *ACS Energy Letters*, vol. 4, pp. 2301–2307, 2019.

[13] Y. Zhang, C. Li, H. Zhao, Z. Yu, X. Tang, J. Zhang, Z. Chen, J. Zeng, P. Zhang, L. Han, and H. Chen, "Synchronized crystallization in tin-lead perovskite solar cells," *Nature Communications 2024 15:1*, vol. 15, pp. 1–11, 2024.

[14] M. M. Byranvand, W. Zuo, R. Imani, M. Pazoki, and M. Saliba, "Tin-based halide perovskite materials: properties and applications," *Chemical Science*, vol. 13, pp. 6766–6781, 2022.

[15] S. Lv, W. Gao, C. Ran, D. Li, L. Chao, X. Wang, L. Song, Z. Lin, L. Fu, and Y. Chen, "Antisolvent-free fabrication of efficient and stable Sn-Pb perovskite solar cells," *Solar RRL*, vol. 5, p. 5, 2021.

[16] Y. Sun, S. Yang, Z. Pang, Y. Quan, R. Song, Y. Chen, W. Qi, Y. Gao, F. Wang, X. Zhang, Y. Sun, J. Yang, L. Yang, and F. Rosei, "Preferred film orientation to achieve stable and efficient Sn-Pb binary perovskite solar cells," *ACS Applied Materials and Interfaces*, vol. 13, pp. 10822–10836, 2021.

[17] X. Lian, J. Chen, Y. Zhang, M. Qin, J. Li, S. Tian, W. Yang, X. Lu, G. Wu, H. Chen, X. Lian, J. Chen, Y. Zhang, J. Li, S. Tian, W. Yang, G. Wu, H. Chen, M. Qin, and X. Lu, "Highly efficient Sn/Pb binary perovskite solar cell via precursor engineering: A two-step fabrication process," *Advanced Functional Materials*, vol. 29, p. 1807024, 2019.

[18] J. Werner, T. Moot, T. A. Gossett, I. E. Gould, A. F. Palmstrom, E. J. Wolf, C. C. Boyd, M. F. V. Hest, J. M. Luther, J. J. Berry, and M. D. McGehee,

"Improving low-bandgap tin-lead perovskite solar cells via contact engineering and gas quench processing," *ACS Energy Letters*, vol. 5, pp. 1215–1223, 2020.

[19] H. Liu, L. Wang, R. Li, B. Shi, P. Wang, Y. Zhao, and X. Zhang, "Modulated crystallization and reduced Voc deficit of mixed lead-tin perovskite solar cells with antioxidant caffeic acid," *ACS Energy Letters*, vol. 6, pp. 2907–2916, 2021.

[20] J. Zhou, S. Fu, S. Zhou, L. Huang, C. Wang, H. Guan, D. Pu, H. Cui, C. Wang, T. Wang, W. Meng, G. Fang, and W. Ke, "Mixed tin-lead perovskites with balanced crystallization and oxidation barrier for all-perovskite tandem solar cells," *Nature Communications 2024 15:1*, vol. 15, pp. 1–10, 2024.

[21] J. Xi, H. Duim, M. Pitaro, K. Gahlot, J. Dong, G. Portale, and M. A. Loi, "Scalable, template driven formation of highly crystalline lead-tin halide perovskite films," *Advanced Functional Materials*, vol. 31, p. 31, 2021.

[22] E. Ruggeri, M. Anaya, K. Gałkowski, G. Delport, F. U. Kosasih, A. Abfalterer, S. Mackowski, C. Ducati, S. D. Stranks, E. Ruggeri, M. Anaya, K. Gałkowski, G. Delport, A. Abfalterer, S. D. Stranks, S. Mackowski, F. U. Kosasih, and C. Ducati, "Controlling the growth kinetics and optoelectronic properties of 2D/3D lead-tin perovskite heterojunctions," *Advanced Materials*, vol. 31, p. 1905247, 2019.

[23] T. Bu, J. Li, H. Li, C. Tian, J. Su, G. Tong, L. K. Ono, C. Wang, Z. Lin, N. Chai, X. L. Zhang, J. Chang, J. Lu, J. Zhong, W. Huang, Y. Qi, Y. B. Cheng, and F. Huang, "Lead halide-templated crystallization of methylamine-free perovskite for efficient photovoltaic modules," *Science*, vol. 372, pp. 1327–1332, 2021.

[24] S. Macpherson, T. A. Doherty, A. J. Winchester, S. Kosar, D. N. Johnstone, Y. H. Chiang, K. Galkowski, M. Anaya, K. Frohna, A. N. Iqbal, S. Nagane, B. Roose, Z. Andaji-Garmaroudi, K. W. Orr, J. E. Parker, P. A. Midgley, K. M. Dani, and S. D. Stranks, "Local nanoscale phase impurities are degradation sites in halide perovskites," *Nature 2022 607:7918*, vol. 607, pp. 294–300, 2022.

[25] T. A. Doherty, S. Nagane, D. J. Kubicki, Y. K. Jung, D. N. Johnstone, A. N. Iqbal, D. Guo, K. Frohna, M. Danaie, E. M. Tennyson, S. Macpherson, A. Abfalterer, M. Anaya, Y. H. Chiang, P. Crout, F. S. Ruggeri, S. M. Collins, C. P.

Grey, A. Walsh, P. A. Midgley, and S. D. Stranks, "Stabilized tilted-octahedra halide perovskites inhibit local formation of performance-limiting phases," *Science*, vol. 374, pp. 1598–1605, 2021.

[26] D. P. McMeekin, P. Holzhey, S. O. Fürer, S. P. Harvey, L. T. Schelhas, J. M. Ball, S. Mahesh, S. Seo, N. Hawkins, J. Lu, M. B. Johnston, J. J. Berry, U. Bach, and H. J. Snaith, "Intermediate-phase engineering via dimethylammonium cation additive for stable perovskite solar cells," *Nature Materials 2022 22:1*, vol. 22, pp. 73–83, 2022.

[27] Z. Zhang, J. Liang, J. Wang, Y. Zheng, X. Wu, C. Tian, A. Sun, Z. Chen, and C. C. Chen, "Resolving mixed intermediate phases in methylammonium-free Sn-Pb alloyed perovskites for high-performance solar cells," *Nano-Micro Letters*, vol. 14, pp. 1–19, 2022.

[28] C. C. Stoumpos, L. Mao, C. D. Malliakas, and M. G. Kanatzidis, "Structure-band gap relationships in hexagonal polytypes and low-dimensional structures of hybrid tin iodide perovskites," *Inorganic Chemistry*, vol. 56, pp. 56–73, 2017.

[29] K. Meng, L. Wu, Z. Liu, X. Wang, Q. Xu, Y. Hu, S. He, X. Li, T. Li, G. Chen, K. Meng, L. Wu, Z. Liu, X. Wang, Q. Xu, Y. Hu, S. He, T. Li, G. Chen, and X. Li, "In situ real-time study of the dynamic formation and conversion processes of metal halide perovskite films," *Advanced Materials*, vol. 30, p. 1706401, 2018.

[30] M. Senno and S. Tinte, "Mixed formamidinium-methylammonium lead iodide perovskite from first-principles: hydrogen-bonding impact on the electronic properties," *Physical Chemistry Chemical Physics*, vol. 23, pp. 7376–7385, 2021.

[31] J. H. Lee, J. H. Lee, E. H. Kong, and H. M. Jang, "The nature of hydrogen-bonding interaction in the prototypic hybrid halide perovskite, tetragonal CH3NH3PbI3," *Scientific Reports 2016 6:1*, vol. 6, pp. 1–12, 2016.

[32] H. X. Dang, K. Wang, M. Ghasemi, M. C. Tang, M. D. Bastiani, E. Aydin, E. Dauzon, D. Barrit, J. Peng, D. M. Smilgies, S. D. Wolf, and A. Amassian, "Multi-cation synergy suppresses phase segregation in mixed-halide perovskites," *Joule*, vol. 3, pp. 1746–1764, 2019.

[33] P. Ahlawat, "Crystallization of FAPbI3: Polytypes and stacking faults," *Journal of Chemical Physics*, vol. 159, p. 151102, 2023.

[34] Z. Li, M. Yang, J. S. Park, S. H. Wei, J. J. Berry, and K. Zhu, "Stabilizing perovskite structures by tuning tolerance factor: Formation of formamidinium and cesium lead iodide solid-state alloys," *Chemistry of Materials*, vol. 28, pp. 284–292, 2016.

[35] G. Zhou, J. Wu, Y. Zhao, Y. Li, J. Shi, Y. Li, H. Wu, D. Li, Y. Luo, and Q. Meng, "Application of cesium on the restriction of precursor crystallization for highly reproducible perovskite solar cells exceeding 20efficiency," *ACS Applied Materials and Interfaces*, vol. 10, pp. 9503–9513, 2018.

[36] C. J. Bartel, C. Sutton, B. R. Goldsmith, R. Ouyang, C. B. Musgrave, L. M. Ghiringhelli, and M. Scheffler, "New tolerance factor to predict the stability of perovskite oxides and halides," *Science Advances*, vol. 5, p. 23752548, 2019.

[37] V. M. Goldschmidt, "Krystallbau und chemische zusammensetzung," *Berichte der deutschen chemischen Gesellschaft (A and B Series)*, vol. 60, pp. 1263–1296, 1927.

[38] C. Li, K. C. K. Soh, and P. Wu, "Formability of ABO3 perovskites," *Journal of Alloys and Compounds*, vol. 372, pp. 40–48, 2004.

[39] J. Cao, X. Jing, J. Yan, C. Hu, R. Chen, J. Yin, J. Li, and N. Zheng, "Identifying the molecular structures of intermediates for optimizing the fabrication of high-quality perovskite films," *Journal of the American Chemical Society*, vol. 138, pp. 9919–9926, 2016.

[40] K. Yamada, S. Funabiki, H. Horimoto, T. Matsui, T. Okuda, and S. Ichiba, "Structural phase transitions of the polymorphs of CsSnI3 by means of Rietveld analysis of the X-ray diffraction," *Chemistry Letters*, vol. 20, pp. 801–804, 1991.

[41] T. Moot, A. R. Marshall, L. M. Wheeler, S. N. Habisreutinger, T. H. Schloemer, C. C. Boyd, D. R. Dikova, G. F. Pach, A. Hazarika, M. D. McGehee, H. J. Snaith, and J. M. Luther, "CsI-antisolvent adduct formation in all-inorganic metal halide perovskites," *Advanced Energy Materials*, vol. 10, p. 1903365, 2020.

[42] F. Hao, C. C. Stoumpos, P. Guo, N. Zhou, T. J. Marks, R. P. Chang, and M. G. Kanatzidis, "Solvent-mediated crystallization of ch3nh3sni3 films for heterojunction depleted perovskite solar cells," *Journal of the American Chemical Society*, vol. 137, pp. 11445–11452, 2015.

[43] P. Gratia, I. Zimmermann, P. Schouwink, J. H. Yum, J. N. Audinot, K. Sivula, T. Wirtz, and M. K. Nazeeruddin, "The many faces of mixed ion perovskites: Unraveling and understanding the crystallization process," *ACS Energy Letters*, vol. 2, pp. 2686–2693, 2017.

[44] Z. A. Nan, L. Chen, Q. Liu, S. H. Wang, Z. X. Chen, S. Y. Kang, J. B. Ji, Y. Y. Tan, Y. Hui, J. W. Yan, Z. X. Xie, W. Z. Liang, B. W. Mao, and Z. Q. Tian, "Revealing phase evolution mechanism for stabilizing formamidinium-based lead halide perovskites by a key intermediate phase," *Chem*, vol. 7, pp. 2513–2526, 2021.

[45] A. Otero-De-La-Roza and E. R. Johnson, "Van der Waals interactions in solids using the exchange-hole dipole moment model," *Journal of Chemical Physics*, vol. 136, p. 174109, 2012.

[46] A. Bochkarev, Y. Lysogorskiy, and R. Drautz, "Graph Atomic Cluster Expansion for semilocal interactions beyond equivariant message passing," *Physical Review X*, vol. 14, p. 021036, 2024.

[47] G. Bussi, D. Donadio, and M. Parrinello, "Canonical sampling through velocity rescaling," *Journal of Chemical Physics*, vol. 126, p. 22, 2007.

[48] M. I. Saidaminov, I. Spanopoulos, J. Abed, W. Ke, J. Wicks, M. G. Kanatzidis, and E. H. Sargent, "Conventional solvent oxidizes Sn(II) in perovskite inks," *ACS Energy Letters*, vol. 5, pp. 1153–1155, 2020.

[49] J. Pascual, G. Nasti, M. H. Aldamasy, J. A. Smith, M. Flatken, N. Phung, D. D. Girolamo, S. H. Turren-Cruz, M. Li, A. Dallmann, R. Avolio, and A. Abate, "Origin of Sn(II) oxidation in tin halide perovskites," *Materials Advances*, vol. 1, pp. 1066–1070, 2020.

[50] D. Ju, T. Zhao, D. Yangyang, G. Zhang, X. Hu, D. Cui, and X. Tao, "Gas induced conversion of hybrid perovskite single crystal to single crystal for great

enhancement of their photoelectric properties," *Journal of Materials Chemistry A*, vol. 5, pp. 21919–21925, 2017.

Chapter 8

Conclusions and future outlook

The first part of this thesis presents detailed studies of novel organic-inorganic hybrid systems for piezoelectric applications. While inorganic ceramic oxides like PZT dominate the piezoelectric materials landscape, their high production costs, brittleness, and environmental concerns have driven the search for sustainable alternatives. Organic-inorganic hybrid systems emerge as a promising solution, potentially combining the superior piezoelectric performance of inorganic ceramics with the cost-effectiveness and flexibility of organic materials. However, current high-performance organic-inorganic metal halides predominantly contain toxic metals such as Pb, Cd, and Mn. Addressing this limitation, we have developed a new family of organic-inorganic hybrid metal halides based on the "quasi-spherical" theory design principles, utilising the low-toxicity transition metal cation Bi^{3+}.

First, in Chapter 4 we demonstrated the development of a 0D bismuthate framework based on discrete $(Bi_2I_9)^{3-}$ anions paired with "quasi-spherical" $(TMIM)^+$ cations, forming $(TMIM)_3Bi_2I_9$. This material exhibits a highly distorted, non-centrosymmetric, and polar structure due to halogen-halogen interactions between the inorganic and organic components. Remarkably, even at temperatures above its phase transition at 139 °C, the distorted piezoelectric phase is maintained. Through variable temperature single crystal X-ray diffraction and solid-state nuclear magnetic resonance spectroscopy, we revealed that $(TMIM)_3Bi_2I_9$ undergoes a phase transition with simultaneous order-disorder and displacive characteristics, driven by the breaking of halogen bonding at elevated temperatures. The material's versatility for

piezoelectric applications is further demonstrated by its ease of processing into single crystals, microcrystalline powders, and thin films using low-cost, low-temperature techniques. Our comprehensive characterisation using *in situ* electric field dependent X-ray diffraction confirmed the piezoelectric nature of $(TMIM)_3Bi_2I_9$, while piezoresponse force microscopy measurements revealed a substantial piezoelectric response of 161.5 pC N^{-1}. This performance is comparable to $BaTiO_3$ and previously reported high-performance Pb- or Cd-based hybrid materials, while significantly exceeding the performance of previously reported Bi-based hybrid materials.

In order to further explore the potential of bismuthate frameworks for piezoelectric applications, we also investigated structural modifications to $(TMIM)_3Bi_2I_9$ in Chapter 5. This investigation yielded three novel materials: $(TMBM)_3Bi_2Br_9$, $(TMCM)_3Bi_2Cl_9$, and $(TMIM)_3Sb_2I_9$. The first two compounds represent systematic modifications of $(TMIM)_3Bi_2I_9$ through simultaneous halogen and halide substitution, crystallizing in the polar, non-centrosymmetric space group $P6_3mc$. Thermal analysis and second harmonic generation (SHG) measurements demonstrated that these materials maintain their non-centrosymmetric structure at elevated temperatures, exhibiting superior thermal stability with decomposition temperatures of 280 °C and 320 °C, respectively, compared to $(TMIM)_3Bi_2I_9$'s stability limit of 250 °C. $(TMIM)_3Sb_2I_9$ is isostructural with $(TMIM)_3Bi_2I_9$, maintaining the distorted inorganic framework previously observed. Using variable temperature single crystal X-ray diffraction and solid-state nuclear magnetic resonance spectroscopy, we revealed that $(TMBM)_3Bi_2Br_9$ and $(TMCM)_3Bi_2Cl_9$ exhibit phase transitions predominantly driven by order-disorder characteristics, where each transition is associated with restricted modes of orientational disorder. In each transition, the $P6_3mc$ space group is maintained. For $(TMIM)_3Sb_2I_9$, as with $(TMIM)_3Bi_2I_9$, the phase transition is driven by both an order-disorder and displacive mechanism at 126 °C. Whilst the impact of this on their piezoelectric performance is not yet known, these materials represent a promising step towards the structural understanding and systematic design of high-performance organic-inorganic hybrid metal halides.

Throughout our investigations on these materials, we also synthesised a series of novel hybrid metal halides. We found that by attempting to induce halide mixing in $(TMIM)_3Bi_2I_9$, instead $(TMIM)_3BiBr_6$ was formed, a centrosymmetric orthorhombic structure composed of isolated $(BiBr_6)^{3-}$. Chloride-doping, however, led to the

formation of another non-centrosymmetric material, $(TMIM)_3Bi_2Cl_9$, which crystallizes in the polar, non-centrosymmetric space group $P6_3mc$, and consists of isolated $(Bi_2Cl_9)^{3-}$ anions, isostructural with $(TMBM)_3Bi_2Br_9$ and $(TMCM)_3Bi_2Cl_9$. On the other hand, inserting $(TMCM)^+$ cations into a $(Bi_2I_9)^{3-}$ and $(Bi_2Br_9)^{3-}$ framework led to the formation of hexagonal, centrosymmetric $(TMCM)_3Bi_2I_9$ and $(TMCM)_3Bi_2Br_9$ with space groups $P6_3/mmc$. Whilst these materials have not yet been investigated in detail, there is clearly more to be understood about fine-tuning the (non)-centrosymmetry of these materials. Furthermore, we synthesised Sb-based single crystals of $(TMIM)_3Sb_2Br_9{\cdot}Br_2$ (polar and non-centrosymmetric Pna_21) and $(TMCM)_3Sb_2I_9{\cdot}I_2$ (centrosymmetric $C2/c$), although these materials are unlikely to be thermally stable owing to the inclusion of molecular Br_2 or I_2. In order to understand the impact of using a much larger cation, $(FMTMA)^+$ cations were inserted into the $(Bi_2X_9)^{3-}$ frameworks, leading to the formation of a series of centrosymmetric materials.

Finally, we investigated solution-based crystallization of lead and mixed Pb-Sn halide perovskite thin films in Chapter 7. First, the crystallization of pure-Pb halide perovskite films from mixed DMF:DMSO precursor solutions led to crystallization of 3D perovskite phases via well-known intermediates $MA_2Pb_3I_8$ and the 2H polytype. Mixed Pb-Sn (50:50) perovskite films, however, suppressed the formation of any crystalline intermediates until the Cs content was increased to 30% on the A-site. At this point, a novel crystalline solvent intermediate was identified, and determined to be a coordination between $CsSnI_3$ and DMSO. A different solvent intermediate, $CsSnI_3{\cdot}3DMSO$, was separately identified via single-crystal growth. We also sought to answer the question of the rationale for the lack of presence of reported hexagonal polytypes in Sn-containing perovskites. Using machine learning potentials to assist molecular dynamics simulations, we demonstrate that the formation of the hexagonal polytypes in Sn-perovskites is thermodynamically unfavourable compared with Pb-perovskites. However, by incorporating dimethylammonium $(DMA)^+$ cations into the crystallization process, we were able to induce the formation of 3D perovskite via a novel hexagonal polytype, leading to larger, more uniform crystal grains.

8.1 Concluding Remarks

This thesis has significantly advanced our understanding of both the design of novel hybrid materials and their crystallization processes. Through comprehensive structural characterisation using X-ray diffraction techniques, we have established clear relationships between chemical design parameters and material properties, particularly in the context of piezoelectric applications. The development of numerous novel materials, most notably the high-performance Bi-based systems, represents a major step toward addressing the toxicity concerns in the piezoelectric materials industry. Furthermore, our detailed investigation of crystallization processes, especially in thin film halide perovskites, has provided valuable insights into controlling material morphology and properties through intermediate phase engineering. The integration of advanced characterisation techniques, particularly *in situ* X-ray diffraction, has proven crucial for understanding both the static structure and dynamic processes in these materials. This work underscores the importance of fundamental structural understanding in the development of next-generation energy materials and provides a solid foundation for future research in this rapidly evolving field.

8.2 Future outlook

The work of this thesis opens several promising avenues for future research. Further optimisation and characterisation of the Bi-based hybrid materials and their applications in devices, as well as the development of new characterisation techniques to study dynamic processes in hybrid materials, will allow us to further understand the relationship between crystal structure and device performance. Specific areas of future research include:

Tuning intermolecular interactions in piezoelectric hybrid materials: In order to further explore the potential of and optimise Bi-based hybrid materials for piezoelectric applications, it is clear from the work in Chapters 4-6 that binding interactions between the organic and inorganic components can be essential for inducing highly non-centrosymmetric structures. Employing novel organic cations with a 'quasi-spherical' nature similar to $TMIM^+$ offers a route to finely tune halogen bonding

within the inorganic framework, thereby enhancing polarization. This could be achieved by modifying key properties such as the cation's size, the position of the halogen-bonding atom, and the number or type of halogen atoms. Furthermore, other types of intermolecular interactions could be explored within a given structural framework, or combined with halogen bonding.

Tuning the nature of the inorganic framework: Halobismuthates are known to form a large diversity of frameworks such as isolated BiX_6 units, edge-sharing $(Bi_2X_9)^{3-}$ dimers, or even larger units consisting of mixed edge- and face-sharing connectivities. Future work could explore the use of these different frameworks and assess their impact on centrosymmetry within a material.

Developing a geometrical descriptor for centrosymmetry: An even broader approach may be to work towards the development of a geometrical descriptor, akin to the tolerance factor for perovskites, in determining the centrosymmetry of a hybrid material, given shape, size and nature of the organic components and the choice and dimensionality of the inorganic framework.

Monitoring the coordination environment of metal and halide ions in precursor solutions *in situ*: To better understand perovskite crystallization, it is crucial to monitor the coordination environment of metal and halide ions in precursor solutions *in situ*. Combining these experimental observations with machine-learning-assisted molecular dynamics simulations would provide valuable insights. Suitable techniques for this purpose include X-ray absorption spectroscopy and solution NMR methods, such as Diffusion-ordered spectroscopy (DOSY).

Appendix A

Crystallographic Data and structural analysis

A.1 Simple point charge model calculations

A.1.1 Point charge calculations for $(TMIM)_3Bi_2I_9$

For a unit cell of volume V and atoms with point charge q_i, a simple point charge calculation for polarisation can be made using the following equation:

$$P = \frac{1}{V} \sum_{\substack{\text{atoms} \\ \text{in unit cell}}} q_i \mathbf{r}_i \tag{A.1}$$

Where $\mathbf{r}_i$ denotes atomic positions with respect to the centre of the unit cell. We assign a charge +3 for Bi, -1 for I, and +1 for N.

For example:

$$P_{\text{dimer 1}} = \frac{1}{V} \left(3 \sum_{1}^{2} \mathbf{r}_{\text{Bi}} - \sum_{1}^{9} \mathbf{r}_{\text{I}} \right) \tag{A.2}$$

And using

$$\frac{eV}{\text{Å}^2} = 1.602 \frac{\mu\text{C}}{\text{cm}^2} \tag{A.3}$$

For the 4 $[Bi_2I_9]^{3-}$ dimer in the unit cell for $(TMIM)_3Bi_2I_9$:

TABLE A.1: Point charge model calculations for the dimers in $(TMIM)_3Bi_2I_9$

Net polarisation ($\mu C/cm^2$)	P_x	P_y	P_z (polar axis)	$\|P\|$
Dimer 1	-12.21396763	2.12832658	-1.72544624	12.5175055
Dimer 2	-5.00238945	8.02502742	15.4909185	18.1492017
Dimer 3	5.00239711	15.0880381	7.33073354	17.504643
Dimer 4	12.21396379	9.42820620	15.4909185	21.8641382
Net polarisation	3.83469E-06	34.66959838	36.58712431	50.4043522

A similar calculation for the $(TMIM)^+$ cations (12 in the unit cell) leads to:

TABLE A.2: Point charge model calculations for the cations in $(TMIM)_3Bi_2I_9$

	P_x	P_y	P_z (polar axis)	$\|P\|$
Net polarisation ($\mu C/cm^2$)	0	3.60822E-16	-3.19816407	3.19816407

TABLE A.3: Total point charge polarisation for $(TMIM)_3Bi_2I_9$

	P_x	P_y	P_z (polar axis)	$\|P\|$
Total point charge polarisation ($\mu C/cm^2$)	3.83469×10^{-6}	34.66959838	33.38896024	48.12814773

A.1.2 Point charge calculations for $[(CH_3)_4N]_3Bi_2I_9$

For the $[Bi_2I_9]^{3-}$ dimers in the unit cell:

For the contribution from the $[(CH_3)_4N]^+$ cations:

TABLE A.4: Point charge model calculations for the dimers in $[(CH_3)_4N]_3Bi_2I_9$

	P_x	P_y	P_z (polar axis)	$\|P\|$
Dimer 1	-0.02171015	5.054497875	-15.61933435	16.4168214
Dimer 2	11.93737179	-1.850070094	12.64892235	17.4905358
Net polarisation from dimers	11.91566164	3.204427781	-2.970411999	12.6915207

TABLE A.5: Point charge model calculations for the cations in $[(CH_3)_4N]_3Bi_2I_9$

	P_x	P_y	P_z (polar axis)	$\|P\|$
Net polarisation ($\mu C/cm^2$)	-11.9156375	-3.204427781	3.248958533	12.7595653

TABLE A.6: Total point charge polarisation for $[(CH_3)_4N]_3Bi_2I_9$

	P_x	P_y	P_z (polar axis)	$\|P\|$
Total point charge polarisation ($\mu C/cm^2$)	2.41403×10^{-5}	-5.32907×10^{-15}	0.278546534	0.27854654

A.2 Berry phase polarisation calculations

TABLE A.7: Calculated polarisation vectors using Berry phase theory. All calculations in group (i) were conducted based on or by modifying the crystal structure of $(TMIM)_3Bi_2I_9$ in space group $Pna2_1$ at a temperature of 293 K (Fig. 1a in main text). The calculation for $Cs_3Bi_2I_9$ ($[(CH_3)_4N]_3Bi_2I_9$) in group (ii) was conducted by replacing the $[(CH_3)_4N]^+$ cation with Cs^+ in the crystal structure of $[(CH_3)_4N]_3Bi_2I_9$ in the space group $P3_1c$ as reported by Feldmann et al. (2001), discusseed in Chapter 4.

Composition	Space group	Polarisation vector (μC/cm^2)			$\lvert P\rvert/\lvert P_{ref}\rvert$
		P_x	P_y	P_z	
(i) $(TMIM)_3Bi_2I_9$	$Pna2_1$	0.000	3.57	0.000	10.2
(i) $[(CH_3)_4N]_3Bi_2I_9$	$Pna2_1$	0.000	2.31	0.000	6.6
(i) $Cs_3Bi_2I_9$	$Pna2_1$	0.000	2.28	0.000	6.5
(ii) $Cs_3Bi_2I_9$ / $[(CH_3)_4N]_3Bi_2I_9$	$P3_1c$	0.000	0.000	0.035	1.0

A.3 Crystallographic data for $(TMIM)_3Bi_2I_9$

TABLE A.8: Crystallographic data for $(TMIM)_3Bi_2I_9$at temperatures 273-323 K

Temperature /K	273	293	313	323
Empirical formula	$C_{24}H_{56}I_9N$	$C_{24}H_{56}I_9N$	$C_{24}H_{56}I_9N$	$C_{24}H_{56}I_9N$
Formula weight	2160.17	2160.17	2160.17	2160.17
Crystal system	orthorhombic	orthorhombic	orthorhombic	orthorhombic
Space group	$Pna2_1$	$Pna2_1$	$Pna2_1$	$Pna2_1$
a/Å	29.51660(16)	29.52090(17)	29.94670(19)	29.9956(2)
b/Å	9.81640(6)	9.83970(6)	9.86750(6)	9.88250(7)
c/Å	14.16770(7)	14.18660(8)	14.21300(8)	14.22780(8)
α, β, γ/°	90	90	90	90
Volume/Å^3	4160.68(4)	4178.11(4)	4199.31(4)	4211.24(5)
Z	4	4	4	4
ρ_{calc}/g/cm^3	3.449	3.434	3.416	3.407
μ/mm^{-1}	6.451	6.424	6.391	6.374
F(000)	3712	3712	3712	3712
Crystal size/mm^3	0.13 × 0.09 × 0.03	0.13 × 0.09 × 0.03	0.13 × 0.09 × 0.03	0.13 × 0.09 × 0.03
Radiation	Synchrotron (λ = 0.4859)	Synchrotron (λ = 0.4859)	Synchrotron (λ = 0.4859)	Synchrotron (λ = 0.4859)
2Θ range for data collection/°	3.724 to 40	3.724 to 40.582585	3.724 to 40.615298	3.718 to 40
Index ranges	-42 ≤ h ≤ 42, -11 ≤ k ≤ 13, -19 ≤ l ≤ 19	-42 ≤ h ≤ 42, -11 ≤ k ≤ 13, -19 ≤ l ≤ 19	-42 ≤ h ≤ 42, -11 ≤ k ≤ 13, -20 ≤ l ≤ 20	-42 ≤ h ≤ 42, -11 ≤ k ≤ 13, -20 ≤ l ≤ 20
Reflections collected	40487	38081	36063	30301
Independent reflections	11810 (R_{int} = 0.0730, R_{sigma} = 0.0363)	11810 (R_{int} = 0.0661, R_{sigma} = 0.0350)	11943 (R_{int} = 0.0646, R_{sigma} = 0.0326)	11580 (R_{int} = 0.0672, R_{sigma} = 0.0332)
Data/restraints/parameters	11810/1/270	11646/38/270	11943/38/270	11580/53/270
Goodness-of-fit on F^2	1.051	1.051	1.093	1.092
Final R indices [I>=2σ(I)]	R_1 = 0.0302, wR_2 = 0.0724	R_1 = 0.0321, wR_2 = 0.0899	R_1 = 0.0363, wR_2 = 0.1031	R_1 = 0.0391, wR_2 = 0.1079
Final R indices [all data]	R_1 = 0.0411, wR_2 = 0.0754	R_1 = 0.0441, wR_2 = 0.0904	R_1 = 0.0441, wR_2 = 0.1100	R_1 = 0.0538, wR_2 = 0.1165

TABLE A.9: Crystallographic data for $(TMIM)_3Bi_2I_9$at temperatures 333-363 K

Temperature /K	333	343	353	363
Empirical formula	$C_{24}H_{56}I_9N$	$C_{24}H_{56}I_9N$	$C_{24}H_{56}I_9N_1$	$C_{24}H_{56}I_9N_1$
Formula weight	2160.17	2160.17	2160.17	2160.17
Crystal system	orthorhombic	orthorhombic	orthorhombic	orthorhombic
Space group	$Pna2_1$	$Pna2_1$	$Pna2_1$	$Pna2_1$
a/Å	29.9544(2)	29.9545(3)	29.9482(3)	29.9339(3)
b/Å	9.89870(8)	9.91700(10)	9.93700(11)	9.96020(9)
c/Å	14.24460(11)	14.25390(14)	14.28574(15)	14.31310(12)
α, β, γ/°	90	90	90	90
Volume/Å^3	4223.66(6)	4237.22(7)	4251.36(8)	4267.42(7)
Z	4	4	4	4
ρ_{calc}/g/cm^3	3.397	3.386	3.375	3.362
μ/mm^{-1}	6.356	6.335	6.314	6.29
F(000)	3712	3712	3712	3712
Crystal size/mm^3	0.13 × 0.09 × 0.03	0.13 × 0.09 × 0.03	0.13 × 0.09 × 0.03	0.13 × 0.09 × 0.03
Radiation	Synchrotron (λ = 0.4859)	Synchrotron (λ = 0.4859)	Synchrotron (λ = 0.4859)	Synchrotron (λ = 0.4859)
2Θ range for data collection/°	3.724 to 40.583241	3.724 to 39.778859	3.39327 to 39.130358	3.724 to 39.99
Index ranges	-42 ≤ h ≤ 42, -11 ≤ k ≤ 13, -20 ≤ l ≤ 20	-42 ≤ h ≤ 42, -11 ≤ k ≤ 13, -20 ≤ l ≤ 20	-42 ≤ h ≤ 42, -11 ≤ k ≤ 13, -20 ≤ l ≤ 20	-42 ≤ h ≤ 42, -11 ≤ k ≤ 13, -20 ≤ l ≤ 20
Reflections collected	28900	24914	20004	30806
Independent reflections	12023 (R_{int} = 0.0737, R_{sigma} = 0.0362)	12044 (R_{int} = 0.0882, R_{sigma} = 0.0425)	12072 (R_{int} = 0.0894, R_{sigma} = 0.0430)	12088 (R_{int} = 0.0745, R_{sigma} = 0.0377)
Data/restraints/parameters	12023/99/267	12044/99/267	12072/99/265	12088/89/267
Goodness-of-fit on F^2	1.087	1.118	1.022	1.027
Final R indices [I>=2σ(I)]	R_1 = 0.0438, wR_2 = 0.1284	R_1 = 0.0493, wR_2 = 0.1394	R_1 = 0.0481, wR_2 = 0.1404	R_1 = 0.0511, wR_2 = 0.1496
Final R indices [all data]	R_1 = 0.0666, wR_2 = 0.1467	R_1 = 0.0666, wR_2 = 0.1636	R_1 = 0.0635, wR_2 = 0.1534	R_1 = 0.0680, wR_2 = 0.1622

TABLE A.10: Crystallographic data for $(TMIM)_3Bi_2I_9$at temperatures 373-403 K

Temperature /K	373	383	393	403
Empirical formula	$C_{24}H_{56}I_9N_1$	$C_{24}H_{56}I_9N_1$	$C_{24}H_{56}I_9N_1$	$C_{24}H_{56}I_9N_1$
Formula weight	2160	2160	2160	2160
Crystal system	orthorhombic	orthorhombic	orthorhombic	orthorhombic
Space group	$Pna2_1$	$Pna2_1$	$Pna2_1$	$Pna2_1$
a/Å	29.9141(3)	29.8895(3)	29.8367(3)	29.7386(4)
b/Å	9.98170(10)	10.00330(11)	10.03340(11)	10.07620(19)
c/Å	14.33974(13)	14.36939(13)	14.41049(13)	14.47960(18)
α, β, γ/°	90	90	90	90
Volume/Å^3	4281.74(7)	4296.93(7)	4313.95(8)	4338.84(12)
Z	4	4	4	4
ρ_{calc}/g/cm^3	3.351	3.339	3.327	3.307
μ/mm^{-1}	6.269	6.247	6.222	6.186
F(000)	3712	3712	3712	3712
Crystal size/mm^3	0.13 × 0.09 × 0.03	0.13 × 0.09 × 0.03	0.13 × 0.09 × 0.03	0.13 × 0.09 × 0.03
Radiation	Synchrotron (λ = 0.4859)	Synchrotron (λ = 0.4859)	Synchrotron (λ = 0.4859)	Synchrotron (λ = 0.4859)
2Θ range for data collection/°	3.370284 to 39.402213	3.726 to 40	3.724 to 39.998	3.746 to 40
Index ranges	-42 ≤ h ≤ 42, -11 ≤ k ≤ 13, -20 ≤ l ≤ 20	-42 ≤ h ≤ 42, -11 ≤ k ≤ 13, -20 ≤ l ≤ 20	-42 ≤ h ≤ 42, -11 ≤ k ≤ 13, -20 ≤ l ≤ 20	-41 ≤ h ≤ 41, -11 ≤ k ≤ 11, -20 ≤ l ≤ 20
Reflections collected	21144	81609	81999	83684
Independent reflections	12119 (R_{int} = 0.0716, R_{sigma} = 0.0365)	12182 (R_{int} = 0.0688, R_{sigma} = 0.0368)	12182 (R_{int} = 0.0666, R_{sigma} = 0.0217)	12260 (R_{int} = 0.0584, R_{sigma} = 0.0356)
Data/restraints/parameters	12119/99/264	12182/99/264	12182/132/262	12260/144/285
Goodness-of-fit on F^2	0.987	0.938	0.796	0.796
Final R indices [I>=2σ(I)]	R_1 = 0.0523, wR_2 = 0.1534	R_1 = 0.0546, wR_2 = 0.1632	R_1 = 0.0557, wR_2 = 0.1680	R_1 = 0.0572, wR_2 = 0.1682
Final R indices [all data]	R_1 = 0.0722, wR_2 = 0.1622	R_1 = 0.0797, wR_2 = 0.1632	R_1 = 0.0805, wR_2 = 0.1680	R_1 = 0.1006, wR_2 = 0.1682

TABLE A.11: Crystallographic data for $(TMIM)_3Bi_2I_9$at 413 K

Temperature /K	413
Empirical formula	$Bi_2C_{24}H_{112}N_{12}$
Formula weight	1959.63
Crystal system	orthorhombic
Space group	$Pna2_1$
a/Å	10.1691(4)
b/Å	14.6803(4)
c/Å	14.6936(3)
α, β, γ/°	90
Volume/Å^3	2193.54(11)
Z	2
ρ_{calc}/g/cm^3	2.967
μ/mm^{-1}	5.885
F(000)	1641
Crystal size/mm^3	0.13 × 0.09 × 0.03
Radiation	Synchrotron ($\lambda = 0.4859$)
2Θ range for data collection/°	3.33 to 40.612
Index ranges	$-13 \leq h \leq 11$, $-20 \leq k \leq 20$, $-20 \leq l \leq 20$
Reflections collected	44465
Independent reflections	6768 ($R_{int} = 0.0369$, $R_{sigma} = 0.0256$)
Data/restraints/parameters	6768/49/133
Goodness-of-fit on F^2	0.788
Final R indices [I>=2σ(I)]	$R_1 = 0.0592$, $wR_2 = 0.1792$
Final R indices [all data]	$R_1 = 0.1062$, $wR_2 = 0.2131$
Largest diff. peak/hole / e Å^{-3}	1.28/-1.14
Flack parameter	0.003(6)

A.4 Thermal ellipsoids for (TMIM)$_3$Bi$_2$I$_9$

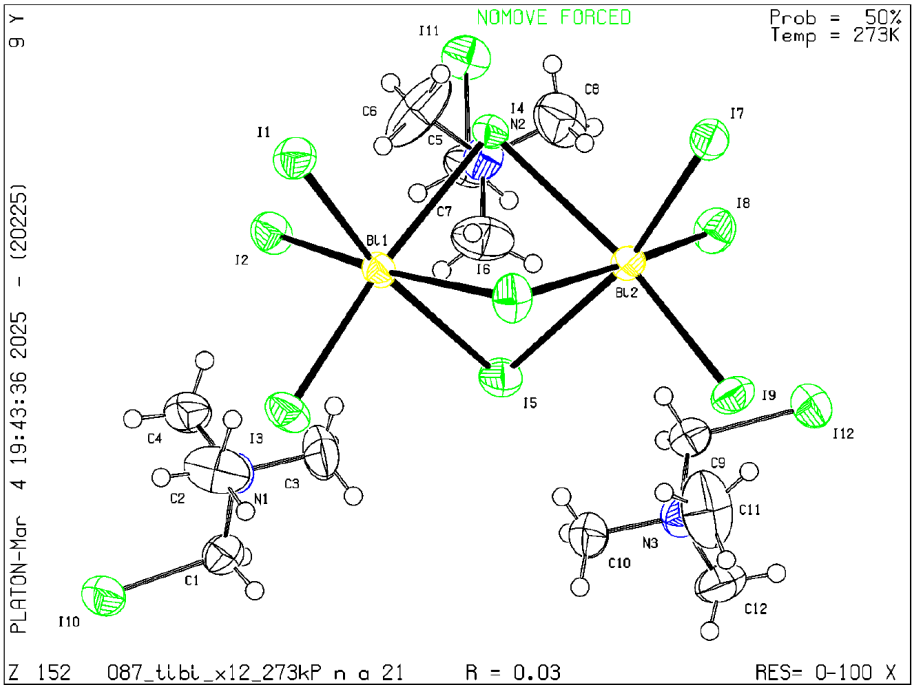


FIGURE A.1: Oak Ridge Thermal Ellipsoid Plot (ORTEP) diagram of (TMIM)$_3$Bi$_2$I$_9$at 273K, ellipsoids at 50%.

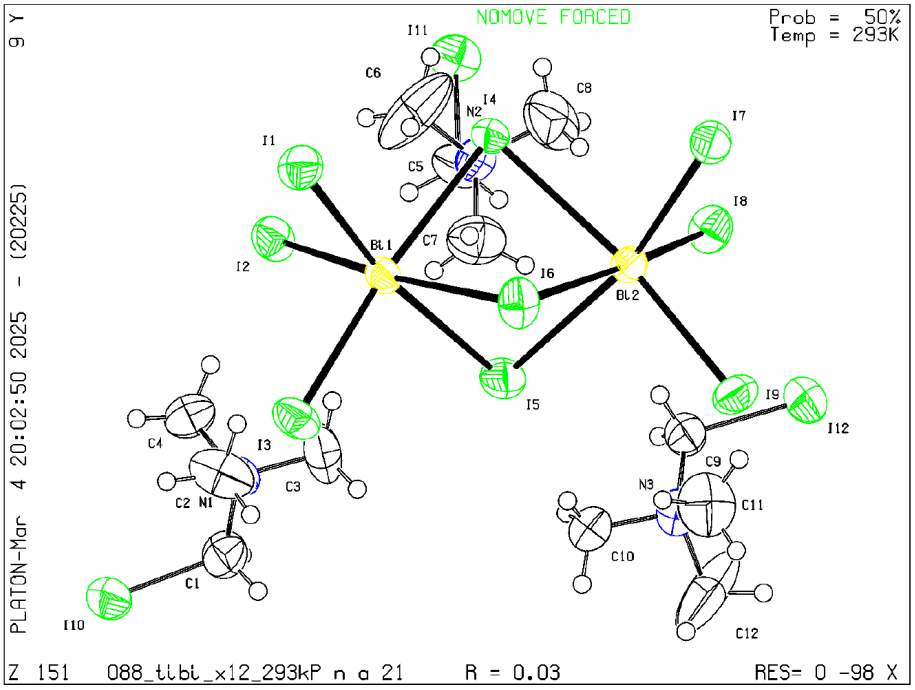


FIGURE A.2: ORTEP diagram of $(TMIM)_3Bi_2I_9$at 293K, ellipsoids at 50%.

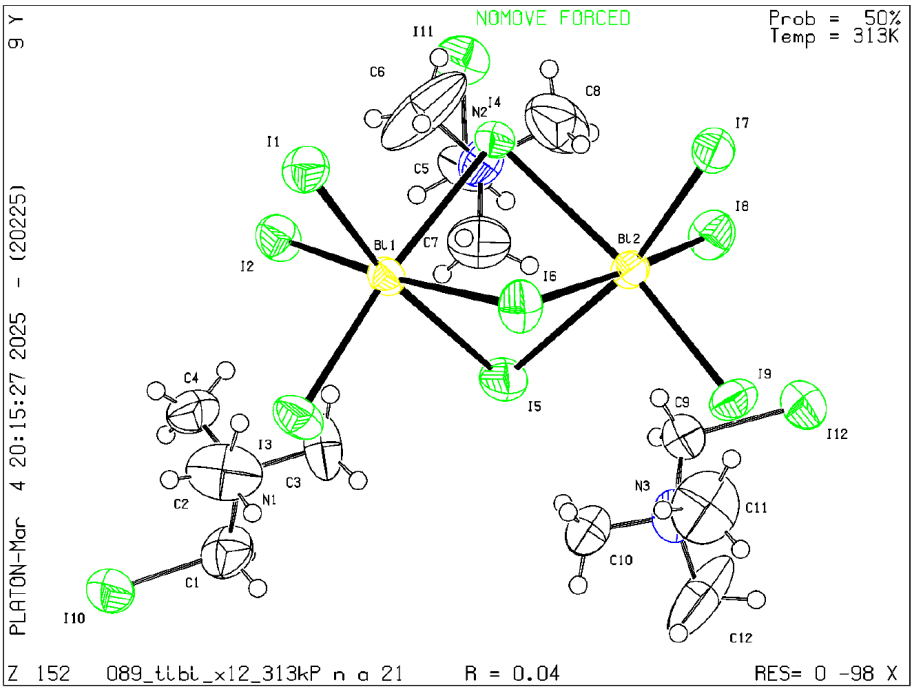


FIGURE A.3: ORTEP diagram of $(TMIM)_3Bi_2I_9$at 313K, ellipsoids at 50%.

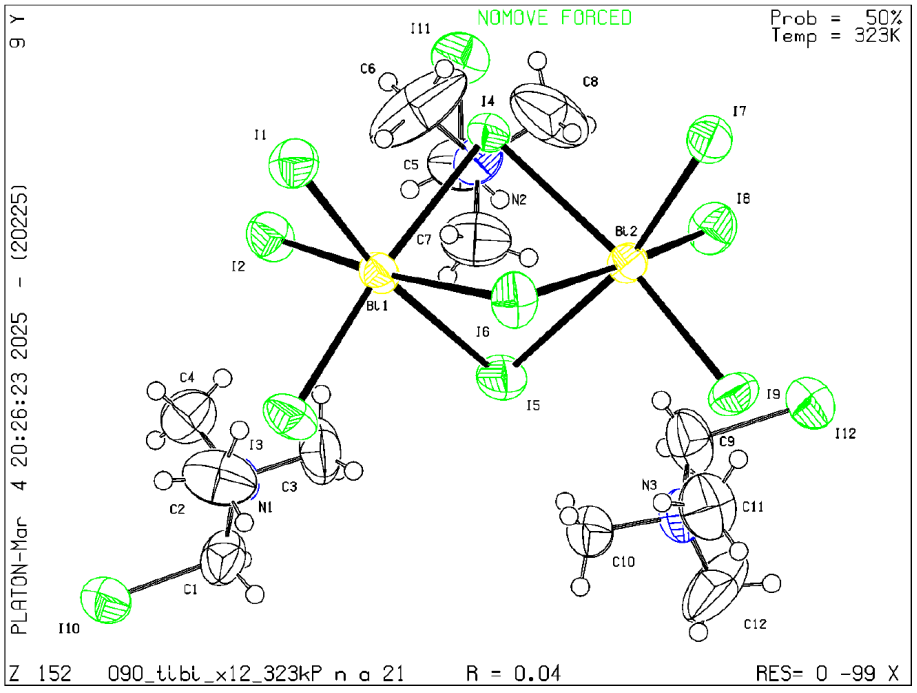


FIGURE A.4: ORTEP diagram of $(TMIM)_3Bi_2I_9$at 323K, ellipsoids at 50%.

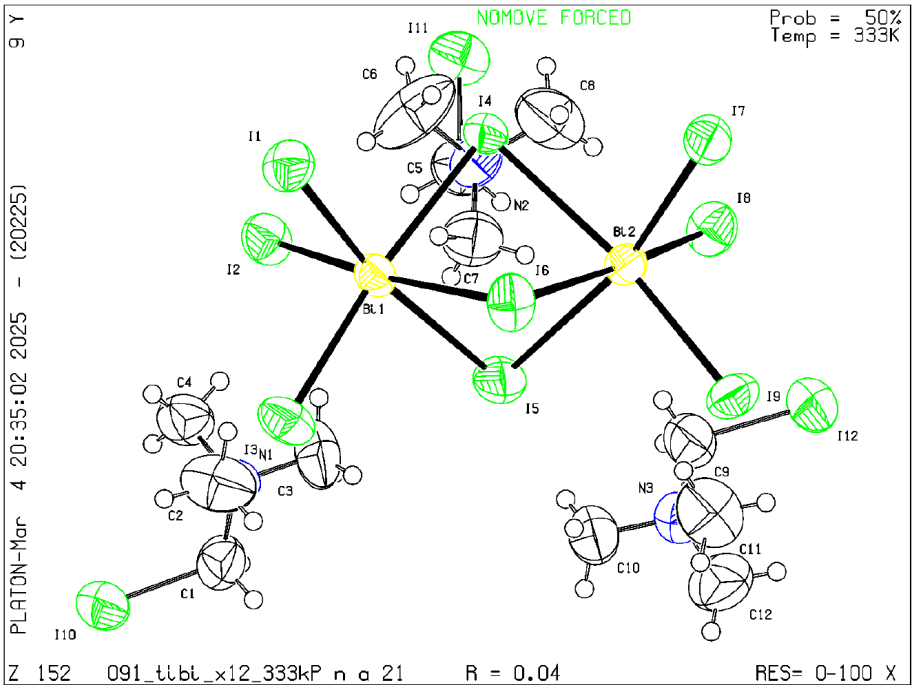


FIGURE A.5: ORTEP diagram of $(TMIM)_3Bi_2I_9$at 333K, ellipsoids at 50%.

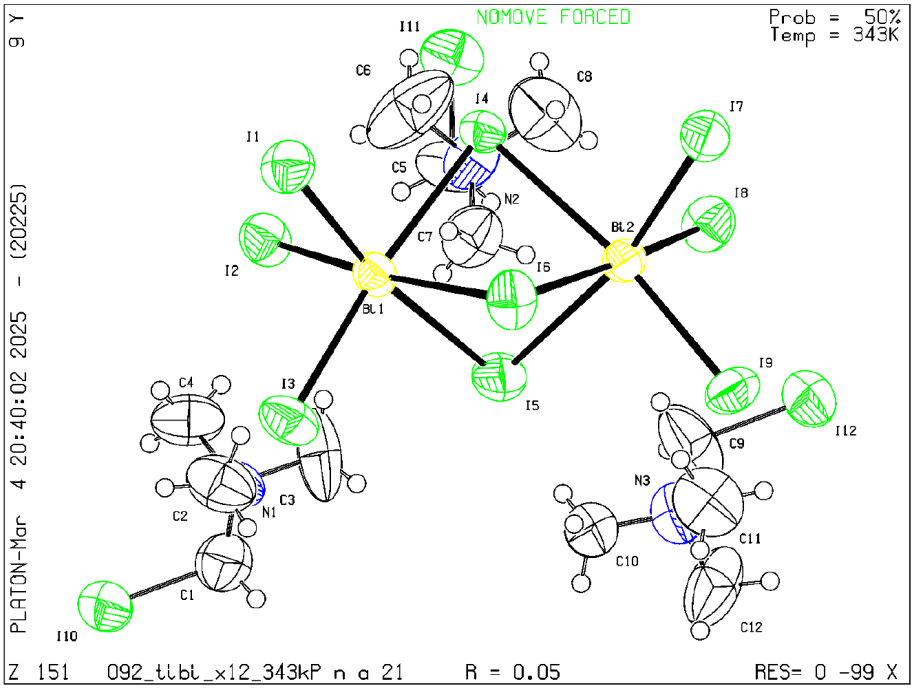


FIGURE A.6: ORTEP diagram of $(TMIM)_3Bi_2I_9$at 343K, ellipsoids at 50%.

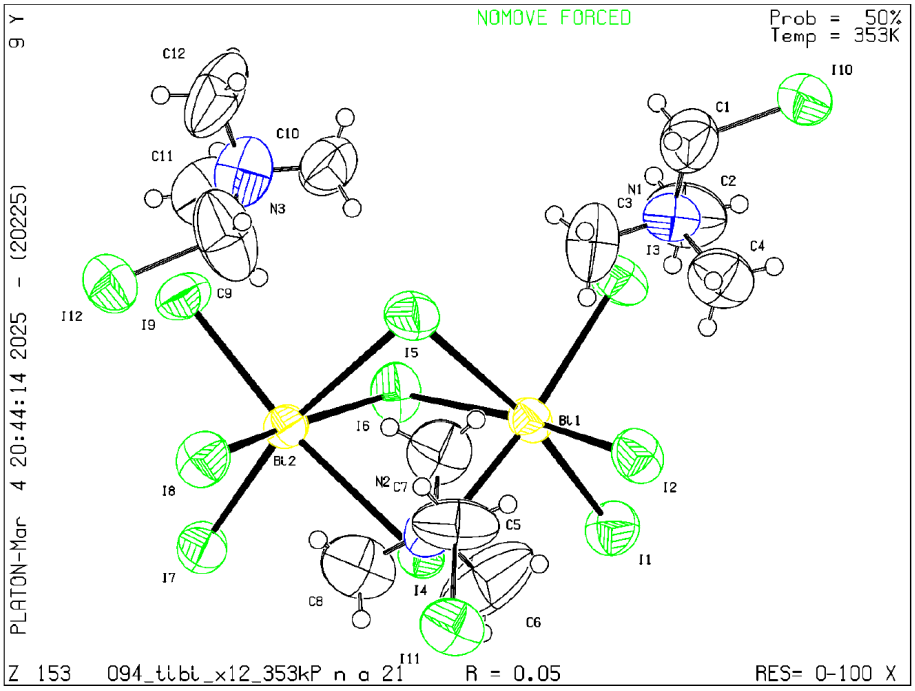


FIGURE A.7: ORTEP diagram of $(TMIM)_3Bi_2I_9$at 353K, ellipsoids at 50%.

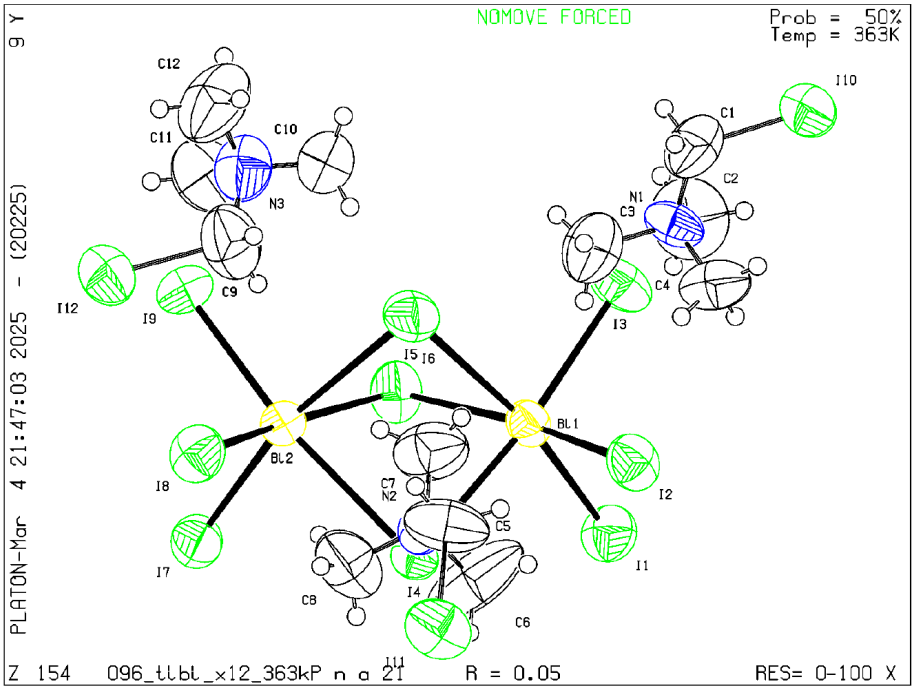


FIGURE A.8: ORTEP diagram of $(TMIM)_3Bi_2I_9$at 363K, ellipsoids at 50%.

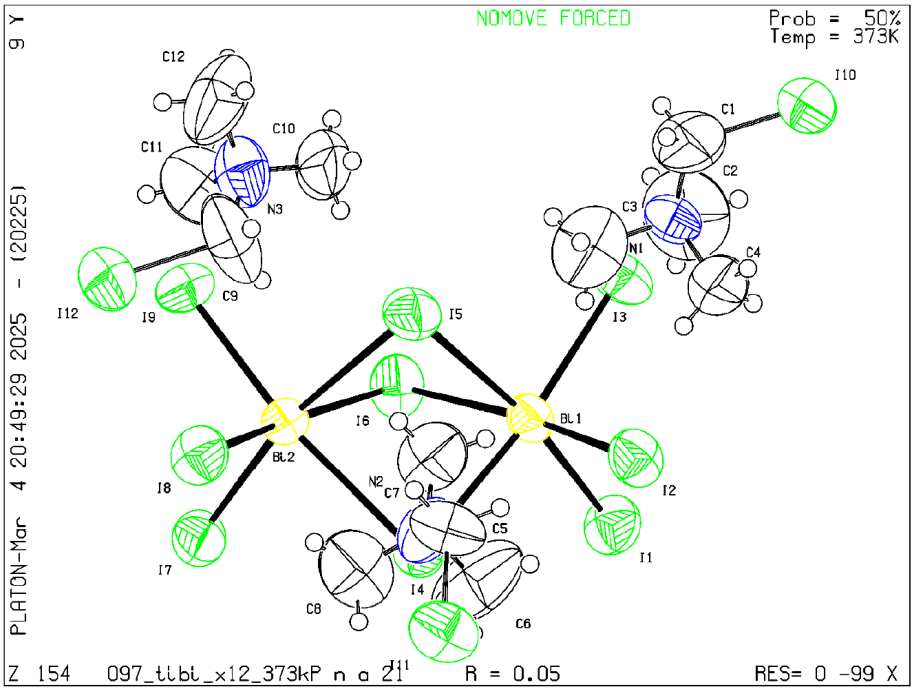


FIGURE A.9: ORTEP diagram of $(TMIM)_3Bi_2I_9$at 373K, ellipsoids at 50%.

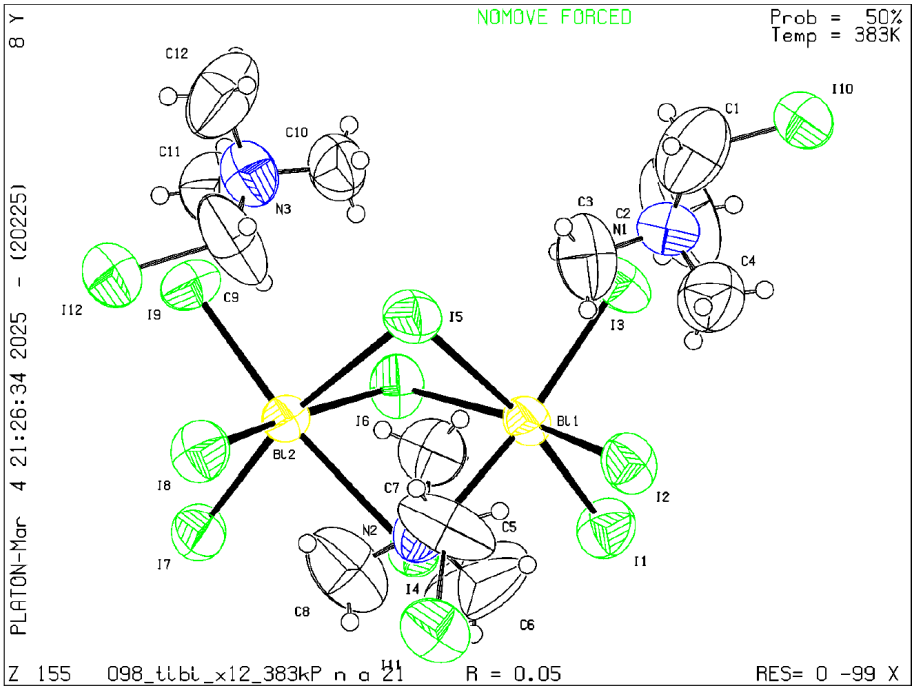


FIGURE A.10: ORTEP diagram of $(TMIM)_3Bi_2I_9$at 383K, ellipsoids at 50%.

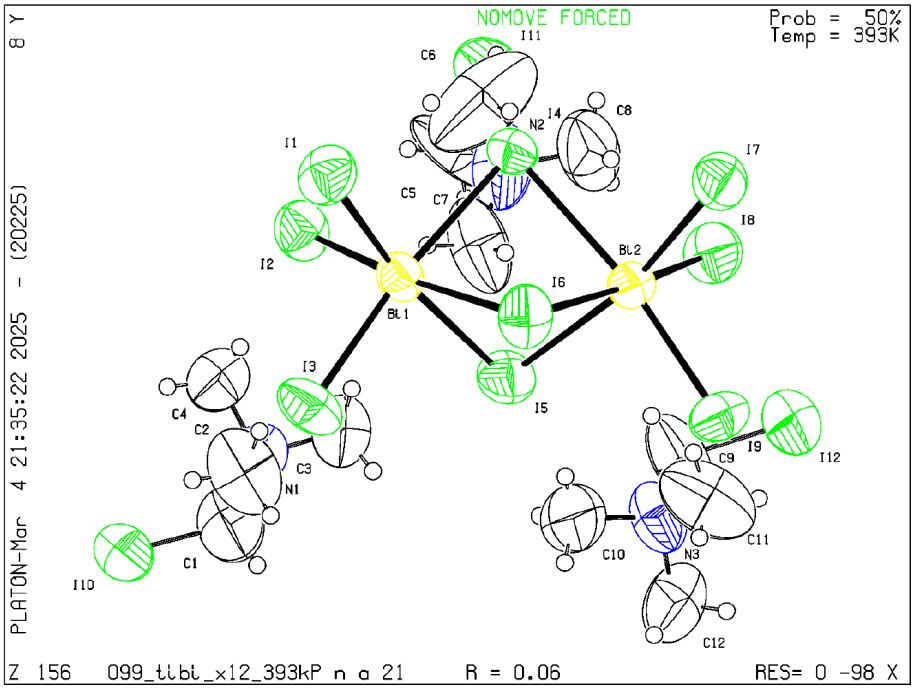


FIGURE A.11: ORTEP diagram of $(TMIM)_3Bi_2I_9$at 393K, ellipsoids at 50%.

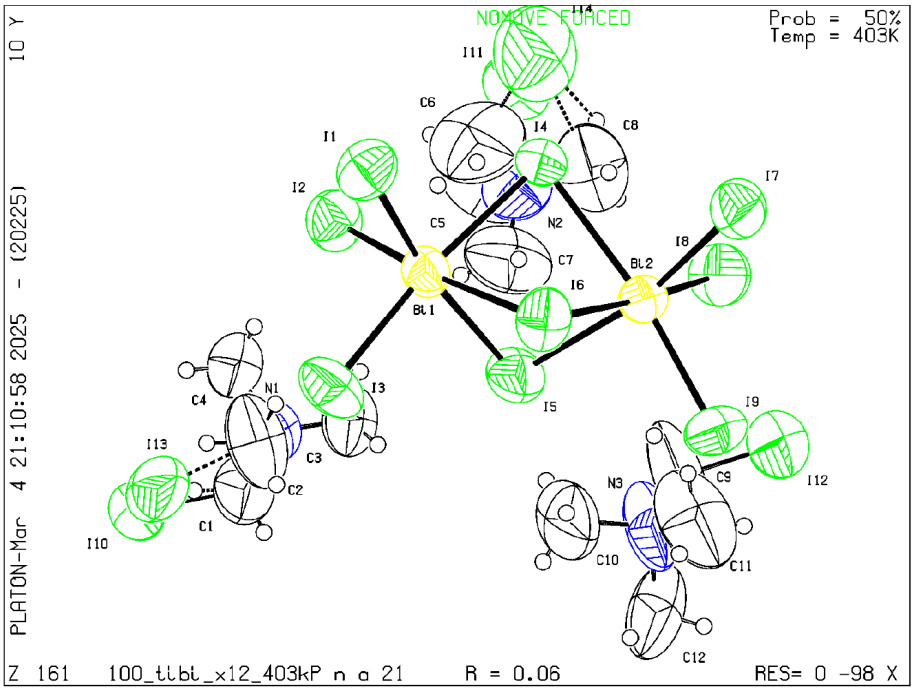


FIGURE A.12: ORTEP diagram of $(TMIM)_3Bi_2I_9$at 403K, ellipsoids at 50%.

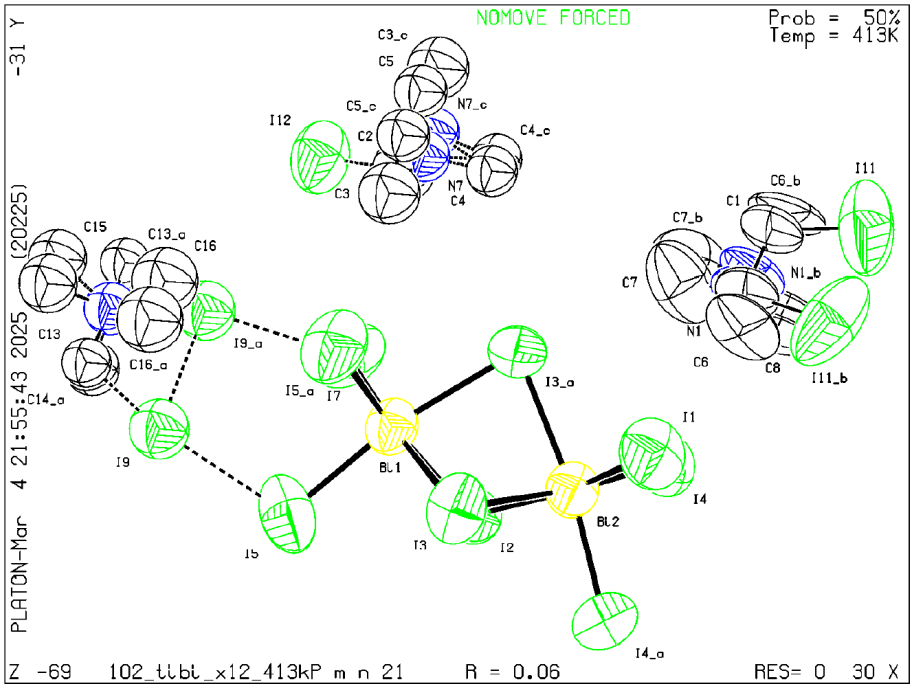


FIGURE A.13: ORTEP diagram of $(TMIM)_3Bi_2I_9$at 413K, ellipsoids at 50%.

Appendix B

Chapter 5: Crystallographic Data

B.1 Crystallographic Data for $(TMBM)_3Bi_2Br_9$

TABLE B.1: Crystallographic data for $(TMBM)_3Bi_2Br_9$ at 315 K

Temperature /K	315
Empirical formula	$C_{12}H_{33}N_3Cl_{12}Bi_2$
Formula weight	1062.77
Crystal system	hexagonal
Space group	$P6_3mc$
a/Å	9.4578(4)
b/Å	9.4578(4)
c/Å	22.4632(9)
α, β, γ/°	90, 120
Volume/Å^3	1740.12(16)
Z	2
ρ_{calc}/g/cm^3	2.028
μ/mm^{-1}	4.106
F(000)	992.0
Crystal size/mm^3	0.185 × 0.17 × 0.073
Radiation	Synchrotron (λ = 0.4859)
2Θ range for data collection/°	3.4 to 50.508
Index ranges	-15 ≤ h ≤ 15, -15 ≤ k ≤ 15, -38 ≤ l ≤ 38
Reflections collected	39692
Independent reflections	3372 (R_{int} = 0.0366, R_{sigma} = 0.0242)
Data/restraints/parameters	3372/1/31
Goodness-of-fit on F^2	1.051
Final R indices [I>=2σ(I)]	R_1 = 0.0866, wR_2 = 0.2400
Final R indices [all data]	R_1 = 0.1317, wR_2 = 0.2694
Largest diff. peak/hole	1.61/-0.86
Flack parameter	0.43(4)

B.2 Crystallographic Data for $(TMIM)_3Sb_2I_9$

TABLE B.2: Crystallographic data for $(TMIM)_3Sb_2I_9$ at temperatures 280 and 413 K

Temperature /K	280	413
Empirical formula	$C_{12}H_{33}I_{12}N_3Sb_2$	$C_{7.7}I_{10.93}N_{1.93}Sb_2$
Formula weight	1985.71	1751.16
Crystal system	orthorhombic	orthorhombic
Space group	$Pna2_1$	$Pmn2_1$
a/Å	29.76980(12)	10.2183(3)
b/Å	9.87470(4)	14.4645(4)
c/Å	14.00320(6)	14.6828(5)
α, β, γ/°	90	90
Volume/Å^3	4116.49(3)	2170.16(11)
Z	4	2
ρ_{calc}/g/cm^3	3.204	2.680
μ/mm^{-1}	3.794	5.901
F(000)	3456.0	1483.0
Crystal size/mm^3	0.2 × 0.16 × 0.1	0.2 × 0.16 × 0.1
Radiation	Synchrotron (λ = 0.4859)	Synchrotron (λ = 0.4859)
2Θ range for data collection/°	2.73 to 39.998	3.32 to 40.598
Index ranges	-41 ≤ h ≤ 41, -13 ≤ k ≤ 13, -19 ≤ l ≤ 19	-14 ≤ h ≤ 14, -20 ≤ k ≤ 20, -20 ≤ l ≤ 20
Reflections collected	78135	43769
Independent reflections	11968 (R_{int} = 0.0484, R_{sigma} = 0.0484)	6926 (R_{int} = 0.0450, R_{sigma} = 0.0341)
Data/restraints/parameters	11968/11/270	6926/49/133
Goodness-of-fit on F^2	1.137	0.706
Final R indices [I>=2σ(I)]	R_1 = 0.0304, wR_2 = 0.0867	R_1 = 0.0764, wR_2 = 0.2392
Final R indices [all data]	R_1 = 0.0336, wR_2 = 0.0978	R_1 = 0.1500, wR_2 = 0.2886
Largest diff. peak/hole	2.74/-1.32	1.03/-0.71
Flack parameter	-0.03(5)	0.513(4)

Appendix C

Chapter 6:Crystallographic Data

C.1 Crystallographic data for $CsSnI_3 \cdot 3(C_2H_6OS)$

TABLE C.1: Crystallographic data for $CsSnI_3{\cdot}3(C_2H_6OS)$ at 293 K

Temperature /K	293
Empirical formula	$CsSnI_3{\cdot}3(C_2H_6OS)$
Formula weight	866.68
Crystal system	orthorhombic
Space group	$Pna2_1$
a/Å	21.5772(5)
b/Å	10.3764(2)
c/Å	9.7866(3)
α, β, γ/°	90
Volume/Å^3	2191.14(9)
Z	4
ρ_{calc}/g/cm^3	2.627
μ/mm^{-1}	7.312
F(000)	1560.0
Crystal size/mm^3	$1 \times 0.5 \times 0.3$
Radiation	Synchrotron ($\lambda = 0.4859$)
2Θ range for data collection/°	6.858 to 61.676
Index ranges	$-21 \leq h \leq 27$, $-12 \leq k \leq 12$, $-12 \leq l \leq 14$
Reflections collected	10305
Independent reflections	4817 ($R_{int} = 0.0197$, $R_{sigma} = 0.0292$)
Data/restraints/parameters	4817/1/160
Goodness-of-fit on F^2	1.071
Final R indices [I>=2σ(I)]	$R_1 = 0.0316$, $wR_2 = 0.0632$
Final R indices [all data]	$R_1 = 0.0406$, $wR_2 = 0.0697$
Largest diff. peak/hole / e Å^{-3}	0.63/-1.38
Flack parameter	0.025(13)